Search for new physics in proton-proton collision events with a lepton and missing transverse energy

Der Fakultät für Mathematik, Informatik und Naturwissenschaften
der RWTH Aachen University vorgelegte Dissertation
zur Erlangung des akademischen Grades eines
Doktors der Naturwissenschaften

von

Diplom-Physiker Mark Olschewski

aus Aachen

Zusammenfassung

Zerfälle in ein einzelnes Lepton und fehlende Transversalenergie sind eine interessante Signatur für die Suche nach Physik jenseits des Standardmodells. Kollisionen mit 8 TeV Schwerpunktsenergie, wie sie 2012 am CERN LHC stattfanden, haben das Entdeckungspotential für solche Signale erweitert. In dieser Arbeit wurden Ereignisse des CMS-Experiments, die einer Luminosität von 19.7 fb^{-1} entsprechen, im Elektron- und im Myonkanal untersucht.

Diese Daten werden im Kontext mehrerer Modelle interpretiert: Das dem Standardmodel W-Boson ähnelnde W′-Boson, helizitätsverändernde Kontaktinteraktionen und ein Modell mit paarproduzierter dunkler Materie sind in diesem Zusammenhang entdeckbar.

Eine signifikante Abweichung der Daten von der Standardmodellvorhersage konnte nicht gefunden werden. Eine Ausschlussgrenze auf die Masse des W′-Bosons von 3.28 TeV wurde bestimmt. Im Kontaktinteraktionsmodell kann eine Interaktionsskala unterhalb von 12.4 TeV ausgeschlossen werden. Im Modell mit dunkler Materie können Grenzen auf die Masse der Dunkle-Materie-Teilchen und die Energieskala der Interaktion bestimmt werden.

Diese drei Modelle werden auch im Hinblick auf das Potential des zukünftigen LHC-Programms mit hoher Luminosität von 3000 fb^{-1} bei einer Schwerpunktsenergie $\sqrt{s} = 14\,\text{TeV}$ untersucht. Hierbei ist ein W′-Boson mit einer Masse von 7 TeV entdeckbar.

Wenn eine signifikante Abweichung der Daten von der Standardmodellvorhersage auftritt, können verschiedene konkurrierenden Modelle eine Erklärung dafür liefern. Es wird die integrierte Luminosität bestimmt, die notwendig ist um die verschiedenen Modelle zu unterscheiden.

Abstract

The production of a single lepton with opposing missing transverse energy is a distinct signature and provides an interesting opportunity to search for physics not explained by the standard model. The 8 TeV run of the CERN LHC in 2012 improved the discovery range for such a signal. In this thesis collisions of the CMS experiment corresponding to $19.7\,\text{fb}^{-1}$ with an electron or a muon are examined.

The data are interpreted in terms of a number of different models. The sequential standard model W′ boson, the helicity nonconserving contact interaction model, and a model with pair-produced dark matter are all expected to be discoverable in this framework.

No significant deviation of the data from the standard model expectation is observed. A limit of 3.28 TeV on the W′ boson mass in the sequential standard model is determined. In the contact interaction model an interaction scale below 12.4 TeV is excluded. In the dark matter model limits in terms of the mass of the dark matter particle and the scale of the considered theory are determined.

The three models are also evaluated to determine the future potential of the high luminosity LHC run with $3000\,\text{fb}^{-1}$ at $\sqrt{s} = 14\,\text{TeV}$. A sequential standard model with a mass of 7 TeV is expected to be discoverable with such a configuration. In case a significant deviation of the data compared to the standard model expectation occurs, competing models describing the signal must be discriminated. In this context the distinction potential is determined, providing a measure of how well two models can be distinguished. The integrated luminosity required to discriminate different models is determined using this measure.

Contents

1. Introduction

The standard model of particle physics is a well tested and established model. However, the description of physics is not complete and the search for new phenomena is always ongoing. The particle collider LHC provides excellent conditions for testing the standard model and searching for new physics. In this thesis, events with a lepton and missing transverse energy are examined using the CMS detector.

The lepton and missing transverse energy final state is a distinct event signature. It is constituted from only one identified particle, an electron or a muon. One or more particles in the event remain undetected but their incidence can be reconstructed from the total transverse momentum in the event.

It is a promising search channel in terms of the discovery of new physics. The missing transverse energy can originate from neutrinos but also from new unknown particles, such as dark matter particles. The event signature is that of a W boson and several theories suggest the existence of a heavy analogue to the standard model W boson. The clear signature of the channel does not require complicated selection criteria and therefore enables a model independent analysis to some degree. The accessible energy range extends far into the multi TeV regime.

Events acquired by the CMS detector from proton-proton collisions at a center-of-mass energy of 8 TeV are analyzed. The data was recorded in 2012 and corresponds to 19.5 fb^{-1}. The recorded events are selected based on model independent quality criteria.

A particle decaying into a lepton and one or more invisible particles, e.g. a neutrino, manifests itself as a resonance in the invariant mass distribution. However, the momenta of the invisible particles are not accessible, but their total transverse momentum can be reconstructed as the transverse momenta of all particles must be balanced. The missing transverse momentum/energy is the total transverse momentum of the invisible particles and can be used to determine the transverse mass of the originally decaying particle. Neglecting the mass of the decay products, the transverse mass can be calculated as:

$$M_T = \sqrt{2 \cdot E_T^{\mathrm{miss}} \cdot p_T^{\ell} \cdot \cos(\Delta\varphi(\vec{E_T^{\mathrm{miss}}}, \vec{\ell}))}, \tag{1.1}$$

where E_T^{miss} is the missing transverse energy, p_T^{ℓ} (hereafter: p_T) is the transverse momentum of the lepton, and $\Delta\varphi$ is the angle in the ϕ–ρ plane between the lepton and the direction of the missing transverse energy. The transverse mass distribution of a decaying massive particle shows a Jacobian peak, which can be described as a distribution gradually increasing up to the mass of the particle followed by a steep decline. Non-resonant signals also show distinctive signatures in the M_T distribution. Therefore, this quantity is used throughout this work as the main discriminating variable.

The M_T distributions of the electron and muon channels are compared to the standard model prediction and the simulation of several beyond the standard model (BSM) signals. A statistical

interpretation is performed to find significant deviations and to determine exclusion limits in terms of the new physics models.

The operation of the LHC continues, in the long term running with $\sqrt{s} = 14\,\text{TeV}$ is envisaged accumulating a total integrated luminosity of $3000\,\text{fb}^{-1}$. Such a large project will only be funded and performed if it is conclusively substantiated. The potential of the analysis is evaluated by determining the discovery thresholds for different BSM signals. In case a significant deviation is found, it will be important to identify those models that are compatible with the deviation. A distinction potential is determined describing how much luminosity is required to discriminate different signals.

This thesis is structured as follows. This introductory chapter is followed by two theoretical chapters: chapter 2 summarizes the physical theories which are relevant for the following analyses, standard model as well as beyond the standard model theories; and chapter 3 explains the statistical methods that are used for the analyses. Chapter 4 provides a synopsis of the experimental setup used for the later analysis and also of the envisaged upgrades, which are of importance for the study of the future sensitivity. Chapter 5 contains the details of the analysis performed with the $\sqrt{s} = 8\,\text{TeV}$ data, the results of which is derived in chapter 6. The last part of this thesis gives an outlook to the future sensitivity of the lepton and missing transverse energy channels at the CMS detector. Again this is split up into the analysis in chapter 7 and the results in chapter 8.

Parts of the described analyses and their results have already been published. The $\sqrt{s} = 8\,\text{TeV}$ analysis is published in reference [1] and its predecessor in reference [2], which uses a subset of the data. The individual electron and muon channels have been thoroughly studied in references [3] and [4] respectively. Parts of the $\sqrt{s} = 14\,\text{TeV}$ extrapolations are publicly available in references [5] and [6]. Figures prepared by others than me are cited in the first sentence of the figure caption. No citation is given for figures that are already included in one of the mentioned publications if they have been created by me.

2. Theory

The standard model of particle physics describes all known particles together with the interaction between them. It includes the electromagnetic, the weak, and the strong interactions. Besides gravity this covers all fundamental forces known today. It is widely acknowledged inside the scientific community, as it has been thoroughly tested and could not be disproved.

In the first section of this chapter, a short overview of the standard model is presented, mainly based on references [7, 8]. Of special importance for the presented analysis is the electroweak interaction. This interaction does not only provide the dominant background of the analysis and therefore is the one tested in this analysis, but it is also the foundation for most of the examined signal hypotheses. Their theories are discussed in the second section of this chapter.

2.1. Standard model of particle physics

2.1.1. Particles and interactions

Today, a number of different elementary particles are known. These are expected to be pointlike and structureless. They may have a mass and have quantum numbers associated, such as spin, electric charge, color charge, etc. Obeying certain rules, the particles can couple to each other and thereby can be transformed into each other.

Matter is composed from fermions, namely quarks and leptons, which are spin-1/2 particles. There are six flavors of quarks, grouped into three generations: up and down quark, charm and strange quark, top and bottom quark. The leptons can also be subdivided into three generations, each composed from one charged lepton and its respective neutrino: electron, muon, and tau. For each fermion a respective antiparticle is postulated, which has the same mass but inverted charge. The fermion properties are listed in table 2.1.

Interactions are mediated by integer spin particles, called bosons. The strong interaction is carried by gluons, the electromagnetic interaction by photons and the weak interaction by W and Z bosons. The Higgs boson is generated by the Higgs-mechanism and couples to other particles with the strength of their mass.

2.1.2. Electroweak interactions

Electroweak interactions are a combination of electromagnetic and weak interactions and are mediated by photons, W, and Z bosons. The photon, which mediates the electromagnetic interactions, is massless and stable, therefore it has an infinite range. The large masses of the W and Z bosons result in a very short lifetime and a limited range of the weak interactions.

Table 2.1.: Elementary particles and some of their properties [9].

	Name	Letter	Spin	Charge	Mass
Quarks	up quark	u	1/2	2/3	2.3 MeV
	down quark	d	1/2	-1/3	4.8 MeV
	charm quark	c	1/2	2/3	1.275 GeV
	strange quark	s	1/2	-1/3	95 MeV
	top quark	t	1/2	2/3	173.21 GeV
	bottom quark	b	1/2	-1/3	4.18 GeV
Leptons	electron neutrino	ν_e	1/2	2/3	< 2 eV
	electron	e	1/2	2/3	511 keV
	muon neutrino	ν_μ	1/2	2/3	< 0.19 MeV
	muon	μ	1/2	2/3	106 MeV
	tau neutrino	ν_τ	1/2	2/3	< 18.2 MeV
	tau	τ	1/2	2/3	1.777 GeV
Bosons	Photon	γ	1	0	0
	Gluon	g	1	0	0
	Z boson	Z	1	0	91.2 GeV
	W boson	W	1	± 1	80.4 GeV
	Higgs boson	H	0	0	125.7 GeV

Weak interactions are subject to two distinct features: They are parity violating and can be flavor changing. The W boson exclusively couples to left-chiral fermions and right-chiral antifermions. The coupling of the Z boson depends on both, the fermion flavor and the chirality. While only left-chiral neutrinos couple to Z bosons, the coupling to other fermions exists for both chiralities but is stronger for left-chiral cases. For charged leptons, this asymmetry is relatively small, for down-type quarks it is relatively strong, and the up-type quark asymmetry is in between.

Flavor change only happens with charged weak interactions, e.g. an electron coupling to a W boson yields an electron neutrino. Quarks interacting with a W boson can even yield a quark of a different generation, although the probability for this effect, called quark mixing, is small. The transition probabilities are given by the squares of the Cabibbo-Kobayashi-Maskawa matrix (CKM matrix).

The Glashow-Weinberg-Salam (GSW) model describes the electroweak interactions using a $\mathrm{SU}(2)_L \times \mathrm{U}(1)$ symmetry group. The $\mathrm{SU}(2)$ has three generators and therefore gives rise to

three gauge bosons, W_0, W_1, and W_2. They only couple to left chiral fermions. This is described by a quantum number, the weak isospin I. The left-handed charged lepton and neutrino form a doublet with $I = 1/2$ and the right handed charged lepton forms a singlet with $I = 0$.

The $\mathrm{U}(1)$ group generates a fourth boson B. The associated quantum number is called the weak hypercharge Y.

The observable boson eigenstates are formed as linear combinations:

$$W^+ = \frac{1}{\sqrt{2}}(W_1 - iW_2), \tag{2.1}$$

$$W^- = \frac{1}{\sqrt{2}}(W_1 + iW_2), \tag{2.2}$$

$$A = \cos\theta_W \cdot B + \sin\theta_W \cdot \mathrm{W}_0, \tag{2.3}$$

$$Z = -\sin\theta_W \cdot B + \cos\theta_W \cdot \mathrm{W}_0. \tag{2.4}$$

The parameter θ_W describes the mixing of the Z boson and the photon and is called the Weinberg angle. Its value is not predicted by the standard model and has been measured to $\sin^2(\theta_W) \approx 0.23$ [9].

2.1.3. Strong interactions

The Δ^{++} baryon is made of three u quarks and has a spin of $3/2$, i.e. all quarks must have the same spin direction. This appears to be a contradiction to the Pauli principle, but can be explained by introducing an additional quantum number, called color charge. It can take three different states, red, green, and blue, as well as the corresponding antistates for antiquarks.

The strong interaction can be described by quantum chromodynamics, which is a gauge theory with an underlying $\mathrm{SU}(3)$ symmetry group. It's eight degrees of freedom give rise to eight additional gauge bosons, called gluons. Each gluon also carries a color charge, which is a linear combination of a color state and an anti-color state.

As gluons carry a color charge themselves, they also couple to each other. This leads to an increase of the effective coupling at small energies, due to higher order loop corrections. At small distances, such as in the bound state of a hadron, the effective coupling is quite small, resulting in a phenomenon called asymptotic freedom. For small couplings, processes involving strong interactions can be calculated using perturbative techniques.

The asymptotic freedom is linked to quark confinement, an effect describing the fact that quarks never appear alone but always in bound states with a total vanishing color charge.

2.1.4. Higgs mechanism

When introducing masses to the standard model bosons, the theory is no longer invariant under local gauge transformations. However, the W and Z bosons have been found to be massive. To account for these masses, a mechanism called electroweak symmetry breaking has been introduced. By adding a scalar potential $V(\Phi)$ to the Lagrangian with its minimum not located at $\Phi = 0$, the symmetry is broken. The Higgs field Φ is a complex $\mathrm{SU}(2)_L$ doublet, and thus has four degrees of freedom.

Three degrees correspond to the W^+, W^-, and Z boson masses. The forth degree corresponds to a new massive gauge boson, called the Higgs boson. The photon field remains massless, and the masses of the W and Z bosons are connected by:

$$\frac{M_W}{M_Z} = \cos\theta_W \quad . \tag{2.5}$$

In 2012, the ATLAS and CMS collaborations found a new particle with a mass of around 125 GeV, which is compatible with a standard model Higgs boson [10, 11].

2.2. Beyond the standard model

The standard model is very successful in describing particle physics observations. Nevertheless there are some observations not described by the standard model. Also theoretical considerations indicate the existence of beyond the standard model physics [12].

- The Higgs mass has been found to be 126 GeV, while loop corrections indicate an effective mass near the Planck scale. A cancellation of these corrections would require an enormous fine tuning.
- Cosmological observations indicate the existence of dark matter. One candidate for this is a weakly interacting massive particle (WIMP).
- The electroweak symmetry breaking is introduced ad-hoc in the theory. Is there an origin to this?

Today, there are a number of models predicting beyond the standard model (BSM) physics in the lepton and missing transverse energy channel. In the sequential standard model, a heavy charged gauge boson W′ is introduced in an ad-hoc way by using a carbon-copy of the SM W boson with a different mass. The universal extra dimensions model includes a heavy charged gauge boson because of intrinsic model features. The mediator between the initial quarks and the final state lepton and neutrino is replaced by an effective contact interaction in the helicity non conserving contact interaction model. In the dark matter model, the $\ell + E_T^{\text{miss}}$ signature originates from a standard model W boson. Additional missing transverse energy arises from the dark matter particles.

2.2.1. Heavy charged gauge boson W′

A heavy charged gauge boson W′ is essentially a heavier copy of the standard model W boson, see figure 2.1. It is predicted by a number of different BSM models. The sequential standard model provides an ad-hoc implementation of a W′ boson and is often used as a reference. Other models, such as the left-right symmetric model or models with extra dimensions are not necessarily motivated by a heavy charged gauge boson but give inevitably rise to a W′ boson.

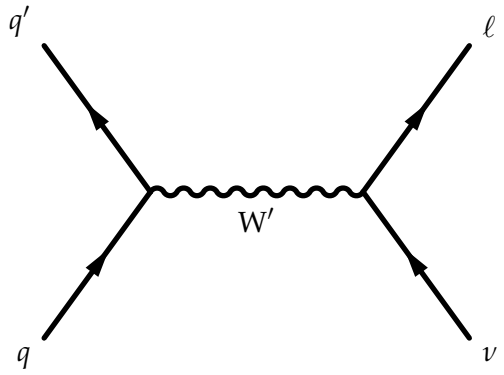

Figure 2.1.: Leading order Feynman graph of W′ boson production and decay.

Sequential standard model without interference

The reference model described by [13], predicts new heavy charged (W′) and neutral (Z′) gauge bosons with the same couplings as the couplings of the conventional W and Z bosons. For the W′ boson this means, it can couple to a W and Z boson, to a charged lepton and a neutrino, or to two quarks. In such a model, the dominant decay channel for a W′ with a mass $M_{\mathrm{W}'} > 250\,\mathrm{GeV}$ would be the Z W channel. Some models however predict a suppression of this bosonic decay channel. In extended gauge models, the W′ Z W coupling can even vanish completely.

Inspired by this, the W′ boson in the sequential standard model (SSM) assumes a coupling to fermions with the same coupling strength as the W boson. The coupling to top and bottom quarks is allowed if the mass of the W′ boson is larger than their combined masses. The tri-vector coupling W′ Z W coupling is assumed to be zero. Mixing and interference effects between the W boson and the W′ boson are neglected. The cross section for the production of a new particle can sometimes be approximated assuming the particle is produced on-shell only (narrow width approximation). This is not applicable here, as the scattering energy $\sqrt{s}$ is not necessarily much larger than the boson mass [14]. Instead, W′ bosons with large masses are produced predominantly off-shell.

Although it is not based on strong physical motivations, this model has been used as the reference model in $\mathrm{W}' \to \ell\nu$ analyses for some time. It has a conceivable signal signature, it is relatively straightforward to implement and analyze, and its long tradition makes different analyses comparable. Moreover, its signature is at least very similar to more motivated models such as the left-right symmetric models (section 2.2.1).

The partial decay width for each decay channel can be calculated as [15]

$$\Gamma_{\mathrm{W}'\to\bar{f}f'} = m_{\mathrm{W}'}\frac{g^2_{\mathrm{W}'}C_{\bar{f}f'}}{2\cdot 48\pi}F\left(\frac{m_{\bar{f}}}{m_{\mathrm{W}'}},\frac{m_{f'}}{m_{\mathrm{W}'}}\right) \tag{2.6}$$

where $C_{\bar{f}f'}$ is a color factor (1 for leptons and 3 for quarks), $g_{\mathrm{W}'}$ is the coupling constant, and

$$F(x_1,x_2) = \left(2 - x_1^2 - x_2^2 - (x_1^2 - x_2^2)^2\right)\sqrt{\left(1-(x_1+x_2)^2\right)\left(1-(x_1-x_2)^2\right)}\ . \tag{2.7}$$

For the coupling $g_{\mathrm{W}'}$ the standard model weak coupling is assumed

$$g_{\mathrm{W}'} = g_{\mathrm{W}} = \sqrt{4\pi\alpha_{\mathrm{em}}/\sin^2\theta_W} \approx 0.65\ , \tag{2.8}$$

where α_{em} is the fine-structure constant.

Except for the top-bottom decay channel, the fermion masses are much smaller than the W′ boson mass. This results in $F(0,0) = 2$ and the total decay width can be written as:

$$\Gamma_{\mathrm{W}'} = m_{\mathrm{W}'} \frac{g^2_{\mathrm{W}'}}{2 \cdot 48\pi} \left(18 + 3F\left(\frac{m_t}{m_{\mathrm{W}'}}, \frac{m_b}{m_{\mathrm{W}'}}\right)\right) \quad . \tag{2.9}$$

For very high W′ boson masses, even the top mass can be neglected, yielding:

$$\Gamma_{\mathrm{W}'} = m_{\mathrm{W}'} \frac{g^2_{\mathrm{W}'}}{4 \cdot \pi} \quad , \tag{2.10}$$

and for $g_{\mathrm{W}'} = g_W$

$$\Gamma_{\mathrm{W}'} = \frac{4}{3} \frac{m_{\mathrm{W}'}}{m_W} \Gamma_W \quad . \tag{2.11}$$

The branching fraction to the leptonic channels is about 8 %, because of the additional top-bottom channel this is smaller than the leptonic branching fraction of the standard model W decay.

Typical decay widths are denoted in table 2.2.

Table 2.2.: Total decay widths of a SSM W′ boson considering couplings to fermions only.

Mass m	Width Γ
1 TeV	33 GeV
5 TeV	170 GeV
6 TeV	200 GeV

Sequential standard model with interference

The SSM has the advantage of a clear signature which can be easily added to the standard model background. In the model described here, interference effects between the standard model W boson and the W′ boson are considered.

The Lagrangian for the W′ boson couplings can be assumed in analogy to the standard model W boson Lagrangian:

$$\mathcal{L} = \frac{\lambda_f V_{i,j}}{2\sqrt{2}} g_{\mathrm{W}'} \bar{f}_i \gamma^\mu (1 - \gamma^5) \mathrm{W}'_\mu f_j + \mathrm{h.c.}, \tag{2.12}$$

where $V_{i,j}$ is the CKM matrix if i, j are quarks and the unity matrix otherwise, λ is a factor with the absolute value of one, characterizing the type of interference, and $g_{\mathrm{W}'}$ is the W′ boson coupling constant.

In the following, $g_{\mathrm{W}'}$ is usually given in terms of the standard model weak coupling constant $g_W = e/\sin\theta_W$. The factor λ is introduced to define the sign of the coupling, which can be

different for quarks and leptons and which describes the nature of the interference. We consider two cases: In the sequential standard model with same-sign couplings (SSMS), we define $\lambda_\ell = \lambda_q = 1$, and in the opposite sign case (SSMO), we chose $\lambda_\ell = -\lambda_q = 1$.

If a W′ is a copy of the standard model W boson with the same couplings, their possible initial and final states are the same. Therefore, a W′ boson and a W boson produced at the same mass are indistinguishable. Their cross section is proportional to the square of the sum of their matrix elements

$$\sigma \propto |\mathcal{M}_W + \mathcal{M}_{W'}|^2 = |\mathcal{M}_W|^2 + |\mathcal{M}_{W'}|^2 + 2\,\mathrm{Re}\,(\mathcal{M}_W^* \times \mathcal{M}_{W'})\,. \tag{2.13}$$

The first term describes the standard model W boson, the next term is the same as in the SSM model. The last term is the interference term, mixing together contributions from the standard model W and the W′ boson [16]. The cross section then translates to [17]:

$$\begin{aligned}\frac{\sigma}{s} \propto & \frac{g_W^4}{(s-m_W^2)^2+\Gamma_W^2 m_W^2} + \frac{g_{W'}^4}{(s-m_{W'}^2)^2+\Gamma_{W'}^2 m_{W'}^2} \\ & \pm 2 g_W^2 g_{W'}^2 \frac{(s-m_W^2)(s-m_{W'}^2)+\Gamma_W\Gamma_{W'}}{((s-m_W^2)^2+\Gamma_W^2 m_W^2)((s-m_{W'}^2)^2+\Gamma_{W'}^2 m_{W'}^2)}\ .\end{aligned} \tag{2.14}$$

Or when neglecting the decay widths [16]:

$$\sim \left(\frac{g_W^2}{s-m_W^2}\right)^2 + \left(\frac{g_{W'}^2}{s-m_{W'}^2}\right)^2 \pm 2\left(\frac{g_W^2}{s-m_W^2} \times \frac{g_{W'}^2}{s-m_{W'}^2}\right). \tag{2.15}$$

where the $\pm$ becomes $+$ for the SSMS and $-$ for the SSMO model [16].

In the SSMS model the interference terms of equation 2.14 yield a negative cross section contribution in the invariant mass region between the standard model W boson mass and the W′ boson mass. Couplings with opposite signs for leptons and quarks (SSMO) result in a positive cross section contribution in that region. A complete comparison of the different contributions of the interference term to the cross section can be found in table 2.3.

Table 2.3.: Comparison of the contributions of the interference term to the overall cross section for the SSMS and SSMO models.

	SSMS	SSMO
$\sqrt{s} < m_W$	constructive	destructive
$m_W < \sqrt{s} < m_{W'}$	destructive	constructive
$\sqrt{s} > m_{W'}$	constructive	destructive

In addition to the mass $m_{W'}$, the coupling $g_{W'}$ can be regarded as a free, unknown parameter. It choice affects the cross section, the decay widths and also the magnitude of the interference effects.

Left-right symmetric models

Left-right symmetric models predict a W′ boson as complement to the W boson with right-handed interactions.

The $V - A$ coupling of charged current weak interactions only couples to left-handed fermions and right handed anti-fermions The minimal scheme to introduce a right handed coupling to fermions, $(V + A)$, is attained by extending the $\mathrm{SU}(2)_L \times U(1)$ gauge group to $\mathrm{SU}(2)_L \times \mathrm{SU}(2)_R \times \mathrm{U}(1)$ [18].

This mechanism restores the conservation of parity at high energies [19], which must be broken at low energies. An additional vector boson W_R corresponding to the $V + A$ coupling is introduced, mixing with the $V - A$ boson W_L to two mass eigenstates W_1 and W_2:

$$W_L = W_1 \cos\zeta + W_2 \sin\zeta \tag{2.16}$$

$$W_R = e^{i\omega}(-W_1 \sin\zeta + W_2 \cos\zeta), \tag{2.17}$$

with mixing angle ζ and a CP-violating phase ω. In a symmetric model, the coupling constants for W_L and W_R are assumed to be the same, though in principal they can be different [20]. A small mixing angle makes the mass eigenstate W_1 coupling predominantly left-handed, which then corresponds to the W boson. The heavier mass eigenstate W_2 would correspond to a W′ boson observable in the $\ell + E_T^{\mathrm{miss}}$ channel. By examining the phase space distribution of polarized muons, the mixing angle ζ has been restricted to $-0.020 < \zeta < +0.017$ [21] with 90 % confidence level.

Consequently, neutrinos must have the ability to have either helicities, meaning that all neutrinos of all generations have a mass. If neutrinos are Dirac particles, left- and right-handed neutrinos have the same mass [22]. Assuming neutrinos are Majorana fermions, ν_L and ν_R are expressed as Majorana spinors with two different mass terms. The seesaw mechanism then gives rise to a small neutrino mass for ν_L and a large mass for ν_R [23–25]. Therefore the existence of a heavy W′ boson coupling to right-handed fermions may be connected to the nature of the neutrino (Majorana or Dirac) and the smallness of the neutrino mass.

The SSM model W′ boson is compatible with a left-right symmetric W′ boson in case the neutrinos are Dirac particles or if the right-handed neutrinos are very light [9, 26].

Split universal extra dimensions model

The universal extra dimensions (UED) model is based on an extended spacetime with one or more additional compact dimensions with size $L = \pi R/2$ [27]. The extra dimensions are universal in the sense that all of the standard model particles propagate in the extra dimensions [28]. This is in contrast to other models, e.g. the ADD model [29, 30], where standard model particles are confined to a four-dimensional brane and only interact gravitationally in the extra dimensions.

Considered here is a model with one additional dimension. The model postulates Kaluza-Klein (KK) excitation states of all particles, the excitation mode is denoted with n in the following. These additional particles ($n > 0$) have larger masses than their standard model equivalents, which are the zero modes ($n = 0$) of the KK tower.

The UED model has some similarities to the prevalent supersymmetry model [28]. The model enforces the conservation of KK-parity $(-1)^n$, similar to R parity in supersymmetry. In contrast to supersymmetric theories, the new KK particles have the same spin as their standard model partners. The lightest KK particle with $n = 1$ is stable and therefore a viable dark matter candidate.

In the split UED (sUED) model an additional bulk mass parameter μ is introduced, increasing the masses of the KK fermion states. This model could explain observations made by the PAMELA [31] and AMS [32] experiments. They detected an excess of positrons in cosmic rays compared to the expectation, which could result from dark matter annihilation. On the other hand, such an excess is not observed in the antiproton flux, which would be expected. The bulk mass parameters can be chosen such that the KK quark masses increase, reducing the cross section of the dark matter annihilation into quark pairs [33].

The increased μ parameter comes along with a quasi localization of the SM fermions at the center or the boundaries of the fifth dimension. This split of the wave function profile and the split in the KK mass spectrum of fermions inspired the name split UED [34].

The localization of the SM fermions modifies their couplings to the gauge fields, enabling tree-level couplings to KK number even gauge bosons [28]. Because of the KK parity conservation, a coupling of odd excitation states to standard model fermions is forbidden. The $W_{n=2}$ boson is the lightest W boson excitation acting as a W′ boson. It can couple to standard model quarks and leptons [35].

The mass of the nth excitation state of the W boson is determined by:

$$m_{W_n} = \sqrt{m_W^2 + \left(\frac{n}{R}\right)^2}. \tag{2.18}$$

The coupling of the W_n boson to standard model fermions is determined by the wave function overlap $\mathcal{F}_n$ between the boson and the fermion:

$$g_n^{KK} = g^W \mathcal{F}_n(\pi\mu R) \tag{2.19}$$

with

$$\mathcal{F}_n(x) = \begin{cases} 0 & \text{if } n = 2m+1 \text{ (odd)} \\ \frac{x^2[-1+(-1)^m e^{2x}](\coth x - 1)}{\sqrt{2(1+\delta_{m0})}(x^2+m^2\pi^2/4)} & \text{if } n = 2m \text{ (even)} \ . \end{cases} \tag{2.20}$$

For $n = 0$ the standard model couplings are restored as $\mathcal{F}_0(x) = -1$. The coupling to standard model fermions is enhanced with increasing bulk mass. Additionally, the branching fraction to KK fermions is decreased as their masses become larger [28]. In the limit of $x \to \infty$ a coupling reaches its maximum value of $g_n^{KK} = -\sqrt{2} \times g_W$.

Following reference [28], the same bulk mass parameter for all fermions is chosen.

By taking into account the modified cross sections, results from the SSM model can be adapted for the sUED model parameters R and μ [36]. Considering interference effects, the SSMS model W′ mass and coupling strength can also be translated to the sUED model with the parameters R and μ.

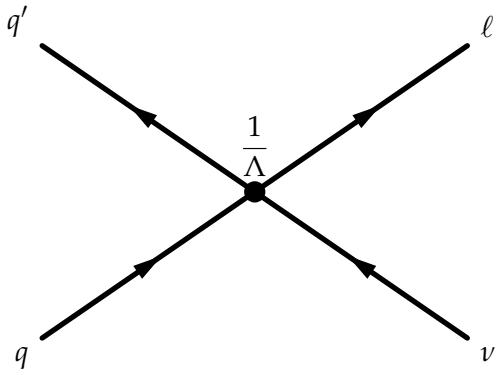

Figure 2.2.: Leading order Feynman graph of a contact interaction. The black dot indicates the contact interaction.

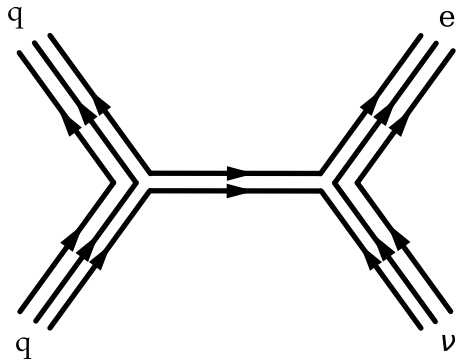

Figure 2.3.: Possible interaction of composited fermions that can be described with a contact interaction. The exchange is mediated by a bound state of subparticles with masses of the scale Λ [40].

2.2.2. Helicity nonconserving contact interaction model

Prior to the discovery of the W boson, Fermi developed a model describing the β decay with a four particle contact interaction, as shown in figure 2.2 [37]. It provides a good description of the physics process if the momentum transfer of the process is much lower than the mass of the mediator. The approximation made for a contact interaction compared to the consideration of a mediator particle is discussed in section 2.2.3.

Such an effective interaction can be used to describe physics beyond the standard model. It can mimic a mediator at a momentum transfer small compared to its mass. And assuming that the fermions are constituted from smaller particles, the model can also describe the interaction of these sub-fermionic particles [38, 39]. A possible interaction where the standard model particles are compounds of three subparticles is depicted in figure 2.3.

The Lagrangian for a helicity nonconserving contact interaction (HNC-CI) can be expressed as:

$$\mathcal{L} = \frac{-4\pi}{\Lambda^2} \left(\bar{d}_{iL} u_{iR}\right) \left(\bar{\nu}_{jL} \ell_{jR}\right) + \text{h.c.}, \tag{2.21}$$

where Λ is the scale of the contact interaction.

In contrast to the W boson, the contact interaction describes a coupling to right handed quarks and left handed anti-quarks. The outgoing particles are left handed leptons and right handed anti-leptons, prohibiting the generation of right handed neutrinos. As the helicity is changed in the currents (see equation 2.21), the interaction is called "helicity nonconserving". As a result of this coupling configuration no interference between the CI and the W boson occur [41]. From a theoretical point of view, the model is considered rather unlikely [42]. But as it does not show interference effects, it is used as a reference model.

The only parameter Λ scales the cross section of the process, with $\sigma \propto \Lambda^{-4}$. The kinematic structure and topology of the events are not affected, keeping the shape of any kinematic distribution constant for all Λ.

2.2.3. Dark matter model

Cosmological observations of gravitational effects, such as the rotation speed of galaxies and gravitational lensing, suggest the existence of otherwise unobservable dark matter. One candidate for dark matter is the existence of weakly interacting massive particles (WIMPs).

Such dark matter particles (χ) are not detectable in CMS and would give rise to missing transverse energy in the detector. The demand for a clear signature, which can be triggered and analyzed, requires an additional detectable particle in the event. This analysis is sensitive to the production of two dirac type dark matter particles ($\chi\bar{\chi}$) together with a W boson decaying to a lepton and a neutrino as shown in figure 2.4.

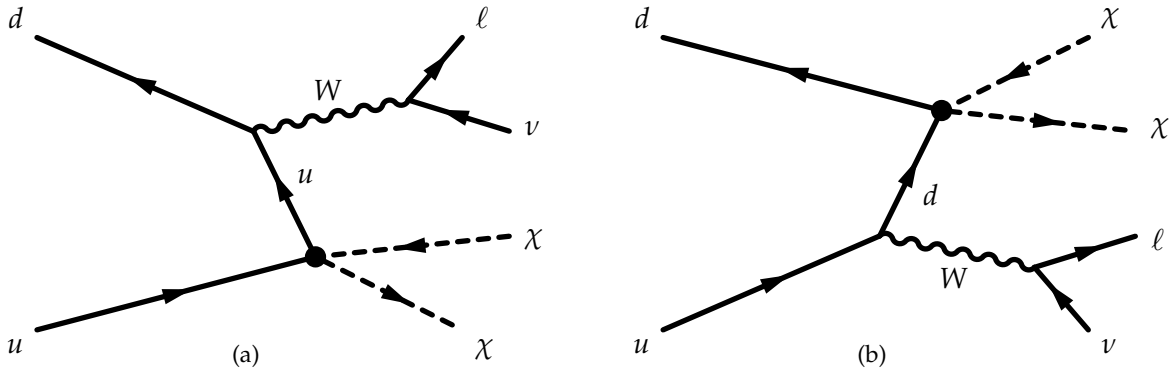

Figure 2.4.: Leading order Feynman diagrams of pair-produced dark matter in association with a W boson decaying leptonically. The black dot indicates the contact interaction.

The interaction between the standard model quarks and the dark matter particles must be mediated by another unknown particle. If the mass of the mediating particle is large compared to the transferred momentum q, the mediator propagator can be approximated [43]:

$$\frac{1}{q^2 - M^2_{\text{mediator}}} = -\frac{1}{M^2_{\text{mediator}}}\left(1 + \frac{q^2}{M^2_{\text{mediator}}} + \mathcal{O}\left(\frac{q^4}{M^4_{\text{mediator}}}\right)\right) \tag{2.22}$$

keeping only the leading order of the expansion. Thus, the interaction can be described as a four-fermion contact interaction using an effective field theory (EFT) [44].

We consider two types of couplings, a vector and an axial-vector interaction. The axial-vector coupling is spin dependent while the vector coupling is spin independent. They are described

by:

$$\mathcal{L} = \frac{1}{\Lambda^2} \left(\bar{\chi}\gamma_\mu\chi\right) \lambda_i \left(\bar{q}_i\gamma^\mu q_i\right) \qquad \text{vector,} \tag{2.23}$$

$$\mathcal{L} = \frac{1}{\Lambda^2} \left(\bar{\chi}\gamma_\mu\gamma_5\chi\right) \lambda_i \left(\bar{q}_i\gamma^\mu\gamma_5 q_i\right) \qquad \text{axial vector,} \tag{2.24}$$

$$\tag{2.25}$$

where Λ is the scale of the contact interaction, and λ_i modifies the coupling depending on the quark type. The mass of the WIMP M_χ is contained in the spinor χ.

The scale corresponds to

$$\Lambda = \frac{M_{\text{mediator}}}{g_{\text{mediator}}} \tag{2.26}$$

when considering a mediator particle with mass M_{mediator} and coupling g_{mediator} to quarks and to the dark matter particles.

The coupling can affect up-type quarks and down-type quarks differently, therefore three cases for the λ_i are considered, which are labeled with a single new parameter ξ, following reference [44]:

$$\xi = -1 \qquad \lambda_u = +1,\ \lambda_d = -1, \tag{2.27}$$

$$\xi = 0 \qquad \lambda_u = +1,\ \lambda_d = 0, \tag{2.28}$$

$$\xi = +1 \qquad \lambda_u = +1,\ \lambda_d = +1. \tag{2.29}$$

In the two cases $\xi = -1$ and $\xi = +1$, both Feynman diagrams of figure 2.4 are realized and as their initial and final states are indistinguishable, an interference between the two must be considered. The signature of the $\lambda_u = +1, \lambda_d = 0$ case is very similar to $\lambda_u = 0, \lambda_d = +1$, therefore all results for $\xi = 0$ are applicable to both cases.

As this is an effective field theory, the validity of the model is constrained [43, 45, 46]. To allow perturbative calculation, the coupling must be constrained to $g_{\text{mediator}} < 4\pi$. Applying this to equation 2.26 and taking into account that the mediator mass must be larger than the WIMP mass, the validity is constrained to:

$$\Lambda > \frac{M_\chi}{4\pi}. \tag{2.30}$$

Considering the approximation made in equation 2.22, the validity of the model is limited to cases where $q^2 \ll M^2_{\text{mediator}} \sim \Lambda^2$:

$$\Lambda > \frac{q}{g_{\text{mediator}}}. \tag{2.31}$$

Thus the validity constrain depends on the coupling g_{mediator}. When considering again $g_{\text{mediator}} < 4\pi$ and requiring the momentum transfer $q > 2M_\chi$, the energy scale is at least constrained to:

$$\Lambda > \frac{q}{4\pi} > \frac{M_\chi}{2\pi}. \tag{2.32}$$

The validity of the $\xi = 0$ and $\xi = -1$ cases has been generally questioned. It is argued in reference [47] that the increased cross section in these two scenarios is due to events with longitudinally polarized W bosons. They originate from unphysical terms that grow like s/m_W^2 and are violating unitarity. Considering this, these two signals can still be regarded as benchmark models.

3. Statistical inference

To make a profound claim about the physical meaning of an observation, methods of statistical inference are used. For this, the observation is compared to the expectation, which is called the null hypothesis H_0 and usually corresponds to the standard model, and to the signal hypothesis H_1.

The significance of the data when compared to the null hypothesis H_0 is an important measure to claim the discovery of new physics. If no significant deviation can be found, certain new physics models can be excluded at a certain level. Often, the model depends on one or more parameters and instead of the whole model, just a certain parameter space can be excluded. Eventually, an exclusion limit on the parameter can be provided.

To determine the sensitivity of an analysis, the expected significance and the expected limit can be determined. This is of special importance to probe the reach of future analyses, but also allows the comparison of the expected limit to the observed limit of a current analysis.

3.1. Limit setting

Setting limits is an important technique in the search for new physics, as they describe the parameter space of a certain model that is excluded. Therefore, they fulfill the demand for falsification in the framework of the scientific method.

There are a number of different methods to calculate limits with different advantages and disadvantages. All of them have in common to provide an exclusion interval for a parameter of interest. Often, this is the signal cross section but it can also be e.g., a coupling or an energy scale.

Two different approaches are used throughout this thesis, the frequentist and the bayesian [48]. Although they usually yield similar results, their meanings are different.

The frequentist method provides a confidence interval, which is supposed to include the true value of the parameter of interest. For each experiment, this is true only within a certain probability, i.e. when carrying out a large number of experiments and determining a confidence interval for each of them, the fraction of (possibly differing) confidence intervals containing the true parameter of interest should be at least as large as the confidence limit.

The bayesian method on the other hand determines a credible interval, and claims the true value lies within that very interval with a certain probability. Making a statement not about the probability of the interval but about the probability of the parameter of interest.

Table 3.1.: Overview of important symbols as used in this chapter.

H_0, H_1	The null hypothesis and the alternative (signal) hypothesis.
α	Size of the test, probability to falsely reject the null hypothesis. Must be specified in advance.
p_{s+b}, p_b	The p-values (probability to find a deviation at least as significant as the observed one) of the signal + background hypothesis and the background hypothesis, respectively.
λ	The test statistic (measure for the magnitude of a deviation (large λ) or agreement (small λ)).
θ	Parameter of interest, e.g. the signal cross section. The signal hypothesis corresponds to $\theta = \theta_s$, the background hypothesis corresponds to $\theta = 0$.
ν	The nuisance parameters, variables that are undetermined and influence the result, but which are not of interest for the result.
D	Actual observation, usually a measurement of the number of events (data).
$P(\lambda\|\theta)$	The probability density function (pdf) of the test statistic under a parameter of interest assumption θ. It corresponds to a convolution of the test statistic λ and the pdf of the possible observations (event numbers).
$L(D\|\theta,\nu)$	The likelihood to observe data D under the assumption of a parameter of interest θ and a set of nuisance parameters ν.
$P(H\|D)$	Probability density function for the hypothesis H when observing data D.
$L(D\|H)$	Likelihood function for the observation D under the hypothesis H.
$\pi(H)$	Prior probability function for the hypothesis H.

This can be expressed shortly as:

$$CL_{\text{frequentist}} = \frac{\text{Number of experiments with an interval that contain the true value}}{\text{Total number of experiments}} \tag{3.1}$$

$$CL_{\text{bayesian}} = \frac{\text{Number of true values lying within the interval}}{\text{Total number of possible true values}} \tag{3.2}$$

Some results in this work have a history of predecessor analyses, which have used the bayesian method. Therefore, they are determined using this very same method. Otherwise, the frequentist CL_s method is used. An overview of the most important symbols used in this chapter and their meaning is shown in table 3.1.

3.1.1. CL_s

The CL_s method [49–51] is a modified frequentist approach to calculate exclusion limits. A frequentist confidence interval at a confidence level (CL) of $1 - \alpha$ (e.g. 95 %) claims to be con-

structed with a chance of $1-\alpha$ (95 %) to contain the true value of a certain parameter of interest θ (e.g. the signal cross section or the signal coupling strength). To construct such an interval, a statistical test is carried out for different values of the parameter of interests. Values of θ accepted by the test constitute the confidence interval. The upper limit on θ is defined by the upper threshold of the confidence interval. In the CL_s method, all signal hypotheses with a confidence level

$$CL_s < \alpha \tag{3.3}$$

are excluded with a confidence level of $1-\alpha$.

The confidence level for a certain signal + background hypothesis $s(\theta)+b$ and a background hypotheses b is determined by:

$$CL_s = \frac{CL_{s+b}}{CL_b} = \frac{p_{s+b}}{p_b} \overset{!}{<} \alpha, \tag{3.4}$$

where p_{s+b} is the p-value of the signal + background hypothesis and p_b is the p-value for the background only hypothesis. A p-value is the probability to find a deviation that is at least as significant as the observed one considering a certain hypothesis. It is based on a test statistic, which is a measure of how compatible the outcome of an experiment is with respect to the expectation. A large value of the test statistic corresponds to a strong deviation and a small value means a good compatibility. The fraction of possible outcomes with a larger test statistic than that of the observed outcome determines the p-value. Therefore a smaller p-value corresponds to a more unlikely, i.e. a more significant deviation.

The CL_s method is not a strict frequentist method, because CL_s is not a p-value but the fraction of two p-values. However, it is more conservative than the pure p-value p_{s+b} [50]. One very unique feature of the CL_s statistic is its ability to not reject hypotheses for which the test is not powerful, i.e. in case the test cannot separate the s+b hypothesis from the b hypothesis. This is due to the denominator, which is small in case the data is compatible with the background hypothesis.

The two p-values from equation 3.4 are determined based on the signal + background and the background only hypothesis as:

$$p_{s+b} = \int_{-\infty}^{\lambda_{\text{obs}}} P(\lambda|\theta_s)d\lambda \tag{3.5}$$

$$p_b = \int_{-\infty}^{\lambda_{\text{obs}}} P(\lambda|0)d\lambda, \tag{3.6}$$

where $P(\lambda|\theta_s)$ is the probability density function (pdf) of the test statistic λ under the signal + background hypothesis with the parameter of interest θ_s. It can be determined by generating pseudo experiments with the $s+b$ hypothesis. Analogously $P(\lambda|0)$ is the pdf of the test statistic λ for the background hypothesis. An example of the two test statistic distributions and how the p-values are determined from this is shown in figure 3.1.

Following the Neyman-Pearson-Lemma, the most powerful test statistic is the likelihood ratio [52]. The likelihood depends on the observed data D, the parameter of interest θ, and additional nuisance parameters ν, which are not of interest for the statistical interpretation,

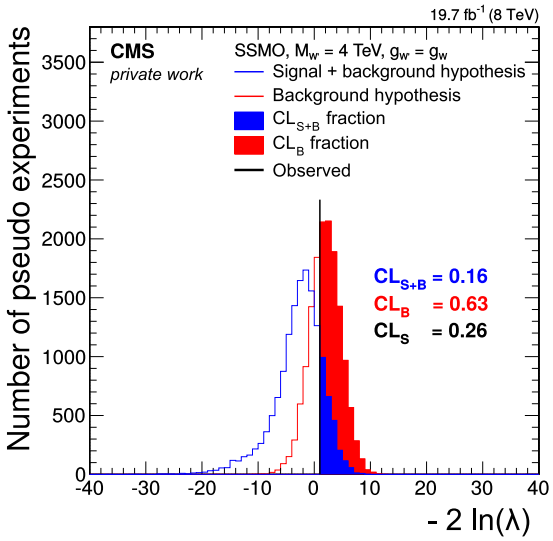

Figure 3.1.: Example for the determination of p_{s+b} and p_b from the test statistic distributions and the observed value of the test statistic. This example corresponds to a SSMS W′ boson with a mass of 4 TeV and a coupling of $g_{W'} = g_W$ at $\sqrt{s} = 8$ TeV, see section 6.3.3. With a result of $\mathrm{CL}_s = 0.26 > 0.05$ this parameter point is not excluded.

e.g., the luminosity or the reconstruction efficiency. The nuisance parameters can be "profiled out" by maximizing the likelihoods with respect to ν.

$$\lambda(\theta) = \frac{L(D|\theta, \hat{\hat{\nu}})}{L(D|0, \hat{\nu})}, \tag{3.7}$$

where $L(D|\theta, \hat{\hat{\nu}})$ is the likelihood for the s+b hypothesis maximized with respect to ν and $L(D|0, \hat{\nu})$ is the likelihood for the null hypothesis, also maximized with respect to ν.

Equation 3.7 is used in this analysis for the SSMS and SSMO limits. Another commonly used (e.g. for the LHC Higgs analyses) test statistic is the following profile likelihood:

$$\lambda_L(\theta) = \frac{L(D|\theta, \hat{\hat{\nu}})}{L(D|\hat{\theta}, \hat{\nu})}. \tag{3.8}$$

The denominator likelihood is chosen such that it is maximized with respect to θ and ν, instead of considering the background hypothesis $\theta = 0$.

The likelihood is the Poisson probability of the number of events. When considering a multi-bin / multi-channel limit, the total likelihood is the product of the Poisson probabilities for all bins and channels, multiplied by the pdf for the nuisance parameters, $\pi(\nu)$:

$$L(D|\theta, \nu) = \prod_{i \in \text{bins} \otimes \text{channels}} \frac{\epsilon_i(\theta, \nu)^{n_i} \exp(-\epsilon_i(\theta, \nu))}{n_i!} \times \pi(\nu), \tag{3.9}$$

where n_i is the number of events in bin i (so: $n_i = n_i(D)$) and ϵ_i is the expectation value for the number of events.

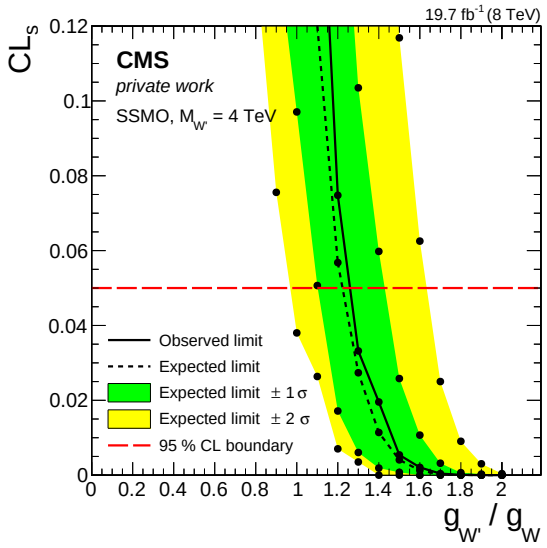

Figure 3.2.: Example for the determination of the parameter of interest (here: coupling strength) corresponding to $CL_s = 0.05$ using a linear interpolation between parameter points. This example corresponds to a SSMO W′ boson in the electron channel with a mass of 4 TeV at $\sqrt{s} = 8$ TeV, see section 6.3.3. The markers indicate the CL_s values determined for a given coupling strength. For each coupling strength 6 values are calculated: The expected median, the ±68 % interval, the ±95 % interval, and the observed value. A linear extrapolation yields the best value for the 95 % CL limit.

Technical implementation

For the technical implementation used for the CL_s method, not all values of θ can be probed to find $CL_s = \alpha$. Instead, a reasonably dense sampling of θ is used. Starting from the two values of θ whose CL_s values are the nearest neighbors of α, an interpolation is performed to find θ_α. An example of how such an interpolation is used to determine the 95 % CL limit of the parameter of interest can be found in figure 3.2.

For this analysis, $\alpha = 0.05$ or $\alpha = 0.10$ are used, denoted as 95 % CL and 90 % CL, respectively.

3.1.2. Approximations of the CL_s method

To establish the test statistic distributions for the CL_s method, pseudo experiments have to be performed. The number of required pseudo experiments can be very large, especially for small values of α, as the sampling rate must be substantially larger than $1/\alpha$. To avoid this computing intensive procedure, an approximated method can be used if the number of events is not too small and the expected number of events considering the signal + background hypothesis is larger compared to the background hypothesis [53].

We assume that the parameter of interest θ corresponds to a signal strength modifier $\mu(\theta)$, which manipulates the expected number of events in a bin i such that:

$$\epsilon_i = \mu s_i + b_i, \tag{3.10}$$

with the signal distribution s and the background distribution b. Following the Wald theorem [54], for a sufficiently large number of events, the test statistic 3.8 can be approximated by a normal distribution [53]:

$$-2\ln\lambda(\mu) \approx \frac{(\mu-\hat{\mu})^2}{\sigma^2} + \mathcal{O}(1/\sqrt{N}), \tag{3.11}$$

where $\hat{\mu} = \mu(\hat{\theta})$. The pdf $P(\lambda|\mu)$ of the test statistic λ then follows a noncentral chi-square distribution, with one degree of freedom for a single parameter of interest, and with the noncentrality parameter

$$\Lambda = \frac{(\mu-\mu')^2}{\sigma^2} \tag{3.12}$$

as the only free parameter [53]. The parameter μ' is the expectation value of the gaussian distributed $\hat{\mu}$.

It can be determined using a boundary condition. One possible method to determine Λ is to consider the so-called "Asimov" dataset. This is defined as the representative dataset, for which the estimators of all parameters correspond to the true parameters. It can be shown [53], that this is the case for $\hat{\mu} = \mu'$. Combining equations 3.11 and 3.12 for the Asimov dataset yields therefore:

$$-2\ln\lambda_A(\mu) = \frac{(\mu-\mu')^2}{\sigma^2} = \Lambda. \tag{3.13}$$

So by evaluating the test statistic of the Asimov dataset λ_A, the noncentrality parameter Λ can be calculated, which determines the asymptotic approximation for $P(\lambda|\mu)$.

With some calculations, the p-value can be derived as:

$$p_{s+b} = 1 - \Phi(\sqrt{-2\ln\lambda(\mu)}), \tag{3.14}$$

where Φ is the cumulative distribution of the standard gaussian.

3.1.3. Bayesian

Bayesian inference is a statistical method which takes the prior belief for the parameter of interest into account. It is based on Bayes' theorem, which can be considered as a way to translate the probability to make a certain observation D assuming a certain hypothesis H into the probability for the hypothesis H being true when making the observation D.

$$P(H|D) = \frac{L(D|H)\times\pi(H)}{\int dH' L(D|H')\times\pi(H')}, \tag{3.15}$$

where $P(H|D)$ is the probability for H being true when observing D, $L(D|H)$ is the likelihood that D will be observed under the hypothesis H, and $\pi(H)$ is the prior probability distribution of H. The integral in the denominator is a normalization factor calculated using the probabilities of all possible hypotheses H' [9].

The hypothesis H depends on the parameter of interest θ and further nuisance parameters ν. With that, Bayes theorem reads:

$$P(\theta, \nu|D) = \frac{L(D|\theta, \nu) \times \pi(\theta) \times \pi(\nu)}{\int d\theta' d\nu' L(D|\theta', \nu') \times \pi(\theta') \times \pi(\nu')}. \tag{3.16}$$

The prior probability distributions are assumed to factorize. They may be derived from independent measurements, but can also be assumed based on formal rules derived from mathematical principals. For the parameter of interest, we assume a uniform distribution for $\theta > 0$ and 0 otherwise. This is a common choice when denying any knowledge about the parameter of interest based on Laplace's rule [55]. It should be noted though, that other formal rules based priors exist and the choice of a uniform prior is sometimes disfavored, because it is not invariant under non-linear parameter transformations [55].

The prior distributions for the nuisance parameters usually express the corresponding systematic uncertainties. Common choices for them are the normal, the log-normal, and the gamma distribution. To eliminate the dependence of the nuisance parameters, one has to integrate over them

$$P(\theta|D) = \frac{\int d\nu L(D|\theta, \nu) \times \pi(\theta) \times \pi(\nu)}{\int d\theta' d\nu' L(D|\theta', \nu') \times \pi(\theta') \times \pi(\nu')}. \tag{3.17}$$

Technically, this integration is performed using a Markov chain Monte Carlo method, because the number of dimensions can be large.

The credible interval $[\theta_{\text{lo}}, \theta_{\text{up}}]$ at a confidence level (credible level) $1 - \alpha$ is then given by:

$$1 - \alpha = \int_{\theta_{\text{lo}}}^{\theta_{\text{up}}} P(\theta|D) d\theta. \tag{3.18}$$

This interval is not well-defined, as it still has one free parameter. For the exclusion interval, we set $\theta_{\text{lo}} = 0$ to obtain the upper limit on θ. So to obtain the upper limit at 95% CL, one has to solve the following equation for θ_{up}:

$$0.95 = \int_{0}^{\theta_{\text{up}}} P(\theta|D) d\theta. \tag{3.19}$$

3.1.4. Systematic uncertainties

Two different types of uncertainties are considered: global (or uniform) uncertainties and shape-based uncertainties. For global systematic uncertainties, e.g. on the luminosity, the relative impact of the uncertainty is assumed to be the same for all bins in the M_T distribution. The probability density function for these uncertainties are modeled using a log-normal distribution with the expectation value being the measured best value. This pdf is used as the prior for the nuisance parameter.

In contrast to the normal distribution, the log-normal distribution $\mathcal{N}_{\ln}(x)$ converges to 0 for $x \to 0$, which is often a desired property when modeling systematic uncertainties.

The second type of systematic uncertainties comprises shape-dependent uncertainties, examples for this type are energy scale and pileup uncertainties. For those, the M_T distribution is

recalculated with $1\,\sigma$ and $-1\,\sigma$ shifts of the corresponding uncertainty. The uncertainties may have an impact on the M_T value or the weight of an event, as illustrated in the following two examples. For the electron energy scale uncertainty the energy of the electron is shifted by its uncertainty, yielding a different M_T value for each event. For the uncertainty on the parton distribution function, the weight of each event is recalculated.

In either case, two additional M_T distributions are determined, one for the upward and one for the downward shift. The effect on the M_T distribution can be asymmetric or, in some cases, both shifts may even affect the resulting distribution (or a certain bin of the distribution) in the same direction (up or down) compared to the best estimated value. So for each bin, three event numbers are determined: the best estimated value $h(0)$, the upward shifted value $h(+1)$, and the downward shifted value $h(-1)$. In a next step, a smooth inter- and extrapolation is determined, resulting in a function $h(\lambda)$. This function is convolved with an assumed prior distribution of the systematic uncertainty. That way, the probability density function for the number of events in any bin can be determined.

For this, a vertical template morphing technique is used. The region in between $h(-1)$ and $h(+1)$ is interpolated using a second degree polynomial $h(\lambda)$, considering $h(0)$, $h(-1)$, and $h(+1)$. Three examples for this are shown in figure 3.3. For instance, both $h(-1)$ an $h(+1)$ can be positive, resulting in an interpolation such as the green line of figure 3.3.

Outside of the interval $-1 < \lambda < +1$, the $h(\lambda)$ extrapolated linearly. This technique provides a steady and differentiable uncertainty distribution, at the same time it takes into account possible asymmetries in the uncertainty distribution.

For all shape dependent uncertainties, the nuisance parameter's prior is assumed to be Gaussian. To determine the test statistic pdf, as shown in figure 3.1, pseudo experiments are performed, determining values of λ following this Gaussian pdf. Following the interpolation $h(\lambda)$, this value is translated to a shifted bin value h^{new}. As the systematic uncertainty is assumed to be correlated over all bins, the same outcome of a pseudo experiment is used to determine the shifted values for all bins, using a different translation for each bin. From performing a sufficiently large number of pseudo experiments, the pdf of the test statistic is determined.

3.2. Significances

The p-value p_b corresponds to the probability to observe a (signal like) deviation at least as significant as the tested one, if the background hypothesis is true. Therefore, p_b is called the significance of the deviation. Note that p_b depends on the signal hypothesis, as the test statistic λ depends on the signal hypothesis. Loosely speaking, the dependence of the signal hypothesis on the test statistic takes care that only those bins enter the significance determination that are sensitive to the signal, i.e. have a large statistical power.

In particle physics, significances are often given as a z-value (also called z-score) instead of a p-value. The z-value is the number of Gaussian standard deviations corresponding to the tail probability of the corresponding p-value. If not stated otherwise, in this thesis the one-sided probability is considered, i.e. a p-value of 0.5 corresponds to a z-value of 0, following reference [53]. Thus p-values smaller than 0.5 correspond to z-values larger than 0.

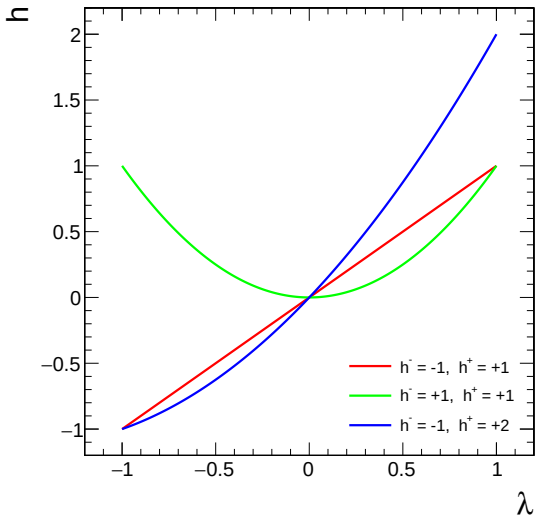

Figure 3.3.: Three examples for the application of the template morphing technique: The uncertainty is determined for $-1\,\sigma$ (resulting in $h(-1)$) and $1\,\sigma$ ($h(+1)$), together with the expectation value ($h(0)$), a quadratic interpolation is performed to determine the function $h(\lambda)$.

A deviation of $z = 5\,\sigma$ corresponding to $p = 2.87 \times 10^{-7}$, is considered to be significant in the particle physics community.

3.3. Expected limits and expected significances

To determine the expected limit, pseudo experiments are determined under the assumption of the background hypothesis. The same pseudo experiments that are used to determine the pdf of the background test statistic can be used for this. For each of these pseudo experiments, the CL_s value is determined. The expected limit is then defined as the median of these values. To provide a measure for the possible spread of the limit, the $\pm 1\,\sigma$ and $\pm 2\,\sigma$ interval can be provided by determining the corresponding quantiles of the ensemble of CL_s values.

For the expected significance, the signal hypothesis is assumed. So the median p_b value from a sufficiently large number of signal pseudo experiments provides the expected significance value.

4. Experiment

Challenging today's standard model physics can only be done by extending the experimental sensitivity beyond the current frontiers. Such frontiers are for example the energy range, the amount of acquired events (total luminosity), and the ability to resolve measured quantities more precisely. The Large Hadron Collider (LHC), together with its experiments, is currently the most sensitive particle collider system to probe standard model physics. In this chapter, first the experimental setup of run 1 is described, which has been used to acquire the data for the analysis described in chapters 5 and 6. After that the upgrades, envisaged ones as well as already installed ones, are described, which enhance the future experimental reach as studied in chapters 7 and 8.

4.1. Large Hadron Collider

The LHC [56] is a ring particle accelerator and collider operated at CERN and situated in an underground tunnel between the Jura Mountains and the Lake Geneva. It is capable of handling heavy ions as well as protons, of which only the latter ones are of importance for this analysis.

The accelerator was designed to reach a maximum center of mass energy of 14 TeV and a peak instantaneous luminosity of $1 \times 10^{34}\,\mathrm{cm}^{-2}\mathrm{s}^{-1}$. A total of 2808 bunches per beam and bunch crossings every 25 ns have been envisaged.

In 2012 during run 1, protons have been collided with a center of mass energy of $\sqrt{s} = 8\,\mathrm{TeV}$. The LHC has four interaction points, each affiliated to an experiment.

The LHC consists of two rings with oppositely rotating particle beams inside. This design is necessary as the colliding protons in each of the beams are of the same charge and therefore need opposing electric fields for being accelerated and opposing magnetic fields to be forced on parallel circular trajectories. A proton-proton design has been favored over a proton-antiproton design because of the higher achievable luminosity.

The LHC is fed by a cascade of different accelerators. Ionized hydrogen is passed through the Linac2, Proton Synchrotron Booster, Proton Synchrotron, and Super Proton Synchrotron, reaching an energy of 450 GeV. The LHC itself uses a radio frequency (RF) accelerator, which requires the injected particles to already have a velocity close to the speed of light. It runs with a frequency of 400 MHz and accelerates the beams, compensates the energy loss because of synchrotron radiation, and stabilizes the longitudinal profile of the bunches. Each beam is accelerated by an RF system of eight cavities, each fed by an individual klystron. All cavities have accelerating voltages of 2 MV.

To force the beams onto a ring-shaped track, dipole magnets are used. Because of the restricted space available inside the tunnel, a twin-bore magnet design has been chosen, which magnetically couples the two rings [57]. As the bending power is the limiting factor for the maximum beam energy, a total of 1232 dipole magnets are installed. The supra-conducting magnets are cooled using superfluid helium below 2 K and can reach magnetic fields above 8 T. To focus the beam in the transverse plane, corrector magnets of higher order (quadrupole up to decapole) are used. Additionally, insertion magnets are put into place, which force the beams to collide at the interaction points or have special tasks such as beam dumping and beam cleaning.

For its operation, the LHC is equipped with sophisticated cooling, vacuum, powering, and control systems.

4.2. Compact Muon Solenoid

The Compact Muon Solenoid (CMS) is a particle detector at the LHC, located in the north of the accelerator ring. Together with the ATLAS detector, it is one of the two major, multi-purpose experiments at the LHC.

The detector has a cylindrical shape and is built around an interaction point of the two beams. It consists of five wheels in the barrel region enclosed by two endcaps. The beam pipe at the interaction point is made out of beryllium [58]. This material has a very low density to minimize particle interactions but is capable of maintaining the vacuum inside. As shown in figure 4.1 the detector is structured in several concentric layers, from inside to outside these are: the tracker, the electromagnetic calorimeter, the hadronic calorimeter, the solenoid magnet, the muon system, and the iron return yoke.

4.2.1. Coordinate system

A coordinate system is used to describe positions and directions in the CMS detector. The origin of the coordinate system is the center of the detector, which is the nominal interaction point. The x-axis points to the center of the accelerator ring, the y-axis points upwards, and the z-axis points west, parallel to the nominal beam axis.

Instead of the Cartesian coordinates, often spherical coordinates are used. The azimuthal angle ϕ in the x-y plane is measured from the x-axis. The polar angle θ is defined as the angle starting from the z-axis. Often, instead of the polar angle, the pseudorapidity is specified, defined as

$$\eta = -\ln\left(\tan\frac{\theta}{2}\right). \tag{4.1}$$

Differences in pseudorapidity are invariant under Lorentz boosts along the z-axis [9].

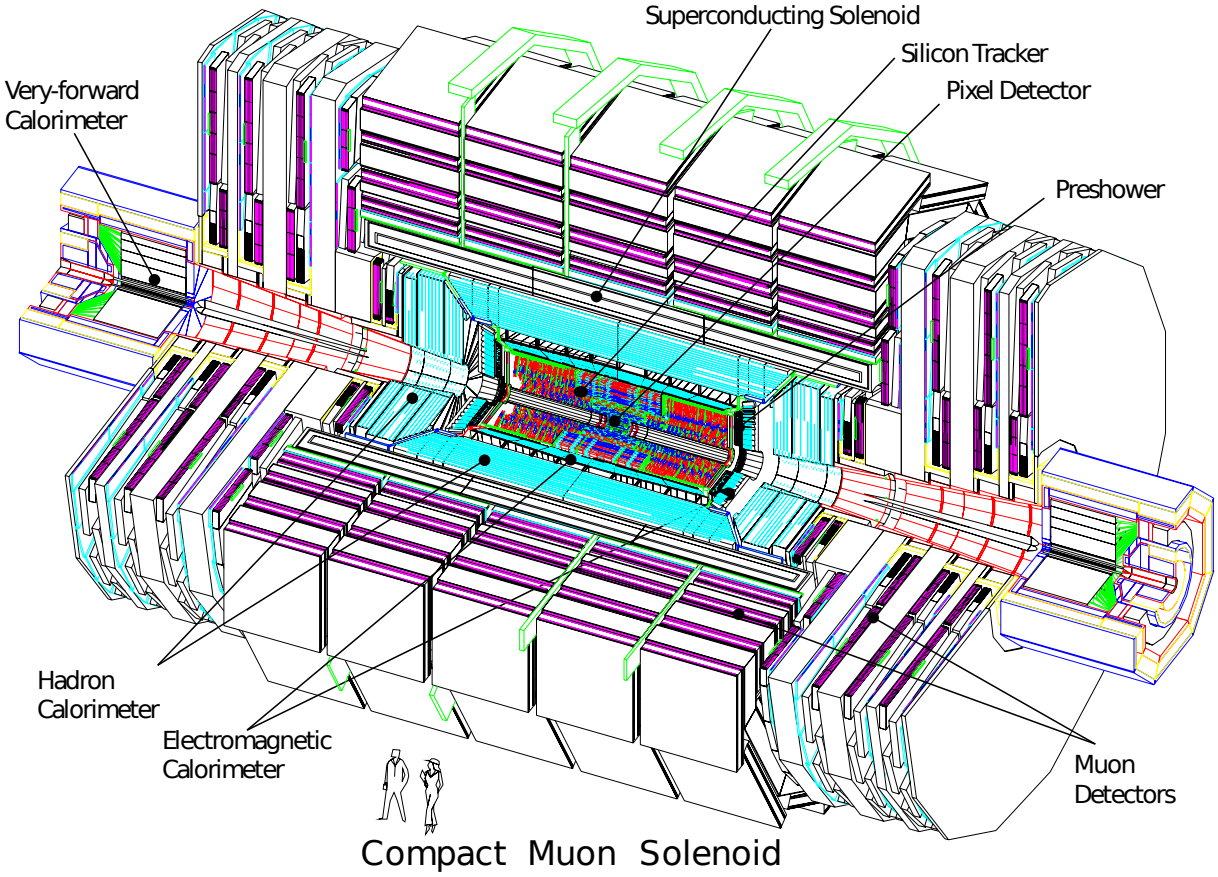

Figure 4.1.: Schematic view of the CMS detector [59].

4.2.2. Tracker

The tracker is the innermost subdetector starting at a distance of 4.4 cm from the interaction point. Its purpose is to detect charged particles with a high spatial resolution in order to reconstruct the trajectory of the particle. It consists of silicon pixels and strips arranged in several layers, as shown in figure 4.2.

By reconstructing the particle trajectories the primary vertices from which the particles originated can be determined. This is of special importance for the identification of long-lived particles, such as b quarks, and to distinguish the vertices of different simultaneous interactions (pileup interactions, resulting from multiple proton-proton interactions when colliding large bunches). A homogeneous magnetic field of 3.8 T is present inside the tracker, bending the trajectories accordingly. This enables the reconstruction of the charged particles' momenta.

In the barrel region, the three innermost layers are pixel layers, followed by 10 layers of silicon strips. In the endcaps, there are 2 layers of pixel and 12 layers of strip sensors. The detector covers a pseudorapidity range of up to $|\eta| = 2.5$. The pixels on the inside are necessary for a precise spatial resolution near the interaction point but also to distinguish different trajectories from each other, as the particle rate near the interaction point is very high. On the outside, this is less critical and therefore strip detectors are sufficient.

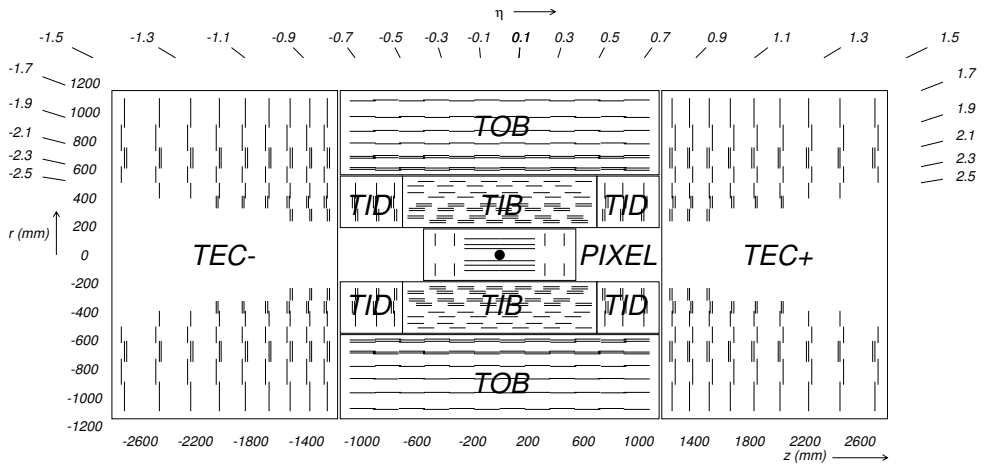

Figure 4.2.: Layout of the CMS pixel and strip tracker in the r-z plane. PIXEL are the inner pixel layers, TIB the inner barrel strip layers, TOB the outer barrel strip layers, TID the inner disk layers and TEC the end cap layers [59].

Each pixel covers an area of about $100 \times 150\,\mu\text{m}$. The pitches of the silicon strips range from 80 µm to 205 µm [60]. In the presence of the magnetic field, the induced charges are distributed over more than one pixel. By combining the information of multiple sensors, a spatial resolution of 15 µm for the pixels and 23 µm to 53 µm for the strips is achieved [59].

The resolution of the reconstructed momentum depends on its magnitude. A transverse momentum of 1 TeV can be reconstructed with a precision of about 5%, a low momentum of 1 GeV with a precision of 0.7 % [61]. A typical impact parameter resolution for a high-momentum track is 10 µm [61].

4.2.3. Electromagnetic calorimeter

The purpose of the electromagnetic calorimeter (ECAL) is to determine the energy of electrons, positrons and photons, but also of hadrons, which deposit a substantial fraction of their energy in the ECAL. The barrel region covers $|\eta| < 1.479$ and the endcap region has a range of $1.479 < |\eta| < 3.0$. A three-dimensional scheme of the subdetector is shown in figure 4.3.

The ECAL is composited from 61200 lead tungstate crystals in the barrel and another 7324 crystals in the endcaps. The material has a Molière radius of 2.2 cm and a radiation length of 0.89 cm. An electromagnetic shower deposits on average 90 % of its energy inside the Molière radius and the radiation length is the distance after which the energy of an electron drops to $1/e$. The crystal lengths correspond to about 25 radiation lengths and they have a width of about 1 Molière radius, providing a good granularity while keeping the design compact. A fraction of 80% of the scintillation light is emitted within 25 ns, which is the smallest envisaged time span between two LHC bunch crossings. The emitted scintillation light is detected by avalanche photodiodes in the barrel and vacuum phototriodes in the endcaps.

The energy resolution has been determined using test beams to [62]:

$$\frac{\sigma}{E} = \frac{2.8\%}{\sqrt{E/\text{GeV}}} \oplus \frac{12\%}{E/\text{GeV}} \oplus 0.3\%, \tag{4.2}$$

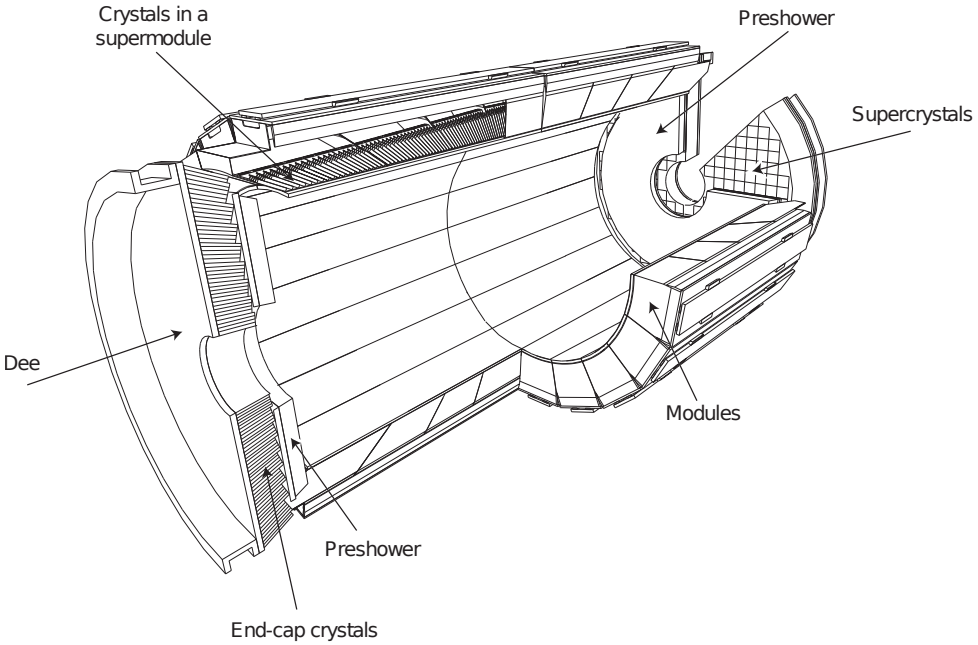

Figure 4.3.: Layout of the CMS electromagnetic calorimeter [59].

where $\oplus$ stands for the quadratic summation of the terms. This means the resolution improves with increasing energy. For a high energy particle, such as an electron with an energy of 1 TeV, the plateau resolution of 0.3 % is reached.

Being exposed to the radiation from the collisions, the ECAL properties may change over time. A study has been made by exposing crystals to radiation corresponding to 500 fb^{-1} [63], showing that the scintillation properties of the crystals are not affected. However, the transparency suffers from the radiation. As the light output is only affected by the reduced transparency, the energy determination can be recalibrated using the test pulses.

4.2.4. Hadronic calorimeter

The hadronic calorimeter (HCAL) is the second calorimetric layer and is important to completely measure the energy of hadronic jets. Also, the determination of the missing transverse energy relies on the comprehensive energy measurement of all detectable particles. A hadron interacts via the strong force with the atomic nucleus and because of that the interaction length of a hadronic particle is larger than the radiation length of an electron or photon.

The HCAL is separated into four parts, which are shown in figure 4.4: The HCAL barrel covers a pseudorapidity up to $|\eta| = 1.3$, the endcaps extend the range up to $|\eta| = 3$. The forward calorimeter covers $|\eta| < 5.2$ and is therefore exposed to a very large particle flux. Another calorimetric layer in the barrel, the hadron outer (HO), is located outside the solenoid, measuring particles not contained by the HCAL barrel.

The HCAL barrel is a sandwich calorimeter composed of plastic scintillators as active material and brass absorbers, only the first absorber is made from stainless steel. The endcap is composed similarly. Both detectors are read out via hybrid photo-diodes.

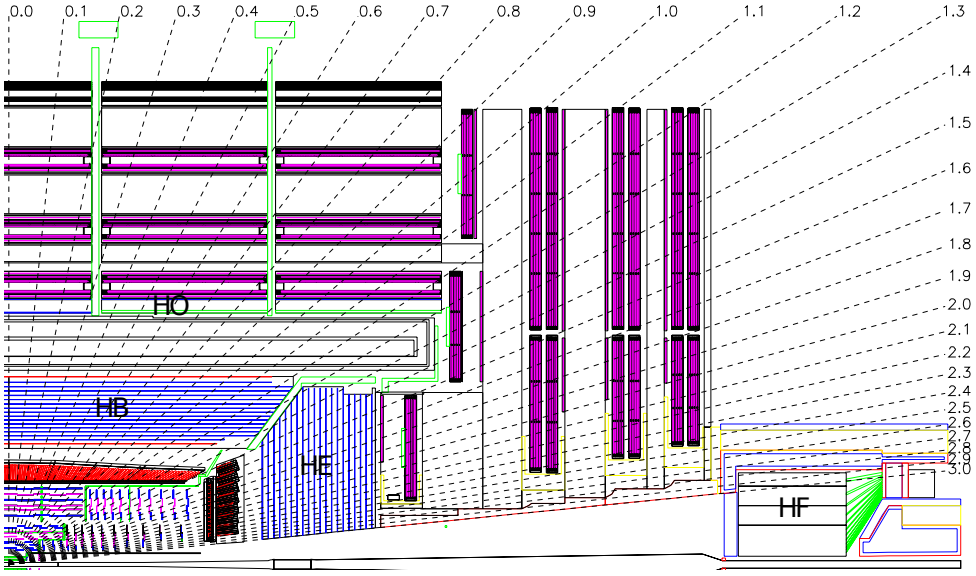

Figure 4.4.: Layout of the CMS hadronic calorimeter [59].

As the particle flux is highly increased in the forward direction, the forward HCAL is composed from steel with inserted quartz fibers, a design which is very radiation hard. They are read out using 8-stage photomultiplier tubes.

The hadron outer extends the calorimeter depth from 5.82 interaction lengths to 11.8 interaction lengths by using the magnet as an absorber. Plastic scintillator tiles are used as active material. They are connected by wavelength shifting fibers with the read out electronics. During the first long stop long shutdown 1 (LS 1), the HPD sensors have been replaced by silicon photo-multiplier sensors.

Test beams studies showed, that for the complete calorimetric systems, pion energies can be reconstructed with a resolution of [64]:

$$\frac{\sigma}{E} = \frac{101\%}{\sqrt{E/\mathrm{GeV}}} \oplus 4\% \tag{4.3}$$

4.2.5. Muon system

The muon system is built to identify muons and measure their trajectories. Muons are the only known charged particles, that are able to traverse the whole detector without depositing a lot of their energy in the dense detector parts, such as the calorimeters or the iron return yoke. Therefore, the muon chambers are located at the outside of the solenoid, as shown in figure 4.5.

Three different types of muon chamber make up the CMS muon system. A total of four stations made from drift tubes chambers (DT) are located around the iron return yoke structures, covering a pseudorapidity range of $|\eta| < 1.2$. Their choice is possible due to the low magnetic field, which is mainly contained in the return yoke, and the small particle flux in that region. Each chamber contains eight drift tube layers measuring the r-ϕ-coordinates of a muon trajectory. The inner three chambers also include four layers rotated by 90°, providing a measurement of the z coordinates as well.

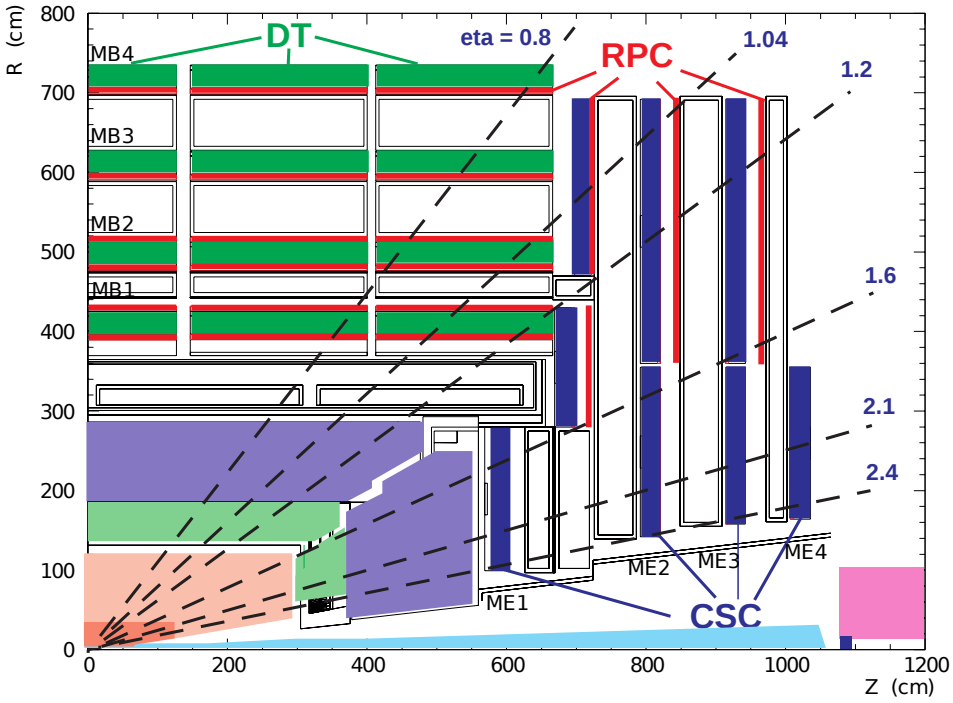

Figure 4.5.: Layout of the CMS muon system, as originally installed [59].

The end cap muon system is equipped with 3–4 stations of cathode strip chambers (CSC), covering $|\eta < |2.4$. They are multiwire proportional chambers with six anode wire layers surrounded by seven cathode strip layers. Wires and strips are positioned perpendicular to each other and both, the cathode strip and the anode wire are read out, providing three dimensional coordinates as well as timing information.

Muon chambers of a third kind, resistive plate chambers (RPC), are placed next to the DT and CSC chambers. They are gaseous parallel plate detectors with two gaps and read-out strips in between. Their time resolution of around 2 ns [65] is an important feature for the triggering of muons. In the barrel region, six layers of RPCs are installed, whereas in the barrel region three layers up to $\eta = 1.6$ exist.

The transverse momentum of a muon is reconstructed using information of both, the tracker and the muon system. The resolution for a low p_T muon ($p_T < 100\,\text{GeV}$) is around 1 % to 2 %. For a high-p_T muon (350 GeV¡p_T ¡2 TeV) the transverse momentum can be determined with a resolution of around 8 % [66].

4.3. Trigger

The time between two collisions (bunch spacing) was 50 ns during the $\sqrt{s} = 8\,\text{TeV}$ run, resulting in a collision rate of 20 MHz. To cope with this rate, a triggering system is used. It consists of two stages. The level 1 trigger is a custom electronic system with input from the calorimeter and the muon system. It reduces the event rate to around 100 kHz.

In a second step, a basic event reconstruction using the high level trigger (HLT) system is performed. It is a software system processing the events in parallel using a large computing infrastructure. The rate of events remaining after these steps, which are subsequently stored and which can be used for the physics analyses is of the order of a few 100 Hz [59].

4.4. Upgrade plans

The envisaged LHC run time is separated into two phases [67]:

- The first period, *Phase I*, started in March 2010 and ends with the third long shutdown (LS 3), up to which a total luminosity of 300 fb^{-1} will be collected. The design energy and instantaneous luminosity is planned to be achieved during Phase I. To accomplish this, a number of upgrades are planned, of which some have already taken place during LS 1, others will be performed during the winter breaks and LS 2.
- After LS 3 the second period of LHC running, *Phase II*, will start. Although the center-of-mass energy is planned to stay at 14 TeV, the envisaged instantaneous and integrated luminosity during this period goes beyond the design scope of the LHC and its experiments. This means, the detector will suffer from more radiation damage while at the same time, the number of particles in a single event will increase, making the reconstruction of particles more challenging. Therefore, major upgrades are planned for LS 3 to prepare CMS for an instantaneous luminosity of $5 \times 10^{34}\,\text{cm}^{-2}\text{s}^{-1}$ and a total integrated luminosity of 3000 fb^{-1}. This scenario, named high-luminosity LHC (HL-LHC), goes beyond the original design scope of the CMS experiment.

A timeline showing the long shutdowns and describing the development of luminosity and energy is shown in figure 4.6.

4.4.1. Phase I upgrades

The list of upgrades stated in this section is not intended to be exhaustive. It concentrates itself on upgrades which may directly affect the performance of the $\ell + E_T^{\text{miss}}$ analysis. A detailed overview of the Phase I upgrades can be found in reference [67].

Tracker

The current pixel detector is designed for a maximum luminosity of $1 \times 10^{34}\,\text{cm}^{-2}\text{s}^{-1}$. Larger event rates will lead to an inefficiency of around 15% at 25 ns bunch spacing and a luminosity of $2 \times 10^{34}\,\text{cm}^{-2}\text{s}^{-1}$ because of readout speed and buffer size limitations. Therefore, the pixel detector is going to be replaced as part of the Phase I upgrades.

As shown in figure 4.7, both, the barrel and the endcaps receive an additional layer, upgrading the barrel to 4 layers and the endcap disks to 3 layers each. This ensures a 4-hit coverage for $|\eta| < 2.5$, which will improve both, the efficiency and misidentification probability when reconstructing charged particles. This redundancy could also cope with the unlikely event of a faster than expected degradation of the innermost pixel layer. Additionally, the new pixel

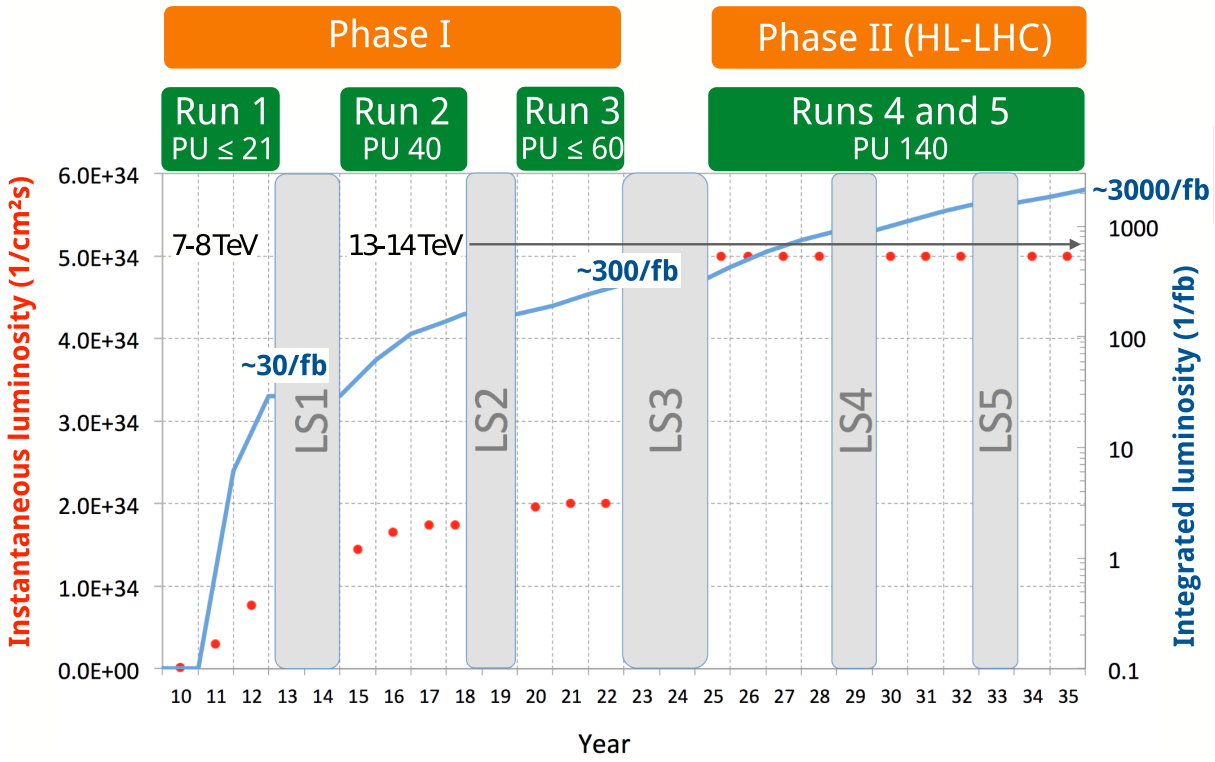

Figure 4.6.: Overview of the LHC runs in the past and as planned for the future. The values before LS 1 have been actually achieved, whereas beyond LS 1 the plans are shown. Modified version of [68].

detector will be made out of less material, which improves the tracking and calorimeter measurements, and the material is chosen to be as radiation hard as possible. Because the innermost layer is located closer to the interaction point, the new pixel detector will improve the vertex resolution by almost 100 % (for $\mathcal{L} = 2 \times 10^{34}\,\mathrm{cm^{-2}s^{-1}}$, $t_{\mathrm{bx}} = 25\,\mathrm{ns}$), e.g. for an event with 50 tracks, the resolution improves from 20 µm to 10 µm [69].

Calorimetry

The HO has already been upgraded during LS1 by changing the read out electronics from HPDs to silicon photomultipliers (SiPMs). An SiPM is an array of photodiodes operated in Geiger-mode. Its quantum efficiency is better than that of an HPD, and its gain is about 50–500 times larger. They work well in magnetics fields up to 4 T and are operated at lower voltages of about 100 V, compared to kV for HPDs. Because of the higher rates in the HB and HE, further developments are required before installing SiPMs there.

In the sandwich calorimeter design used for the HCAL, 17 layers of active tiles are stacked together with absorber material to towers and are connected to the read out via optical fibers.

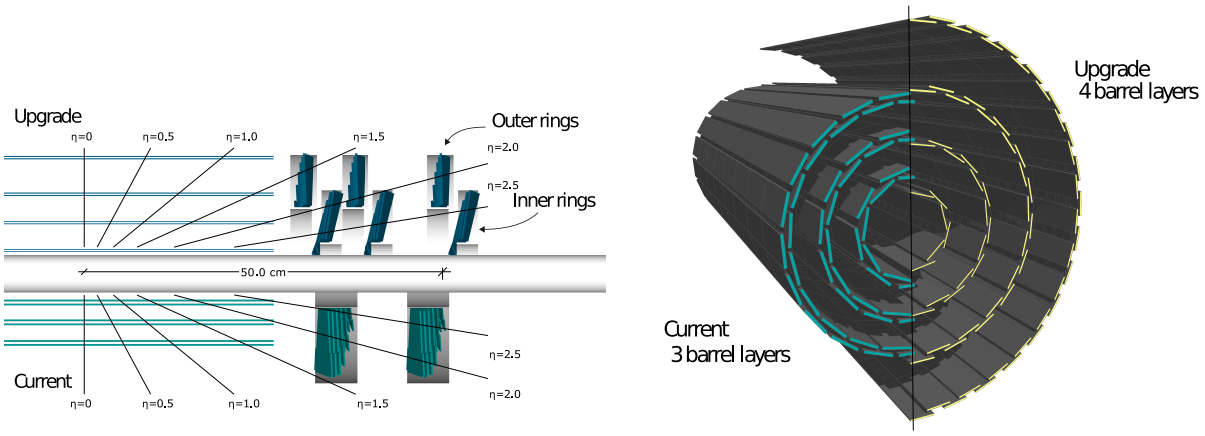

Figure 4.7.: Comparison of the original and the upgraded pixel detector [69]. A fourth layer is added to both, the barrel and the endcap subsystem.

Currently for each of most of the towers only one photodetector exists, on which the light of all the tiles of the tower is collected. A longitudinal segmentation of the calorimeter read out into four sections is envisaged. This upgrade can improve the energy resolution and the ability to identify particle types. For example, the electron identification can profit by excluding the inner layer of the HCAL from the isolation criteria.

Additionally, a better timing resolution of the calorimeter is envisaged to improve the distinction of different bunch crossings. As a result, the so-called "out of time pileup" is going to be reduced.

Muon system

A fourth layer of CSCs and RPCs has been inserted into the forward muon system during LS1. Figure 4.8 shows the additional stations, labeled ME4/2, RE4/2, and RE4/3.

4.4.2. Phase II upgrades

The Phase I detector is designed for an integrated luminosity of 500 fb^{-1} and a pileup (average number of simultaneous interactions) of 60 events. The HL-LHC is going to record 3000 fb^{-1} and is planned to be run with 140 pileup events. With such an intensive exposure of the detector to radiation, many components will suffer and substantial degradation effects are expected. Details about the proposed CMS Phase II detector can be found in reference [6].

Tracker

Because of radiation damage and the increased instantaneous luminosity at the HL-LHC, the tracker will be completely exchanged for the Phase II data taking. The new tracker is not to be replaced again during Phase II and therefore should sustain a total luminosity of 3000 fb^{-1}. To be able to handle 200–250 collisions per bunch crossing, a high granularity is required. The

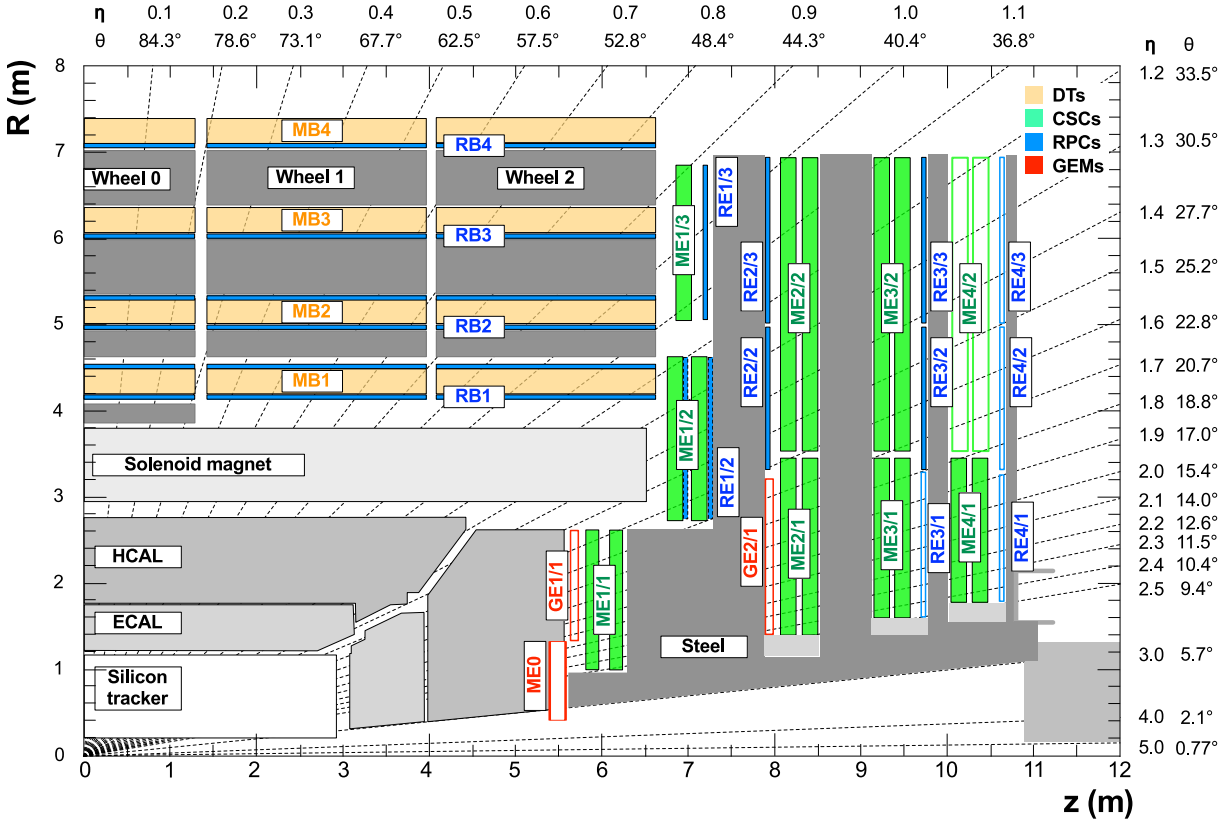

Figure 4.8.: Phase I and II upgrades to the muon system [70]. The filled in stations have been present from the beginning of the LHC, the outlined stations have been or will be added later. The stations ME4/2, RE4/2, and RE4/3 have been inserted during LS 1 as part of the Phase I upgrades. The stations GE1/1, GE2/1, RE3/1, and RE4/1 are part of the Phase II upgrades. A possible Phase II upgrade for a larger acceptance can be accomplished with ME0.

total occupancy should not exceed a few percent at any time to ensure a proper reconstruction of the tracks [71].

The research and development for the most suitable sensors is still ongoing. The most promising option are 200 µm thick p-type sensors.

The pixel tracker is envisaged to cover $|\eta| < 4$, whereas the outer tracker plans foresee a coverage of $|\eta| < 3$, as shown in figure 4.9.

Additionally, the new tracker should have trigger capabilities. During Phase I, the tracker information is used only in the high level trigger. It is envisaged to include modules that determine the transverse momentum of the tracks and feed them to the level 1 trigger. This allows triggering on p_T thresholds of tracks [71].

Calorimetry

The Phase I ECAL barrel can sustain the radiation damage dealt by 3000 fb^{-1} of luminosity. Nevertheless issues can arise from the large number of pileup events and a higher APD noise,

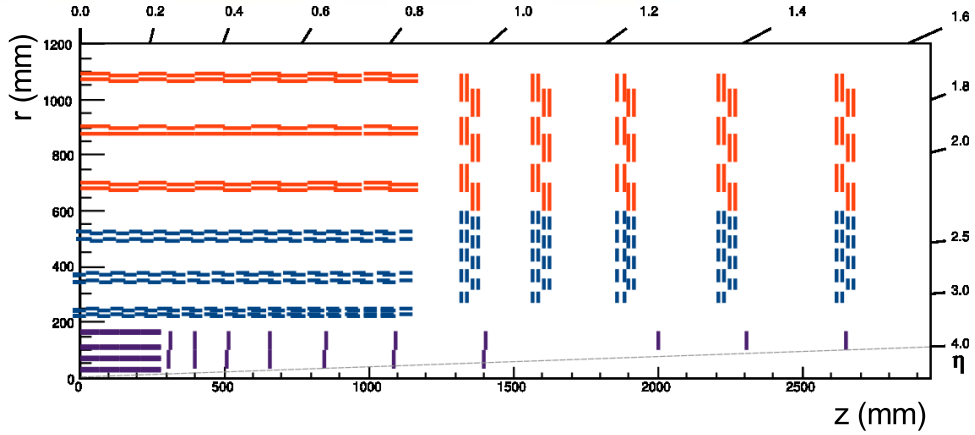

Figure 4.9.: Upgraded tracker system as envisaged with the Phase II upgrades. The pixel tracker covers $|\eta| < 4$, while the strip detector reaches up to $|\eta| = 3$ [71].

which are due to the large instantaneous luminosity. In the endcap regions, the radiation damages will be more severe, because of the increased particle flux. Figure 4.10a shows the degradation of light output for different aging scenarios as a function of the pseudorapidity in the endcap range ($\eta > 1.5$). Even at the smallest pseudorapidity in the endcap, the light output is reduced by about a factor of 2, and for larger values of η it is further reduced to nearly 10^{-3} [72].

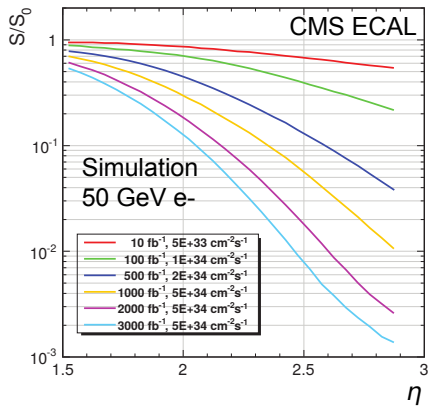

(a) Relative light output of the CMS Phase I ECAL as a function of the pseudorapidity for different integrated luminosities [72].

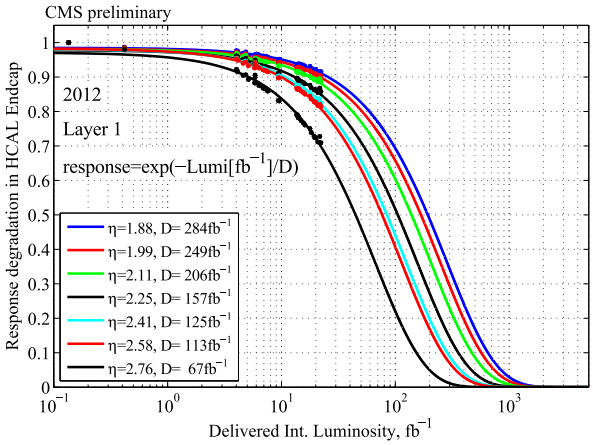

(b) Response degradation of the Phase I HCAL parts as a function of the integrated luminosity [73]. The markers show the measured degradation effects during the 2012 run.

Figure 4.10.: Degradation of the calorimeters with increasing integrated luminosity.

As a result, the energy resolution is degraded. Test beam studies with a 100 GeV beam energy show a change in energy resolution from about 1% with no radiation damage to more than 10% when using an aged crystal corresponding to an integrated luminosity of 3000 fb^{-1} at a pseudorapidity of $|\eta| = 2.6$ [72].

Similarly, the HCAL suffers from the radiation damage. The response will be degraded down to a few percent in the endcaps, as shown in figure 4.10b. To compensate for the degradation, a new endcap calorimeter is proposed for Phase II.

The proposed design is an endcap calorimeter with a high granularity, able to track the development of the showers and covering $1.5 < |\eta| < 3.0$. The electromagnetic part of the calorimeter uses silicon as the active material and tungsten as the absorber material. The HCAL is divided into two parts. The inner part is a silicon/brass sampling calorimeter while the outer part uses plastic scintillators as active material and brass as absorber.

With this design the ECAL depth corresponds to 26 radiation lengths and the total calorimeter depth measures about 10 interaction lengths [6].

Muon system

Additional muon stations in the forward detector region are proposed [74]. A scheme of the suggested chambers, including those of the Phase I upgrade, is depicted in figure 4.8.

The Phase I endcaps will be upgraded with two stations of gas electron multiplier (GEM) chambers and two additional RPC stations in the region of $1.5 < |\eta| < 2.4$. The GEM stations have a good spatial resolution, whereas the RPC are required for a good time resolution. This muon system upgrade is required to retain the trigger performance in the presence of the increased particle flux in forward direction. It will also improve the momentum resolution of very high p_T muons. This is of special importance, as the transverse component of the momentum is rather small in this regime [75].

Additionally, a forward muon station, ME0, is planned outside of the proposed forward calorimeter to extend the muon coverage up to $|\eta| = 3$ [74].

5. Analysis of 8 TeV data

In this chapter, the analysis of the $\sqrt{s} = 8\,\text{TeV}$ data is described, the physics results from this can be found in the next chapter. More detailed descriptions of the analyses can be found in reference [3] for the electron channel and reference [4] for the muon channel.

5.1. Data and luminosity

The events considered in this analysis were acquired in 2012 with $\sqrt{s} = 8\,\text{TeV}$. A total luminosity of $21.8\,\text{fb}^{-1}$ has been recorded by CMS of which $19.7\,\text{fb}^{-1}$ have been certified by the CMS Data Quality Monitoring group and are used for this analysis.

The SingleElectron and SingleMuon data streams are used for the electron and muon analysis, respectively, with the reconstruction as of Jan 21 2013. In the electron channel, the two high level triggers `HLT_Ele80_CaloIdVT_TrkIdT` and `HLT_Ele80_CaloIdVT_GsfTrkIdT` are used, depending on their availability. They require at least one electron in the event with an energy of at least 80 GeV with calorimetric and track based quality criteria.

The events in the muon channel are triggered with `HLT_Mu40_eta2p1`, requiring at least one muon with at least 40 GeV within $|\eta| < 2.1$. As muons are the only particles reaching the muon system, they are easily identified and a lower trigger threshold than the one used for the electrons is possible. The misidentification probability for low energy electrons is relatively large [76], requiring a higher p_T threshold to reduce the event rate appropriately.

The luminosity is measured using the pixel cluster counting method [77]. The instantaneous luminosity $\mathscr{L}$ is proportional to the average number of pixel clusters $< n >$ in zero-bias events, i.e. events with the only requirement that a bunch crossing must have happened:

$$\mathscr{L} = \frac{\nu < n >}{\sigma_{\text{vis}}} \ , \tag{5.1}$$

where $\nu = 11\,246\,\text{Hz}$ is the beam revolution frequency and σ_{vis} is the total visible inelastic proton-proton cross section.

The visible cross section is calibrated using Van-der-Meer scans [78]. For these the beams are displaced vertically and horizontally, scanning the beam profile. From the scan, the beam overlap

$$\Sigma_x \Sigma_y = (\Sigma_{1x}^2 + \Sigma_{2x}^2) \times (\Sigma_{1y}^2 + \Sigma_{2y}^2) \tag{5.2}$$

can be determined, where Σ_{ix} is the effective size of beam i in coordinate x (analogously for coordinate y) [79]. The total visible cross section can then be determined by:

$$\sigma_{\text{vis}} = \frac{2\pi \Sigma_x \Sigma_y < n >}{N_1 N_2} \tag{5.3}$$

where N_i is the number of protons in beam i, which are determined by the LHC beam current transformers [77].

5.2. Object Reconstruction

5.2.1. Electrons

Electrons are measured by the calorimeter and the tracker. While traversing the tracker material, they radiate bremsstrahlung photons, which can convert into electron-positron pairs. Because of the magnetic field, this results in a spread in ϕ of the energy depositions in the ECAL. About 35 % of the electrons lose at least 70 % of their energy via bremsstrahlung. The electron itself deposits its remaining energy in a small number of ECAL crystals. Test beam studies showed a 120 GeV electron deposits 97 % of its energy inside a 5×5 ECAL crystal array. Such a fixed size array of crystals is combined to a cluster [80, 81].

The reconstruction starts by summing up confined energy depositions of adjacent crystals to so-called clusters. A high energy seed cluster is chosen and a supercluster is built from several clusters located around the seed cluster in ϕ direction. By this the energy depositions from bremsstrahlung photons are collected. An additional tracker based seeding algorithm exists but it is only beneficial for low momentum electrons ($p_T < 10\,\text{GeV}$) and therefore not used by this analysis [80, 81].

In the next step, the trajectory of the electron is reconstructed. Considering the supercluster position and energy, a possible trajectory of the electron is calculated. In the two innermost tracker layers, a pixel hit compatible with this trajectory is searched for. Based on this, a hit in the next layer is searched for. A new trajectory candidate is computed at each layer using a Gaussian sum filter, modeling the electron energy loss due to bremsstrahlung. This procedure is performed for each tracker layer. Possibly a number of trajectory candidates are found. If so, at any stage only the two trajectories with the best χ^2 of the track fit are kept. A final fit considering all found hits is performed. For this, at least 5 hits are required [80, 81].

Both, the trajectory and the calorimeter measurements allow a determination of the electron momentum/energy. The momentum measurement from the track is only advantageous for very low energy electrons and therefore not used in this analysis.

The energy is determined from the supercluster and corrected depending on the number of affected crystals. Particles deposit their energy in a crystal and scintillation light is emitted. Using the photo detector, an electronic pulse is generated. The deposited energy is proportional to the pulse amplitude obtained from the sensor read-out. The proportionality factor is different for each crystal and can change over time. It was initially determined from test beam studies and recalibrated using data of well known physics processes, such as $Z \to ee$. To ensure the compatibility of measurements of different crystals, additional methods are used, e.g., by assuming that the average energy deposited must be ϕ symmetric. The time dependent change in crystal transparency is corrected for with the help of laser/LED test pulses, which can be immited into the crystals at any time [82].

5.2.2. Muons

Muons can be measured in the tracker and the muon system. As they are the only known charged particles able to traverse the whole detector, they can be identified by their presence in the muon system.

Muons are minimum ionizing particles, therefore their energy cannot be measured by a calorimeter but must be determined from the curvature of their trajectory in the presence of a magnetic field. From the equilibrium of Lorentz force and centrifugal force, one obtains

$$p_T = r \times q \times B \ , \tag{5.4}$$

where r is the radius of the curvature, q is the charge of the particle and B is the magnetic field. The radius is determined from the sagitta s and the arc length l by [83]

$$r = \frac{l^2}{8s} \ . \tag{5.5}$$

The uncertainty on the measurement of the sagitta is the dominant uncertainty in this measurement and can be modeled with a Gaussian distribution [83].

In the tracker, trajectories are reconstructed starting from a two hit seed in the pixel detector. The track building method is similar to the one described in section 5.2.1. The Kalman filter method is used to propagate the track from layer to layer, taking into account material effects and the magnetic field. The collection of possible tracks is cleaned for ambiguities sharing the same hits.

Independently of the tracker reconstruction, trajectories in the muon system are determined. They are based on segments which are short tracks reconstructed in a single muon chamber. At least two segments are required to reconstruct a track in the muon system.

Two different basic algorithms are used to reconstruct muons. The *global muon* reconstruction matches a tracker track to each muon system track. A common trajectory is found by fitting the associated hits of both systems using the Kalman-filter technique. In the *tracker muon* approach, all tracker tracks with $p_T > 0.5\,\text{GeV}$ and $p > 2.5\,\text{GeV}$ are propagated to the muon system. At least one matching segment is required to declare a tracker muon. This method is especially favorable for low energy muons, as they often do not reach the outer muon chambers [66].

In this analysis more sophisticated methods are used, which are based on these two algorithms.

The particle flow (PF) algorithm makes use of all detector components to derive a consistent picture of all particles in an event without ambiguities [84,85]. The *particle flow muon* algorithm is based on the global muon and tracker muon reconstruction. Adaptive quality criteria are applied ensuring on the one hand the reconstruction of low p_T muons that are part of jets and on the other hand minimizing the misidentification of charged hadrons as muons.

Two specialized algorithms meet the particular demands when reconstructing high p_T muons. Such muons might not act as a minimum ionizing particle and can change their trajectory by emitting bremsstrahlung. This can lead to showers detectable by the muon system. *TPFMS muons* (tracker plus first muon station) are global muons whose trajectories are refitted taking only the tracker information and the innermost available segment of the muon system into

account. This algorithm works well even if a high energy muon produces a shower while interacting with the iron return yoke material. The *picky muon* algorithm also reevaluates the trajectory of the global muon reconstruction. Chambers with a high occupancy are assumed to be subject to an electromagnetic shower. A χ^2 test is performed for all hits in such a chamber, rejecting hits which are not compatible with the tracker trajectory. Using the remaining hits, the muon trajectory is refitted.

To combine the advantages of the tracker, global, TPFMS, and picky algorithms, a meta algorithm, *Tune P*, choses for each individual muon the one with the best performance based on the reconstructed muon momentum and the goodness-of-fit. For high p_T muons in all but a few per cent of the cases this means that either TPFMS or picky are chosen. This analysis is based on the Tune P algorithm.

5.2.3. Missing transverse energy

As there is no initial transverse momentum in the pp collisions, an imbalance of the outgoing transverse momenta indicates additional undetected outgoing particles. Although the negative sum of all reconstructed particle transverse momenta has a direction and therefore is better described as a momentum, it is commonly referred to as the missing transverse energy [86].

$$\vec{p}_T^{\,\text{miss}} = -\sum_i \vec{p}_T{}^{\,i}. \tag{5.6}$$

Its modulus is:

$$E_T^{\text{miss}} = |\vec{p}_T^{\,\text{miss}}|. \tag{5.7}$$

This analysis uses the missing transverse energy as reconstructed by the particle flow (PF) algorithm. The PF algorithm reconstructs an unambiguous set of particles — namely electrons, muons, photons, charged hadrons, and neutral hadrons — by using all detector components and cleaning the set for ambiguities. Nevertheless, a number of corrections have been developed, improving the accuracy of the reconstruction.

Muon correction

As described in section 5.2.2 muons are reconstructed using the Tune P algorithm. The results of that may differ from the PF muon reconstruction which enters the determination of the PF E_T^{miss}. Therefore the E_T^{miss} is corrected for the muon by removing the particle flow muon from it and replacing it with the Tune P muon. This is especially important for high p_T muons as their results of the two reconstructions differ substantially. Sometimes multi-TeV muons are reconstructed with a momentum of a few hundred GeV with the particle flow muon algorithm, although they are correctly (within the resolution) reconstructed with the Tune P algorithm. If this correction is neglected, the signal efficiency for $p_T > 1\,\text{TeV}$ declines rapidly.

Type 1 correction

Different types of energy corrections for jets (JEC) have been developed to ensure a correct and uniform energy determination independent of where in the detector the energy is deposited.

These corrections are propagated to the missing transverse energy determination and are called Type 1 E_T^{miss} corrections [87].

The Type 1 correction is subdivided into three levels. The corrected energy for a jet is determined as:

$$E^{\text{T,miss}}_{\text{jet, Type 1}} = (E^{\text{jet}}_{\text{uncorrected}} - C_1) \times C_2(|\eta|) \times C_3(p_T) \tag{5.8}$$

The level 1 correction subtracts energy not originating from the primary interaction. Such an energy bias can be due to pileup events and electric noise in the calorimeter read out electronic. An offset energy C_1 is determined for each jet taking into account the average jet energy density in the event, the jet pseudorapidity and the jet size. However the dependence on the pseudorapidity is small.

The level 2 or relative correction is determined as a function of η. It ensures that on average the same energy is measured independently of where in the detector the particle has been observed.

Monte Carlo studies show that the average reconstructed jet p_T is smaller than the generated jet p_T and varies as a function of p_T. This is addressed by the level 3 correction. It is also called absolute correction as it sets the absolute energy scale.

ϕ correction

The ϕ distribution of the particle flux is expected to be uniform because of the symmetry of the experimental setup. However, studies showed a modulation of the ϕ distribution, present in both data and simulated events. The cause could be a misalignment of detector subsystems or the beamline or it could arise from a ϕ dependence of the detector response. The missing transverse energy is corrected by applying:

$$E_x^{\text{miss}} = E_x^{\text{miss, uncorrected}} - (c_{x0} + c_{xs} \times N_{\text{vtx}}) \tag{5.9}$$

$$E_y^{\text{miss}} = E_y^{\text{miss, uncorrected}} - (c_{y0} + c_{ys} \times N_{\text{vtx}}) \tag{5.10}$$

with the parameters given in table 5.1 [88].

The influence of the correction on the number of events as a function of ϕ in the electron channel is shown in figure 5.1. For an easier comparison The Monte Carlo simulation is scaled to data. All events fulfilling the muon selection are included. The Measurement and the simulation show a different modulation in ϕ, which both vanish after the correction.

Table 5.1.: Correction parameters for the ϕ correction of missing transverse energy [88].

	c_{x0} (GeV)	c_{xs} (GeV)	c_{y0} (GeV)	c_{ys} (GeV)
Data	0.27	0.32	-0.23	-0.17
Simulation	0.12	0.02	0.28	-0.13

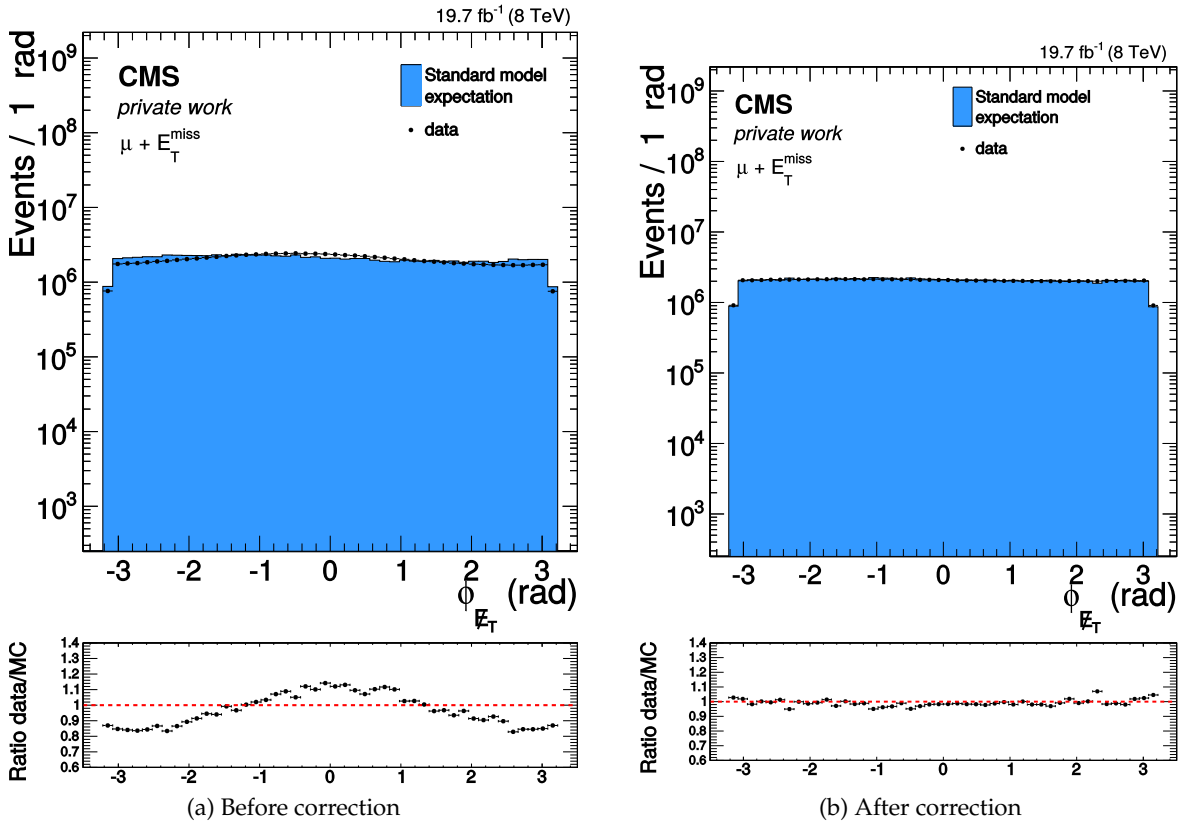

(a) Before correction

(b) After correction

Figure 5.1.: Azimuthal angle correction of the missing transverse energy [4] (modified). Before the correction a modulation in ϕ is visible in both, data and simulation. After the correction, the two distributions are uniform in ϕ.

5.3. Selection

Of all triggered events a subset is selected, based on different criteria. One set of selection criteria is used, which reject events that contain detector artifacts, i.e. detector responses that do not originate from collisions.

To identify the particles (and the missing transverse energy) in the event, for each object a set of criteria has been developed to efficiently identify the object while reducing its misidentification probability.

Further criteria are chosen such that the number of background events is reduced while maintaining the number of signal events. As the analysis covers a wider range of different models and also provides a model independent interpretation, the selection criteria are rather lose in order to not lose discovery potential in any signal.

5.3.1. Common selection

All events are required to have a well reconstructed vertex located within a distance $|z| < 24\,\text{cm}$ measured from the nominal interaction point.

The CMS JetMET group provides a set of filters rejecting events with significant E_T^{miss} contributions not related to the collision physics [89, 90]. The number of affected events is relatively small ($< 2\,\%$). To prevent a selection bias, the filters have been thoroughly studied and the rejection of events must be based on good reasons. The following events are rejected by applying filters to both, the data as well as the Monte Carlo samples:

- *CSC tight beam halo*: Events with beam halos interactions identified using CSC information.
- *HBHE noise*: Events with noise in the hadron barrel (HB) or endcap (HE).
- *ECAL dead cell*: Events depositing a large amount of energy in malfunctioning cells.
- *HCAL laser*: Events during which the HCAL calibration laser was active.
- *Tracking failure*: Events with too few tracks.
- *Bad EE Supercrystal*: Events where two endcap crystals measure a too large amount of energy.
- *ECAL Laser correction*: Events with a wrong laser correction.
- *Tracking algorithm*: Events where the tracking algorithm failed.

5.3.2. Electron selection

To identify the electrons, a scheme originally developed for high energy electron pairs (HEEP 4.1 [91]) was chosen. It combines a number of selection criteria, which are specified separately for the barrel and endcap region. A summary is listed in table 5.2. The following variables are taken into account:

η The pseudorapidity η of the calorimeter supercluster separates the barrel and endcap region.

isEcalDriven Only electrons seeded by calorimeter entries are used.

$\Delta\eta_{\text{in}}$, $\Delta\phi_{\text{in}}$ These two variables describe the difference of the track position as measured from the inner layer of the tracker and from the calorimeter supercluster.

H/E The ratio of energy deposited in the ECAL and HCAL, measured in a cone of radius 0.15 around the electron position.

$\sigma_{i\eta i\eta}$ A measure for the energy distribution in η direction determined in the number of crystals in a 5×5 crystal matrix around the seed crystal. An exact definition can be found in [3].

$E^{x\times5}/E^{5\times5}$ Additional measures for the energy distribution. The quantity $E^{1\times5}$ is the energy contained in a strip of 5 crystals in ϕ with the center being the seed crystal. For $E^{2\times5}$ the energy of an array spanning 2 crystals in η and 5 crystals in ϕ is summed up around the crystal seed. The ambiguity for the direction of the second η strip is resolved by always selecting the strip with the larger energy. The energies are normalized by dividing them by the energy contained in the 5×5 crystal array around the seed, $E^{5\times5}$.

EM + had isolation A combined electromagnetic and hadronic isolation is used. The ECAL energy inside a cone of $\Delta R < 0.3$ excluding an inner cone with a 3-crystal radius. Energy

Table 5.2.: Electron identification criteria as specified by HEEP 4.1.

Criterion	Barrel	Endcap
η	$\lvert\eta\rvert < 1.442$	$1.56 < \lvert\eta\rvert < 2.5$
E_T	$> 35\,\text{GeV}$	$> 35\,\text{GeV}$
isEcalDriven	isEcalDriven	isEcalDriven
$\lvert\Delta\eta_{\text{in}}\rvert$	< 0.005	< 0.007
$\lvert\Delta\phi_{\text{in}}\rvert$	< 0.06	< 0.06
H/E	< 0.05	< 0.05
$\sigma_{i\eta i\eta}$		< 0.03
$E^{x\times5}/E^{5\times5}$	$E^{2\times5}/E^{5\times5} > 0.94$ or $E^{1\times5}/E^{5\times5} > 0.83$	
EM + had isolation	$< 2\,\text{GeV} + 0.03E_T + 0.28\rho$	$< 2.5\,\text{GeV} + 0.03(E_T - 50\,\text{GeV}) + 0.28\rho$
Track isolation	$p_{\text{T,track}} < 5\,\text{GeV}$	$p_{\text{T,track}} < 5\,\text{GeV}$
Inner layer lost hits	< 2	< 2
$\lvert d_{xy}\rvert$	< 0.02	< 0.05

depositions with $E_T \leq 0.08\,\text{GeV}$ in the barrel and $E_T \leq 0.1\,\text{GeV}$ in the endcaps are not considered. For the hadronic isolation towers inside a cone of $\Delta R < 0.3$ are considered, excluding those inside of $\Delta R < 0.15$. The sum of electromagnetic and hadronic isolation is compared to the sum of an absolute value, a relative value compared to the candidate's E_T, and a relative value compared to the mean energy density per unit area ρ originating from pileup.

Track isolation The track isolation is the absolute energy measured from tracks inside a cone of $\Delta R < 0.3$ excluding an inner cone of $\Delta R < 0.04$.

Inner layer lost hits A lost hit is a tracker sensor in the line of the trajectory that has not responded to the electron candidate. A lost hit in the inner layer can be an indication for a photon conversion inside the tracker.

$|d_{xy}|$ The impact parameter describes the distance of the track to the primary vertex. It is used to reject non-prompt electrons.

Events containing a second electron identified with the HEEP criteria and with an energy of at least 35 GeV are rejected. Those events likely originate from a standard model process such as $Z \to ee$ and do not represent the signal signature.

The trigger efficiency as a function of the electron p_T is shown in figure 5.2. As the electron energy determination used for the trigger differs from the one used in the final reconstruction, the electron efficiency gradually increases between $80\,\text{GeV} \lesssim E_T \lesssim 100\,\text{GeV}$. This behavior

is not well simulated and therefore the $E_T > 100\,\text{GeV}$ criterion is introduced to avoid events within this so-called trigger turn-on region.

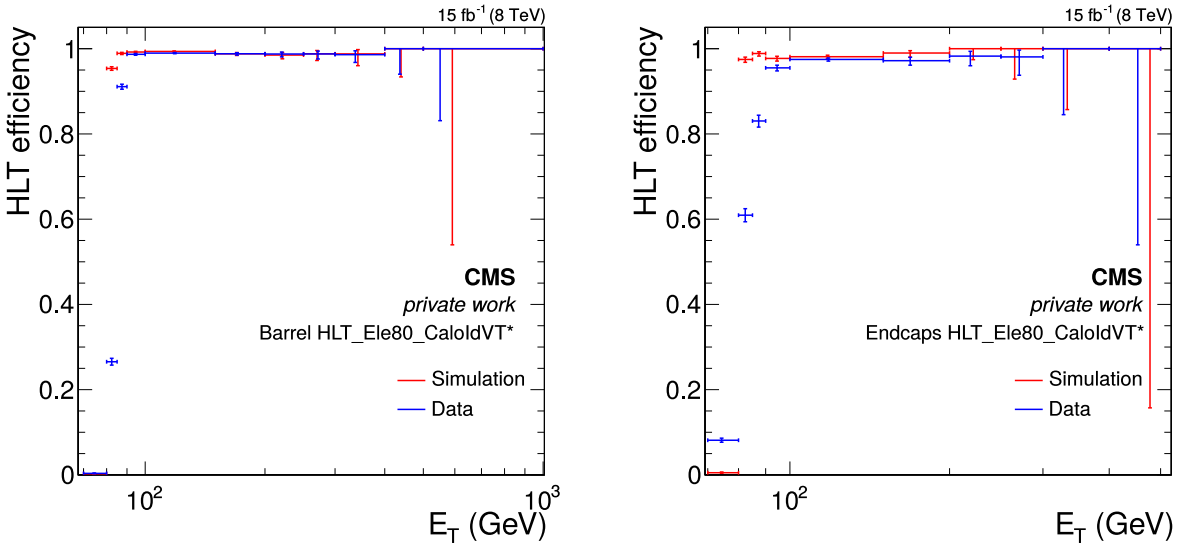

(a) Barrel region

(b) Endcap region

Figure 5.2.: Efficiency of the electron trigger as a function of the electron p_T for both, simulation and data [92] (modified).

5.3.3. Muon selection

Muons are selected based on the CMS HighPT muon identification [66, 93, 94]. If one of the following criteria is not fulfilled by the leading muon the event is rejected:

- The muon candidate must be identified as a global muon.
- At least one muon chamber hit is included in the global muon track fit. Suppresses punch through as well as non-prompt muons.
- A minimum of two muon stations contain muon segments. This criterion is in accordance with the muon trigger and reduces misidentifications from punch through as well as incorrect tracker to muon system matches.
- Transverse impact parameter with respect to the primary vertex $d_{xy} < 0.2\,\text{cm}$. This reduces cosmic muons and non-prompt muons.
- Longitudinal impact parameter $d_z < 0.5\,\text{cm}$.
- At least one hit in the pixel detector.
- A minimum of five tracker layers contain hits of the muon.
- The relative p_T uncertainty is less than 30 %.

The identified muon must have a transverse momentum $p_T > 45\,\text{GeV}$ to avoid the trigger turn-on region and must lie within $|\eta| < 2.1$, which is the coverage of the muon trigger. If a

second global muon with $p_T > 25\,\text{GeV}$ is present in the event, the event is rejected to reduce the Drell–Yan background.

5.3.4. Common kinematic selection

To reduce the number of background events, two kinematic criteria are introduced. The signal events are expected to be dominated by the lepton and missing transverse energy. Because of the conservation of momentum, they should point at opposite directions and have similar energies. Their angle in ϕ is constrained to

$$\Delta\phi(\ell, \vec{p}_T^{\,\text{miss}}) > 2.5 \tag{5.11}$$

and the ratio of the lepton p_T (precisely: E_T for the electron) must fulfill the criterion

$$0.4 < p_T / E_T^{\text{miss}} < 1.5. \tag{5.12}$$

5.4. Detector simulation

5.4.1. Simulation process chain

The background and signal predictions are based on different Monte Carlo simulations. The backgrounds are simulated using PYTHIA [95], POWHEG [96–98], and MCATNLO [99]. Details on this can be found in section 5.5. The SSM W′ and the HNC-CI signals are generated using PYTHIA, for the SSMS/SSMO W′ samples and the dark matter EFT samples MADGRAPH [100] is used. More details about the signal samples can be found in section 5.6.

For all samples, background as well as signal, the simulation program PYTHIA is used for showering and hadronization of the events subsequently (or, if the events are originally produced with PYTHIA, this is performed in one step). The showering adds additional jets to the events, that are not simulated by the Monte Carlo generator.

The events are then passed onto the FULLSIM CMS detector simulation. It uses GEANT 4 [101, 102] to simulate the particle interactions in the detector material. Subsequently, the responses of the electronic devices and the triggers are emulated and the same reconstruction algorithms as for the actual data are used to reconstruct the objects in the events. The same selection as for data events is applied to the simulated events.

5.4.2. Scale factors

The detector simulation is of high quality and only small deviations to the output of the actual detector is expected. To account for these small differences, the selection efficiencies in both data and Monte Carlo are studied and a scale factor is determined, matching the Monte Carlo efficiency to the data efficiency.

The efficiencies are estimated using the tag-and-probe method. It is based on events with a Z boson decaying into two leptons. One lepton, which fulfills strict quality criteria, is declared

the tag lepton. The other probe lepton can then be independently tested on whether it passes e.g. the trigger or identification criteria [103].

For both, the electron and muon channel, the efficiencies of the lepton identification criteria is very compatible between data and simulation. Slight differences in the trigger efficiencies yield an electron scale factor of 0.975 ± 0.023 in the barrel and 0.970 ± 0.042 in the endcaps [3]. For the muon channel, the scale factor is 0.969 ± 0.027 [4].

Since only Z boson decays are tested, the examined energy range is limited. Variations of the scale factors in the examined p_T regime are considered in the uncertainty on the scale factor. There is no indication whatsoever that the scale factor changes at large energies.

5.5. Background prediction

The background prediction is based on different Monte Carlo simulations. The generated events are then passed onto the FULLSIM CMS detector simulation. Subsequently, the same reconstruction algorithm as for the actual data are used, and the same selection is applied. Notwithstanding, the QCD background in the electron channel is derived from data.

5.5.1. Processes

A number of different standard model processes contribute to the $\ell + E_T^{\text{miss}}$ channels. These have to be simulated separately and in total yield the standard model prediction of the channels.

The dominant process for the complete M_T range is W boson production. Other contributing processes are $t\bar{t}$ production, single top, QCD multijet, Drell-Yan, and diboson. In the electron channel, also photon events affect the standard model prediction because photons can be misidentified as electrons. A list of all processes with their corresponding cross sections can be found in the appendix in section A.1.

$W \to \ell\nu$ The W boson is the dominant background process. A W boson event produced at the same (virtual) mass as a W′ boson is indistinguishable from the W′ boson. Parts of this background contribution is therefore irreducible. The $W \to \tau\nu$ branch also contributes to the background, as the tau lepton is not stable and decays to an electron or a muon and two neutrinos with a branching fraction of about 17 % [9].

$t\bar{t}$, single t Top quarks decay into a W boson and a b quark, and the W boson may give rise to a single lepton. Events with top pairs are simulated using MCATNLO at next-to-leading order (NLO). Single top quarks can be produced in association with W bosons or additional quarks. They are produced using the POWHEG event generator including next-to-leading order (NLO) corrections [104].

DY The Drell-Yan ($Z/\gamma \to \ell\ell$) process produces two charged leptons. In case one of them is not identified, e.g. because it is outside of the acceptance or does not fulfill a quality criterion, the event signature may appear like $\ell + E_T^{\text{miss}}$. Also the production of two taus and

the subsequent decay of one of them into a lighter lepton and two neutrinos contributes to the background prediction.

Diboson Diboson production, namely WW, WZ, and ZZ, may give rise to a $\ell + E_T^{\text{miss}}$ signature. While one of the bosons decays into leptons, the second may decay into quarks, or in case of the Z boson into two neutrinos, resulting in a $\ell + E_T^{\text{miss}}$ final state. Misidentification or trajectories outside the detector acceptance can also change the event signature such that it appears to include just one lepton and missing transverse energy. All diboson samples are produced with the PYTHIA event generator at leading order (LO).

QCD Multijet events are produced with a very large cross section via QCD interactions. Usually such events do not contain well isolated high p_T leptons, but due to its high rate the process should be considered in the background. Especially in the electron channel, jets may be misidentified as electrons. In the muon channel, QCD multijet events are produced using PYTHIA. In the electron channel, the background is determined from data using the ABCD method [3].

γ + jets Photons radiated from the initial or final state particles may be misidentified as electrons if they can be matched to a track. Therefore, the γ + jets process adds to the background in the electron channel. It is simulated using PYTHIA.

The muon pseudorapidity distribution of the background processes and the data is shown in figure 5.3. Also displayed are two example signal distributions. The standard model prediction is compatible with the data. The production of W bosons is the dominant background process, followed by top and top-pair production. Contributions from QCD, Drell-Yan, and diboson processes are negligible over the whole pseudorapidity distribution.

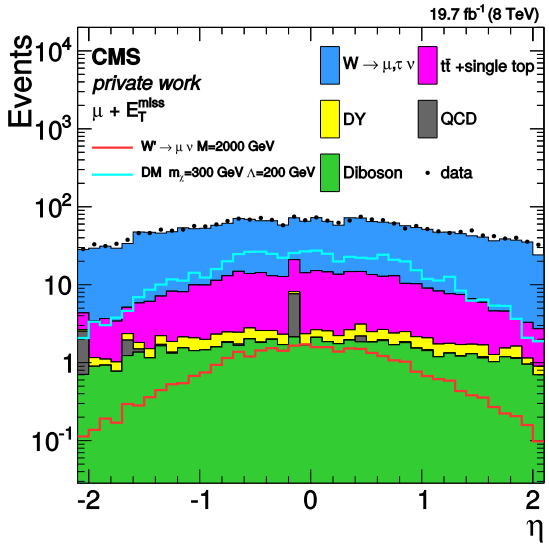

Figure 5.3.: Pseudorapidity distribution in the muon channel [4] (modified). The dominant background process results from W boson production, followed by top and top-pair production.

5.5.2. W boson higher order corrections

To get a good description of the background, higher order corrections have to be taken into account. This is of special importance for the dominant W boson background. A simple scaling of the total cross section will not lead to a sufficient description of the transverse mass distribution, as the corrections depend on the energy scale. Following a prescription by reference [105], the electro-weak and QCD corrections are calculated separately and are subsequently combined. The NLO QCD corrected events can contain a quark loop in the initial state or can radiate a gluon from the initial state. Electro-weak corrected events can radiate a photon from the initial or final state or can show a photon loop in the final state.

Electro-weak corrected events and cross section are determined using the HORACE event generator [106] with the NLO CT10 PDF set [107]. The events include one-loop corrections as well as bremsstrahlung photons radiation from the initial state, the W boson, and the final state. For higher orders, a QED parton shower is matched to the NLO calculation.

Events with QCD corrections are calculated by the MCATNLO generator, also using the CT10 PDF set. They include the full NLO description, including virtual and real emissions.

The LO W boson sample is produced with the LO Cteq6l1 PDF [108] set. Corrections due to the NLO CT10 PDF set on LO events are incorporated both in the HORACE and the MCATNLO samples. In order to not account for this correction twice, a PYTHIA CT10 sample is used. It includes the corrections of the PDF set without the EW or QCD NLO corrections.

To combine the electro-weak and QCD corrections, reference [105] proposes two different methods, an additive and a factorized combination. The correction factors (K-factors) are determined as:

$$K^{\text{CT10}}_{\text{QCD}\,\oplus\,\text{EW}} = \frac{\left[\frac{d\sigma}{dM_T}\right]^{\text{CT10}}_{\text{QCD}} + \left[\frac{d\sigma}{dM_T}\right]^{\text{CT10}}_{\text{EW}} - \left[\frac{d\sigma}{dM_T}\right]^{\text{CT10}}_{\text{LO}}}{\left[\frac{d\sigma}{dM_T}\right]^{\text{Cteq6l1}}_{\text{LO}}}, \tag{5.13}$$

$$K^{\text{CT10}}_{\text{QCD}\,\otimes\,\text{EW}} = \frac{\left[\frac{d\sigma}{dM_T}\right]^{\text{CT10}}_{\text{QCD}}}{\left[\frac{d\sigma}{dM_T}\right]^{\text{Cteq6l1}}_{\text{LO}}} \times \frac{\left[\frac{d\sigma}{dM_T}\right]^{\text{CT10}}_{\text{EW}}}{\left[\frac{d\sigma}{dM_T}\right]^{\text{Cteq6l1}}_{\text{LO}}} \times \frac{\left[\frac{d\sigma}{dM_T}\right]^{\text{Cteq6l1}}_{\text{LO}}}{\left[\frac{d\sigma}{dM_T}\right]^{\text{CT10}}_{\text{LO}}}, \tag{5.14}$$

where $\left[\frac{d\sigma}{dM_T}\right]$ is the differential cross section, the upper index gives the PDF set name and the lower index gives the type of correction applied.

The idea of the additive method, QCD $\oplus$ EW, is to add up all differences of the QCD and the electro-weak corrected samples compared to the LO sample. For this the differential cross sections from the EW corrected and QCD corrected samples are added up. The sum includes the leading order cross section twice. To compensate for this, the leading order calculation with the NLO PDF set is subtracted. This compensates also for the double consideration of the NLO PDF set. The K-factor is determined by dividing the result by the differential cross section of the original sample, produced at LO with the LO PDF set.

For the factorized combination, QCD $\otimes$ EW, the individual K-factors for the EW and QCD corrections are multiplied. As this includes the difference to the NLO PDF set twice, the inverse of the K-factor describing this correction is multiplied to the result.

The results are displayed in figure 5.4. The K-factors for QCD $\oplus$ EW and QCD $\otimes$ EW are averaged and the result is fitted to obtain a parametrization of the mean of the two K-factors. Half the difference between the two K-factors is considered as an additional uncertainty.

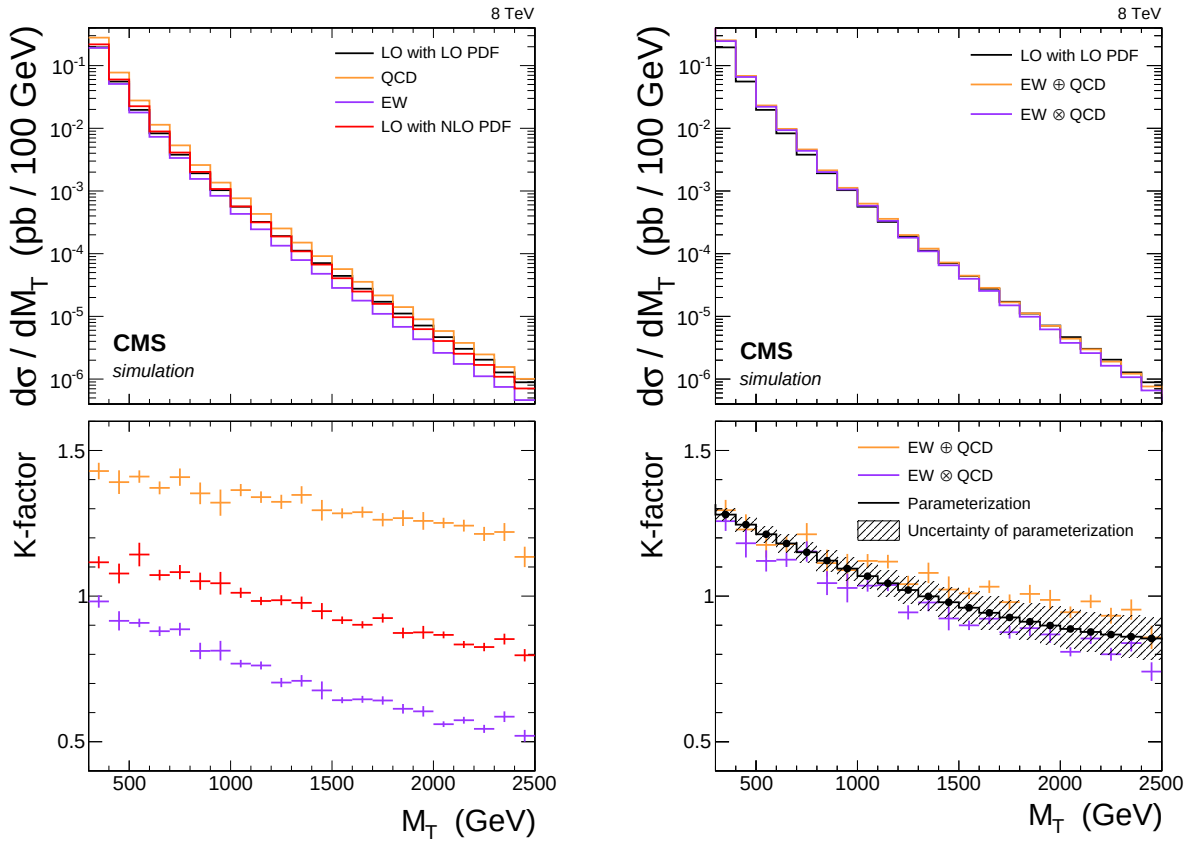

(a) M_T distribution and K-factors for QCD, electroweak, and NLO PDF set corrections.

(b) M_T distribution and K-factors for the additive and factorized combination of higher order corrections.

Figure 5.4.: W boson higher order corrections.

When looking at the conceptual difference between additive and factorized methods, one can argue, that the additive method considers the QCD and EW corrections as independent and therefore their contributions are added to the LO cross section independently, whereas the factorized method considers them to be correlated, applying the electroweak K-factor to the already QCD corrected cross section (or vice versa).

The next-to-next-to-leading order (NNLO) electroweak corrections are not included in the K-factor. However, they are expected to be small. Calculation with W^+ bosons at $\sqrt{s} = 14\,\text{TeV}$ determined the Sudakov terms of the NNLO corrections to contribute a cross section correction of 1.3 % for $M_T > 1\,\text{TeV}$ which is one order of magnitude smaller than NLO electroweak corrections [109].

Also not included are corrections from photon induced processes, such as $q\gamma \to q'\ell\nu$. The high $M_T > 1\,\text{TeV}$ cross section is expected to be affected by 0.4 %, which is about two orders of magnitude smaller NLO electroweak corrections [109].

5.5.3. Parametrization

The transverse mass spectra of all background contributions are added up. To avoid unphysical fluctuations of the total background, which may arise from an insufficient number of simulated events of a single sample, the resulting total is parametrized. For this, the distribution is fitted using a heuristic function. The functions for the electron and muon channel are chosen as:

$$f_{\text{electron},M_T<293\,\text{GeV}}(x = M_T) = \text{Landau}(x) \tag{5.15}$$

$$f_{\text{electron},M_T\geq 293\,\text{GeV}}(x = M_T) = \exp(a + b \cdot x + c \cdot x^2) \cdot x^d \tag{5.16}$$

$$f_{\text{muon}}(x = M_T) = \exp(a + b \cdot x + c \cdot x^2) \cdot x^d + \exp(e \cdot x + f) \cdot x^{-1} \tag{5.17}$$

The function for the electron channel is piecewise defined for the low M_T and the high M_T regimes. The same functions are used for the best estimated backgrounds as well as for the shifted backgrounds when considering systematic uncertainties. This is described in section 5.7.

5.6. Beyond the standard model signals

5.6.1. SSM W′ boson

The SSM W′ boson is a heavy analogue of the standard model W boson. For masses not too large (e.g. $M_{\text{W}'} = 1\,\text{TeV}$) it shows a comparable transverse mass signal. A similar Jacobian peak structure emerges at the W′ boson mass. The decay width increases linearly with larger masses.

Very heavy W′ bosons are predominantly produced off their mass shell at lower masses. This is due to an insufficient phase space at large energies. The available energy, quantifiable by the parton distribution function and the proton energy $\sqrt{s}$, is mostly too low to reach the W′ boson mass. This can be seen in figure 5.5, for example for $M_{\text{W}'} = 4\,\text{TeV}$.

The signal samples for the SSM W′ boson have been generated in LO with PYTHIA. The model has also been implemented in MADGRAPH. Cross checks with different mass points yield very compatible distributions. Higher order QCD corrections affect the initial state of the interaction. They are determined for all samples [110] using FEWZ [111, 112] and are applied as K-factors to the cross section with values ranging between 1.1 and 1.4. Bosons with small and large masses (e.g. 300 GeV and 4000 GeV) are associated similar K-factors, as W′ bosons with large masses are produced predominantly off-shell at low M_T. Intermediate masses (e.g. 3000 GeV) correspond to smaller K-factors. The LO cross sections and the NNLO K-factors for some representative W′ boson masses are listed in table 5.3. Also provided are the relative PDF corrections, which are in the order of about 5 %, variating for different W′ boson masses.

The efficiency for the SSM W′ samples depend on the W′ boson mass. As shown in figure 5.6 for the electron channel, the efficiency has a maximum at around $M_{\text{W}'} = 1.5\,\text{TeV}$. The $E_T > 100\,\text{GeV}$ selection criterion reduces the number of signal events the most. Signals with very low and very high values of $M_{\text{W}'}$ have large event contributions at low energies, thus these sample are affected the most by the criterion. In the muon channel, the $p_T > 45\,\text{GeV}$ criterion is less severe than the $E_T > 100\,\text{GeV}$ criterion of the electron channel. The total SSM W′ efficiencies range from 55 % (for $M_{\text{W}'} = 300\,\text{GeV}$) up to 70 % (for $M_{\text{W}'} = 1.5\,\text{TeV}$) in the muon channel.

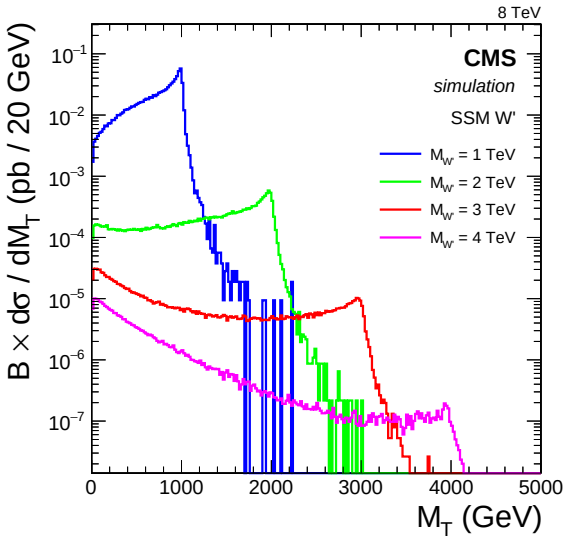

Figure 5.5.: Branching fraction times differential cross section as a function of the transverse mass for SSM W′ bosons as generated with PYTHIA.

Table 5.3.: SSM W′ boson total cross sections as generated with PYTHIA for selected masses, together with the respective K-factors for NNLO QCD corrections and relative PDF uncertainties. For comparison, the W boson cross section amounts to 9.14×10^3 pb, with a QCD K-factor of about 1.3.

Mass (GeV)	Cross section LO $\times$ $\mathcal{B}$ (pb)	QCD NNLO K-factor	relative PDF uncertainty
300	1.14×10^2	1.35	2.19×10^{-2}
900	1.47	1.347	3.45×10^{-2}
2000	2.12×10^{-2}	1.214	4.98×10^{-2}
3000	1.32×10^{-3}	1.151	5.69×10^{-2}
4000	2.51×10^{-4}	1.331	3.72×10^{-2}

5.6.2. SSMS/SSMO W′ bosons

The SSMS and SSMO W′ bosons interfere with the standard model W boson, as described in section 2.2.1. In the mass range $M_W < M < M_{W'}$ the interference term of the SSMS model yields negative contributions to the cross section and the SSMO model a positive contribution. In the other mass regions, the effect is vice versa.

The SSMS/SSMO signals have to be generated together with the dominant W-boson background. An implementation of the model [15] in MADGRAPH at LO is used to determine the cross section and to generate events. As the M_T distribution spans over several orders of magnitude, for each mass point three samples are produced binned in different p_T regions. A list of all samples used can be found in table A.4 in the appendix.

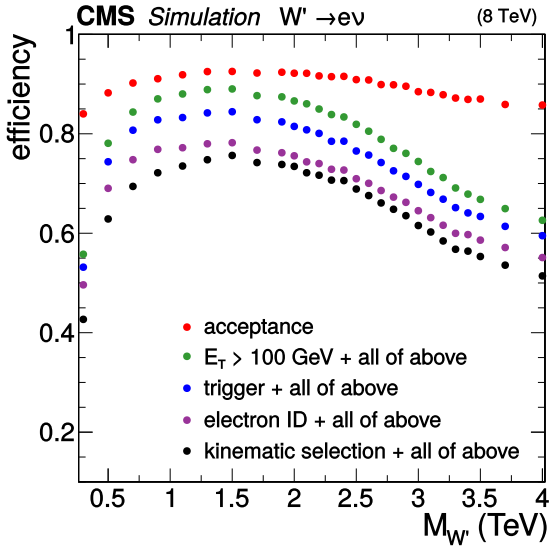

Figure 5.6.: Efficiencies for the SSM W′ boson samples as a function of $M_{W'}$ in the electron channel [92].

Figure 5.7 shows the differential cross section of the W and W′ bosons. In the intermediate mass region the SSMS differential cross section is smaller than the SSM cross section, and partly even smaller than the sole W-boson differential cross section. The total cross section is dominated by the W-boson cross section. The total effective signal cross section (W + W′ bosons cross section minus the W-boson cross section) can even be smaller than zero.

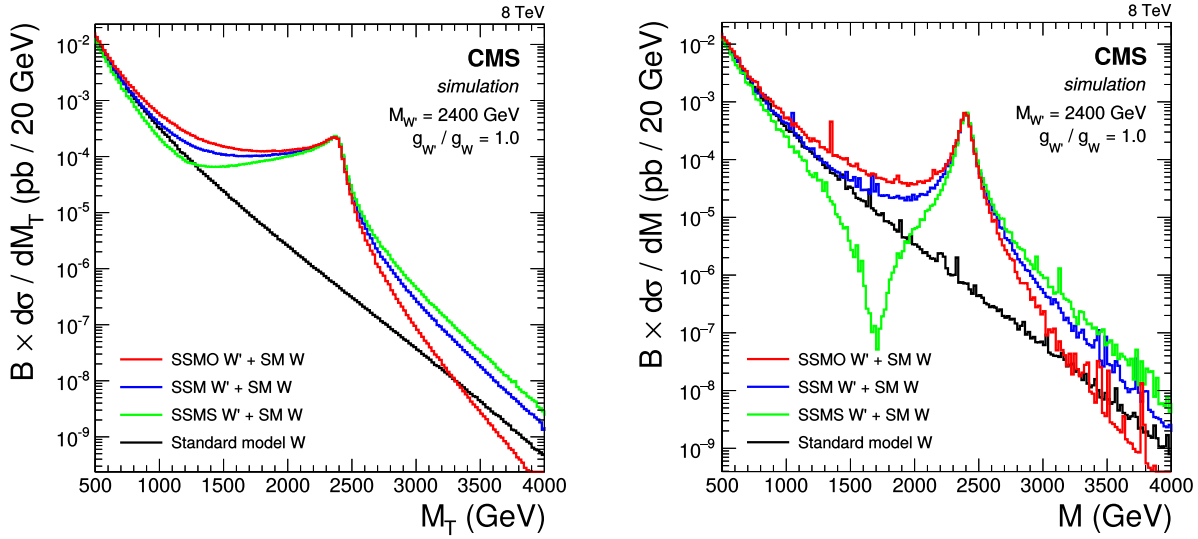

(a) Transverse mass spectrum

(b) Invariant mass spectrum

Figure 5.7.: Comparison of a SSM, SSMS, and SSMO W′ boson, each in conjunction with a standard model W boson.

Reweighting technique for variable coupling strengths

The SSMS/SSMO models are examined in terms of W′ boson mass and the coupling strength $g_{W'}$ of the W′ boson to standard model particles. The coupling strength affects the cross section, the decay width, and the impact of the interference term. There is no strong theoretical argument to assume $g_W = g_{W'}$.

Additionally, the measurement of a W′ boson cross section is of limited meaning in the SSMS/SSMO models. The effective cross section, i.e. the total W + W′ cross section minus the W boson cross section, of such a signal can be smaller than zero, due to the interference effects. The differential effective cross section is increased in some regions and decreased in others. Therefore, the coupling strength parameter provides a measure to quantify a possible deviation in terms of the SSMS/SSMO models, which is not possible with the signal cross section as the parameter of interest.

Total cross sections for the W + W′ processes are not provided, as the W-boson cross section would dominate the values by several orders of magnitude. However, cross sections binned in lepton p_T as produced with MADGRAPH can be found in table A.4 in the appendix.

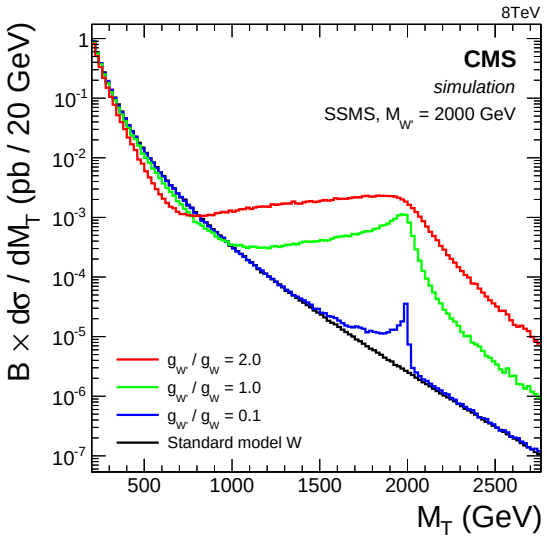

Figure 5.8.: Influence of varying the coupling strength of a SSMS W′ boson.

The two dimensional parameter space $M_{W'}$, $g_{W'}$ results in a large number of Monte Carlo samples, which need to be put through the processing chain. This is a resource and time consuming endeavor.

To avoid this, a reweighting technique is used to reduce the number of samples that have to be processed. This is possible, as the event topology and kinematic does not change when considering an event with the same transverse mass of two different W′ samples. For each mass point listed in table A.4, a sample with the coupling $g_{W'}/g_W = 1$ is produced. The complete generation, simulation, reconstruction, and analysis chain is applied to this sample.

Additionally, a number of different samples with different coupling strengths and the same mass point as the original sample are produced using MADGRAPH. These are excluded from

the rest of the processing chain. A new event weight is calculated as

$$w_x = \frac{d\sigma_x}{dM_T^{\text{gen}}} / \frac{d\sigma_1}{dM_T^{\text{gen}}} \tag{5.18}$$

with σ_1 is the cross section of the sample with the coupling $g_{W'}/g_W = 1$ and σ_x is the cross section of the sample with the coupling $g_{W'}/g_W = x$.

Using these reweighted events, a new M_T^{reco} distribution is determined together with additional M_T distributions altered due to the shift by systematic uncertainties.

This technique reduces the number of processed samples while providing a good description of the M_T distributions with a different W′ boson coupling.

5.6.3. HNC contact interaction

For the HNC contact interaction model, the shape of the M_T distribution is quite different from the W′ boson signals. Instead of a resonant structure, the distribution is smooth and monotonically decreasing, as shown in figure 5.9. The model parameter Λ_{CI} does not influence the shape but only affects the cross section and the validity range of the model. Therefore a single sample is produced using PYTHIA at LO. Example cross sections are provided in table 5.4.

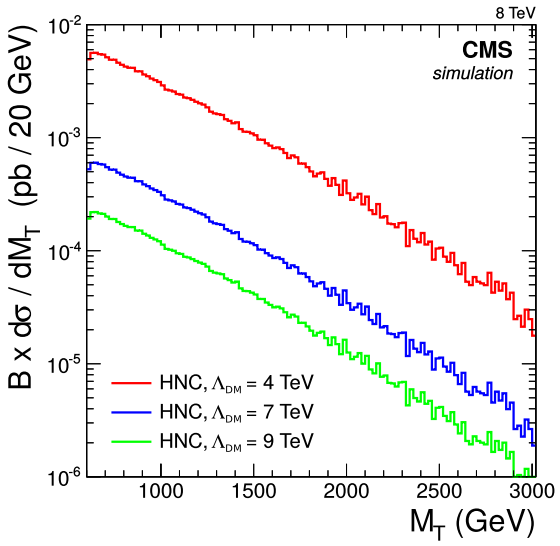

Figure 5.9.: Branching fraction times differential cross section as a function of the transverse mass for HNC contact interaction as generated with PYTHIA.

5.6.4. Dark matter

The dark matter EFT signal shows a structure similar to that of the contact interaction model. It does not show a structure such as a Jacobian peak but has a maximum at about 100 GeV and steadily declines with increasing M_T. The distributions for the three scenarios ($\xi = -1, 0, +1$)

Table 5.4.: Cross sections and PDF uncertainties in the HNC contact interaction model for selected energy scale parameters Λ_{CI}. The cross sections scale with $\sigma \propto \Lambda_{\mathrm{CI}}^{-4}$, as described in section 2.2.2

Scale Λ_{CI} (TeV)	Cross section LO $\times$ $\mathcal{B}$ (pb)	relative PDF uncertainty
4	1.72×10^{-1}	5.25×10^{-2}
6	3.39×10^{-2}	5.26×10^{-2}
8	1.08×10^{-2}	5.30×10^{-2}
10	4.37×10^{-3}	5.25×10^{-2}
12	2.09×10^{-3}	5.42×10^{-2}
14	1.14×10^{-3}	5.48×10^{-2}
16	6.71×10^{-4}	5.51×10^{-2}
18	4.19×10^{-4}	5.51×10^{-2}

are shown in figure 5.10. For low M_χ, the M_T distributions for aixal-vector and vector type couplings are indistinguishable.

The parameter Λ_{DM} and the coupling type (vector or axial vector) change the total cross section but not the shape of the M_T distribution. The cross section scales with $\sigma \propto \Lambda_{\mathrm{DM}}^{-4}$. The $\xi = -1$ and $\xi = 0$ scenarios also show the same M_T spectrum shape. However, the $\xi = 0$ cross section is smaller than the $\xi = -1$ cross section, as only one production channel is allowed compared to two production channels for $\xi = -1$. For the $\xi = +1$ case the shape of the M_T distribution is different. The destructive interference in this case leads to a lower cross section and a more steeply falling M_T distribution.

For low dark matter masses, the cross section is independent of the dark matter mass. Only at dark matter masses of about 100 GeV the cross section starts to decrease. A list of cross sections for different dark matter masses is shown in table 5.5.

The dark matter EFT signal is generated with MADGRAPH 5 with one additional jet. PYTHIA is used for the parton shower and jet matching. More information about the dark matter EFT analysis can be found in reference [4].

5.7. Uncertainties

Systematic uncertainties may affect the shape and overall normalization of the M_T distribution. For the background estimation, the thereby altered M_T distributions are fitted again to obtain a parametrization of the background. The uncertainties for both, signal and background, enter the statistical interpretations of the result, as described in section 3.1.4. Some uncertainties, such as the luminosity or E_T^{miss} related uncertainties, affect the electron and muon channel

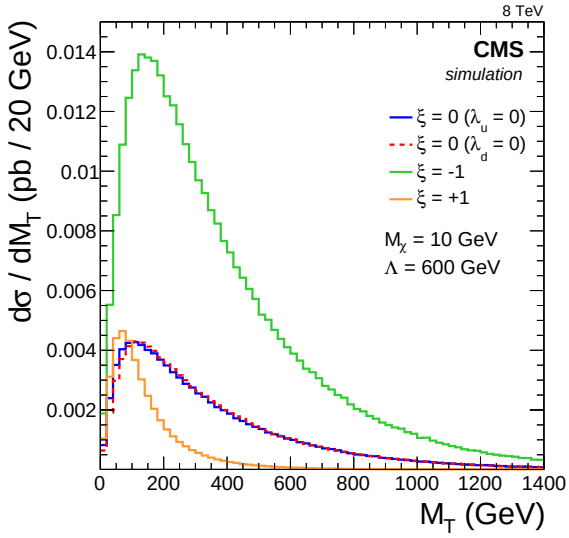

Figure 5.10.: Branching fraction times differential cross section as a function of the transverse mass for the dark matter EFT model as generated with MADGRAPH [1]. For low M_χ such as displayed here, the axial-vector and vector coupling distributions are indistinguishable.

alike. Therefore, correlations between those two channels have to be taken into account when combining them for an overall statistical analysis.

Figure 5.11 shows the influence of the uncertainties on the background prediction as a function of M_T. In the electron channel the dominant uncertainties at high M_T are due to the parton distribution functions and the W-boson higher order corrections. In the muon channel, the muon momentum scale is the most prominent uncertainty, followed by the PDF uncertainty.

Luminosity The luminosity is measured using the pixel detector and calibrated by Van-der-Meer scans, as described in section 5.1. Its uncertainty is determined to be 2.5 % (syst.) and 1 % (stat.) [77]. A total uncertainty of 2.6 % is considered, modeled with a Gaussian probability density function. This uncertainty is the same for both channels and affects the M_T distribution as a whole.

Scale factors In the electron channel, the scale factor uncertainty is M_T dependent as it is determined separately for the different η regions. In the muon channel, an uncertainty of 2.8 % is considered. Details can be found in section 5.4.2.

Electron scale The term energy scale (or momentum scale) describes a general shift of the average energy measurement in the detector from its true value. The energy resolution refers to a deviation of the measured energy to the true energy in a single measurement. Considering the distribution of deviations of the particle's measured energy to the actual energy, the resolution corresponds to the width of the distribution while the scale corresponds to its mean.

The energy scale is determined from fits to the Z boson resonance. Its uncertainty is evaluated to 0.6 % in the barrel region and 1.5 % in the endcaps [113, 114].

Table 5.5.: Cross sections times branching fraction at LO of the dark matter EFT signals with $\Lambda_{\mathrm{DM}} = 200\,\mathrm{GeV}$ for the axial-vector and vector coupling types. The cross sections scale with $\sigma \propto \Lambda_{\mathrm{DM}}^{-4}$.

M_χ (GeV)	LO cross section $\times\ \mathcal{B}$ (pb)		
Spin-independent (V) $\Lambda_{\mathrm{DM}} = 200\mathrm{GeV}$			
	$\xi = +1$	$\xi = 0$	$\xi = -1$
3	3.1	7.4	26.5
100	2.9	7.1	25.2
300	1.9	4.8	17.2
500	1.0	2.5	9.1
1000	0.1	0.3	0.9
Spin-dependent (AV) $\Lambda_{\mathrm{DM}} = 200\mathrm{GeV}$			
	$\xi = +1$	$\xi = 0$	$\xi = -1$
3	3.1	7.4	26.5
100	2.5	6.4	22.8
300	1.2	3.1	11.1
500	0.5	1.2	4.3
1000	0.03	0.1	0.2

Electron resolution The energy resolution uncertainty is also obtained from the fit to the Z boson and is determined as 1.3 % in the barrel and 2.8 % in the endcaps [114].

Muon scale The muon scale is determined from cosmic muons using the end-point method [115]. It is based on the assumption that the rate of muons asymptotically approaches zero for high energies. If the energy scale is shifted, the vanishing rate will correspond to muons with a nonvanishing curvature, i.e. a finite energy. The correction can be described as an offset of the inverse momentum $q/p_T \rightarrow q/p_T + \kappa$. The offset κ changes the momentum of negatively and positively charged muons in opposite directions. It has been determined to $\kappa = 0.05\,\mathrm{TeV}^{-1} \pm 0.05\,\mathrm{TeV}^{-1}$. The uncertainty is used to shift the transverse momentum of the muons to determine its impact on the M_T distribution.

Muon resolution The muon resolution can be determined from cosmic muons by comparing the reconstructed momentum in the upper and lower halves of the detector [66]. For high p_T muons it has been determined to $r = 8.3\,\%$ with an absolute uncertainty of $\sigma_r = 0.6\,\%$ (percent points). Because of the underground position of the CMS detector, only central cosmic muons can be used to determine this uncertainty. It is assumed that the forward muons have the same resolution uncertainty. The standard deviations of two Gaussian distributions can be added in quadrature to determine the standard deviation of the con-

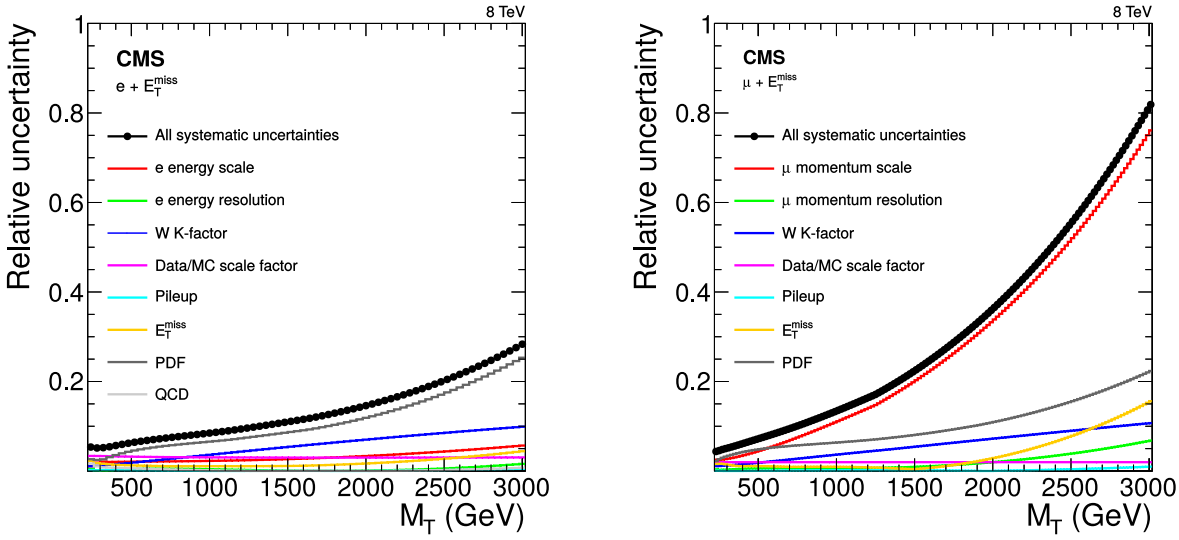

(a) Electron channel

(b) Muon channel

Figure 5.11.: Effect of systematic uncertainties on the number of background events as as a function of M_T in the electron and muon channels [1].

volution of the two distributions, which is again a Gaussian distribution. Therefore, to model the uncertainty the muon momentum is smeared using an additional Gaussian distribution with the standard deviation s with

$$(r + \sigma_r)^2 = r^2 + s^2 \quad . \tag{5.19}$$

This yields an additional smearing of $s = 3.2\,\%$.

Missing transverse energy The particle flow algorithm uses all identified particles to determine the missing transverse energy. To determine the uncertainty, the scale and resolution uncertainties of photons, electrons, muon, taus and jets are evaluated separately. Additionally an uncertainty of 10 % on the unclustered energy is considered.

In the electron channel, the electron scale and resolution uncertainty are taken into account for both, the electron and the missing transverse energy. The influence of this uncertainty is considered to be completely correlated for the two objects. The same applies for the muon channel.

Pileup The determination of the pileup distribution relies on the inelastic proton-proton cross section. Extrapolated from the 7 TeV cross section, a value of 69.4 mb is used at 8 TeV to determine the pileup distribution. A data driven method has yielded a cross section of 73.5 mb. The difference is considered as uncertainty. It is propagated to the M_T distribution by reweighting the events using the corresponding pileup distributions [116].

W-boson higher order corrections This uncertainty is estimated from the difference of the two combination methods explained in section 5.5.2. The K-factor is M_T dependent and therefore also its uncertainty.

Parton distribution functions Parton distribution functions are used in the simulation of hadron collisions to describe the probability for the type and momentum fraction of a single

parton. They are determined from deep inelastic scattering experiments. Several groups provide fits to these data describing the pdf. Experimental uncertainties are propagated to the pdf and yield a set of shifted pdfs X_i^+ and X_i^- together with the best estimate X_0.

A recipe suggested by the PDF4LHC group is used to handle the uncertainties on the pdf [117, 118]. The combined upper uncertainty σ^+ and lower uncertainty σ^- of one pdf set is determined by the individual contributions by the modified tolerance method as [119]

$$\sigma^+_{\text{PDF}} = \sqrt{\sum_i \left(\max(X_i^+ - X_0, X_i^- - X_0, 0)\right)^2}, \tag{5.20}$$

$$\sigma^-_{\text{PDF}} = \sqrt{\sum_i \left(\max(X_0 - X_i^+, X_0 - X_i^-, 0)\right)^2}. \tag{5.21}$$

(5.22)

The impact of the uncertainty on the strong coupling constant on the event weight $\sigma^\pm_{\text{PDF}}$ is also evaluated and added in quadrature to $\sigma^\pm_{\text{PDF}}$.

$$\sigma^\pm = \sqrt{(\sigma^\pm_{\text{PDF}})^2 + (\sigma^\pm_{\text{PDF}})^2} \tag{5.23}$$

To determine the impact on he M_T distribution, the events are reweighted using the shifted pdf values $f^\pm$ and the original pdf value f^0:

$$w^\pm = \frac{f^\pm(x_1, Q^2) f^\pm(x_2, Q^2)}{f^0(x_1, Q^2) f^0(x_2, Q^2)}, \tag{5.24}$$

where Q^2 is the momentum transfer of the interaction and x_1, x_2 are the momentum fractions of the two interacting partons.

This method yields $\pm 1\,\sigma$ histograms for each pdf set. In this analysis the CT10 [107], MSTW2008 [120], and the NNPDF [121] sets are considered. The envelope of all $\pm 1\,\sigma$ distributions is used as the pdf uncertainty to the M_T distribution.

6. Results derived from 8 TeV data

Based on the analysis described in chapter 5, the transverse mass distributions of the electron and muon channels are derived. From the CMS measurements, the standard model predictions, and the signal assumptions, interpretations are made. The significances of possible deviations are determined. If no new phenomena are discovered, exclusion limits on the new physics model parameters are derived.

6.1. Transverse mass distribution

After applying all selection criteria, the transverse mass distributions as shown in figure 6.1 are obtained. Both distributions are binned by their estimated resolution and the bin contents are normalized by their respective bin widths. The different background contributions are stacked, adding up to the total standard model expectation. The uncertainty on the total number of expected background events is displayed as a shaded bar.

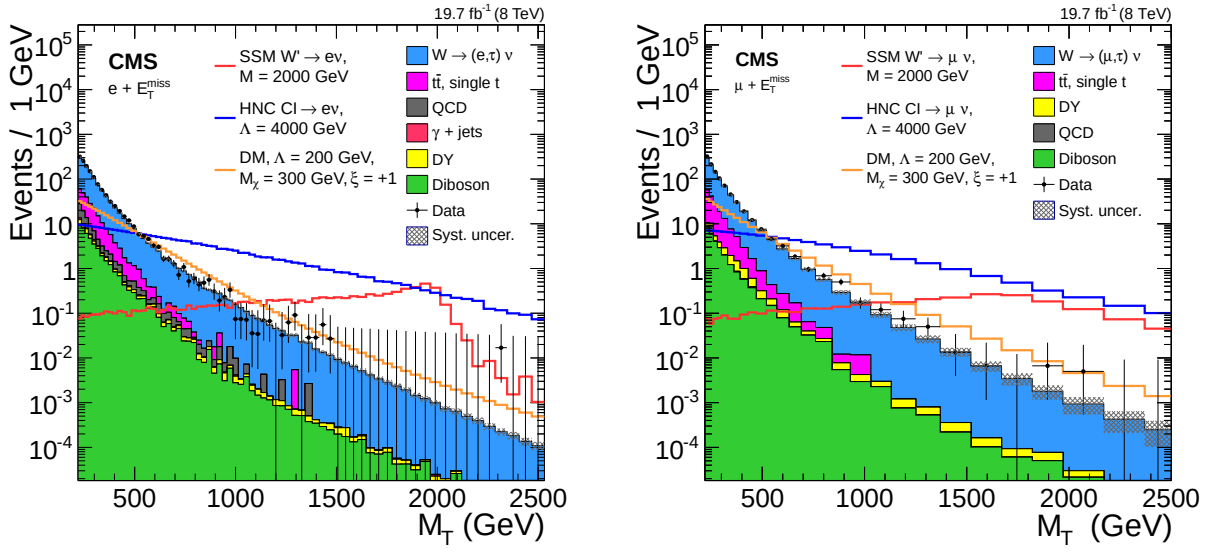

(a) Electron channel

(b) Muon channel

Figure 6.1.: Invariant mass distributions of the electron and muon channel [1]. The filled areas show the stacked background distributions while the signals are drawn as solid lines. The binning in both distributions is chosen to represent the M_T resolution. The uncertainty bars of the data markers correspond to the 68 % confidence intervals.

A SSM W′ boson, a contact interaction, and a dark matter EFT model signal are shown as examples for possible signatures of new physics. The data markers include uncertainty bars marking a frequentist 68 % confidence interval as derived in reference [122], instead of the often provided standard deviation of the Poisson distribution. A short description of confidence intervals is given in section 3.1.

In the electron channel (figure 6.1a), the data agree well with the standard model simulation. The maximum transverse mass of all observed events is 2.3 TeV. In the muon channel (figure 6.1b), there is a slight excess of data events compared to the standard model expectation starting from about 600 GeV. The maximum observed transverse mass is 2.1 TeV.

6.2. Significance of deviations

In order to claim a discovery of an unusual phenomenon, a deviation more significant than $5\,\sigma$ must be observed. The method used to determine the significances is described in section 3.2. Figure 6.2 shows the significances of the upward deviations as a function of the M_T bin. In the electron channel, the most significant deviation of about $2.6\,\sigma$ can be found at around 2300 GeV. It is caused by a single event observed in a bin with a standard model expectation of about 0.012 events. For $M_T > 2.3$ TeV the background expectation is 0.06 events. Being the highest M_T event, this event would certainly be an interesting candidate for new physics.

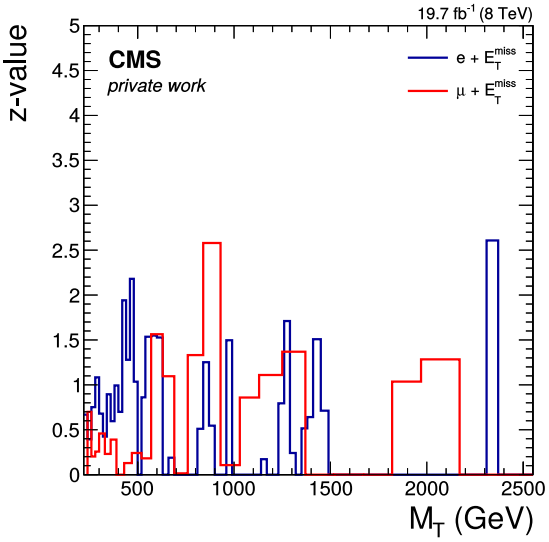

Figure 6.2.: Observed significances per bin for the electron and muon channels in Gaussian sigmas (z-value). Significances with a p-value of $p \geq 0.5$ correspond to $z = 0$.

In the muon channel, the most significant deviation in a single bin is located at around $M_T = 900$ GeV. It corresponds to an event excess with a significance of $2.6\,\sigma$.

Considering the deviations in some bins and also the overall agreement between the data and the simulation, the M_T distributions do not reveal significant deviations from the standard model and therefore, no evidence for new physics has been found.

The significance can also be determined in terms of a signal hypothesis. The significances for SSM W′ boson signals is shown in figure 6.3. The most significant deviations in the electron channel correspond to W′ masses of 500 GeV and 2.4 TeV, both corresponding to a significance of less than 2σ. In the muon channel, the excess at $M_T = 900\,\text{GeV}$ results in a significance of $2.6\,\sigma$ for a W′ boson with a mass of 900 GeV. Combining both channels, the most significant deviations at $M_{W'} = 900\,\text{GeV}$ and $M_{W'} = 2.4\,\text{TeV}$ both correspond to significances of less than 2σ.

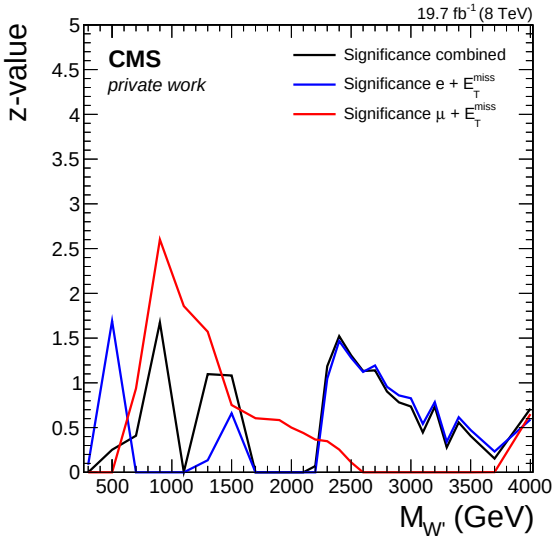

Figure 6.3.: Observed significances as a function of the SSM W′ boson mass for the electron channel, muon channel, and their combination.

In the muon channel a small excess at $M_T = 2\,\text{TeV}$ is visible. Analyses at ATLAS and CMS searching for $W' \to WZ$ decays observe slight excesses at around $M_{W'} = 2\,\text{TeV}$ [123] and $M_{W'} = 1.9\,\text{TeV}$ [124]. However, this cannot be observed in the electron channel and the W′ boson mass significances do not indicate the existence of a heavy charged gauge boson at this point.

In the considered model, the W′ boson decay to WZ is suppressed. Models considering such decays usually claim higher branching fractions for the diboson decay compared to the fermionic decay channels. For such models, the diboson channels are more sensitive and a signal would only appear later (i.e more luminosity and/or center-of-mass energy required) in the $\ell + E_T^{\text{miss}}$ channel [13]. So even though an event excess such as in the $W' \to WZ$ analysis is not visible in the $\ell + E_T^{\text{miss}}$ analysis, the event excess could still be related to a W′ boson.

6.3. Exclusion limits

As no significant deviations can be observed, certain new physics scenarios can be excluded. A generic signal cross section limit is derived, which is independent of the model. From this, the readers can extract their own limits on signal parameters of any arbitrary model which is sensitive to the electron and/or muon M_T distributions.

Additionally, model dependent limits on the signal cross section and important signal parameters are derived. In general, these limits are more sensitive than limits derived from the model independent limits, as the shape of the signal in the M_T distribution is taken into account.

An overview about the statistical methods used to calculate the limits is given in section 3.1.

6.3.1. Model-independent cross section limits

A limit on the cross section times branching fraction of a BSM signal can be used to make statements about the exclusion of a later specified model. As the selection criteria are rather lose, such a cross section limit can be considered model-independent to a certain degree. The background estimation for the total M_T range is very large, therefore figure 6.4 shows the model independent cross section limits for the electron and muon channel as a function of a lower transverse mass threshold M_T^{min}. From these, specific models that have events decaying to $\ell + E_T^{\text{miss}}$ may be excluded. The limits calculated using the Bayesian method with a uniform prior at 95 % CL.

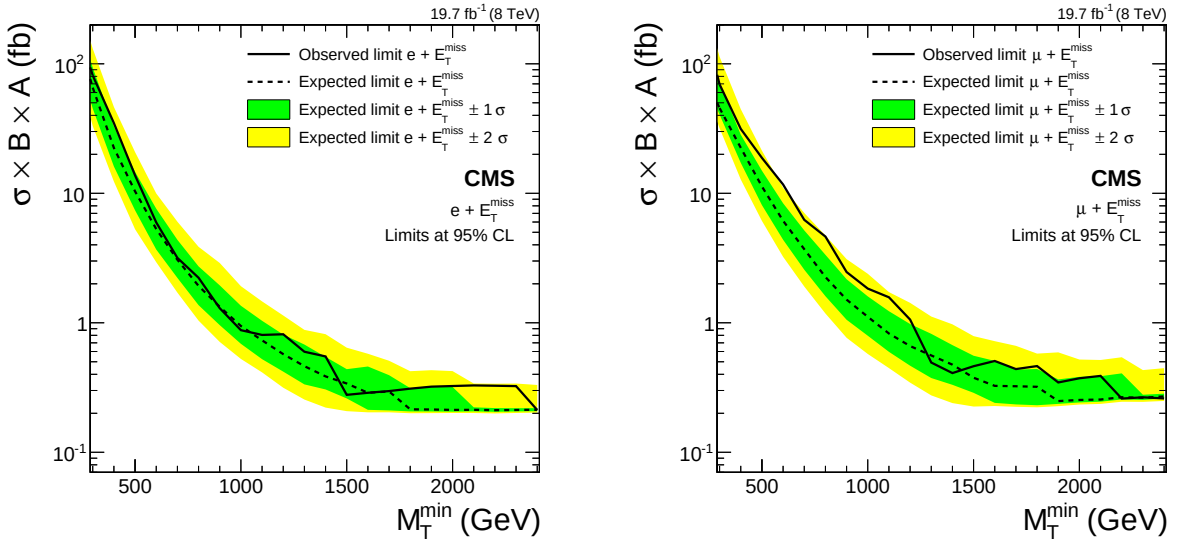

(a) Electron channel

(b) Muon channel

Figure 6.4.: Model-independent upper limits on the effective cross section at 95 % CL as a function of a lower transverse mass threshold M_T^{min} for the individual electron and muon channels. The excluded cross sections correspond to discrete event numbers as seen in data or determined by pseudo experiments. This results in a step-like structure and vanishing 1, and 2σ bands at high M_T^{min}. Each step corresponds to another event not included by the M_T^{min} criterion.

To determine a cross section limit, one needs to know the number of expected background events, the integrated luminosity, and the signal efficiency. The number of background events and the luminosity are independent of the signal and can therefore be included in the model-independent calculation. The signal efficiency can be subdivided into different parts, which may or may not depend on the signal model:

- detection efficiency
- detector acceptance
- kinematic selection efficiency
- M_T^{min} threshold efficiency

The detection efficiencies for electrons as well as for muons have been shown to be stable up to several hundred GeV. For momenta beyond this, there is not enough data to determine the efficiencies in data. However, there is no indication that they decline for higher energies. Therefore the detection efficiencies are assumed to be robust and can be considered to be model independent. The detector acceptance can be model dependent, if the signal has a η distribution, which is not compatible with the W boson η distribution. On the other hand, it is unlikely that a new physics signal produces many events with leptons reaching $\eta > 2.1$, which is the coverage of the muon system. This would require a lot of energy, whereas a large fraction of the energy is already needed for the high transverse momentum of the lepton. The sensitivity of the analysis to signals with small lepton momenta is constrained anyhow, as the background expectation in that regime is large. Considering this, we regard the acceptance to be model independent. The acceptance is constant for high M_T ($M_T > 200\,\text{GeV}$) W boson events. From these events the model independent acceptance values are determined. If one considers a model for which the acceptance is substantially different, the model-independent cross section limit is not applicable.

The detection efficiency and detector acceptance result in a combined efficiency of 83 % in the electron channel and 86 % in the muon channel. As this is the model independent part of the efficiency, it is already included in the limit calculation so that only the following model dependent parts must be considered by the reader when applying the model independent limits to a specific model.

As described in section 5.3.4, two kinematic selection criteria are applied: $0.4 < p_T/E_T^{\text{miss}} < 1.5$ and $\Delta\varphi > 2.5$. The corresponding selection efficiencies depend on the event topology. For example, an additional hard jet would change these kinematic selection efficiencies. Therefore, they are not considered for the model-independent signal efficiency. The same applies to the M_T^{min} threshold. As the shape in M_T depends on the model, the M_T^{min} threshold efficiency is also not considered.

Let A be the product of the model-specific kinematic selection efficiencies and the M_T threshold efficiency, σ be the model cross section, and $\mathcal{B}$ the branching fraction to the considered channel. To determine whether a model can be excluded, one has to calculate the effective cross section:

$$\sigma_{\text{eff}} = A \times \sigma \times \mathcal{B}. \tag{6.1}$$

If σ_{eff} is larger than the value given in figure 6.4, the model can be excluded.

To prevent a selection bias, M_T^{min} should not be chosen based on the observed M_T distribution. Instead, a statistically sound method is to choose M_T^{min} such that it provides the best expected cross section limit, and determine the observed exclusion with the same M_T^{min} threshold.

The SSM W′ model can be used as an example for this method. At $M_{W'} = 3\,\text{TeV}$, the NNLO cross section times branching fraction is $\sigma \times \mathcal{B} = 1.52\,\text{fb}^{-1}$. The best sensitivity is expected for $M_T^{\text{min}} = 1500\,\text{GeV}$. Together with the kinematic selection criteria, this thresholds results in a signal efficiency of $A = 26\,\%$ (coincidentally, the same number for both channels). The effective cross section is therefore $A \times \sigma \times \mathcal{B} = 0.40\,\text{fb}^{-1}$. This number can be compared to the excluded effective cross sections at $M_T^{\text{min}} = 1500\,\text{GeV}$ for the electron channel ($0.28\,\text{fb}^{-1}$) and the muon channel ($0.46\,\text{fb}^{-1}$). As $0.40\,\text{fb}^{-1} > 0.28\,\text{fb}^{-1}$, the SSM W′ boson mass of 3 TeV can be excluded in the electron channel. This is not the case for the muon channel. By comparing this number to the results of section 6.3.2, it can be seen that this method of deriving the limits from the model independent limits is only slightly less sensitive than the multi-bin method used in section 6.3.2. However, this is not necessarily the case for other signal models. As the W′ model has the best sensitivity in the high M_T regime, this method is applicable and provides very strong limits.

Shown in figure 6.4 are the observed limit, the median expected limit and the $\pm1\sigma$ and $\pm2\sigma$ bands. The expected limit as well as its bands show a smooth decline with M_T^{min}, ending in a step like structure and vanishing bands for $M_T^{\text{min}} > 1400\,\text{GeV}$. The excluded cross sections correspond to the discrete numbers of signal events, which are required to reach the 95% CL. For small event numbers, the relative differences between these cross sections is large, so they are visible as steps. Also, for small numbers of signal events, the 1σ and 2σ bands may coincide with the median expected limit, resulting in vanishing bands.

In the muon channel (figure 6.4b), the observed limit lies outside the 1σ band of the expected limit in the M_T range from 400 GeV to 1200 GeV. This corresponds to an overall excess of observed events compared to the standard model expectation in this very range.

Combining both channels, the model-independent cross section limit can be improved. This combination assumes that both channels share a common branching fraction $\mathcal{B} = \mathcal{B}(e) = \mathcal{B}(\mu)$. The resulting cross section limit is shown in figure 6.5. Also shown are the individual observed limits. Comparing them shows that over most of the range, the electron channel provides better (smaller) exclusion limits compared to the muon channel. This is due to the overall event excess in the muon channel and the better resolution in the electron channel. The declined resolution in the muon channel smears out a signal such that it would be less visible. For instance, a prominent excess in a single bin transforms into a small excess in several bin, reducing the significance of the deviation. The resolution also influences the expected limit, so that the electron channel also provides a better expected limit.

6.3.2. SSM W′ limits

Upper limits on the cross section σ times branching fraction $\mathcal{B}$ as a function of the boson mass can be derived for the SSM W′ boson decaying to an electron or muon and a neutrino. They are determined at 95 % CL using the Bayesian method with a uniform prior for the cross section times branching fraction, as described in section 3.1.3. The limits for the individual channels are shown in figure 6.6, their combination is displayed in figure 6.7.

Cross sections larger than the indicated limit are excluded. Also shown is the calculated W′ boson cross section times branching fraction in the SSM for a W′ boson coupling corresponding to the W boson coupling. Therefore masses smaller than indicated by the intersection point of

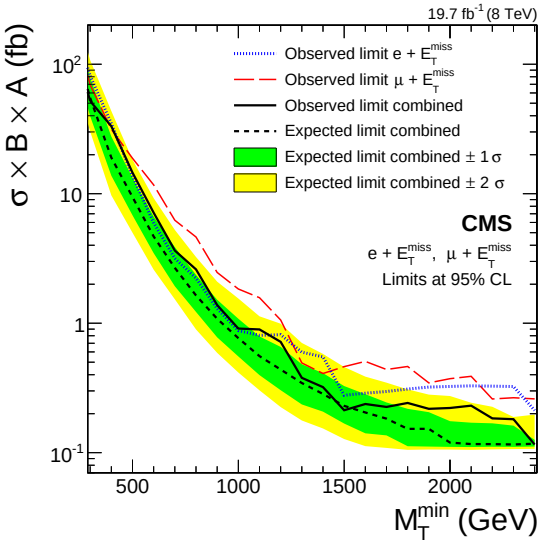

Figure 6.5.: Model-independent upper limits on the effective cross section at 95% CL as a function of a lower transverse mass threshold $M_T^{\min}$ for the combination of the electron and muon channels. The branching fraction $\mathcal{B}$ is assumed to be the same for both channels.

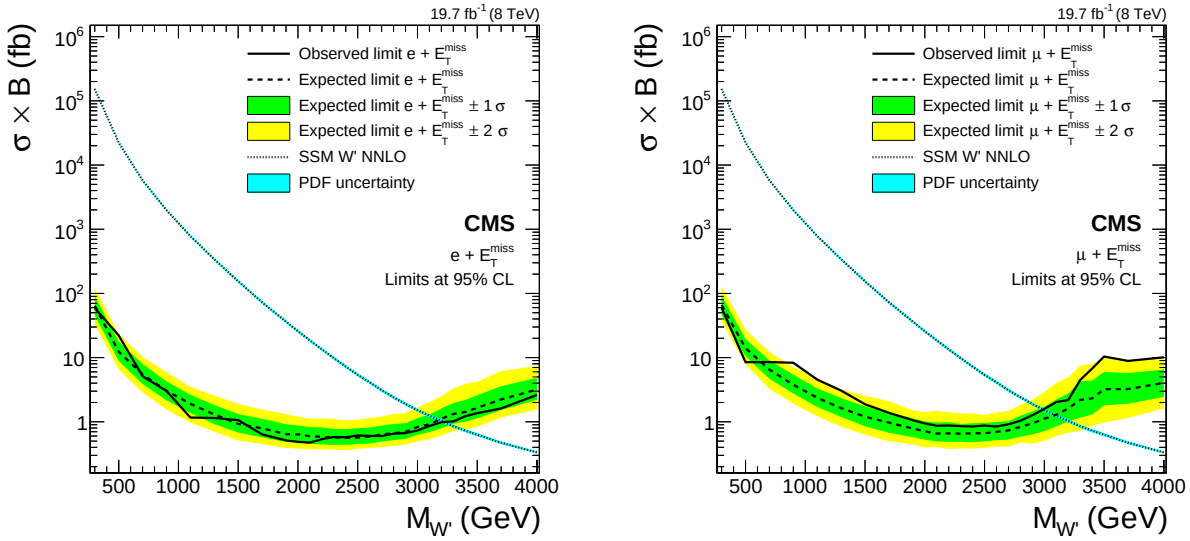

(a) Electron channel

(b) Muon channel

Figure 6.6.: Upper cross section limits at 95% CL of a SSM W′ boson as a function of the boson mass for the individual electron and muon channels.

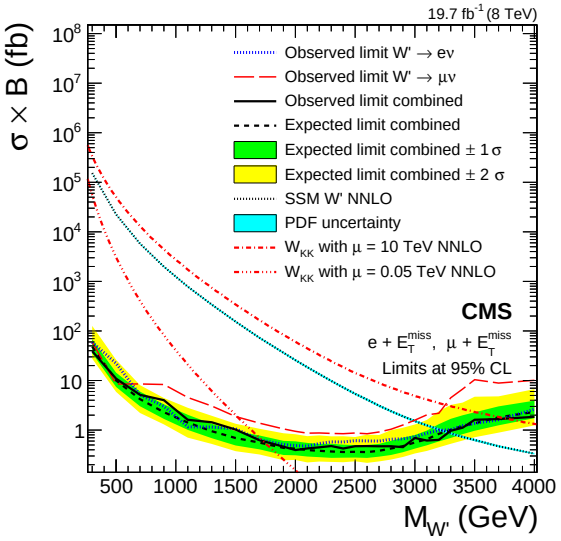

Figure 6.7.: Upper cross section limits at 95% CL of a SSM W′ boson as a function of the boson mass for the combination of the electron and muon channels.

the limit curve and the theoretical cross section curve can be excluded. For the electron channel, this method yields an observed lower mass limit of 3.22 TeV and an expected limit of 3.18 TeV. In the muon channel, the observed limit is 2.99 TeV, compared to an expected limit of 3.09 TeV. The combination of both channels yields an observed limit of 3.28 TeV and an expected limit of 3.26 TeV. Together with the LO limits, these values can also be found in table 6.1.

Table 6.1.: Mass limits at 95 % CL for a W′ boson with in the SSM model for the electron channel, muon channel, and their combination, determined with the NNLO and with the LO signal cross section.

Signal cross section	Channel	Observed lower limit (TeV)	Expected lower limit (TeV)
NNLO	electron	3.22	3.18
	muon	2.99	3.09
	combined	3.28	3.26
LO	electron	3.16	3.14
	muon	2.96	3.05
	combined	3.25	3.21

All cross section limit curves for the SSM W′ boson have a banana shape with the minimum located at between 2 TeV and 2.5 TeV. Up to this point, the W′ boson resonance is shifted towards larger M_T. The majority of the events are therefore produced at larger M_T, where the number of background events decreases. This yields improved cross section limits. At even higher W′ boson masses, the resonance structure in the M_T distribution starts to dissolve. The reason for this is the decrease of available phase space, which can be explained by the parton

distribution functions. This effect can also be seen in figure 5.5: for very high W′ masses, the majority of events have small transverse masses.

In the electron channel, the expected and observed cross section limits are very similar. For the muon channel, the observed limit is slightly worse (larger) than the expected limit over a large range of $M_{W'}$. The reason for this is the slight excess of events in the muon channel, as already described in section 6.3.1. Very prominent is the difference at $M_{W'} = 900\,\text{GeV}$, corresponding to the excess of events at $M_T = 900\,\text{GeV}$.

The signal PDF uncertainties are indicated by a narrow teal band around the signal cross section in figures 6.6 and 6.7. They amount to $\sim 5\%$.

The search for a heavy charged gauge boson has a long history in the examination of the lepton and missing transverse energy channel. This allows for a comparison of the sensitivity and can show why the events corresponding to $5.0\,\text{fb}^{-1}$ from the $\sqrt{s} = 7\,\text{TeV}$ run were not included in this analysis. Since the beginning of the $\sqrt{s} = 8\,\text{TeV}$ run, the impact of these data on the sensitivity decreased rapidly and with a total integrated luminosity of $20\,\text{fb}^{-1}$ for the $\sqrt{s} = 8\,\text{TeV}$ data, its influence is negligible. Figure 6.8a shows the SSM W′ limit after accumulating an integrated luminosity of $3.7\,\text{fb}^{-1}$ at $\sqrt{s} = 8\,\text{TeV}$. The combination of this result together with the data of the $\sqrt{s} = 7\,\text{TeV}$ run is shown in figure 6.8b. Displayed is the limit in terms of the ratio of the excluded cross section and the theoretical cross section. As the cross sections for $\sqrt{s} = 7\,\text{TeV}$ and $\sqrt{s} = 8\,\text{TeV}$ are different, a pure cross section limit would not be meaningful.

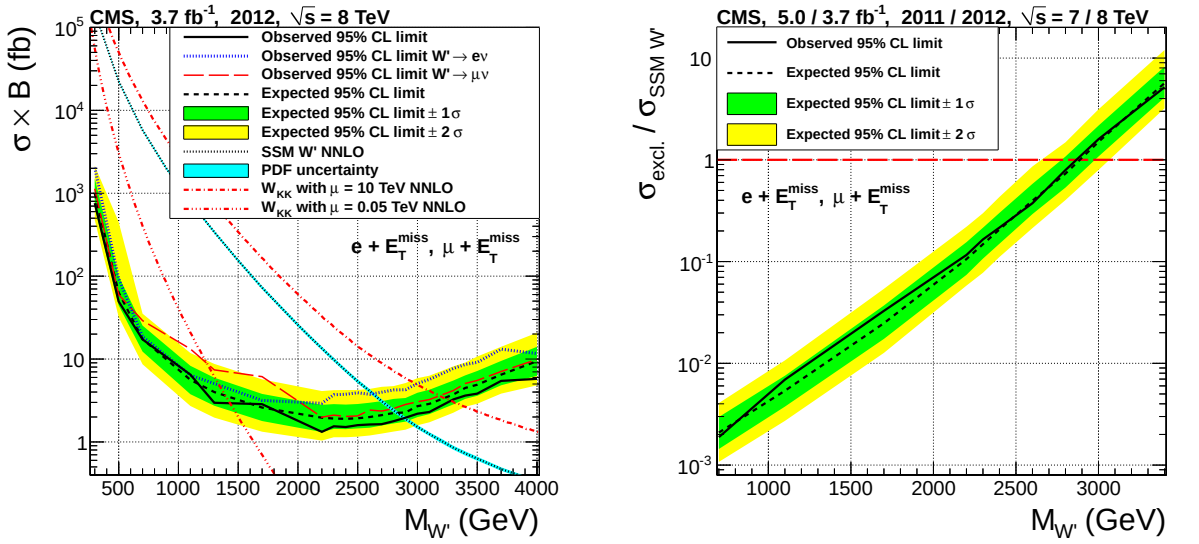

(a) $\sqrt{s} = 8\,\text{TeV}$ ($3.7\,\text{fb}^{-1}$) data

(b) Combination of $\sqrt{s} = 7\,\text{TeV}$ and $\sqrt{s} = 8\,\text{TeV}$ ($3.7\,\text{fb}^{-1}$) data

Figure 6.8.: Upper limits at 95% CL of a SSM W′ boson as a function of the boson mass for the combination of electron and muon channel. The left plot shows the cross section limit derived from $\sqrt{s} = 8\,\text{TeV}$ data with $3.7\,\text{fb}^{-1}$ and the right plot shows the limit on the fraction of the excluded cross section and the theoretical cross section for the combination of $\sqrt{s} = 8\,\text{TeV}$ ($3.7\,\text{fb}^{-1}$) and $\sqrt{s} = 7\,\text{TeV}$ data [2].

The combination with the $\sqrt{s} = 7\,\text{TeV}$ data adds only little to the limit. The expected limit changes from 2.80 TeV to 2.90 TeV and the observed limit from 2.85 TeV to 2.90 TeV. Considering this, a combination of the $\sqrt{s} = 7\,\text{TeV}$ dataset with the $\sqrt{s} = 8\,\text{TeV}$ dataset would not significantly improve the sensitivity of the analysis.

Details about the $\sqrt{s} = 7\,\text{TeV}$ analysis and the combination can be found in [2].

6.3.3. SSMS and SSMO W′ limits with generalized couplings

Although the SSM is an important reference model, it has been disputed whether it is well motivated [16], as it does not consider interference effects of the W and the W′ boson. In case the W′ boson couples to left handed particles (right handed anti-particles), these effects must be taken into account. As described in section 2.2.1, two models are considered. The SSMS with the same-sign coupling to leptons and quarks, and the SSMO where the coupling to leptons and quarks have opposite sign.

The limits for the SSMS and SSMO models are calculated in terms of the W′ boson mass and the coupling strength $g_{W'}$. A limit on the cross section times branching fraction would not be meaningful in this context, because the effect of these models on the differential cross section is negative for some part of the M_T range. This can be seen in figure 5.7. For the SSMS model, the W+W′ cross section is smaller than the W boson cross section for $M_W < M_T < M_{W'}$ and larger otherwise. For the SSMO model this applies vice versa.

Using the reweighted M_T distributions as described in section 5.6.2 , CL_s limits for each mass and coupling strength tuple are determined. For each mass point, the coupling strength is determined which corresponds to 95% CL. For this, a linear interpolation between the two coupling strength points surrounding the 95% CL point is used.

The upper limits on the coupling strength as a function of the W′ boson mass are shown in figures 6.9 (electron channel), 6.10 (muon channel), and 6.11 (combination). Assuming a coupling strength of $g_{W'}/g_W = 1$, the observed mass limit in the SSMS model for the combination of the electron and muon channels is 4.00 TeV with an expected mass limit of 3.83 TeV. For the SSMO model, an observed limit of 3.71 TeV and an expected limit of 3.83 TeV is determined. An overview of all limits including the limits of the individual channels can be found in table 6.2.

In case the W′ boson coupling strength is smaller than that of the standard model W boson, the mass limit decreases. The cross section, decay width, and interference terms are all affected by the coupling strength. For $g_{W'}/g_W = 0.1$ the combined observed limit in the SSMS is 1.96 TeV with an expected limit of 1.80 TeV. In the SSMO channel the observed and expected limits correspond to 1.82 TeV and 1.80 TeV, respectively.

As already discussed before, the muon channels shows a slight excess of events compared to the standard model expectation. For the SSMS model, this results in a slightly better (smaller) observed upper limit on the coupling strength for $M_{W'} > 1.4\,\text{TeV}$ compared to the expected limit. This is shown in figure 6.10a. In the SSMS model, a smaller number of events is expected compared to the standard model (destructive interference). Therefore, an excess of events does not result in a worse (larger) but better (smaller) coupling strength limit.

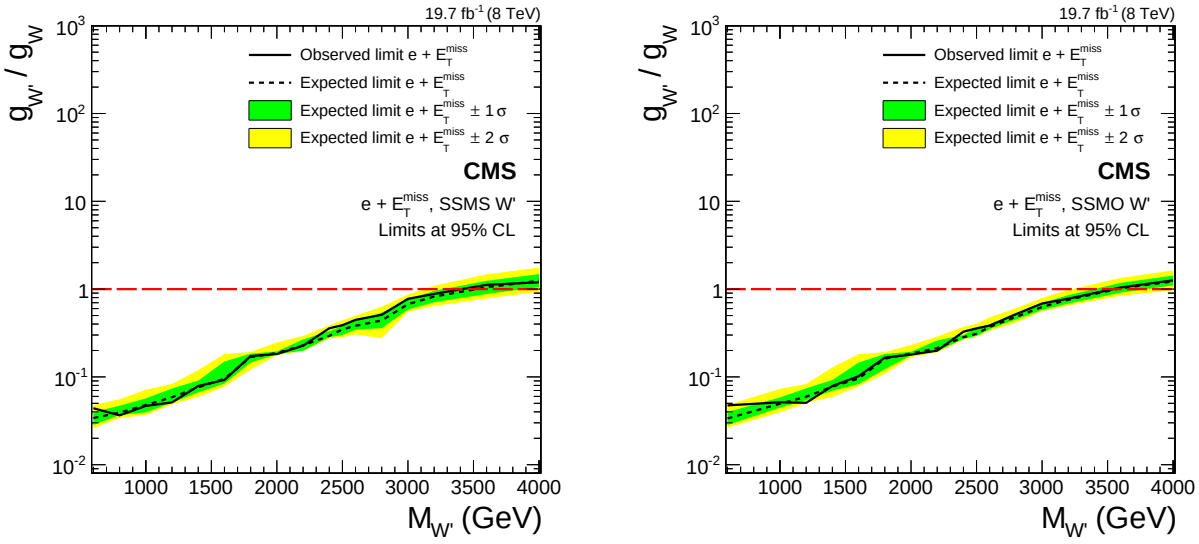

(a) SSMS, electron channel

(b) SSMO, electron channel

Figure 6.9.: Upper limits on the W′ boson coupling at 95% CL of a SSMS/SSMO W′ boson as a function of the boson mass for the electron channel.

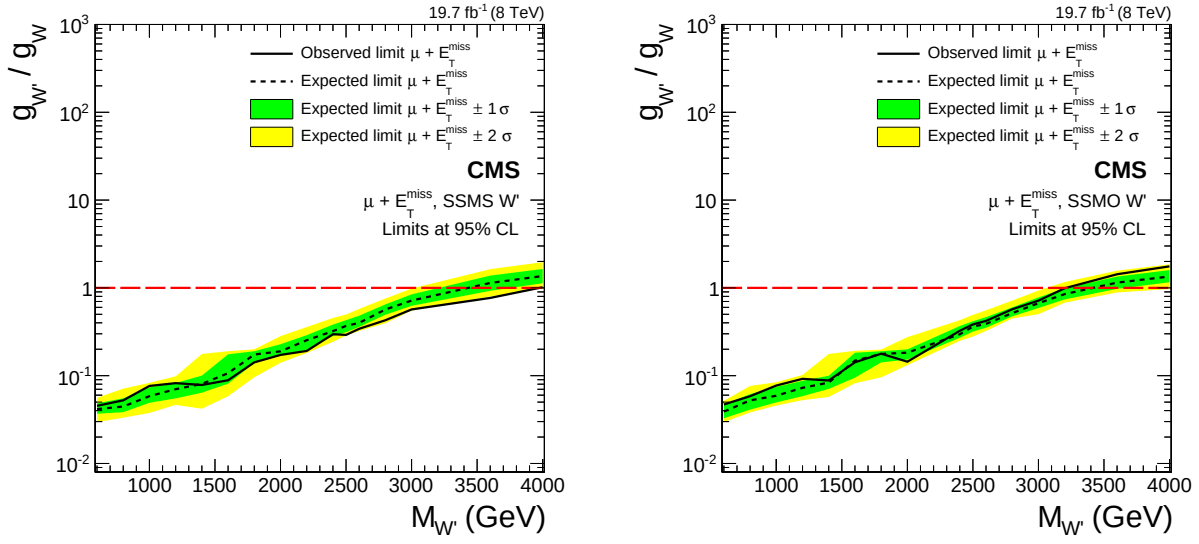

(a) SSMS, muon channel

(b) SSMO, muon channel

Figure 6.10.: Upper limits on the W′ boson coupling at 95% CL of a SSMS/SSMO W′ boson as a function of the boson mass for the muon channel.

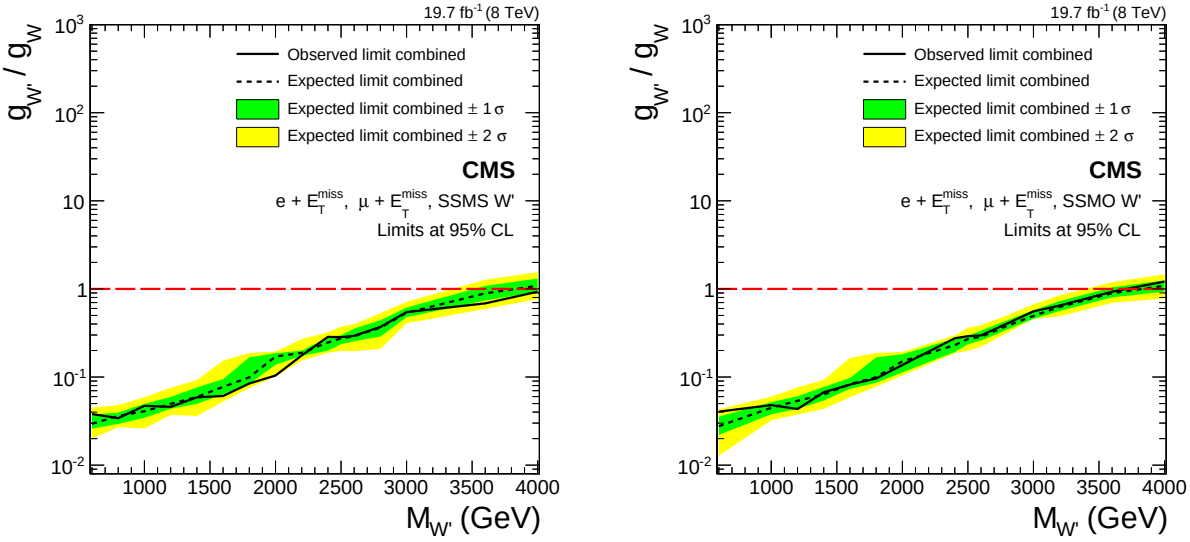

(a) SSMS, combined

(b) SSMO, combined

Figure 6.11.: Upper limits on the W′ boson coupling at 95% CL of a SSMS/SSMO W′ boson as a function of the boson mass for the combination of electron and muon channel.

Table 6.2.: Mass limits for a W′ boson with a coupling of $g_{W'}/g_W = 1$ in the SSMS and SSMO limits for the electron channel, muon channel, and their combination.

Model	Channel	Observed lower limit (TeV)	Expected lower limit (TeV)
SSMS	electron	3.41	3.52
	muon	3.97	3.43
	combined	4.00	3.83
SSMO	electron	3.54	3.57
	muon	3.22	3.38
	combined	3.71	3.83

The SSMS model has also been examined in the $W' \rightarrow tb$ channel in terms of a variable coupling strength [125]. Although the W′ boson branching fraction to tb is larger than to leptons, the discovery reach is substantially smaller due to lower signal efficiencies. For the SSMS model with $g_{W'}/g_W = 1$ a mass limit of 2 TeV has been determined [125].

6.3.4. sUED limits

The limits on the W′ boson in the SSM and the SSMS models may be reinterpreted in terms of the sUED model. For the case of not considering interference to the W boson (SSM), two example cross section distributions for $\mu = 10$ TeV and $\mu = 0.05$ TeV are included in figure 6.7. The radius of the extra dimension R relates to the W′ boson mass and for large masses $M_{W'} \approx 2/R$ applies. The product of R with the bulk mass μ defines the coupling strength and therefore the cross section of the new physics process, see section 2.2.1 for details.

Limits corresponding to the SSM case with 95 % CL in the R–μ plane are shown in figure 6.12. The steep increase of the μ exclusion limit at $1/R \approx 2$ TeV is due to the coupling g_n^{KK} converging to $\sqrt{2} \times g_W$ for large μ. As the cross section is proportional to g^4 (see equation 2.13) it cannot be enhanced above $\sigma_{\text{sUED}} = 4 \times \sigma_{\text{SSM}}$, making an exclusion impossible.

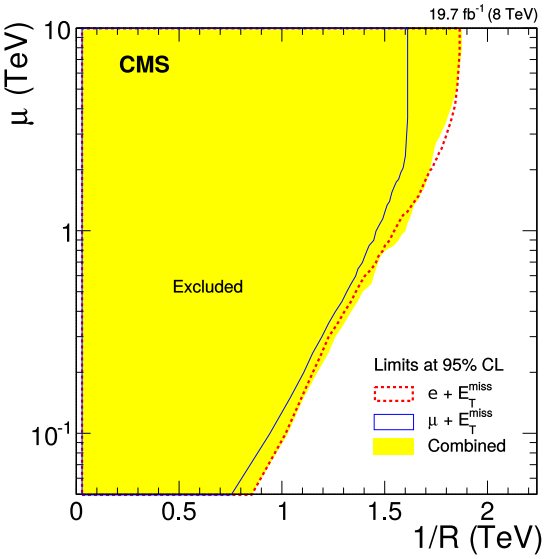

Figure 6.12.: Exclusion limits on the sUED extra dimension radius R and the bulk mass μ derived from the SSM W′ boson limits [1].

Reinterpreting the SSMS limits in term of the sUED model includes the interference effects with the W boson. As the SSMS results provide exclusion limits in terms of the coupling strength, this reinterpretation not only considers the modified cross section but includes an overall description of the modified coupling resulting in a modified decay width and impact of the interference.

Figure 6.13 show the limit in the individual electron and muon channel. The combination of both channels can be found in figure 6.14. The individual channels show an extreme increase of the upper $1\,\sigma$ and $2\,\sigma$ bands at large $1/R$. This is again due to the asymptotic behavior of the coupling strength.

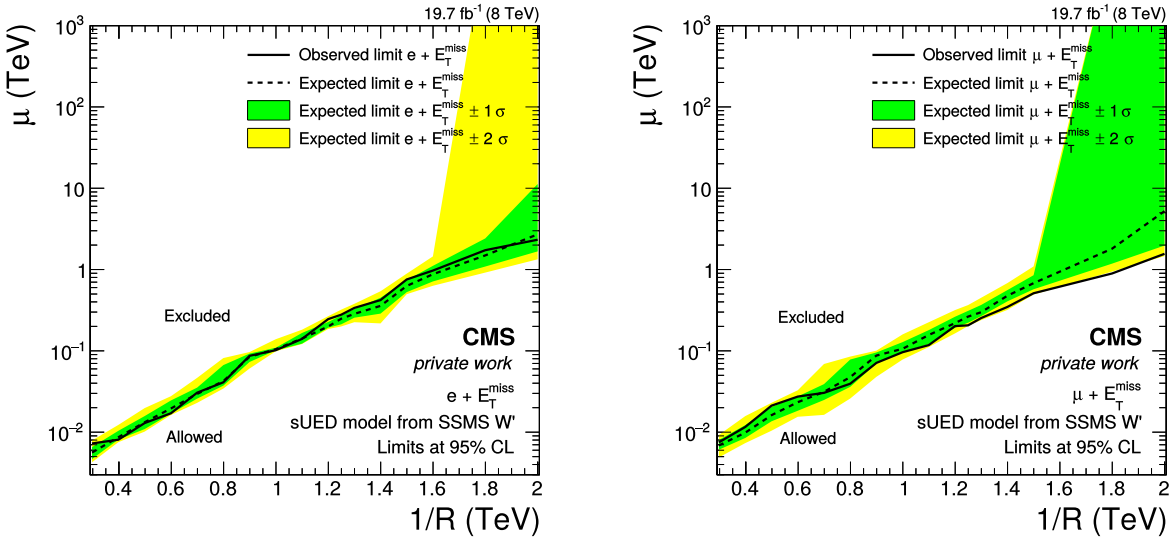

(a) electron channel

(b) muon channel

Figure 6.13.: Exclusion limits on the sUED model parameters R and μ as a reinterpretation of the SSMS limits for the individual electron and muon channel. The extremely steep increase of the $1\,\sigma$ and $2\,\sigma$ bands at large $1/R$ is due to the coupling strength converging to $\sqrt{2}$. As a result, the cross section is restricted and the model cannot be excluded for any value of μ.

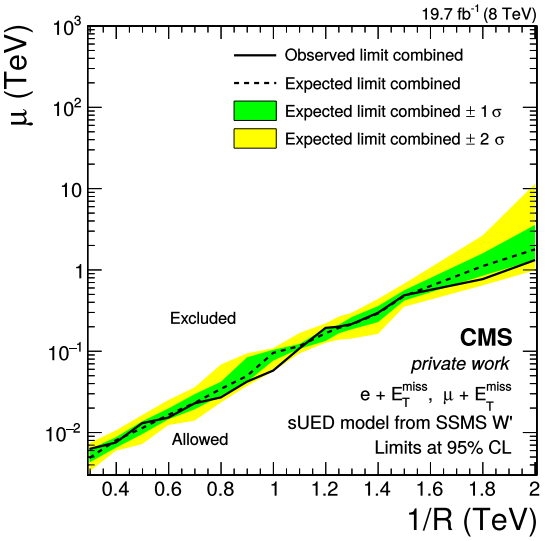

Figure 6.14.: Exclusion limits on the sUED model parameters R and μ as a reinterpretation of the SSMS limits for the combination of the electron and muon channels.

As the SSMS limits are more stringent than the SSM limits, the sUED limits derived from the SSMS model W′ boson show a better exclusion than those derived from the SSM W′ boson. The SSMO model cannot be used for a reinterpretation, as opposite sign couplings to leptons and quarks are not foreseen in the sUED model.

6.3.5. CI limits

In the helicity non conserving contact interaction model, a limit on the interaction scale Λ_{CI} is determined. A Bayesian limit with a binned likelihood (multi-bin limit) is determined. As the choice of the interaction scale does not affect the shape of the distribution but only the cross section, the cross section limit is independent of Λ_{CI}.

The excluded cross section times branching fraction for the individual channels is shown in figure 6.15, the combination of both channels can be seen in figure 6.16. A list of all cross section and energy scale limits is presented in table 6.3. For the combination of electron and muon channel limits, energy scales up to $\Lambda_{CI} = 12.4\,\text{TeV}$ can be excluded.

The limits have been calculated with a prior uniform in cross section time branching fraction. If considering the interaction scale Λ_{CI} as the fundamental physics quantity, it can be argued that a prior depending on Λ_{CI} should be chosen. A determination of the limits with a prior uniform in Λ_{CI} shows results comparable to the choice of the prior uniform in cross section. This robustness increases the confidence in the limit determination method.

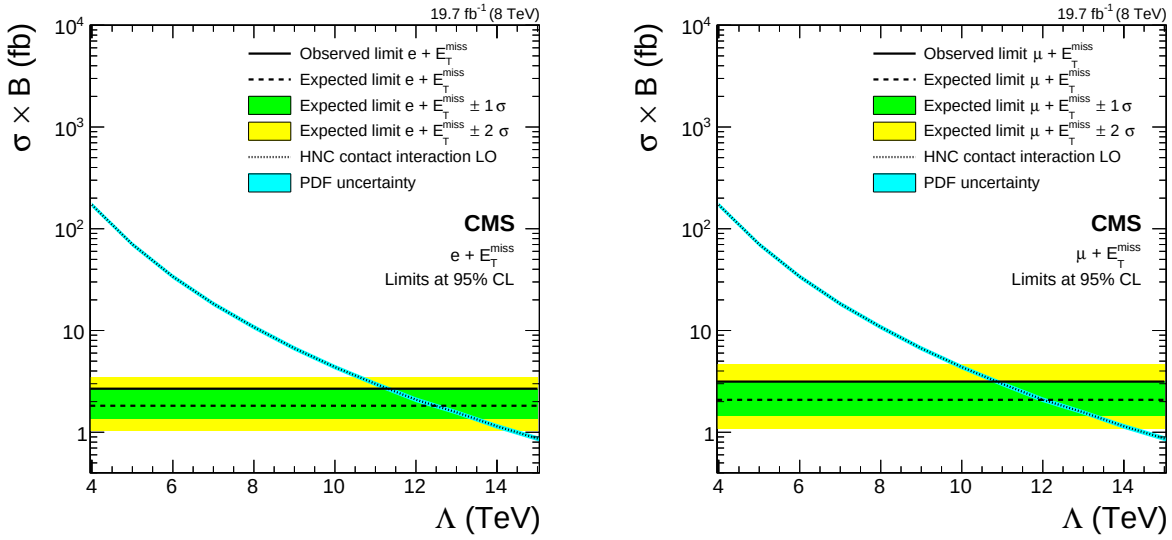

(a) electron channel

(b) muon channel

Figure 6.15.: Upper limits on the contact interaction cross section as a function of the contact interaction energy scale.

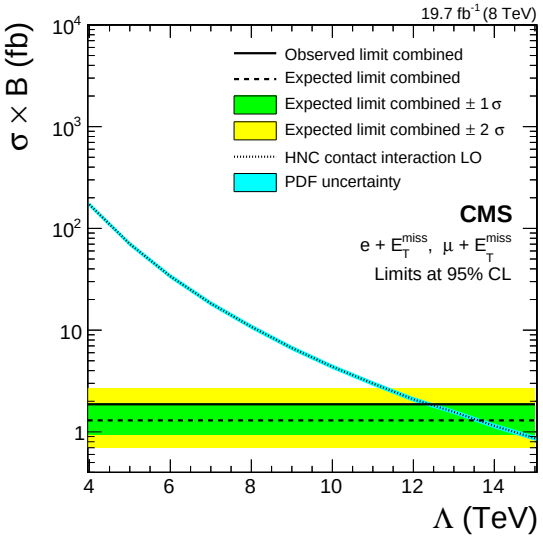

Figure 6.16.: Upper limits on the contact interaction cross section as a function of the contact interaction energy scale for the combination of the electron and muon channels.

Table 6.3.: Exclusion limits at 95 % CL on the cross section times branching fraction and the energy scale Λ_{CI} of the contact interaction model.

Channel	$\sigma \times \mathcal{B}$ (fb)		Λ_{CI} (TeV)	
	Observed	Expected	Observed	Expected
Electron	2.68	1.82	11.3	12.5
Muon	3.15	2.08	10.9	12.0
Combined	1.87	1.30	12.4	13.6

6.3.6. Dark Matter limits

Limits in terms of the dark matter EFT model, which is described in section 2.2.3, are determined using the bayesian method with a binned likelihood. A prior uniform in cross section is assumed. Different to the other models, these limits exclude the model at 90 % CL, as this is common practice in direct dark matter searches. A differentiation between the electron and muon channel is not performed. The lepton originates from the standard model W boson and is not directly connected to the dark matter model. Thus, lepton universality is assumed.

Limits on the EFT scale Λ_{DM} are determined as a function of the mass of the dark matter particle, see figure 6.17.

For low masses, $M_\chi \lesssim 100\,\text{GeV}$, the signal cross sections and therefore also the exclusion limit are independent of M_χ. Similarly, the vector and axial-vector couplings only affect the cross section and the limit at large M_χ.

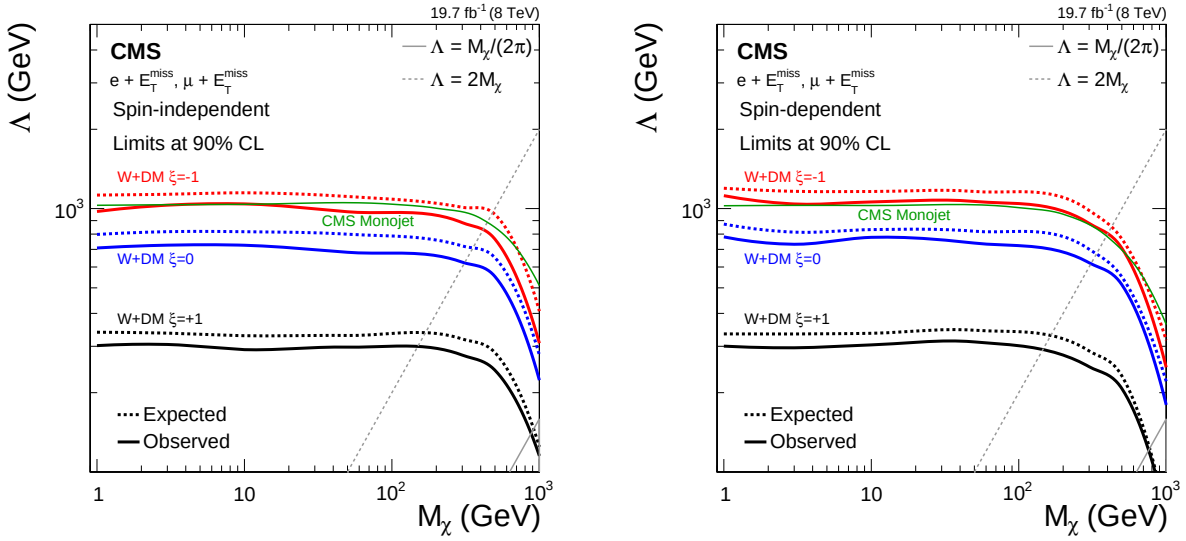

(a) vector coupling

(b) axial-vector coupling

Figure 6.17.: Exclusion limits on the energy scale Λ_{DM} of the dark matter model [1].

The limit derived from the lepton channels for $\xi = -1$ of about 1 TeV for low M_χ is comparable to the limit derived in the monojet channel [126]. The monojet analysis determined a limit, which corresponds $\xi = \pm 1$. In this channel these two values for the coupling parameter cannot be distinguished, as the channel does not contain a flavor changing current. Only for the $\xi = 0$ case the cross section is reduced in the monojet channel, however this is not considered in reference [126] and no limit is provided here.

For $\xi = 0$, where only one production channel is available, the excluded EFT scale is around 600 GeV for low M_χ. For the destructive interference case of $\xi = +1$, the limit is $\Lambda_{\mathrm{DM}} = 300\,\mathrm{GeV}$ for low M_χ.

The two model validity criteria for Λ_{DM} discussed in section 2.2.3 are shown in figure 6.17 as diagonal lines. The more conservative criterion, $\Lambda = M_\chi/2\pi$, restricts the validity of the model to those values of M_χ where the cross section and exclusion limit are flat.

6.4. Summary and Conclusion

A search for new physics in events with a single lepton and missing transverse energy has been presented. It is focused on the medium and high energy regime above 200 GeV. The $\sqrt{s} = 8\,\mathrm{TeV}$ run of CMS has provided an extended sensitivity at these energies.

The dominant standard model background originates from decays of W bosons. At high energies, electroweak corrections become increasingly important and must be combined with QCD corrections. The electron channel provides excellent energy measurements with experimental uncertainties of around 5 % on the number of expected events. Although the momentum measurement in the muon channel is substantially more difficult and yields the dominant

uncertainty on the number of expected events, the overall performance of the channel is only marginally lower.

The electron channel shows good compatibility between the data and the standard model expectation. In the muon channel, the measurement yields slightly higher event rates than expected in the standard model. However, a significant deviation from the standard model expectation has not been found in any of the channels and thus no evidence for new physics emerges.

The presented search is sensitive to a number of different new physics models. Exclusion limits on their parameters have been determined and a model independent cross section limit has been calculated.

SSM W′ bosons have been excluded up to a mass of 3.28 TeV at 95 % CL. Cross section limits for the mass range of 300 GeV to 4 TeV are provided.

For the first time, lepton channel limits in the SSMS and SSMO models, which include the interference effects of the W and the W′ bosons, have been determined. Heavy charged gauge bosons in the SSMS model with a mass below 4.00 TeV and a standard model like coupling have been excluded. In the SSMO model, the exclusion limit is 3.71 TeV. For the mass range from 600 GeV to 4 TeV exclusion limits on the coupling strength have been determined.

A reinterpretation of the SSM W′ boson limit and the SSMS W′ boson limits yields limits in terms of the sUED model. In the helicity nonconserving contact interaction model, energy scales below 1.87 TeV are excluded. An EFT Dark Matter model has been presented and in the $\xi = -1$ case, a limit on the energy scale of around 1 TeV has been determined for low M_χ at 90 % CL.

A summary of representative exclusion limits derived in this chapter is presented in figure 6.18.

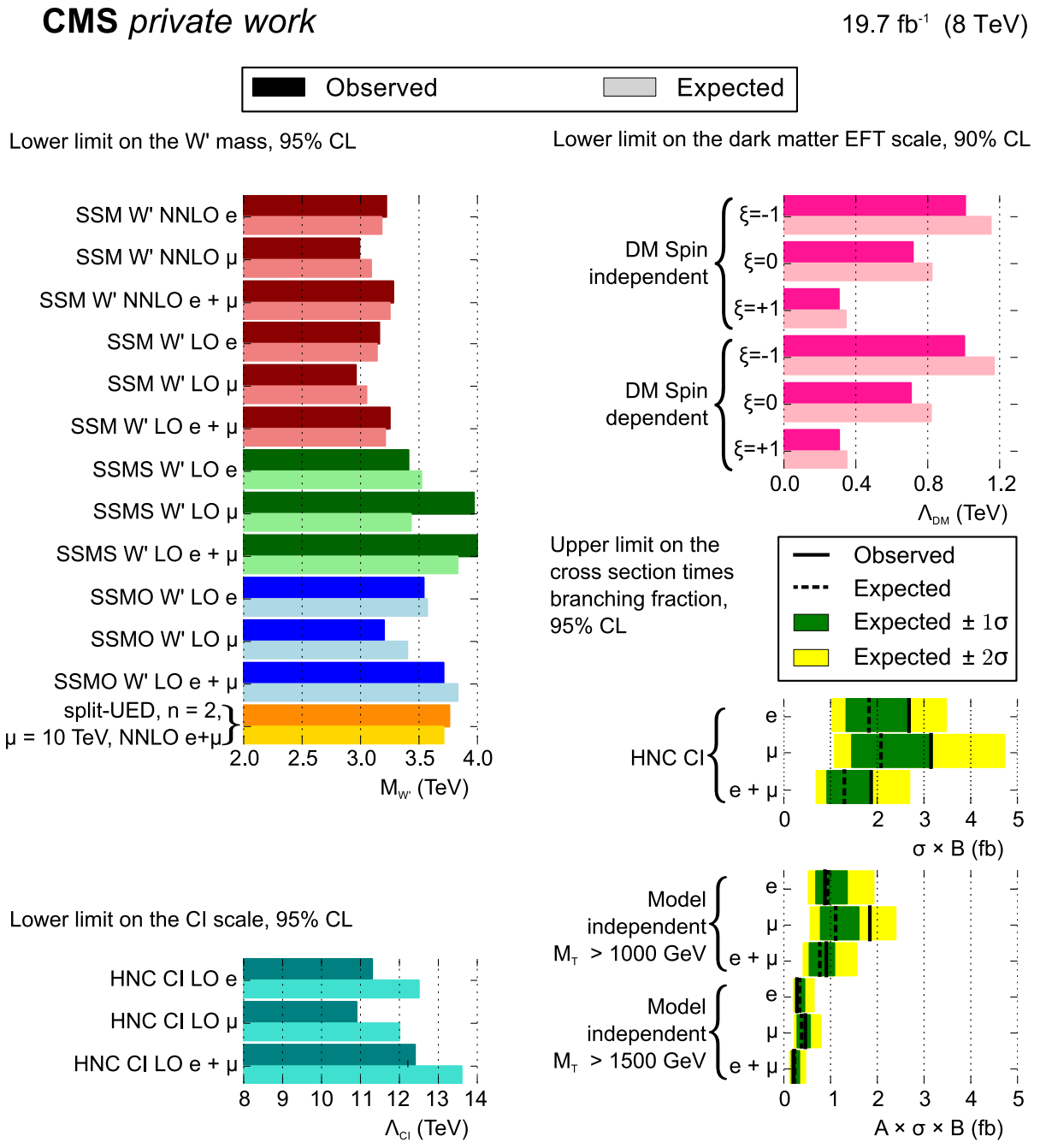

Figure 6.18.: Summary of exclusion limits. The upper darker bar shows the observed limit and the lower lighter bar the expected limit. On the left side, limits on the W′ boson mass and the HNC-CI scale are presented, on the right side the dark matter scale limits and cross section limits on the HNC-CI model as well as model independent cross section limits are displayed.

7. Projections for the HL-LHC with $\sqrt{s} = 14\,\text{TeV}$

The $\sqrt{s} = 7\,\text{TeV}$ and $\sqrt{s} = 8\,\text{TeV}$ runs at the LHC have been very successful. A large number of analyses have been published using these data, substantially improving the understanding of particle physics [127]. Starting in 2015, protons are collided with $\sqrt{s} = 13\,\text{TeV}$, once again pushing the energy frontier of particle colliders. The envisaged maximum center-of-mass energy for the LHC is $\sqrt{s} = 14\,\text{TeV}$.

For the future, the LHC is envisaged to run over a large period of time with a high instantaneous luminosity. This phase, during which an integrated luminosity of $3000\,\text{fb}^{-1}$ is going to be accumulated, is called high-luminosity LHC (HL-LHC). The maximum instantaneous luminosity is planned to be $5 \times 10^{34}\,\text{cm}^{-2}\text{s}^{-1}$. By using beam forming methods, the instantaneous luminosity can be kept constant over a long period of time [128]. Details of the different LHC phases are described in section 4.4, an overview is shown in figure 4.6.

As a result of the large instantaneous luminosity, the mean number of simultaneous interactions per bunch crossing (pileup events) is expected to reach 128 ± 5. About 12% of the bunch crossings are expected to have more than 140 pileup events. The ATLAS and CMS collaborations have agreed to perform HL-LHC studies with a mean pileup expectation of 140 events [128]. One challenge of the HL-LHC will be to efficiently reconstruct particles and to measure their properties in the presence of such a large number of pileup events.

The other issue arising with the high luminosity is the radiation damage afflicted to the detector. Especially detector parts located in the forward direction and/or near the interaction point are subject to extensive radiation. The failure of certain detector components can lead to a degraded detection efficiency and radiation damage can also influence the measurement of particle properties. The calorimeter crystals will suffer from radiation and will be less transparent for the outgoing light [72]. The influence of the radiation damages on the analysis outcome must be estimated to correctly predict the benefits of the HL-LHC for the searches in the $\ell + E_T^{\text{miss}}$ channels.

For a future collider configuration, several questions must be addressed:

- Is a certain detector configuration advantageous to discover new physics?
- Does the radiation damage on the detector impose serious problems in terms of the discovery sensitivity?
- How much integrated luminosity is necessary to discover new physics?
- What is the parameter space of new physics models the HL-LHC is sensitive to?
- If indications for new physics are found, how much integrated luminosity is necessary to determine certain model parameters or to distinguish one possible model from other models?

- Is a $3000\,\text{fb}^{-1}$ run at 14 TeV an interesting opportunity to examine the $\ell + E_T^{\text{miss}}$ channel in terms of new physics?

7.1. Simulation with Delphes

The simulation of the $\sqrt{s} = 8\,\text{TeV}$ analysis is performed using the CMS FULLSIM software, which is based on GEANT to simulate the interaction of the particles with its surroundings. Additionally, CMS has developed FASTSIM, which can handle a factor of ~ 100 more events than FULLSIM in the same time span [129].

To accompany the process of developing a Phase II detector, CMS uses a third detector simulation, DELPHES 3. DELPHES is not specialized to the CMS detector but a generic detector simulation software, which allows the straightforward implementation of different detector scenarios [130]. This is a main advantage, as during the process of developing a Phase II detector, different scenarios can be implemented and tested. Additionally, Delphes is a fast simulation as it mainly relies on parameterizations of detector properties such as resolutions and efficiencies.

The following CMS detector scenarios are considered:

- **Phase I** The Phase I detector configuration as used before LS 2. This configuration is used to compare the Delphes simulation to the CMS FULLSIM simulation in order to validate the Delphes simulation.
- **Phase I aged** The Phase I detector in the condition after being exposed to an integrated luminosity of $1000\,\text{fb}^{-1}$.
- **Phase II** The resolution for the shashlik design of the ECAL end cap has been implemented. The detector components cover up to $\eta = 4.0$.

The analysis is mainly performed with the Phase II specifications. The Phase I scenario is considered for cross checks and the Phase I aged configuration is examined to assess the necessity of the Phase II detector upgrades.

7.1.1. Delphes

Delphes consists of several modules, which are chained and, starting from the events calculated by the Monte Carlo generator, eventually determine the reconstructed physics objects.

After superimposing a number of pileup events to the simulated event, the particles are propagated through the tracker. The magnetic field is taken into account for the trajectories of charged particles. A parametrization is used to describe the reconstruction efficiency of the tracks. The tracker is assumed to have a perfect angular resolution. Tracks from vertices further away than 100 µm from the primary vertex in z-direction are identified as originating from pileup events and are subtracted.

All particles, charged as well as neutral, are then simulated in the calorimeters. The calorimeters are divided into an ECAL and a HCAL, and the fraction of deposited energy in each of them can be specified. For electrons, it is assumed that all the energy is deposited in the ECAL and

for hadrons it is assumed, that all the energy is deposited in the HCAL. The spatial resolution of the calorimeters can be specified, but it is assumed to be isotropic in ϕ and cannot be defined individually for ECAL and HCAL. The energy resolution of each of the two calorimeters is determined as a function of the particle energy and the pseudo rapidity. The resulting energy is the original particle energy smeared by a log-normal distribution. Each particle is assumed to deposit its energy in a single cell and multiple particles can deposit their energy in the same cell if their trajectories overlap within the spatial cell resolution. The energy depositions of the corresponding ECAL and HCAL cells are summed up to a so called calorimeter tower.

Delphes uses a reconstruction method similar to the CMS particle flow algorithm. It combines the information of the different detector parts for the individual particles. This method aims at obtaining the best resolution for each object without considering a single object multiple times. A charged particle can be reconstructed in the calorimeter as well as in the tracker. For low energy particles, the resolution in the tracker is superior. To avoid double counting, in that case the calorimeter entries of that particle must be removed or matched to the track.

Delphes' particle flow algorithm assumes that the tracker resolution is always superior compared to the calorimeter resolution. The charged energy, called particle flow tracks, is therefore obtained from the tracks. This energy is subtracted from the calorimeter entries and the non-negative remainder of the calorimeter energy is assumed to be the neutral energy. It consists of the energies of neutral particles, the energies of charged particles whose tracks are for some reason not reconstructed, and the differences of the charged particle track momentum reconstruction and the calorimeter energy reconstructions (i.e. energy measurements uncertainties). The neutral energy entries from the ECAL and HCAL are combined to particle flow towers.

The electron and muon efficiencies and resolutions are handled separately by special parameterizations, whereas the E_T^{miss} reconstruction relies on the particle flow algorithm. The parameterizations used for electrons and muons are listed in the appendix B.

7.1.2. Electrons

The electron reconstruction is parametrized in DELPHES by an efficiency formula depending on the pseudorapidity and the energy of the electron. Outside of the detector acceptance η range, the efficiency is set to zero. The M_T distributions for the DELPHES CMS Phase I configuration agrees with the one derived from the FULLSIM simulation, as shown in figure 7.1.

To simulate the detector resolution, the energy of the electron is smeared using a Gaussian probability density function, with the resolution following an η and E dependent function as listed in table B. This function is based on the resolution of the different detector parts, taking into account the better resolution of the tracker at low p_T and the excellent energy resolution of the ECAL at high momenta.

7.1.3. Muons

Analogously to the electron reconstruction, the muon reconstruction is performed with a parametrization of the muon reconstruction efficiency and the muon p_T resolution.

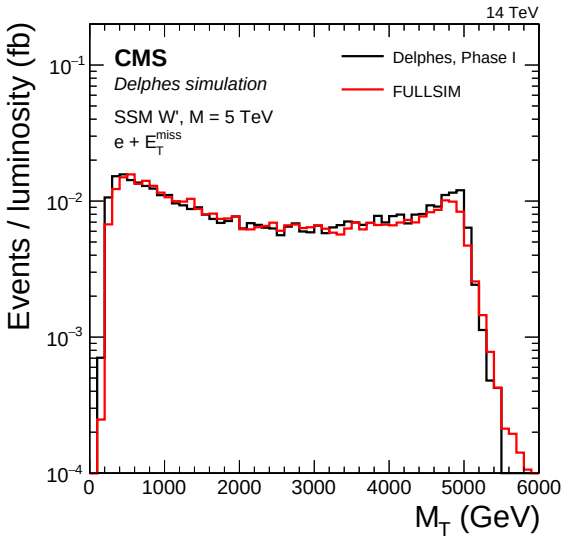

Figure 7.1.: Transverse mass signal distributions in the electron channel for a W′ boson with a mass of 5 TeV. The Delphes CMS Phase I configuration and the FULLSIM simulation are compared.

As described in section 5.2.2, the muon momentum is determined by measuring the sagitta s of its track curvature. As the sagitta is proportional to the inverse transverse momentum, $1/p_T \propto s$, to model the detector resolution, the inverse of the muon transverse momentum must be smeared with a Gaussian pdf. The difference to smearing the muon transverse momentum is especially relevant for high energies, where the sagitta becomes very small and therefore its relative uncertainty is large. Figure 7.2a shows the relative differences of the generated transverse momentum and the reconstructed transverse momentum of muons originating from SSM W′ bosons with a mass of 5 TeV, calculated from the generated transverse momentum p_T^{gen} and the reconstructed transverse momentum p_T^{reco} as

$$\Delta p_T / p_T^{\text{gen}} = \frac{p_T^{\text{reco}} - p_T^{\text{gen}}}{p_T^{\text{gen}}}. \tag{7.1}$$

Especially for high energies, the values are not distributed symmetrically around zero. Contrary, figure 7.2b shows the relative differences of the inverse momenta, calculated as

$$\Delta (p_T)^{-1} / (p_T^{\text{gen}})^{-1} = \frac{\frac{1}{p_T^{\text{reco}}} - \frac{1}{p_T^{\text{gen}}}}{\frac{1}{p_T^{\text{gen}}}}. \tag{7.2}$$

This quantity is distributed symmetrically around zero for the complete p_T spectrum.

DELPHES 3 does not support the inverse momentum smearing. We implemented a new module in DELPHES to perform an inverse momentum smearing. Additionally, we applied new functions for the momentum resolution and reconstruction efficiency by determining them from the FULLSIM 5 TeV SSM W′ boson sample. Figure 7.2 shows the muon momentum scale and resolution with the two different smearing methods for a $W \to \mu\nu$ sample.

The differences between the original CMS Delphes detector configuration, the adapted CMS Delphes configuration, and the FULLSIM simulation is shown in figure 7.3.

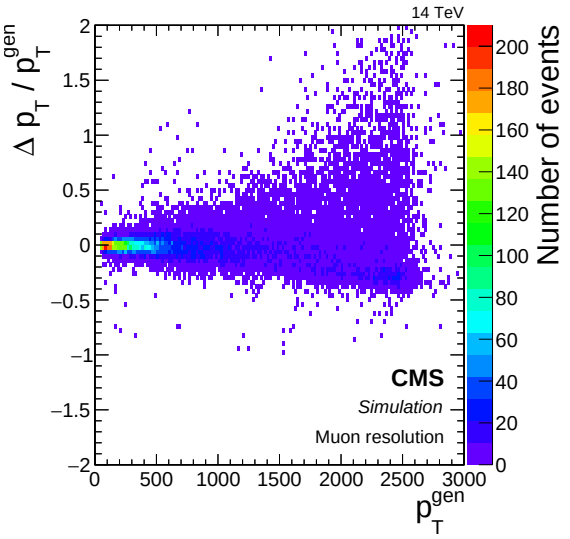

(a) Resolution in terms of the relative difference of the generated muon transverse momenta to the corresponding reconstructed muon momenta

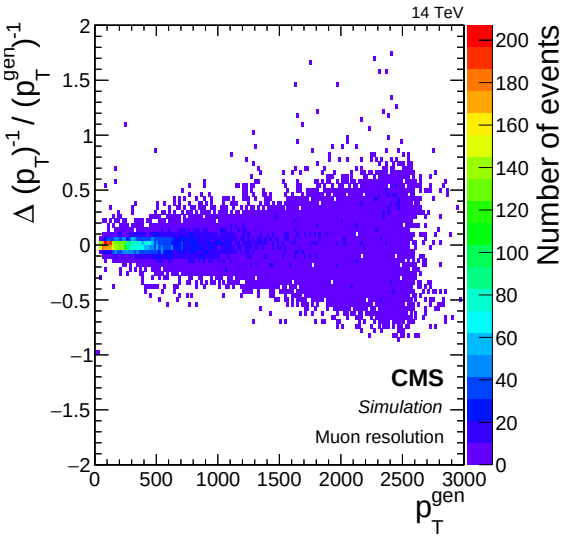

(b) Resolution in terms of the relative difference of the inverse of the generated muon transverse momenta to the corresponding inverse of the reconstructed muon momenta

Figure 7.2.: Muon momentum resolution as derived from a FULLSIM SSM W′ boson sample.

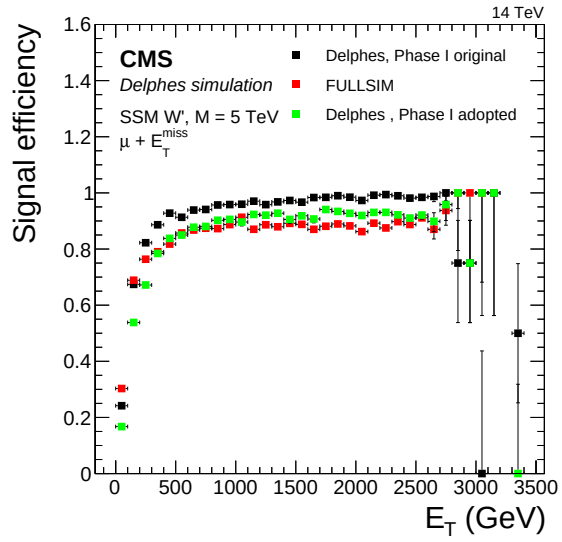

(a) Muon efficiency

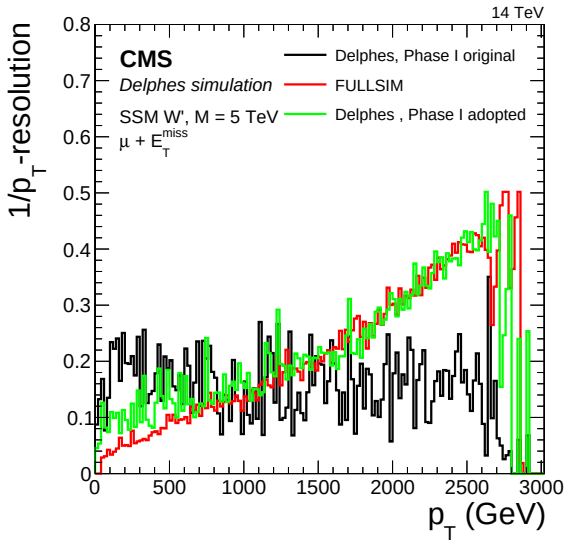

(b) Muon momentum resolution

Figure 7.3.: Muon efficiency and resolution as derived from a SSM W′ boson sample with a W′ boson mass of 5 TeV. The original Delphes CMS detector configuration, the adapted Delphes CMS configuration, and the FULLSIM simulation are compared. Although the adapted values are derived from the FULLSIM simulation sample, the two samples still show some difference.

A comparison of the efficiencies is shown in figure 7.3a. The FULLSIM efficiency is slightly lower than the original Delphes efficiency. The Delphes efficiency was therefore scaled by a factor of 0.96. This change shows a good agreement with the FULLSIM efficiency for the high p_T region. For muon momenta smaller than 300 GeV, which is the region where the selection rejects a rather large fraction of the events, the agreement is not optimal. In this region, the FULLSIM efficiency is already larger than the original Delphes efficiency. Nevertheless, this rather simple modification of the original Delphes efficiency has been chosen. As the changes to the Delphes CMS configuration must be extrapolated to the other configurations, namely the Phase I aged and Phase II configuration, a simple adaption is favored, although it might not be optimal in all parts of the phase space. As the efficiencies of the Phase II detectors can currently only be roughly estimated, this can be accepted. It should also be kept in mind, that these efficiencies are determined with all selection criteria for the analysis applied and the comparison can therefore be different for a different selection.

The transverse momentum resolutions for the three detector simulations are displayed in figure 7.3b. Displayed is the standard deviation σ of the relative inverse p_T differences as a function of the generated p_T:

$$r(p_T) = \sigma\left(\frac{|(p_T^{\text{reco}})^{-1} - (p_T^{\text{gen}})^{-1}|}{(p_T^{\text{gen}})^{-1}}\right). \tag{7.3}$$

This value, sometimes referred to as the root mean square deviation, is calculated from the number of events N, the relative differences x_i, and the mean relative difference $\overline{x}$ as

$$\sigma(x_i) = \sqrt{\frac{\sum_i (x_i - \overline{x})^2}{N}}\ . \tag{7.4}$$

The original Delphes muon momentum resolution does not correspond to the FULLSIM resolution in any way. The FULLSIM resolution is parametrized using a polynomial to:

$$r(p_T) = a_0 + a_1 \cdot \frac{p_T}{\text{GeV}} + a_2 \cdot \left(\frac{p_T}{\text{GeV}}\right)^2 + a_3 \cdot \left(\frac{p_T}{\text{GeV}}\right)^3 \tag{7.5}$$

with the fit parameters:

$$a_0 = 0.0297527 \tag{7.6}$$
$$a_1 = 0.00014987 \tag{7.7}$$
$$a_2 = -6.30357 \tag{7.8}$$
$$a_3 = 2.65056\ . \tag{7.9}$$

There is a slight deviation of the adapted Delphes configuration to the FULLSIM simulation for low p_T.

The effect of these adjustments on the transverse mass distribution for the examined W′ boson sample is shown in figure 7.4. The agreement of the adapted Delphes simulation with the FULLSIM simulation is reasonable. In both distributions the Jacobian peak is no longer recognizable. There are still some differences between the FULLSIM and the adopted Delphes simulation. These may arise from the fact, that the actual resolution does not follow a perfect Gaussian function [66].

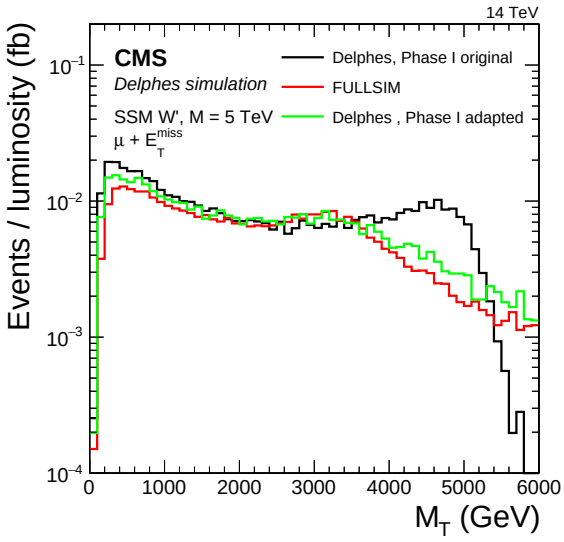

Figure 7.4.: Muon transverse mass distribution as derived from a SSM W′ boson sample with a W′ boson mass of 5 TeV. The original Delphes CMS detector configuration, the adapted Delphes CMS configuration, and the FULLSIM simulation are compared.

7.1.4. Missing transverse energy

The missing transverse energy is determined by summing up the transverse components of particle flow tracks, particle flow calorimeter towers, and muons, denoted by the index i:

$$E_T^{\text{miss}} = |\sum \vec{p_T^i}|. \tag{7.10}$$

Also, the ϕ direction of the missing transverse energy is calculated from the sum of the objects' momenta

$$\phi_{E_T^{\text{miss}}} = \phi(-\sum \vec{p_T^i}). \tag{7.11}$$

A pileup subtraction is not performed to determine the missing transverse energy, i.e pileup events also contribute to E_T^{miss}.

7.1.5. Pileup

At the HL-LHC a pileup mean of 140 events is expected. This is simulated in DELPHES by superimposing additional simulated low-Q^2 QCD events. Their number is determined from a Poisson distribution with mean 140 and their vertices are placed along the beam axis following a Gaussian distribution with a spread of 0.053 m around the interaction point.

7.2. Selection

The selection is adapted following the $\sqrt{s} = 8$ TeV analysis. In the electron channel, an electron with a transverse momentum of at least 100 GeV is required, in the muon channel, the muon is

required to fulfill $p_T > 45\,\text{GeV}$. If a second lepton of the same generation with $p_T > 25\,\text{GeV}$ is present, the event is discarded. An isolation criterion is not enforced. The two kinematic selection criteria $0.4 < p_T / E_T^{\text{miss}} < 1.5$ and $\Delta\phi(\ell, E_T^{\text{miss}}) > 2.5$ are applied.

7.3. Background simulation and samples

For a $3000\,\text{fb}^{-1}$ run, special care has to be taken that in each region of the phase space, an adequate number of Monte Carlo events is available. As a general rule, the number of Monte Carlo events should exceed the number of expected events by a factor of 10. For the $3000\,\text{fb}^{-1}$ run this would require the production of $\mathcal{O} = 10^{10}$ events, which is not feasible. Therefore, the samples are produced for different phase space regions separately.

The main background is due to W boson decay. The off-shell part $M_W > 200\,\text{GeV}$ of this background has been produced in several bins of the boson mass using PYTHIA 8.

All other backgrounds have been produced by the CMS collaboration. They have been generated using MADGRAPH in bins of the scalar p_T sum of all generated particles, resulting in a reasonable number of available events in all phase space regions [131]. The single boson samples also include the W boson events. Those with $M_W > 200\,\text{GeV}$ have been removed from the samples using the generator information to avoid "double counting" with the PYTHIA sample.

The background samples together with their respective cross sections are listed in table 7.1 They have all been simulated using the DELPHES detector simulation with the Phase II configuration.

7.3.1. Higher order corrections for the W boson production and decay

To include higher order corrections for the main W boson background, the method described in section 5.5.2 has been applied. For this, samples using the HORACE, MCATNLO, and PYTHIA 8 generators have been produced. The results can be seen in figure 7.5. Figure 7.5a shows the individual electro-weak and QCD corrections up to a transverse mass of 6 TeV, which corresponds to the maximum energy where events are expected in this distribution at the HL-LHC run.

Figure 7.5b shows the combination of the EW and QCD corrections with the two methods described in section 5.5.2. The mean values are parametrized using a polynomial of the order 3. This parametrization is used to correct the event weights of the W boson events. Half the difference between the additive and factorial method results is considered as uncertainty.

7.4. Signal simulation and samples

Three signal models have been selected for the $\sqrt{s} = 14\,\text{TeV}$ study: The sequential standard model W′ boson, the dark matter model, and the helicity non conserving contact interaction model. All samples and their respective cross sections are listed in table 7.2.

Table 7.1.: Background samples used for the $\sqrt{s} = 14\,\text{TeV}$ analysis and simulated using DELPHES [131]. Except for the W boson background, the samples have been produced by the CMS collaboration using MADGRAPH. The background group corresponds to the name of the background in the M_T plots in chapter 8. The officially produced samples are not restricted to the decay into $\ell + E_T^{\text{miss}}$. The W boson sample however is produced only for the leptonic decay channel, i.e. the combined branching fraction to the three leptonic decay modes is considered in the provided cross sections. It is separated into four different subsamples, each with a different minimum W boson mass, starting at 200 GeV.

Background group	Sample	Description	Cross section (pb)
$W \to \ell\nu$	$W \to \ell\nu$	$M_W > 200\,\text{GeV}$. PYTHIA 8	2.11×10^{1}
		$M_W > 500\,\text{GeV}$ PYTHIA 8	7.43×10^{-1}
		$M_W > 1000\,\text{GeV}$ PYTHIA 8	4.85×10^{-2}
		$M_W > 3000\,\text{GeV}$ PYTHIA 8	1.41×10^{-4}
DY	B	Vector boson, together with 0 or more jets. W bosons with $M_W > 200\,\text{GeV}$ have been removed from this sample. $\mathcal{O}(\alpha_s^n \alpha_w)$.	2.38×10^{5}
	LL	Vector boson and jets, off-shell produced. W bosons have been removed from this sample. $\mathcal{O}(\alpha_s^n \alpha_w^2)$	1.54×10^{3}
Diboson	BB	Diboson and jets. $\mathcal{O}(\alpha_s^n \alpha_w^2)$.	2.90×10^{2}
	BLL	Diboson and jets, off-shell produced $\mathcal{O}(\alpha_s^n \alpha_w^3)$	3.22
$t\bar{t}$ + single top	TT	Top quark pair and jets $\mathcal{O}(\alpha_s^{2+n})$	5.79×10^{2}
	TB	$\mathcal{O}(\alpha_s^{n+1} \alpha_w)$	7.21×10^{1}
	TJ	Single top (s and t-channel) and jets. $\mathcal{O}(\alpha_s^{n-1} \alpha_w^2)$.	1.16×10^{2}
	TTB	Top pair in association with boson production. $\mathcal{O}(\alpha_s^{2+n} \alpha_w^2)$.	2.95

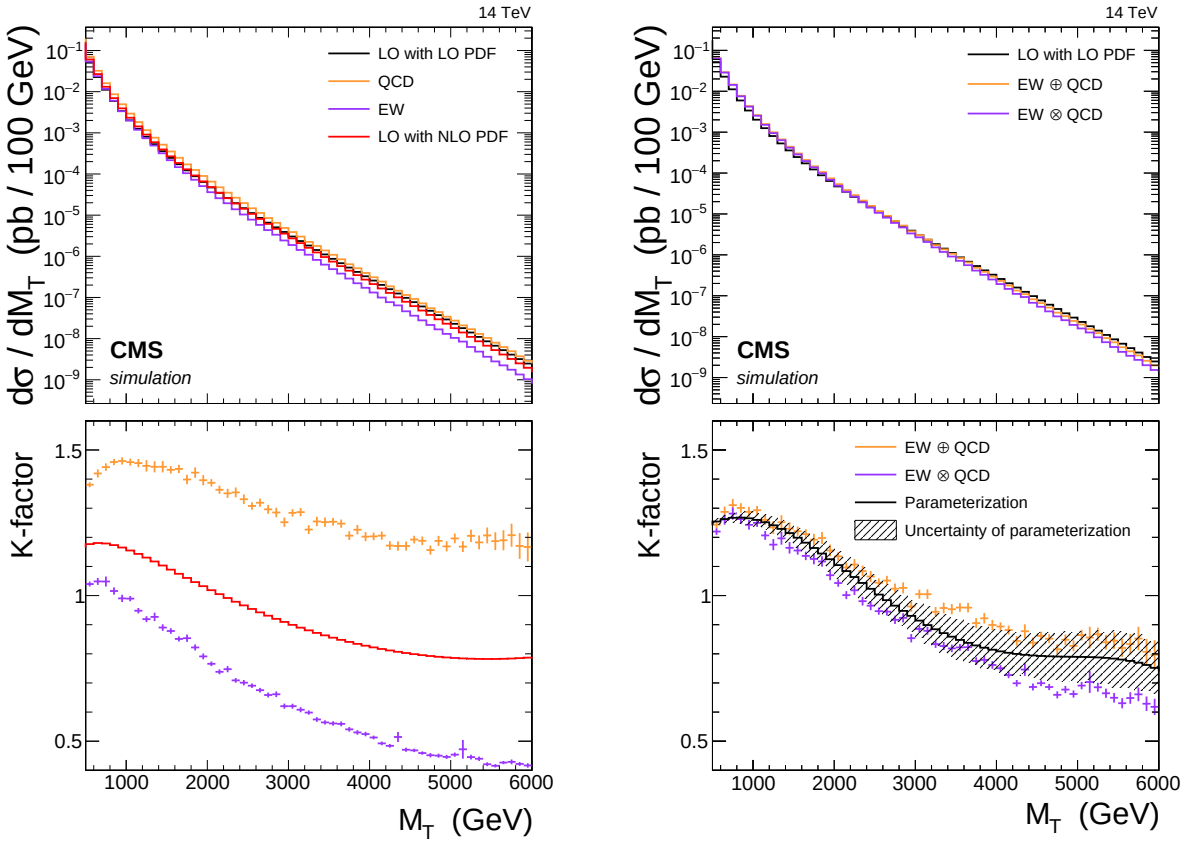

(a) (b)

Figure 7.5.: Electro-weak and QCD next-to-leading order corrections for W boson production at $\sqrt{s} = 14\,\text{TeV}$.

For this analysis, the SSM model is generalized by a variable coupling strength, similar to the approach used with the SSMS/SSMO models at the $\sqrt{s} = 8\,\text{TeV}$ analysis but without considering interference effects. The change of the coupling affects the cross section and the decay width of the SSM W′ boson, as described in section 2.2.1. Only the scenario with $g_W = g_{W'}$ is simulated using Delphes. To determine the M_T distributions of the SSM W′ boson with different couplings, the reweighing technique as described in section 5.6.2 is used.

This allows the determination of the sensitivity of a low-mass small-coupling W′ without considering the more complex SSMS/SSMO models. There is no strong argument to assume the standard model coupling for a W′ boson, in fact models such as the sUED model claim a coupling that is different. The long run time of the HL-LHC can be beneficial especially when it comes to a low-mass small-coupling W′ boson. The prerequisites in this regime are quite different: The number of background events is quite high and the lepton is not necessarily required to traverse the detector centrally. Figures 7.6a and 7.6b show the generator M_T distributions for a W′ boson of different coupling strengths with a mass of 1 TeV and 6 TeV, respectively.

The helicity non conserving contact interaction and dark matter samples have been chosen so that their cross section times branching ratio corresponds to 1 fb, because distinct cross sec-

Table 7.2.: Signal samples as used for the $\sqrt{s} = 14\,\text{TeV}$ analysis. For the dark matter and HNC-CI samples a fixed cross section of $1\,\text{fb}^{-1}$ is chosen, the corresponding values of Λ are given in the table.

Model	Parameters	$\sigma \times \mathcal{B}$ (pb)
SSM W′	$M_{W'} = 1\,\text{TeV}$	3.09
	$M_{W'} = 3\,\text{TeV}$	1.69×10^{-2}
	$M_{W'} = 5\,\text{TeV}$	5.62×10^{-4}
	$M_{W'} = 6\,\text{TeV}$	1.77×10^{-4}
	$M_{W'} = 7\,\text{TeV}$	8.08×10^{-5}
Dark matter	$\xi = +1$, $\Lambda = 1.99\,\text{TeV}$	1.00×10^{-3}
	$\xi = 0$, $\Lambda = 2.80\,\text{TeV}$	1.00×10^{-3}
	$\xi = -1$, $\Lambda = 3.88\,\text{TeV}$	1.00×10^{-3}
HNC-CI	$\Lambda = 25.8\,\text{TeV}$	1.00×10^{-3}

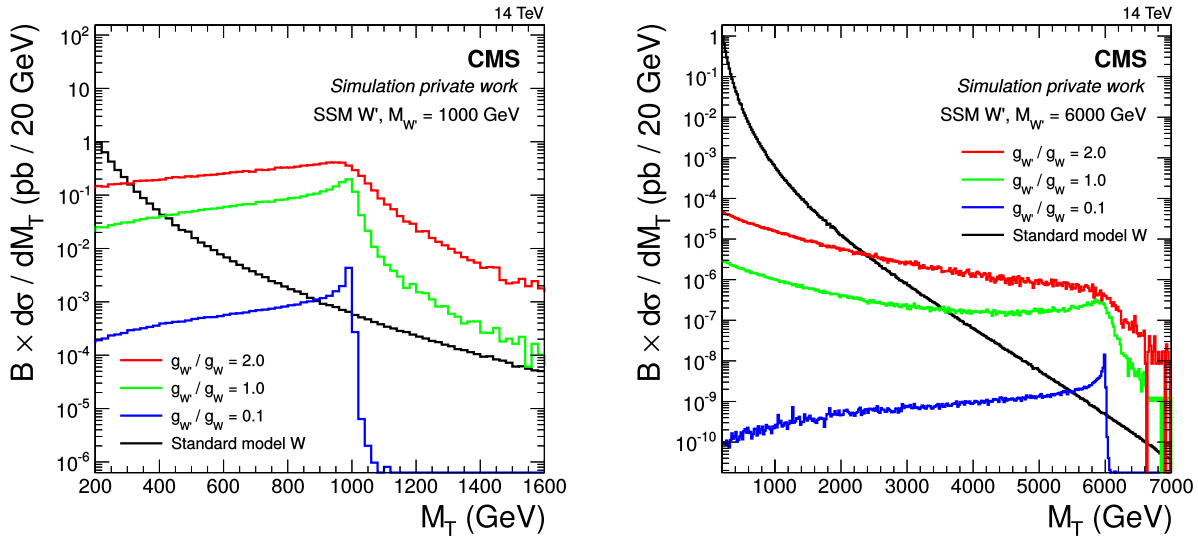

(a) $M_{W'} = 1\,\text{TeV}$ (b) $M_{W'} = 6\,\text{TeV}$

Figure 7.6.: Generated (no detector simulation applied) differential cross section times branching fraction as a function of the transverse mass for a SSM W′ boson (without interference) with different coupling strengths at $\sqrt{s} = 14\,\text{TeV}$. The coupling strength affects the cross section and the decay width of the W boson.

tions for these samples are not well motivated. The cross section has been specified the same for all samples, which allows to study the influence of different distribution shapes. The choice of $\mathcal{B} \times \sigma = 1\,\text{fb}$ is expected to approximately correspond to the detection limit of the HL-LHC for such models. The corresponding values of Λ for this cross section can be found in table 7.2.

7.5. Comparison of detector scenarios

7.5.1. Phase I

As the Phase I detector scenario has been used in adjusting the Delphes simulation to the FULLSIM simulation, its features have already been discussed in section 7.1. Total signal efficiencies for the (adapted) Phase I scenario and the original Phase I scenario are listed in table 7.3.

Of the SSM W′ samples, the signal with a mass of 3 TeV has the maximum efficiency. This is due to the large fraction of high M_T events in this sample. For higher W′ masses, the events are increasingly produced off-shell at lower transverse masses.

For the dark matter signal, the $\xi = -1$ and $\xi = 0$ cases attain efficiencies of around 60 %, whereas the $\xi = +1$ efficiencies lie around 16 % in the electron channel and 25 % in the muon channel. The significantly lower value for the electron channel is due to the more restrictive E_T criterion of 100 GeV, which has a large effect on this specific signal. This is also the reason, why the efficiency of the HNC-CI model signal is 62 % in the electron channel compared to 65 % in the muon channel. Figure 7.7 shows the signal efficiency as a function of the lepton E_T or p_T, illustrating the lower efficiency at small energies in the electron channel.

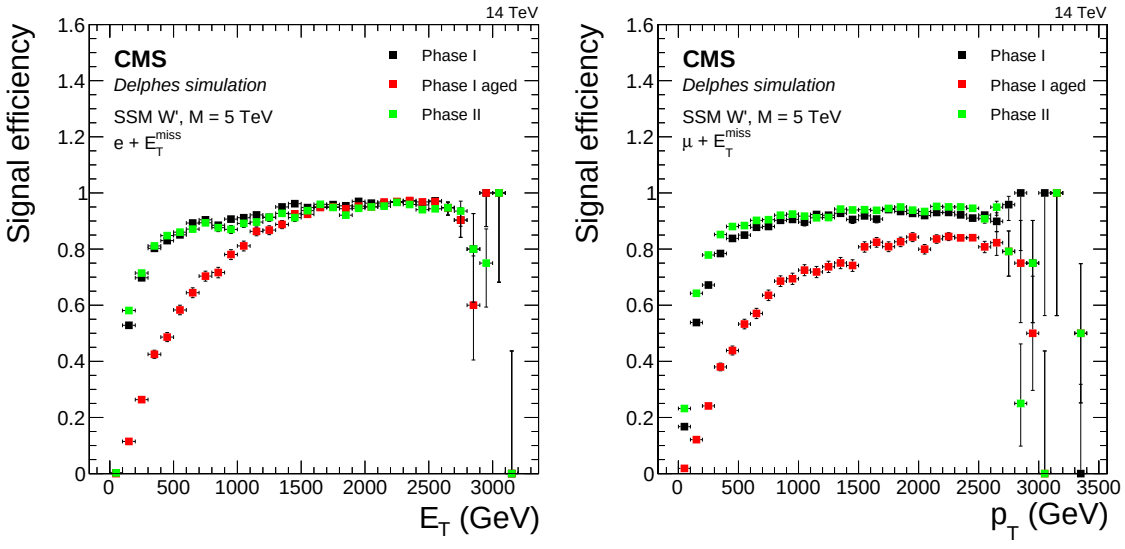

(a) Electron channel

(b) Muon channel

Figure 7.7.: Event efficiency as a function of E_T or p_T for a W′ boson with a mass of 5 TeV after the event selection for Phase I, Phase I aged, and Phase II.

Table 7.3.: Signal efficiencies in the electron and muon channels. Statistical uncertainties originating from the sample production are smaller than 0.01.

Model	Phase I original	Phase I adapted	Phase I aged	Phase II
Electron channel				
SSM W′ $M = 1\,\text{TeV}$	0.78	0.77	0.42	0.78
SSM W′ $M = 3\,\text{TeV}$	0.86	0.86	0.73	0.86
SSM W′ $M = 5\,\text{TeV}$	0.75	0.75	0.60	0.75
SSM W′ $M = 6\,\text{TeV}$	0.68	0.67	0.47	0.68
SSM W′ $M = 7\,\text{TeV}$	0.63	0.62	0.40	0.63
EFT DM $\xi = -1$	0.59	0.60	0.32	0.60
EFT DM $\xi = 0$	0.57	0.57	0.30	0.57
EFT DM $\xi = +1$	0.16	0.16	0.06	0.16
HNC-CI	0.64	0.62	0.37	0.64
Muon channel				
SSM W′ $M = 1\,\text{TeV}$	0.85	0.77	0.37	0.82
SSM W′ $M = 3\,\text{TeV}$	0.92	0.85	0.64	0.88
SSM W′ $M = 5\,\text{TeV}$	0.84	0.76	0.53	0.80
SSM W′ $M = 6\,\text{TeV}$	0.77	0.69	0.41	0.73
SSM W′ $M = 7\,\text{TeV}$	0.73	0.65	0.35	0.70
EFT DM $\xi = -1$	0.68	0.63	0.28	0.65
EFT DM $\xi = 0$	0.66	0.61	0.27	0.63
EFT DM $\xi = +1$	0.28	0.25	0.06	0.27
HNC-CI	0.75	0.65	0.34	0.72

7.5.2. Pileup

Because of the distinct signature of the $\ell + E_T^{\text{miss}}$ events, the influence of pileup has been negligible in the $\sqrt{s} = 8\,\text{TeV}$ analysis. At the HL-LHC, the average number of pileup events will increase to 140. This results in a high number of reconstructed muons in the forward direction, as displayed in the event display in figure 7.8. As these muons are of poor quality and only have small transverse momenta ($p_T \lesssim 10\,\text{GeV}$), they can be easily rejected.

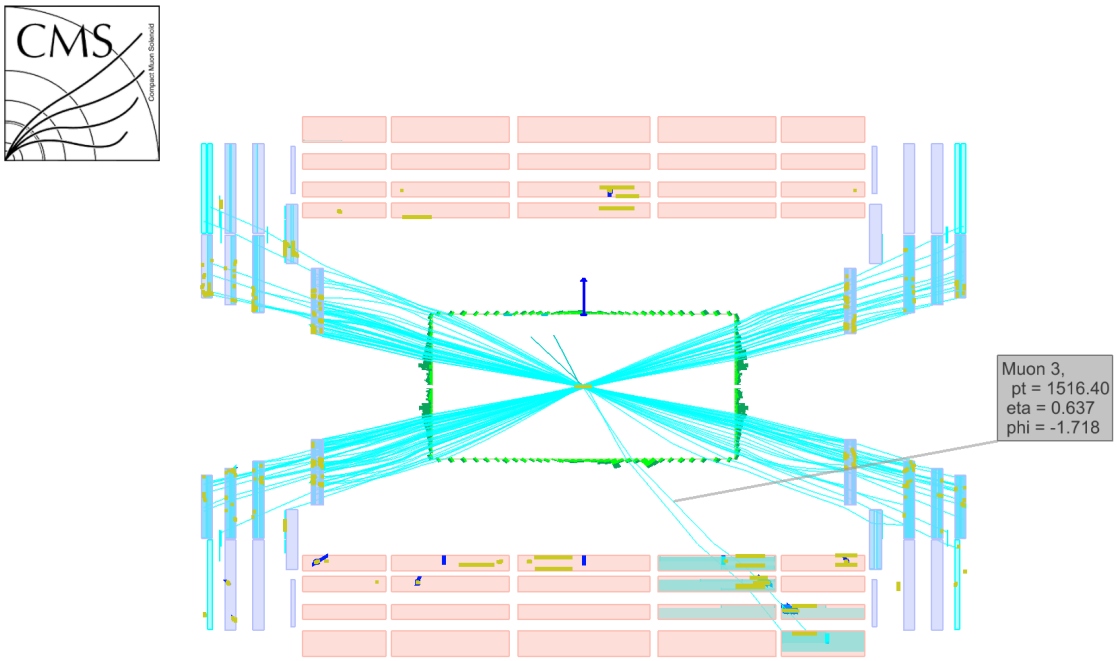

Figure 7.8.: Event display of a simulated W′ boson signal with a mass of 5 TeV. The large number of reconstructed muons, ploted as blue lines, is an effect of the high pileup, they are of low momentum and poor quality and can therefore be easily rejected.

Three different pileup scenarios are studied using the Delphes CMS Phase I detector simulation: No pileup, a mean of 50 pileup events, and a mean of 140 pileup events. Figure 7.9 shows the efficiencies for a SSM W′ boson sample with a mass of 5 TeV. The three pileup scenarios show only marginal differences for high transverse momenta. Only in the low momentum regime, the events with 140 pileup show lower efficiencies. This seems plausible, as high energy leptons, which have a very distinctive signature, are rare and therefore do not appear in the pileup events.

7.5.3. Aging

As described in section 4.2, the exposure to the high particle flux damages the detector and results in the so-called detector "aging". An aged Delphes CMS detector configuration corresponding to an exposure of an integrated luminosity of 1000 fb^{-1} has been implemented by the

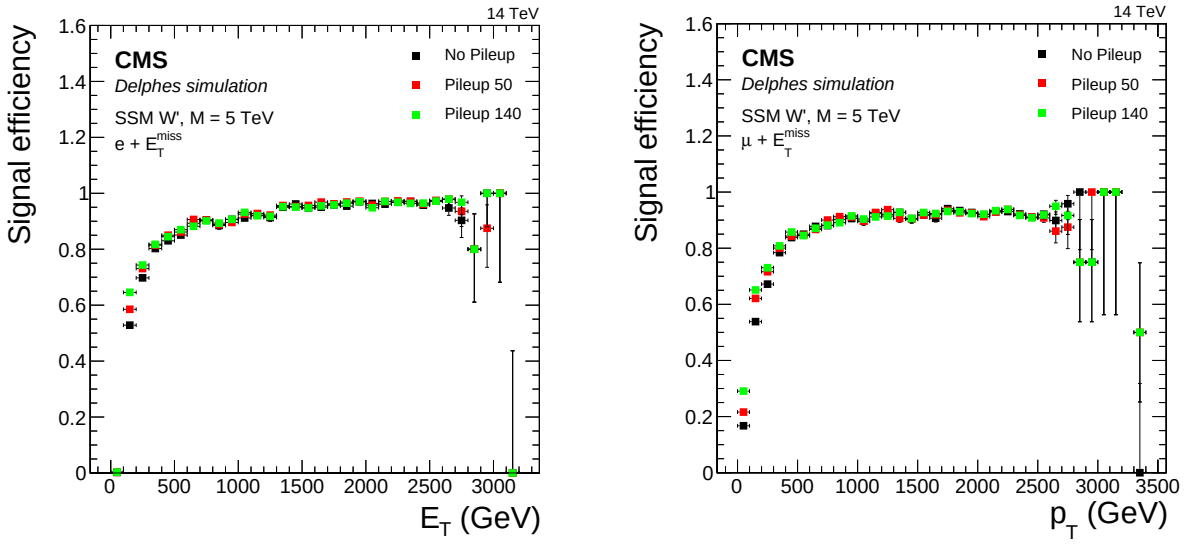

(a) Electron channel

(b) Muon channel

Figure 7.9.: Signal efficiencies for different pileup scenarios with the Delphes Phase I CMS detector simulation determined from a SSM W′ boson sample with a mass of 5 TeV.

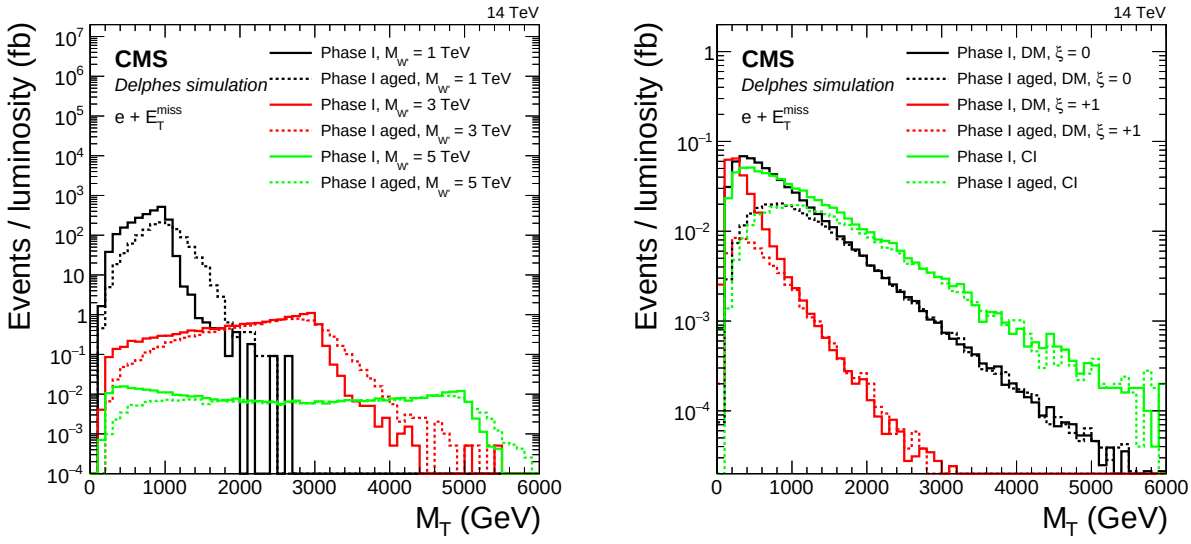

(a) SSM W′ boson signals

(b) DM signals

Figure 7.10.: Comparison of the M_T distributions with the aged and non-aged detector scenarios in the electron channel.

CMS Collaboration. Figures 7.10 and 7.11 show the transverse mass distributions for selected W′ boson, dark matter, and contact interaction signals, if recorded with a non-aged Phase I detector and an aged Phase I detector.

In figure 7.7 the signal efficiency for the aged and non-aged Phase I detector are compared. For the electron channel analysis, the aged detector shows a substantially lower signal effi-

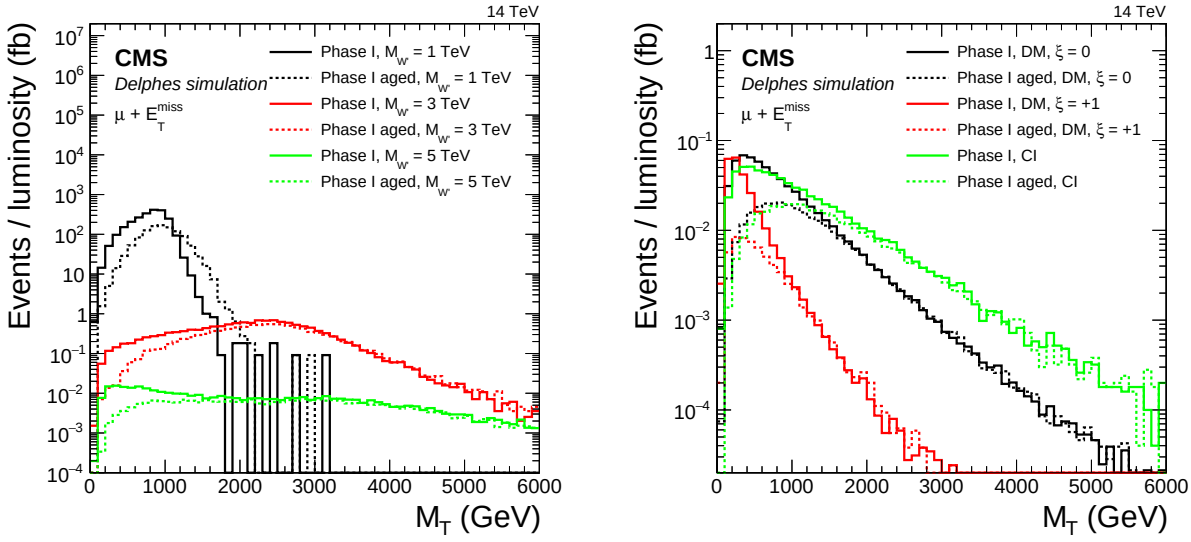

(a) SSM W′ boson signals

(b) DM signals

Figure 7.11.: Comparison of the M_T distributions with the aged and non-aged detector scenarios in the muon channel.

ciency in the region of $E_T < 1000\,\text{GeV}$. For the muon channel, the efficiency is degraded over the whole p_T range, but especially at low energies.

A possible explanation for this could be the degraded detector performance at high η. Leptons with a lower energy are more prone to go in forward direction because of kinematic reasons. The total particle flux is different for the different detector parts. At larger η, the flux increases. Therefore, the aging has a larger impact on detector parts in forward direction. For the aged detector scenario, the electron efficiency is assumed to decrease from 1.0 at $|\eta| = 0$ to 0.68 at $|\eta| = 2.5$.

The efficiency for the aged and non-aged detectors as a function of E_T and η is shown in Figure 7.12. This suggests, that the low signal efficiency is not related to the η dependent lepton reconstruction efficiency decrease.

Figure 7.13 shows the two kinematic selection criteria for SSM W′ samples with masses of 1 TeV and 5 TeV for the aged and non-aged detectors. Especially for the 1 TeV case, the distributions for the aged detector appears to be broadened, which is due to the deteriorated calorimeter resolution. Even worse, the mode (position of the maximum) of the E_T / E_T^{miss} distribution is shifted to a value < 1. As the efficiency and energy resolution for the aged scenario is deteriorated, the energy of hadronic jets cannot be reconstructed with a high precision. This leads to additional, randomly distributed contributions to the missing transverse energy. This is the reason for the reduced signal efficiency in the aged scenario when applying the two kinematic selection criteria. For larger W′ boson masses the effect is less severe as the neutrino contribution dominates the missing transverse energy. Whereas at lower energies, badly reconstructed jets with energies of the order of 100 GeV have a significant impact on the total missing transverse energy. When performing a possible future analysis using an aged detector, one needs to take this into consideration.

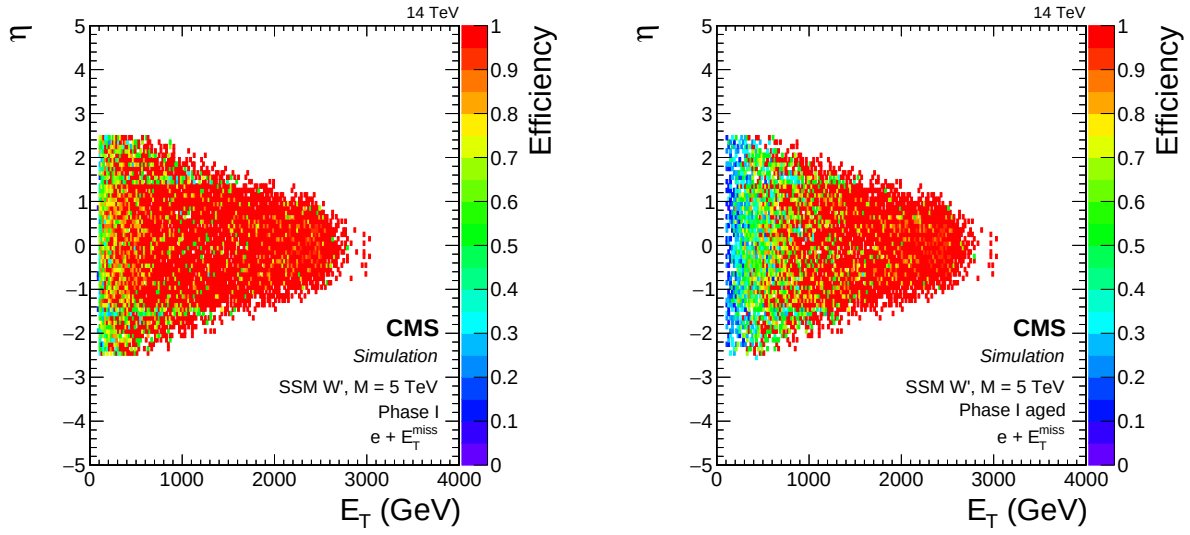

(a) Phase I

(b) Phase I aged

Figure 7.12.: Signal efficiency of a SSM W′ boson with a mass of 5 TeV in the electron channel as a function of the transverse energy and the pseudorapidity. The aged scenario shows a degraded signal efficiency at low transverse energy.

7.5.4. Phase II

The two most prominent features of the Phase II detector, when compared to the Phase I detector, are the higher calorimeter granularity and its larger coverage in η from 2.5 to 4.0. The improved granularity is not expected to be of major importance for the discovery of the discussed signals.

Figure 7.14 shows the M_T–η distribution of a SSM W′ boson with a mass of 1 TeV and the dark matter signal with $\xi = +1$. For all signals, the leading lepton in the event becomes more central with increasing transverse mass. As a large amount of energy in such high energy events is bound to the momenta of the stable particles, the phase space for events with a substantial boost in forward direction diminishes. As a result, only low energy events can profit from the extended η coverage and even of these only a small fraction is in the affected range of $2.5 < \eta < 4.0$. This is reflected in the vanishingly small differences of the Phase I and Phase II efficiencies, as stated in table 7.3.

Nevertheless, even though the improvements of the Phase II detector compared to the Phase I detector do not have a large effect in the considered analyses, it is of major importance to replace the aged Phase I detector with this new detector to compensate for efficiency loss and the deteriorated resolution. The long run time of the HL-LHC is of special importance for the discovery and distinction potential of beyond the standard model signals, as discussed in the next chapter.

The improved granularity and η range will improve other analyses, not considered in this thesis. Signals with multiple particles boosted into the same direction, e.g. $W' \to WZ$, may benefit from an improved spatial resolution in the calorimeter. Many analyses search for substructures in jets, relying on a good calorimeter granularity. The improved η range may im-

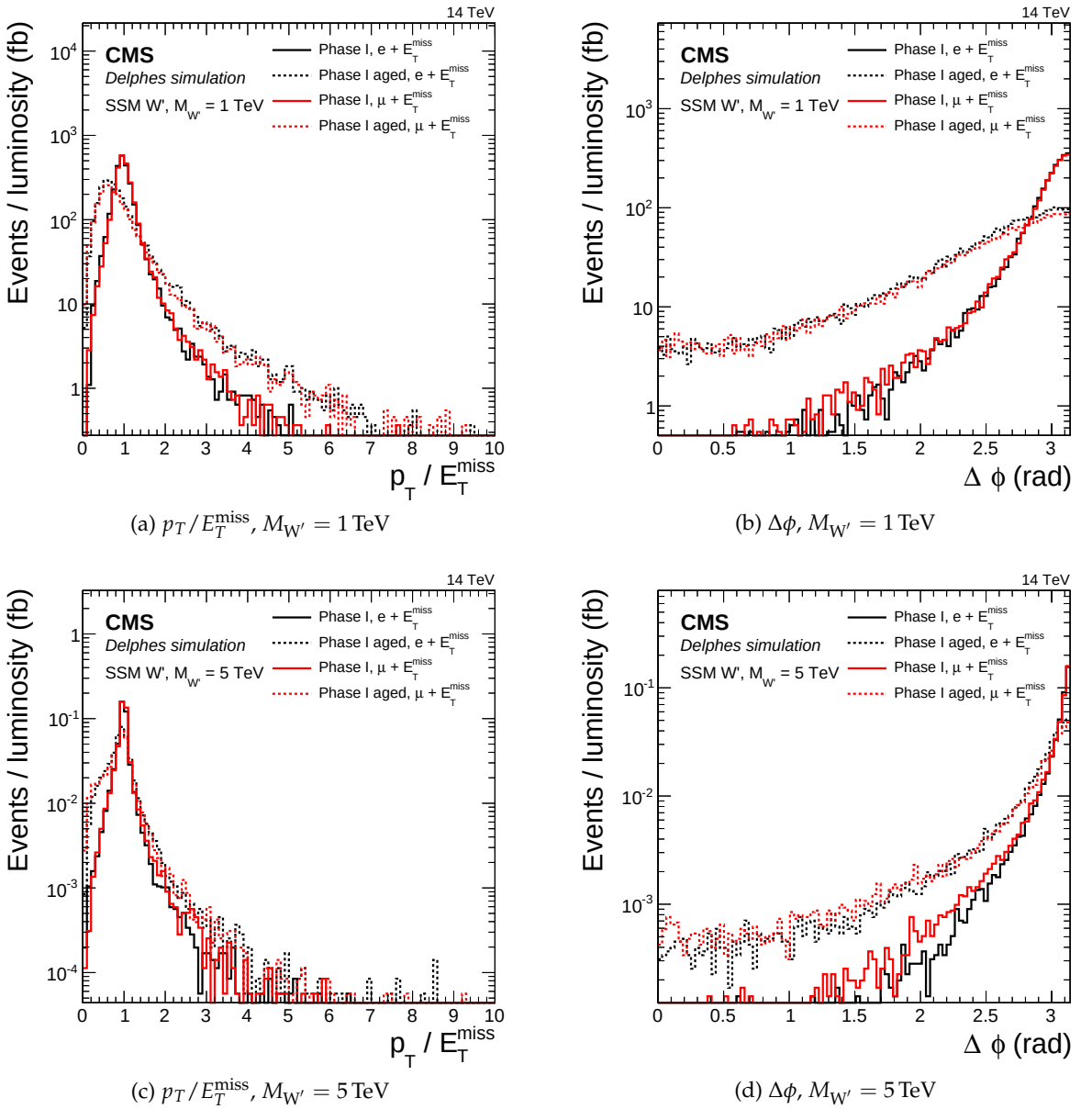

(a) p_T / E_T^{miss}, $M_{\text{W}'} = 1\,\text{TeV}$

(b) $\Delta\phi$, $M_{\text{W}'} = 1\,\text{TeV}$

(c) p_T / E_T^{miss}, $M_{\text{W}'} = 5\,\text{TeV}$

(d) $\Delta\phi$, $M_{\text{W}'} = 5\,\text{TeV}$

Figure 7.13.: Comparison of the variables used as kinematic selection criteria for the aged and non-aged detector scenarios.

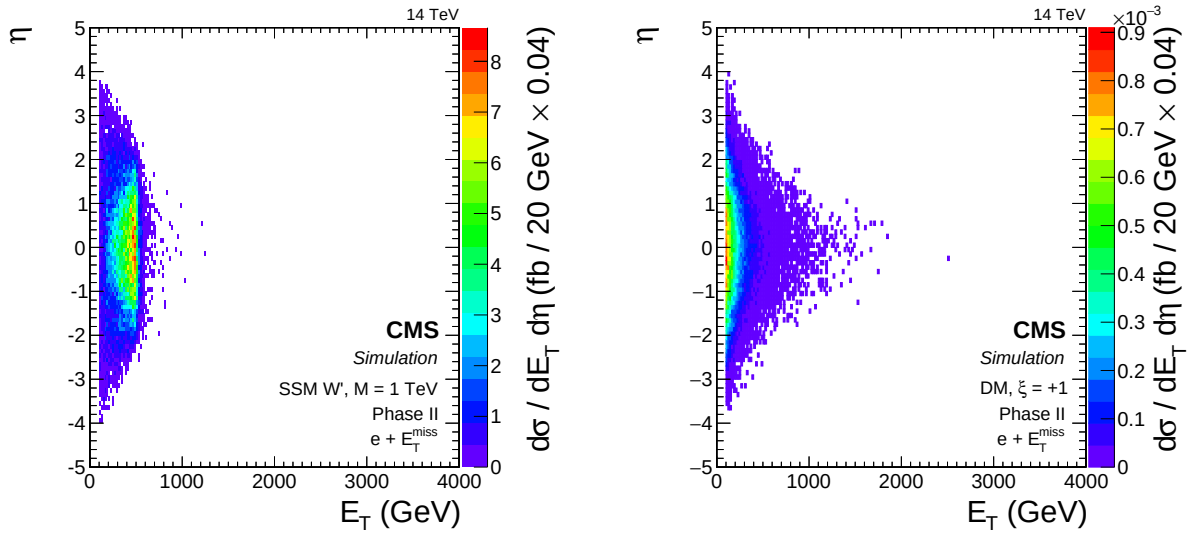

(a) SSM W′, $M_{W'} = 1\,\text{TeV}$

(b) DM, $\xi = +1$

Figure 7.14.: Histograms in the E_T–η plane for a 1 TeV SSM W′ sample and a dark matter sample with $\xi = +1$ in the electron channel. Although both samples are dominated by events with rather low lepton E_T, they hardly make use of the extended η range ($\eta > 2.5$) of the Phase II detector.

prove the sensitivity to low energy signals, which can include particles going into the forward direction.

8. Expected sensitivity of the HL-LHC with $\sqrt{s} = 14\,\text{TeV}$

To address the questions raised in the beginning of chapter 7, the potential of the HL-LHC must be examined. Based on the transverse mass distributions of the electron and muon channels, the expected discovery significances are extrapolated. Additionally, the possibilities of the HL-LHC run to distinguish between different new physics models is determined. This will be of major importance if a significant deviation from the standard model expectation is observed. For a comparison with other publications expected exclusion limits are determined.

8.1. Transverse mass distribution

The transverse mass distributions for the standard model background and selected signal scenarios are shown in figure 8.1 for the electron channel and in figure 8.2 for the muon channel. The left hand sides of both figures show the SSM W′ boson signals scaled to their corresponding cross sections. On the right hand sides, the dark matter and contact interaction models are shown. As described in section 2.2, the cross sections of those two models are not defined by the theory but depend on the free model parameter Λ. Therefore their signals are scaled to a cross section times branching ratio of 1 fb.

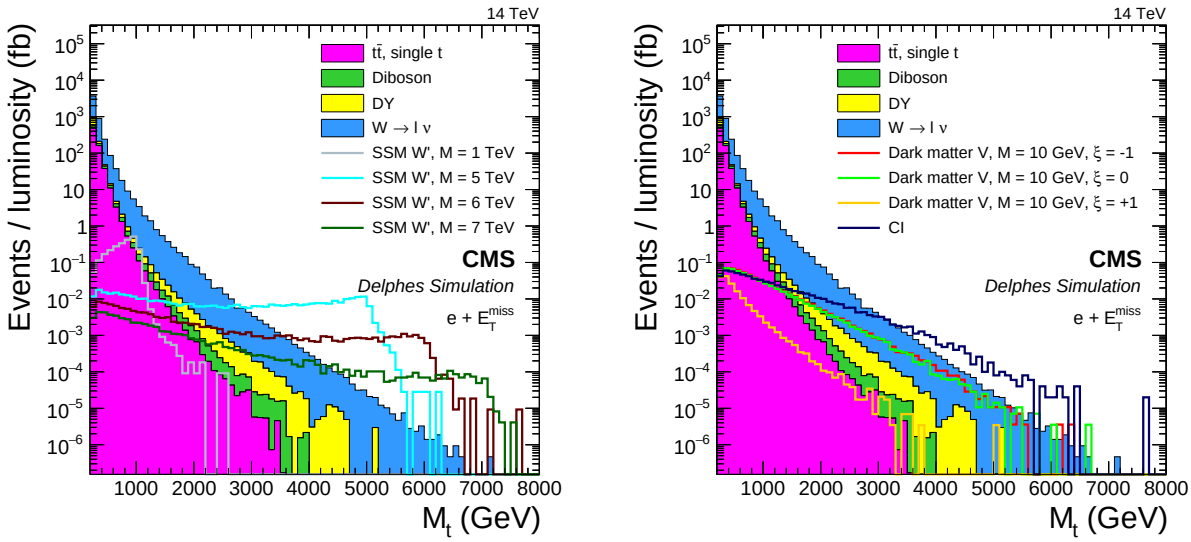

(a) Electron channel, SSM W′ boson signals

(b) Electron channel, DM and CI signals

Figure 8.1.: Expected transverse mass distribution at $\sqrt{s} = 14\,\text{TeV}$ for the standard model background and several signal scenarios in the electron channel.

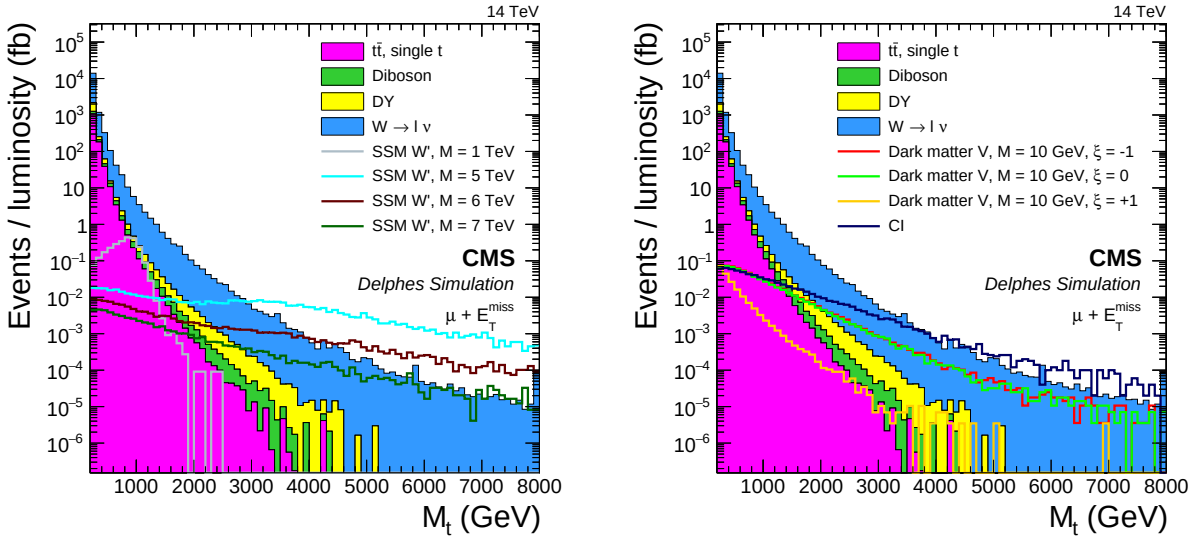

(a) Muon channel, SSM W′ boson signals

(b) Muon channel, DM and CI signals

Figure 8.2.: Expected transverse mass distribution at $\sqrt{s} = 14\,\text{TeV}$ for the standard model background and several signal scenarios in the muon channel.

The spectra show similar features as the $\sqrt{s} = 8\,\text{TeV}$ distributions. The dominant background originates from W boson production. The muon M_T spectrum is smeared at large energies because of the coarser resolution compared to the electron channel. This is especially visible for the three W′ boson signals with masses of 5, 6, and 7 TeV. The contact interaction and dark matter signals gradually decline with larger M_T and do not show any remarkable structures.

Because of the high luminosity accumulated during the HL-LHC run, signals with small cross sections become detectable. To visualize how these signal could actually look like, figure 8.3 show example distributions obtained from Poisson pseudo experiments based on the M_T distributions of figure 8.1. While the SSM W′ signals and the CI signal are visually distinguishable from the standard model, the dark matter limits appear very similar and are arguable compatible with the standard model distribution. This is especially due to the broad distributions of the signals, deploying many events in a region with large background contributions.

8.2. Discovery potential

The discovery potential for the different signal hypotheses is calculated as described in section 3.2 using pseudo experiments. Figure 8.4 shows the expected discovery confidence level as a function of the integrated luminosity for the individual electron and muon channels. Their combination is presented in figure 8.5. In the collider physics community, most often a significance of $5\,\sigma$ is considered as the threshold to claim a significant deviation from the expectation.

The electron channel is more sensitive than the muon channel because of its superior energy resolution. While in the electron channel the discovery of a SSM W′ boson with $M = 7\,\text{TeV}$ is still inside the scope of the HL-LHC, it is not in the muon channel. To discover a SSM W′ boson

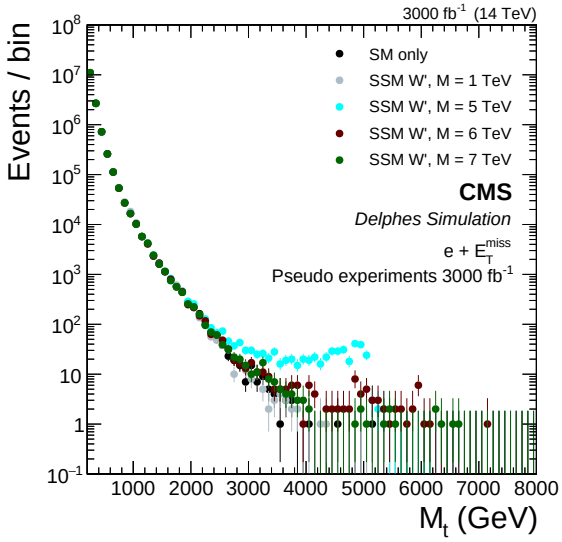

(a) SSM W′ boson signals.

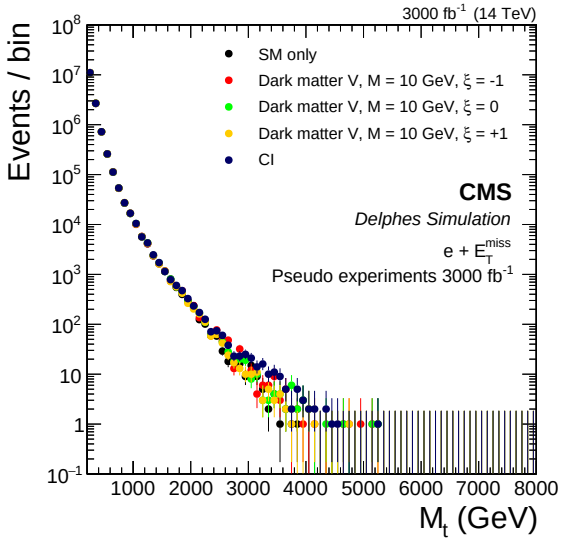

(b) DM and CI signals.

Figure 8.3.: Pseudo experiments of different signal scenarios, all combined with the background expectation at $\sqrt{s} = 14\,\text{TeV}$ for $3000\,\text{fb}^{-1}$.

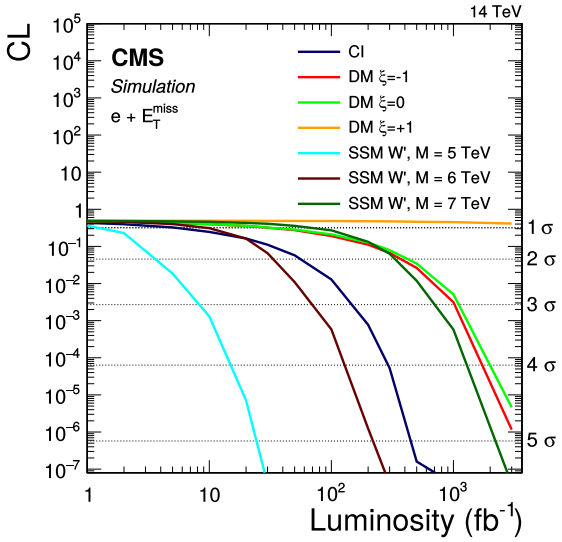

(a) Electron channel

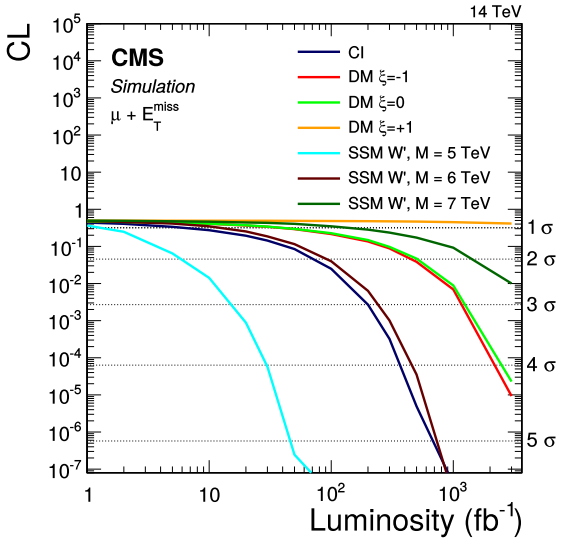

(b) Muon channel

Figure 8.4.: Discovery potential in the individual electron and muon channels of different BSM scenarios at $\sqrt{s} = 14\,\text{TeV}$ as a function of the integrated luminosity.

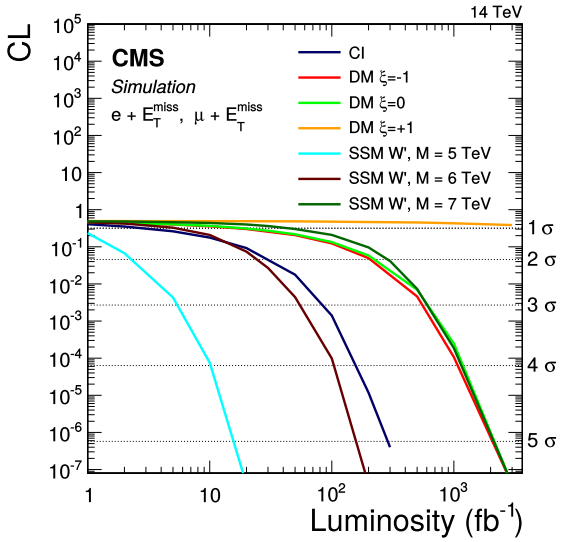

Figure 8.5.: Discovery potential for the combined channels of different BSM scenarios at $\sqrt{s} = 14\,\text{TeV}$ as a function of the integrated luminosity.

with such a significance, an integrated luminosity of $30\,\text{fb}^{-1}$ is required in case the boson has a mass of 5 TeV. For a 6 TeV W′ boson, about $300\,\text{fb}^{-1}$ have to be aggregated and for a 7 TeV W′ boson, nearly the total integrated luminosity planned for the HL-LHC of $3000\,\text{fb}^{-1}$ is necessary.

The HNC-CI model can be discovered after accumulating a luminosity of $300\,\text{fb}^{-1}$, while the dark matter models with $\xi = 0$ and $\xi = -1$ require around $2000\,\text{fb}^{-1}$. The dark matter model with $\xi = +1$ cannot be discovered by the HL-LHC when assuming a cross section times branching fraction of 1 fb, as the transverse mass of the events is usually low and therefore cannot be sufficiently distinguished from the large background contributions in that regime.

The $5\,\sigma$ discovery thresholds for all scenarios are listed in table 8.1. Studies determining the discovery potential of a W′ boson have been performed before [132, 133]. They yield similar results, e.g. they claim a $5\,\sigma$ discovery potential for a 6 TeV W′ boson with an integrated luminosity of $300\,\text{fb}^{-1}$ in the muon channel but with a more optimistic resolution assumption than the one used in this thesis.

8.2.1. SSM W′ with generalized couplings

As a benchmark point, the coupling of the W′ boson to fermions is often assumed to be the same as the coupling of the W boson to fermions. As explained in section 2.2.1 this assumption is not strongly motivated. The reweighting procedure described in section 5.6.2 is used to derive M_T distributions with different coupling strengths. By reweighting the events of a single DELPHES simulated sample per W′ boson mass, M_T distributions with varied coupling strength are determined. The event weights are determined from generated M_T distributions, reducing the required resources by not running the DELPHES detector simulation for each coupling strength.

The cross sections of a W′ boson with a small mass and a small coupling may be similar to that of a W′ boson with a larger mass and a large coupling strength. However, their signa-

Table 8.1.: Integrated luminosities required to claim a $5\,\sigma$ discovery for different BSM scenarios. The scenarios not discoverable with HL-LHC with $5\,\sigma$ are marked with a dash.

Scenario	Luminosity (fb^{-1}) Electron channel	Luminosity (fb^{-1}) Muon channel	Luminosity (fb^{-1}) Combined channels
SSM W′, $M = 5\,\mathrm{TeV}$	25	46	16
SSM W′, $M = 6\,\mathrm{TeV}$	220	530	160
SSM W′, $M = 7\,\mathrm{TeV}$	2300	—	2100
HNC-CI	450	680	290
Dark matter, $\xi = -1$	—	—	2100
Dark matter, $\xi = 0$	—	—	2100
Dark matter, $\xi = +1$	—	—	—

tures are quite distinct, as a small mass W′ boson predominantly produces events with small transverse masses. At small transverse masses, the background expectation is high and the W′ boson may be emitted more in forward direction. A high luminosity run can improve the discovery potential of such a small-mass small-coupling W′ boson.

Figure 8.6 shows the discovery thresholds of a SSM W′ boson in the individual electron and muon channels, figure 8.7 shows their combination. All thresholds are determined using the asymptotic method at a $5\,\sigma$ CL.

The excluded coupling strength increases exponentially with the boson mass. The mass exclusion limit at a fixed coupling of $g_{W'}/g_W = 1$ only slowly improves with increasing luminosity. A boson with a mass of 5 TeV requires about $30\,\mathrm{fb}^{-1}$, while the 6 TeV W′ boson requires about $300\,\mathrm{fb}^{-1}$. It appears that for each 1 TeV of mass exclusion improvement, the luminosity has to increase by an order of magnitude. For a fixed mass, the coupling strength exclusion limit improves (decreases) linearly with the gathered luminosity, as indicated by the equidistant lines for 30, 300 and $3000\,\mathrm{fb}^{-1}$ in the logarithmic scale of the coupling strength.

When combining both channels, a rather low mass W′ boson with a mass of 1 TeV can be excluded with a coupling strength of $g_{W'}/g_W = 0.043$ at $30\,\mathrm{fb}^{-1}$ and $g_{W'}/g_W = 0.014$ at $3000\,\mathrm{fb}^{-1}$.

8.3. Distinction potential

If the number of observed events deviates significantly from the standard model expectation, further examinations must be performed to determine which models are most compatible with the observation. These analyses may require even more accumulated data (integrated luminosity) than the actual discovery of the deviation. A distinction potential describing the amount of integrated luminosity required to favor one signal hypothesis over another can be determined as described in section 3.2.

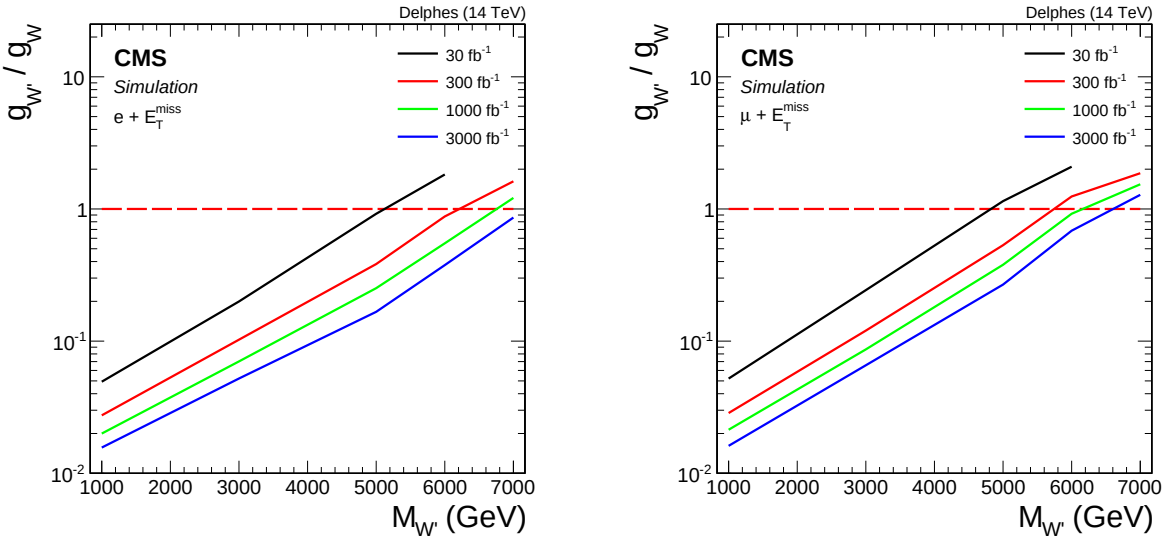

(a) Electron channel

(b) Muon channel

Figure 8.6.: Discovery potential for SSM W′ bosons with a significance of 5σ in the individual electron and muon channels. Each colored line shows the coupling vs. mass discovery threshold for a different integrated luminosity. The red dashed line corresponds to the W′ boson coupling being the same as the W boson coupling.

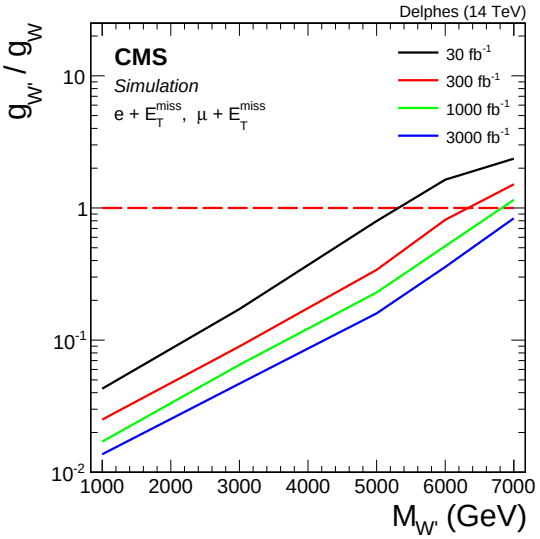

Figure 8.7.: Discovery potential for SSM W′ bosons with a significance of 5σ for the combination of the electron and muon channels. Each colored line shows the coupling vs. mass discovery threshold for a different integrated luminosity. The red dashed line corresponds to the W′ boson coupling being the same as the W boson coupling.

Instead of comparing a signal hypothesis to the standard model hypothesis, two different signal hypotheses are compared to each other. By comparing different mass hypothesis in the SSM model to each other, the achievable W′ mass resolution can be determined.

In the following the $M_{W'} = 6\,\text{TeV}$ signal hypothesis is studied. Comparing it to the standard model, resulted in an integrated luminosity of $160\,\text{fb}^{-1}$ to be detectable with a $5\,\sigma$ CL. Instead of the standard model, the signal hypothesis is compared to other W′ mass hypothesis to determine the resolution. As resolutions are usually provided in terms of the $1\,\sigma$ deviation, this threshold is used here as the distinction criterion between two mass hypotheses.

The significance for different mass hypotheses compared to the 6 TeV signal hypothesis is determined for each luminosity value. To find the mass value corresponding to a $1\,\sigma$ deviation, the significances of the different mass values is interpolating linearly. The result is presented in figure 8.8. Shown are the expected W′ mass resolution of a $M_{W'} = 6\,\text{TeV}$ W′ boson for the electron channel, muon channel, and their combination as a function of the integrated luminosity. For the combination of electron and muon channels, the expected mass resolution at the discovery threshold of $160\,\text{fb}^{-1}$ is around 200 GeV, and improves to around 20 GeV for a luminosity of $1000\,\text{fb}^{-1}$.

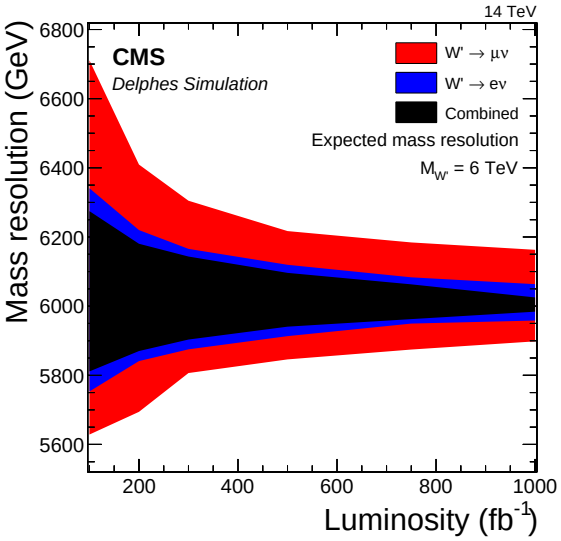

Figure 8.8.: Expected mass resolution of a 6 TeV W′ boson as a function of the integrated luminosity. The band shows the resolvable mass compared to the 6 TeV mass of the considered W′ boson.

Each plot of figure 8.9 corresponds to one test hypothesis specified in the caption of the plot. This hypothesis is compared to several different null hypotheses, as specified in the legend of the plot. Similar to the determination of the discovery potentials, the significance as a function of the acquired integrated luminosity is provided. The line marked as "standard model" corresponds to the discovery potential as described in section 8.2. The method is not invariant when commuting the two hypotheses. Discovering a DM $\xi = -1$ scenario over the CI scenario requires more luminosity than vice versa. However, the order of magnitude of the required luminosities for two commuting cases is comparable.

The DM $\xi = -1$ and $\xi = 0$ scenarios in figures 8.9a and 8.9b cannot be distinguished from each other, because they have the same signal distribution shape and are scaled to the same cross section. The $\xi = 0$ scenario is hardly distinguishable from the standard model at the chosen small cross section. To distinguish the HNC-CI model from the dark matter model ($\xi = -1, 0$) with, for instance, a confidence level of $2\,\sigma$, an integrated luminosity of $70\,\text{fb}^{-1}$ is required.

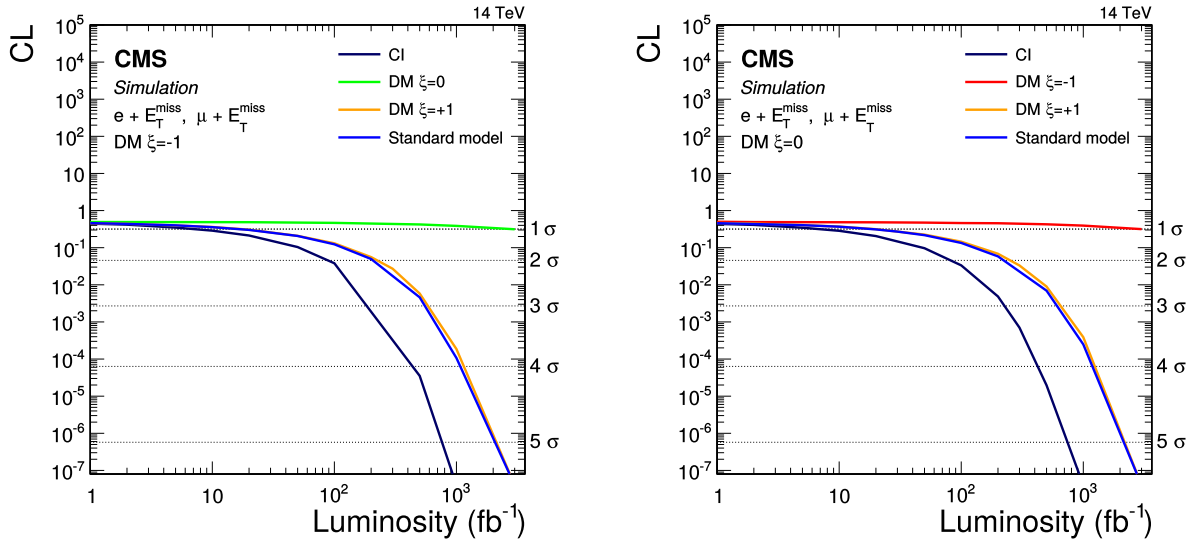

(a) DM, $\xi = -1$

(b) DM, $\xi = 0$

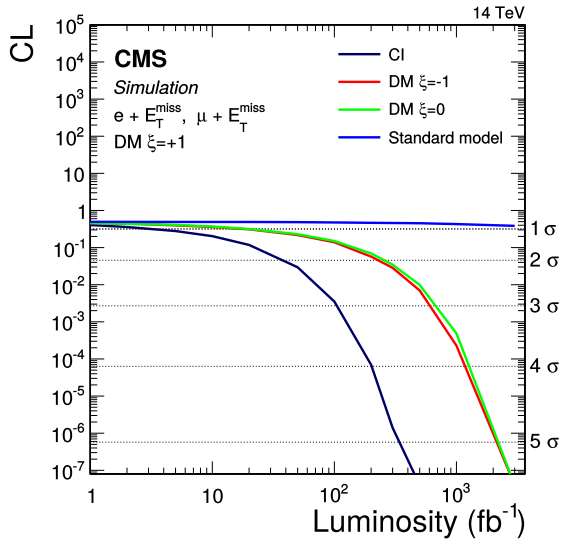

(c) DM, $\xi = +1$

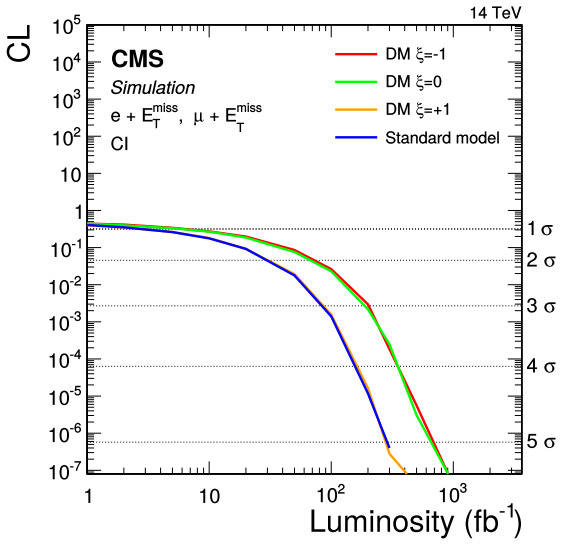

(d) HNC-CI

Figure 8.9.: Distinction potential of the dark matter and contact interaction scenarios to each other for the combination of the electron and muon channels. The different lines indicate different null hypotheses, to which the hypothesis named in the plot label is compared.

8.4. Expected exclusion limits

Considering the case where no strong evidence for new physics can be observed, a certain parameter space of the BSM models can be excluded. These exclusion limits also provide a good benchmark when comparing the HL-LHC sensitivity to the $\sqrt{s} = 7\,\text{TeV}$ and $\sqrt{s} = 8\,\text{TeV}$ runs as well as to the outcome of other experiments, such as the Tevatron experiments. All of these have published exclusion limits but not necessarily expected discovery significances. In this section, expected limits on the SSM W′ boson, the contact interaction model and the dark matter model are derived.

All limits are calculated at 95 % CL using the Bayesian method described in section 3.1.3.

8.4.1. SSM W′ limits

Figures 8.10 and 8.11 show the excluded cross section times branching fraction as a function of the integrated luminosity for W′ boson masses of 5 TeV, 6 TeV, and 7 TeV, together with the theoretically determined cross sections times branching fraction at LO. From the intersection points of those lines, the amount of integrated luminosity required to exclude the boson mass can be determined.

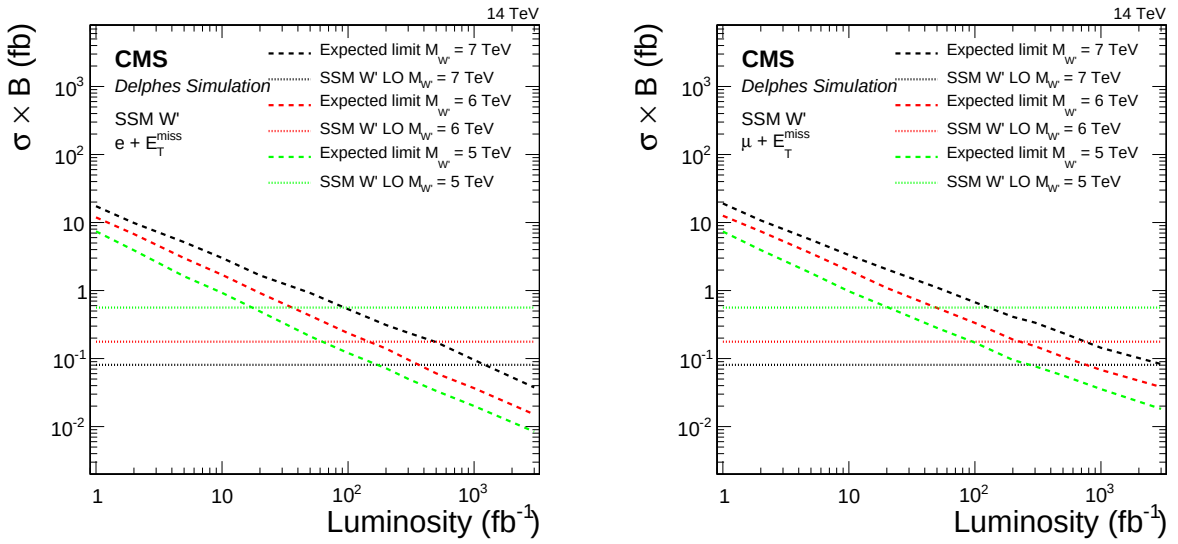

(a) Electron channel

(b) Muon channel

Figure 8.10.: Expected cross section limits of SSM W′ boson scenarios at $\sqrt{s} = 14\,\text{TeV}$ for the individual electron and muon channels.

To exclude a boson with $M_{\text{W}'} = 5\,\text{TeV}$ an integrated luminosity of $9.3\,\text{fb}^{-1}$ is required when combining electron and muon channel. For a mass of 6 TeV a luminosity of $86\,\text{fb}^{-1}$ and for 7 TeV a luminosity of $730\,\text{fb}^{-1}$ must be accumulated.

Figure 8.12 shows the expected SSM W′ limits as determined by different collaborations for their experiments, namely D0, CDF, ATLAS, and CMS. It visualizes the large improvement of the sensitivity when increasing the center-of-mass energy to 14 TeV and when accumulating

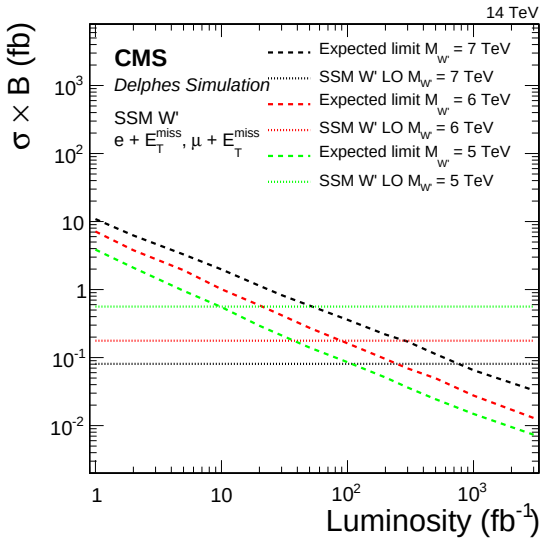

Figure 8.11.: Expected cross section limits of SSM W′ boson scenarios at $\sqrt{s} = 14\,\text{TeV}$ for the combination of the electron and muon channels.

more integrated luminosity, as it is planned for the HL-LHC. While the Tevatron experiments were sensitive in the 1 TeV regime, the LHC experiments improved the limits to around 3 TeV during their $\sqrt{s} = 8\,\text{TeV}$ runs. With the HL-LHC, the sensitivity is better than 7 TeV. Comparing the electron and muon channels of the three $\sqrt{s} = 14\,\text{TeV}$ mass points of 5, 6, and 7 TeV, the sensitivity of the muon declines with larger masses. The reason for this is the deteriorated muon momentum resolution at large p_T.

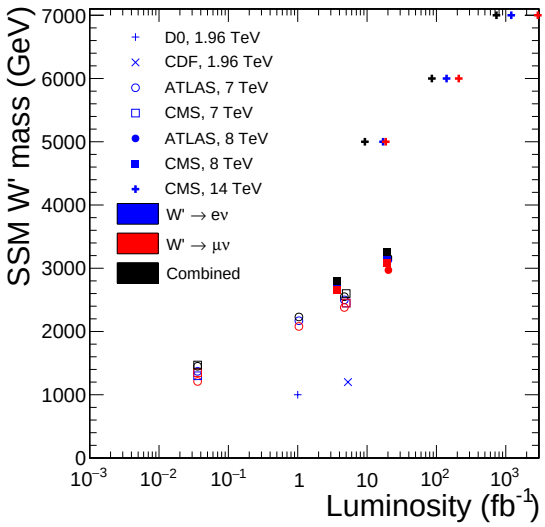

Figure 8.12.: Expected exclusion limits for a SSM W′ boson as determined by the D0, CDF, ATLAS, and CMS collaborations for center-of-mass energies of 1.96, 7, 8, and 14 TeV [2, 134–141].

8.4.2. Contact interaction limits

The limits on the interaction scale Λ of the HNC-CI model are presented in figures 8.13 and 8.14. For the individual electron channel, the full HL-LHC luminosity run yields an expected limit of 42 TeV, while for the muon channel, the exclusion limit is 40 TeV.

When combining both channels, the exclusion on Λ ranges from around 14 TeV for a luminosity of 1 fb^{-1} up to 44 TeV for the total HL-LHC luminosity of 3000 fb^{-1}. This compares to the $\sqrt{s} = 8$ TeV run result of $\Lambda = 13.6$ (expected). Therefore the $\sqrt{s} = 8$ TeV sensitivity is reached within the first collected fb of data in the $\sqrt{s} = 14$ TeV run.

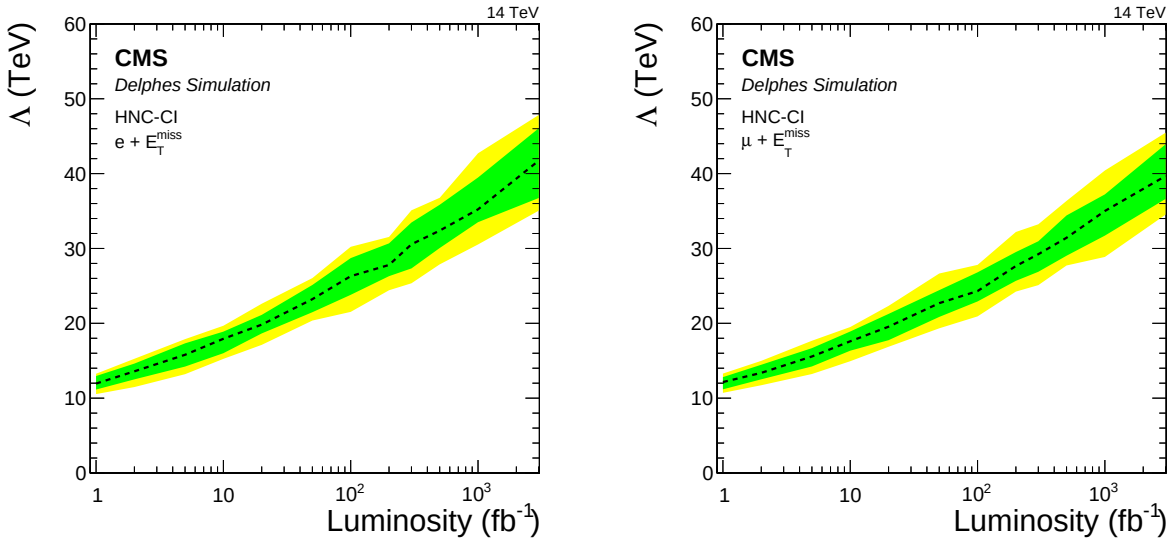

(a) Electron channel

(b) Muon channel

Figure 8.13.: Expected energy scale limits of the HNC-CI scenario at $\sqrt{s} = 14$ TeV for the individual electron and muon channels.

8.4.3. Dark matter limits

The limits on the dark matter model EFT scale for a low dark matter particle mass are shown in figures 8.15 and 8.16.

Considering the total HL-LHC luminosity of 3000 fb^{-1}, EFT scales of 4.9 TeV for $\xi = -1$, 3.5 TeV for $\xi = 0$, and 1.2 TeV for $\xi = +1$ can be excluded. The muon channel limits are slightly lower with 4.6 TeV for $\xi = -1$, 3.3 TeV for $\xi = 0$, and 1.1 TeV for $\xi = +1$. When combining the electron and muon channels the exclusion limit for the $\xi = -1$ scenario on the EFT scale is 5.1 TeV. For the $\xi = 0$ scenario a scale of 3.7 TeV and for $\xi = +1$ a scale of 1.2 TeV can be excluded. An overview of these limits together with their respective cross section times branching fraction values is listed in table 8.2.

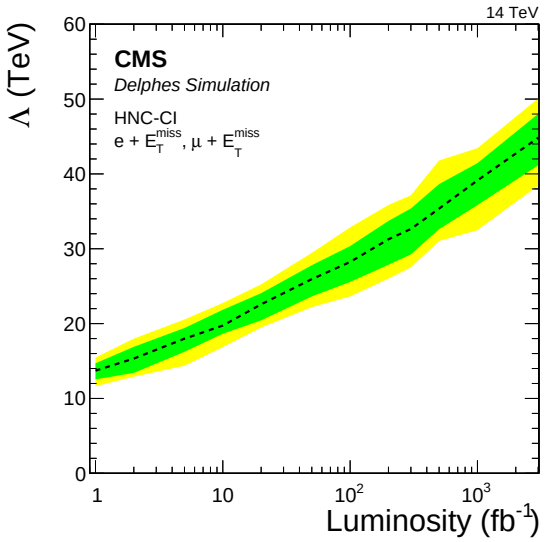

Figure 8.14.: Expected energy scale limits of the HNC-CI scenario at $\sqrt{s} = 14\,\text{TeV}$ for the combination of the electron and muon channels.

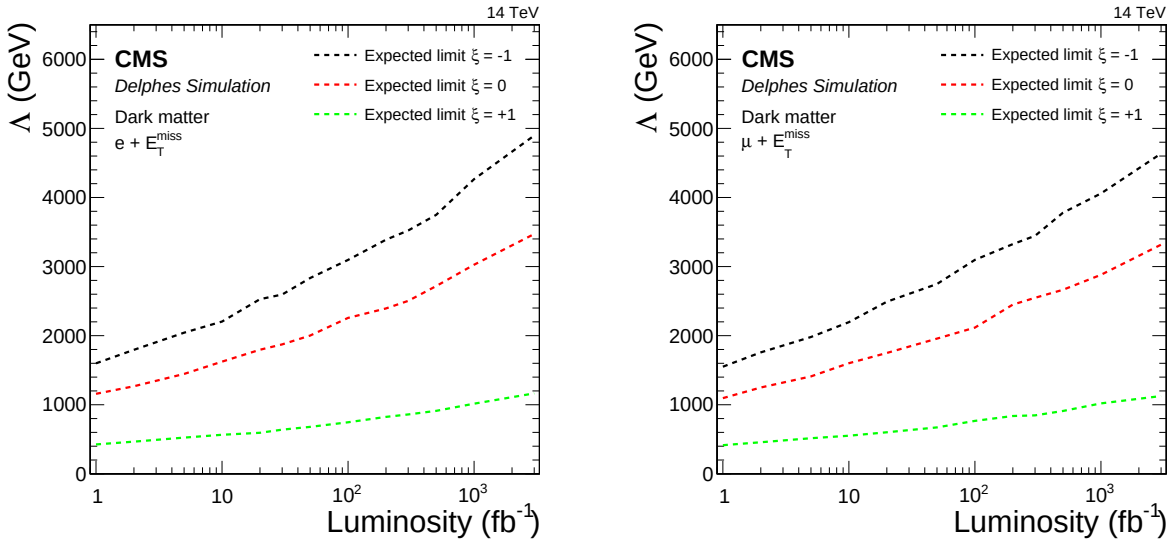

(a) Electron channel

(b) Muon channel

Figure 8.15.: Expected energy scale limits of the dark matter scenarios at $\sqrt{s} = 14\,\text{TeV}$ for the individual electron and muon channels.

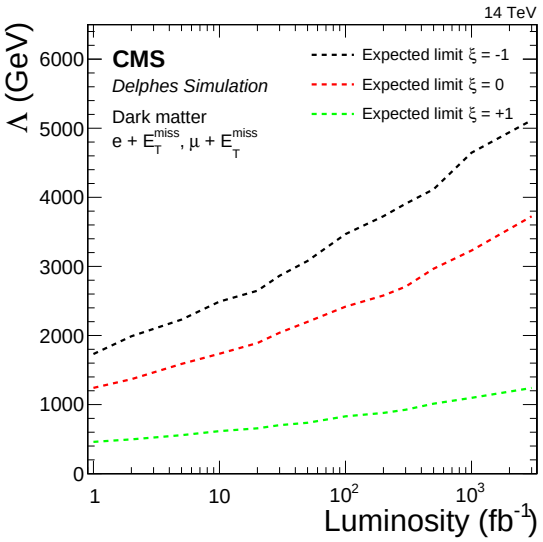

Figure 8.16.: Expected energy scale limits at 95 % CL of the dark matter scenarios at $\sqrt{s} = 14\,\text{TeV}$ for the combination of the electron and muon channels.

Table 8.2.: Expected exclusion limits at 95 % CL on cross section times branching fraction and EFT scale for the different dark matter scenarios at $\sqrt{s} = 14\,\text{TeV}$ and an integrated luminosity of $3000\,\text{fb}^{-1}$.

Channel	ξ	$\sigma \times \mathcal{B}$ (fb)	Λ (TeV)
Electron	-1	0.40	4.9
	0	0.42	3.5
	+1	8.6	1.2
Muon	-1	0.49	4.6
	0	0.50	3.3
	+1	9.8	1.1
Combined	-1	0.33	5.1
	0	0.32	3.7
	+1	6.7	1.2

8.5. Summary and Conclusion

The CMS experiment will be able to handle the challenges imposed by a HL-LHC run. The increase in pileup events is not expected to be a problem for the considered analysis of high-energy events. The aging of the detector due to radiation damage is faced by the Phase I and II upgrade programs. This will keep the decline of the identification efficiencies and the degradation of the energy resolution at a minimum and with that, the good sensitivity of the analysis will be conserved.

The HL-LHC run with $\sqrt{s} = 14\,\text{TeV}$ and $3000\,\text{fb}^{-1}$ will substantially improve the discovery range for the SSM W′, HNC-CI, and dark matter models in the $\ell + E_T^{\text{miss}}$ channels. New heavy gauge bosons in the SSM model can be discovered with masses larger than 7 TeV. The high luminosity also improves the sensitivity to low-mass small-coupling W′ bosons. In the HNC-CI model, a cross section times branching fraction of 1 fb can be discovered already with an accumulated luminosity of $300\,\text{fb}^{-1}$. The dark matter scenarios with $\xi = -1$ and $\xi = 0$ and the same cross section are in the reach of the HL-LHC.

If in the future a deviation of the data to the standard model expectation can be found, which is due to a new physic phenomenon, the more detailed analysis of the effect will benefit from the HL-LHC run. Telling apart different physics models can be even more challenging than identifying a non standard model effect. For example to claim a discovery of the HNC-CI signal over the dark matter $\xi = -1$ signal with the same cross section of 1 fb for both models, a luminosity of $700\,\text{fb}^{-1}$ is required, compared to $300\,\text{fb}^{-1}$ for the discovery over the standard model.

In case no deviation can be found, exclusion limits on the SSM W′ cross section, the contact interaction scale in the HNC-CI model and the effective field theory scale in the dark matter model can be determined. The HL-LHC will greatly improve the possible exclusion limits. As an example, for the HNC-CI model the limit on the interaction scale rises up to 44 TeV for $3000\,\text{fb}^{-1}$.

The HL-LHC program is very beneficial for the search for new physics in the lepton and missing transverse energy channel. It enables the CMS experiment to reach new frontiers and will add to the understanding of the high energy regime. If new physics in the multi-TeV regime exists, the HL-LHC run may be able to reveal it.

9. Summary and Conclusions

The $\ell + E_T^{\text{miss}}$ channel is a versatile final state when searching for beyond the standard model physics. While originally driven by the search for a new heavy gauge boson, the data is also interpreted in terms of other models, such as the contact interaction model and the dark matter model.

The collision events at $\sqrt{s} = 8\,\text{TeV}$ with an electron or a muon and missing transverse energy have been analyzed and no significant deviation from the standard model expectation has been found.

In the SSM new heavy charged gauge bosons up to a mass of 3.28 TeV have been excluded. A special emphasis has been made on the W′ boson and standard model W boson interference cases. For the first time, this effect has been considered in the $\ell + E_T^{\text{miss}}$ channel. As the features of negative and positive interference terms have been considered in the analysis strategy, a higher sensitivity in terms of the W′ mass could be reached for the SSMS/SSMO models than for the standard SSM case. Additionally, the coupling strength has been considered in these models, providing results for a broader spectrum of possible W′ boson scenarios. Considering the standard model coupling strength $g_{W'}/g_W = 1$, W′ bosons with a mass up to 4.00 TeV in the SSMS case and up to 3.71 TeV in the SSMO case have been excluded.

Limits on the bulk mass parameter μ and the extra dimension radius R in the sUED model have been determined as reinterpretations of the SSM and SSMS models. Helicity nonconserving contact interaction with scales lower than 12.4 TeV have been excluded. In the dark matter EFT model, scales of around 1 TeV have been excluded for the $\xi = -1$ case for small dark matter masses. The other coupling configurations $\xi = 0$ and $\xi = +1$ have also been examined¡.

The LHC era is still ongoing and is expected to continue for at least another decade. It is very important to have exact predictions about the future sensitivity of the experiment for promising scenarios of new physics. Based on these studies, analysis strategies are developed and funding decisions are made. The sensitivity studies made in this analysis have been included in the technical proposal for the HL-LHC run [6].

For a center-of-mass energy of 14 TeV, the W′ in the SSM, the HNC contact interaction model, and the EFT dark matter model have been examined. The sensitivity is greatly improved with $\sqrt{s} = 14\,\text{TeV}$ compared to $\sqrt{s} = 8\,\text{TeV}$. A SSM W′ boson with a mass 7 TeV is within the scope of the HL-LHC.

Although the attention has mainly shifted towards other models such as the dark matter interpretation and the SSMS/SSMO models, the SSM W′ interpretation remains an important benchmark test. The long history of this interpretation provides a timeline of the sensitivity of the $\ell + E_T^{\text{miss}}$ channel. Figure 9.1 shows the expected exclusion limits of several past analyses together with the $\sqrt{s} = 8\,\text{TeV}$ analysis and the $\sqrt{s} = 14\,\text{TeV}$ extrapolations presented in this thesis. It demonstrates the improvement in sensitivity of the channel from the Tevatron exper-

iments to the $\sqrt{s} = 7\,\text{TeV}$ and $\sqrt{s} = 8\,\text{TeV}$ runs of the LHC and projects it to the future of the HL-LHC.

However, as long as we don't find evidence for new physics, we do not know whether it is just around the corner, requires $3000\,\text{fb}^{-1}$ of luminosity to be found, is out of scope of the HL-LHC, or does not exist at all.

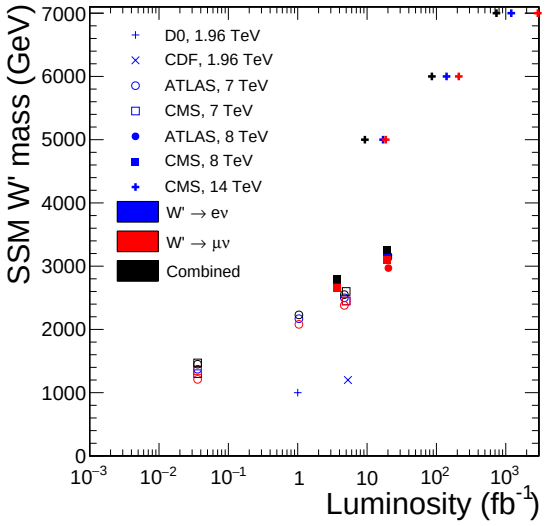

Figure 9.1.: Expected exclusion limits for a SSM W′ boson as determined by the D0, CDF, ATLAS, and CMS collaborations for center-of-mass energies of 1.96, 7, 8, and 14 TeV [2, 134–141]. Same as figure 8.12.

A. Monte Carlo Samples

A.1. Background samples 8 TeV

Table A.1.: Background samples as used in the electron channel analysis [3]. The cross sections are provided as calculated by the generator (LO for PYTHIA and MADGRAPH, NLO for POWHEG and MCATNLO), the influence of higher order corrections is described by a K-factor. The generator constrains in the column "Subsample" are specified without units, meant is always GeV.

Process	Generator	Subsample	cross section (pb)	K-factor
$W \to e\nu$	PYTHIA		9.14×10^3	NLO (section 5.5.2)
$W \to e\nu$	PYTHIA	$100 < \hat{p_T} < 500$	1.46	NLO (section 5.5.2)
$W \to e\nu$	PYTHIA	$\hat{p_T} > 500$	1.53×10^{-3}	NLO (section 5.5.2)
$W \to \tau\nu$	PYTHIA		9.17×10^3	NLO (section 5.5.2)
$W \to \tau\nu$	PYTHIA	$100 < \hat{p_T} < 500$	1.46	NLO (section 5.5.2)
$W \to \tau\nu$	PYTHIA	$\hat{p_T} > 500$	1.53×10^{-3}	NLO (section 5.5.2)
QCD EM enriched	PYTHIA	$30 < \hat{p_T} < 80$	4.62×10^6	
QCD EM enriched	PYTHIA	$80 < \hat{p_T} < 170$	1.83×10^5	
QCD EM enriched	PYTHIA	$170 < \hat{p_T} < 250$	4.59×10^3	
QCD EM enriched	PYTHIA	$250 < \hat{p_T} < 350$	5.57×10^2	
QCD EM enriched	PYTHIA	$\hat{p_T} > 350$	8.91×10^1	
$t\bar{t}$	MCATNLO		2.11×10^2	1.16 (NNLO)
$t \to b\ell\nu$ (s-Channel)	POWHEG		2.82	1.34 (NNLO)
$t \to b\ell\nu$ (t-Channel)	POWHEG		4.70×10^1	1.2 (NNLO)
$t \to b\ell\nu$ (tW-Channel)	POWHEG		1.07×10^1	1.04 (NNLO)
$\bar{t} \to b\ell\nu$ (s-Channel)	POWHEG		1.57	1.12 (NNLO)
$\bar{t} \to b\ell\nu$ (t-Channel)	POWHEG		2.50×10^1	1.23 (NNLO)
$\bar{t} \to b\ell\nu$ (tW-Channel)	POWHEG		1.07×10^1	1.04 (NNLO)
$Z \to ee$	POWHEG	$m_{ee} > 20$	1.87×10^3	1.02 (NNLO)

$Z \to ee$	POWHEG	$m_{ee} > 120$	1.19×10^{1}	1.02 (NNLO)
$Z \to ee$	POWHEG	$m_{ee} > 200$	1.48	1.03 (NNLO)
$Z \to ee$	POWHEG	$m_{ee} > 400$	1.09×10^{-1}	1.02 (NNLO)
$Z \to ee$	POWHEG	$m_{ee} > 500$	4.41×10^{-2}	1.02 (NNLO)
$Z \to ee$	POWHEG	$m_{ee} > 700$	1.03×10^{-2}	1.02 (NNLO)
$Z \to ee$	POWHEG	$m_{ee} > 800$	5.49×10^{-3}	1.02 (NNLO)
$Z \to ee$	POWHEG	$m_{ee} > 1000$	1.80×10^{-3}	1.02 (NNLO)
$Z \to ee$	POWHEG	$m_{ee} > 1500$	1.71×10^{-4}	1.02 (NNLO)
$Z \to ee$	POWHEG	$m_{ee} > 2000$	2.21×10^{-5}	1.02 (NNLO)
$Z \to \tau\tau$	PYTHIA	$m_{\tau\tau} > 20$	1.51×10^{3}	1.27 (NNLO)
$Z \to \tau\tau$	PYTHIA	$100 < m_{\tau\tau} < 200$	3.49×10^{1}	1.27 (NNLO)
$Z \to \tau\tau$	PYTHIA	$200 < m_{\tau\tau} < 400$	1.18	1.27 (NNLO)
$Z \to \tau\tau$	PYTHIA	$400 < m_{\tau\tau} < 800$	8.70×10^{-2}	1.27 (NNLO)
$Z \to \tau\tau$	PYTHIA	$m_{\tau\tau} > 800$	4.50×10^{-3}	1.27 (NNLO)
$\gamma +$ jets	PYTHIA	$80 < \hat{p_T} < 120$	5.58×10^{2}	1.3 (measured)
$\gamma +$ jets	PYTHIA	$120 < \hat{p_T} < 170$	1.08×10^{2}	1.3 (measured)
$\gamma +$ jets	PYTHIA	$170 < \hat{p_T} < 300$	3.01×10^{1}	1.3 (measured)
$\gamma +$ jets	PYTHIA	$300 < \hat{p_T} < 470$	2.14	1.3 (measured)
$\gamma +$ jets	PYTHIA	$470 < \hat{p_T} < 800$	2.12×10^{-1}	1.3 (measured)
$\gamma +$ jets	PYTHIA	$800 < \hat{p_T} < 1400$	7.08×10^{-3}	1.3 (measured)
$\gamma +$ jets	PYTHIA	$1400 < \hat{p_T} < 1800$	4.51×10^{-5}	1.3 (measured)
$\gamma +$ jets	PYTHIA	$\hat{p_T} > 1800$	1.87×10^{-6}	1.3 (measured)
WW	PYTHIA		3.36×10^{1}	1.63 (NLO)
WW	PYTHIA	$\hat{p_T} > 500$	5.24×10^{-3}	1.63 (NLO)
WZ	PYTHIA		1.26×10^{1}	2.63 (NLO)
WZ	PYTHIA	$\hat{p_T} > 500$	1.70×10^{-3}	2.56 (NLO)
ZZ	PYTHIA		5.20	3.4 (NLO)
ZZ	PYTHIA	$\hat{p_T} > 500$	1.07×10^{-3}	1.6 (NLO)

Table A.2.: Background samples as used in the muon channel analysis [4]. The cross sections are provided as calculated by the generator (LO for PYTHIA and MADGRAPH, NLO for POWHEG and MCATNLO), the influence of higher order corrections is described by a K-factor. The generator constrains in the column "Subsample" are specified without units, meant is always GeV.

Process	Generator	Subsample	cross section (pb)	K-factor
$W \to \mu\nu$	PYTHIA		9.13×10^3	NLO (section 5.5.2)
$W \to \mu\nu$	PYTHIA	$500 > \hat{p_T} > 100$	1.46	NLO (section 5.5.2)
$W \to \mu\nu$	PYTHIA	$\hat{p_T} > 500$	1.53×10^{-3}	NLO (section 5.5.2)
$W \to \tau\nu$	PYTHIA		9.13×10^3	NLO (section 5.5.2)
$W \to \tau\nu$	PYTHIA	$500 > \hat{p_T} > 100$	1.46	NLO (section 5.5.2)
$W \to \tau\nu$	PYTHIA	$\hat{p_T} > 500$	1.53×10^{-3}	NLO (section 5.5.2)
$Z \to \mu\mu$	POWHEG	$m_{\mu\mu} > 20$	1.87×10^3	1.02 (NNLO)
$Z \to \mu\mu$	POWHEG	$m_{\mu\mu} > 120$	1.19×10^1	1.02 (NNLO)
$Z \to \mu\mu$	POWHEG	$m_{\mu\mu} > 200$	1.49	1.02 (NNLO)
$Z \to \mu\mu$	POWHEG	$m_{\mu\mu} > 400$	1.09×10^{-1}	1.02 (NNLO)
$Z \to \mu\mu$	POWHEG	$m_{\mu\mu} > 500$	4.42×10^{-2}	1.02 (NNLO)
$Z \to \mu\mu$	POWHEG	$m_{\mu\mu} > 700$	1.02×10^{-2}	1.02 (NNLO)
$Z \to \mu\mu$	POWHEG	$m_{\mu\mu} > 800$	5.49×10^{-3}	1.02 (NNLO)
$Z \to \mu\mu$	POWHEG	$m_{\mu\mu} > 1000$	1.80×10^{-3}	1.02 (NNLO)
$Z \to \mu\mu$	POWHEG	$m_{\mu\mu} > 1500$	1.71×10^{-4}	1.02 (NNLO)
$Z \to \mu\mu$	POWHEG	$m_{\mu\mu} > 2000$	2.21×10^{-5}	1.02 (NNLO)
$Z \to \tau\tau$	PYTHIA	$m_{\tau\tau} > 20$	1.51×10^3	1.27 (NNLO)
$Z \to \tau\tau$	PYTHIA	$200 > m_{\tau\tau} > 100$	3.49×10^1	1.27 (NNLO)
$Z \to \tau\tau$	PYTHIA	$400 > m_{\tau\tau} > 200$	1.18	1.27 (NNLO)
$Z \to \tau\tau$	PYTHIA	$800 > m_{\tau\tau} > 400$	8.70×10^{-2}	1.27 (NNLO)
$Z \to \tau\tau$	PYTHIA	$m_{\tau\tau} > 800$	4.50×10^{-3}	1.27 (NNLO)
$t\bar{t}$	MCATNLO		2.11×10^2	1.16 (NNLO)
$t \to b\ell\nu$ (s-Channel)	POWHEG		2.82	1.38 (NNLO)
$t \to b\ell\nu$ (t-Channel)	POWHEG		4.70×10^1	1.18 (NNLO)
$t \to b\ell\nu$ (tW-Channel)	POWHEG		1.07×10^1	1.04 (NNLO)
$\bar{t} \to b\ell\nu$ (s-Channel)	POWHEG		1.57	1.12 (NNLO)

$\bar{t} \to b\ell\nu$ (t-Channel)	POWHEG		2.50×10^1	1.23 (NNLO)
$\bar{t} \to b\ell\nu$ (tW-Channel)	POWHEG		1.07×10^1	1.04 (NNLO)
WW	PYTHIA		3.36×10^1	1.67 (NLO)
WZ	PYTHIA		1.26×10^1	2.56 (NLO)
ZZ	PYTHIA		5.20	1.59 (NLO)
WW	PYTHIA	$\hat{p_T} > 500$	5.24×10^{-3}	1.67 (NLO)
WZ	PYTHIA	$\hat{p_T} > 500$	1.70×10^{-3}	2.56 (NLO)
ZZ	PYTHIA	$\hat{p_T} > 500$	1.07×10^{-3}	1.59 (NLO)
QCD μ enriched	PYTHIA	$\hat{p_T} > 20$	1.35×10^5	
QCD μ enriched	PYTHIA	$30 > \hat{p_T} > 20$	1.87×10^6	
QCD μ enriched	PYTHIA	$50 > \hat{p_T} > 30$	8.06×10^5	
QCD μ enriched	PYTHIA	$80 > \hat{p_T} > 50$	1.76×10^5	
QCD μ enriched	PYTHIA	$120 > \hat{p_T} > 80$	4.04×10^4	
QCD μ enriched	PYTHIA	$170 > \hat{p_T} > 120$	7.46×10^3	
QCD μ enriched	PYTHIA	$300 > \hat{p_T} > 170$	2.30×10^3	
QCD μ enriched	PYTHIA	$470 > \hat{p_T} > 300$	1.52×10^2	
QCD μ enriched	PYTHIA	$600 > \hat{p_T} > 470$	1.18×10^1	
QCD μ enriched	PYTHIA	$800 > \hat{p_T} > 600$	2.69	
QCD μ enriched	PYTHIA	$1000 > \hat{p_T} > 800$	3.69×10^{-1}	
QCD μ enriched	PYTHIA	$\hat{p_T} > 1000$	8.49×10^{-2}	

A.2. Signal samples 8 TeV

Table A.3.: SSM W′ boson samples.

Mass (GeV)	Cross section LO $\times$ $\mathcal{B}$ (pb)	QCD NNLO K-factor	relative PDF uncertainty
300	1.14×10^2	1.35	2.19×10^{-2}
500	1.65×10^1	1.363	2.63×10^{-2}
700	4.28	1.351	3.07×10^{-2}
900	1.47	1.347	3.45×10^{-2}
1100	5.88×10^{-1}	1.331	3.77×10^{-2}

1300	2.59×10^{-1}	1.317	4.10×10^{-2}
1500	1.19×10^{-1}	1.293	4.22×10^{-2}
1700	5.78×10^{-2}	1.257	4.58×10^{-2}
1900	2.96×10^{-2}	1.23	4.85×10^{-2}
2000	2.12×10^{-2}	1.214	4.98×10^{-2}
2100	1.55×10^{-2}	1.199	5.05×10^{-2}
2200	1.13×10^{-2}	1.194	5.26×10^{-2}
2300	8.39×10^{-3}	1.172	5.20×10^{-2}
2400	6.22×10^{-3}	1.164	5.29×10^{-2}
2500	4.73×10^{-3}	1.14	5.50×10^{-2}
2600	3.57×10^{-3}	1.152	5.65×10^{-2}
2700	2.69×10^{-3}	1.153	5.64×10^{-2}
2800	2.10×10^{-3}	1.145	5.47×10^{-2}
2900	1.65×10^{-3}	1.148	5.53×10^{-2}
3000	1.32×10^{-3}	1.151	5.69×10^{-2}
3100	1.06×10^{-3}	1.178	5.14×10^{-2}
3200	8.69×10^{-4}	1.187	6.08×10^{-2}
3300	7.07×10^{-4}	1.207	5.47×10^{-2}
3400	5.97×10^{-4}	1.22	5.80×10^{-2}
3500	5.07×10^{-4}	1.242	5.50×10^{-2}
3700	3.69×10^{-4}	1.278	4.84×10^{-2}
4000	2.51×10^{-4}	1.331	3.72×10^{-2}

Table A.4.: List of all samples considered in the SSMS and SSMO W′ boson analysis together with their respective cross sections. Each sample is split into three bins of the lepton momentum to ensure a sufficient number of simulated events in each M_T bin.

Mass (GeV)	$p_t^{\min}(\ell)$	$p_t^{\max}(\ell)$	SSMS cross section LO (pb)	SSMO cross section LO (pb)
600	100	300	7.18	9.38
600	300	600	7.24×10^{-1}	4.69×10^{-1}
600	600	∞	2.61×10^{-3}	2.38×10^{-5}
800	100	300	1.92	3.01

800	300	600	1.34	1.36
800	600	∞	3.21×10^{-3}	1.17×10^{-4}
1000	250	500	7.41×10^{-5}	7.68×10^{-1}
1000	500	1000	6.29×10^{-1}	5.08×10^{-2}
1000	1000	∞	9.46×10^{-2}	8.36×10^{-7}
1200	250	500	8.39×10^{-5}	2.45×10^{-1}
1200	500	1000	1.57×10^{-1}	1.59×10^{-1}
1200	1000	∞	7.53×10^{-2}	2.21×10^{-6}
1400	250	500	1.01×10^{-4}	1.20×10^{-1}
1400	500	1000	6.32×10^{-2}	1.01×10^{-1}
1400	1000	∞	1.61×10^{-1}	5.75×10^{-6}
1600	250	500	3.80×10^{-2}	7.75×10^{-2}
1600	500	1000	5.02×10^{-2}	5.73×10^{-2}
1600	1000	∞	1.33×10^{-4}	1.60×10^{-5}
1800	250	500	3.12×10^{-2}	6.04×10^{-2}
1800	500	1000	2.59×10^{-2}	3.21×10^{-2}
1800	1000	∞	2.23×10^{-4}	5.80×10^{-5}
2000	250	500	3.00×10^{-2}	5.24×10^{-2}
2000	500	1000	1.23×10^{-2}	1.75×10^{-2}
2000	1000	∞	1.21×10^{-3}	8.88×10^{-4}
2200	250	500	3.04×10^{-2}	4.83×10^{-2}
2200	500	1000	4.62×10^{-3}	8.51×10^{-3}
2200	1000	∞	2.55×10^{-3}	2.48×10^{-3}
2400	250	500	3.12×10^{-2}	4.58×10^{-2}
2400	500	1000	2.20×10^{-3}	5.14×10^{-3}
2400	1000	∞	1.76×10^{-3}	1.84×10^{-3}
2500	250	500	3.16×10^{-2}	4.48×10^{-2}
2500	500	1000	1.67×10^{-3}	4.25×10^{-3}
2500	1000	∞	1.36×10^{-3}	1.47×10^{-3}

2600	250	500	3.20×10^{-2}	4.42×10^{-2}
2600	500	1000	1.35×10^{-3}	3.63×10^{-3}
2600	1000	∞	1.03×10^{-3}	1.15×10^{-3}
2800	250	500	3.27×10^{-2}	4.30×10^{-2}
2800	500	1000	1.06×10^{-3}	2.90×10^{-3}
2800	1000	∞	5.66×10^{-4}	6.80×10^{-4}
3000	250	500	3.34×10^{-2}	4.22×10^{-2}
3000	500	1000	9.85×10^{-4}	2.51×10^{-3}
3000	1000	∞	2.97×10^{-4}	3.94×10^{-4}
3200	250	500	3.39×10^{-2}	4.16×10^{-2}
3200	500	1000	9.92×10^{-4}	2.28×10^{-3}
3200	1000	∞	1.51×10^{-4}	2.30×10^{-4}
3600	250	500	3.47×10^{-2}	4.06×10^{-2}
3600	500	1000	1.07×10^{-3}	2.02×10^{-3}
3600	1000	∞	3.75×10^{-5}	8.91×10^{-5}
4000	250	500	3.52×10^{-2}	4.00×10^{-2}
4000	500	1000	1.15×10^{-3}	1.89×10^{-3}
4000	1000	∞	1.12×10^{-5}	4.66×10^{-5}

Table A.5.: List of samples for the dark matter model analysis. The cross section are calculated at LO with MADGRAPH.

Mass (GeV)	Axial-vector coupling cross section (pb)	Vector coupling cross section (pb)
1	1.10×10^{-1}	1.12×10^{-1}
3	1.12×10^{-1}	1.12×10^{-1}
5	1.11×10^{-1}	1.12×10^{-1}
10	1.12×10^{-1}	1.12×10^{-1}
50	1.12×10^{-1}	1.06×10^{-1}
100	1.07×10^{-1}	9.32×10^{-2}
300	7.16×10^{-2}	4.30×10^{-2}

500	3.77×10^{-2}	1.68×10^{-2}
1000	4.20×10^{-3}	1.03×10^{-3}
1500	2.29×10^{-4}	3.46×10^{-5}
2000	5.61×10^{-6}	5.67×10^{-7}

B. Delphes parameterizations

In this appendix, the efficiency and resolution parameterizations used for the Delphes simulation of electron and muons are listed [142]. They depend on the pseudorapidity η (labeled eta), the electron energy (energy), and the muon transverse momentum (pt). Energy and pt are provided in units of GeV.

B.1. Phase I original

Listing B.1: Phase I original electron efficiency

```
(pt <= 4.0) * (0.00) +
(abs(eta) <= 1.45 ) * (pt > 4.0 && pt <= 6.0) * (0.50) +
(abs(eta) <= 1.45 ) * (pt > 6.0 && pt <= 8.0) * (0.70) +
(abs(eta) <= 1.45 ) * (pt > 8.0 && pt <= 10.0) * (0.85) +
(abs(eta) <= 1.45 ) * (pt > 10.0 && pt <= 30.0) * (0.94) +
(abs(eta) <= 1.45 ) * (pt > 30.0 && pt <= 50.0) * (0.97) +
(abs(eta) <= 1.45 ) * (pt > 50.0 && pt <= 70.0) * (0.98) +
(abs(eta) <= 1.45 ) * (pt > 70.0 ) * (1.0) +
(abs(eta) > 1.45 && abs(eta) <= 1.55) * (pt > 4.0 && pt <= 10.0) * (0.35) +
(abs(eta) > 1.45 && abs(eta) <= 1.55) * (pt > 10.0 && pt <= 30.0) * (0.40) +
(abs(eta) > 1.45 && abs(eta) <= 1.55) * (pt > 30.0 && pt <= 70.0) * (0.45) +
(abs(eta) > 1.45 && abs(eta) <= 1.55) * (pt > 70.0 ) * (0.45) +
(abs(eta) >= 1.55 && abs(eta) <= 2.0 ) * (pt > 4.0 && pt <= 10.0) * (0.75) +
(abs(eta) >= 1.55 && abs(eta) <= 2.0 ) * (pt > 10.0 && pt <= 30.0) * (0.85) +
(abs(eta) >= 1.55 && abs(eta) <= 2.0 ) * (pt > 30.0 && pt <= 50.0) * (0.95) +
(abs(eta) >= 1.55 && abs(eta) <= 2.0 ) * (pt > 50.0 && pt <= 70.0) * (0.95) +
(abs(eta) >= 1.55 && abs(eta) <= 2.0 ) * (pt > 70.0 ) * (1.0) +
(abs(eta) >= 2.0 && abs(eta) <= 2.5 ) * (pt > 4.0 && pt <= 10.0) * (0.65) +
(abs(eta) >= 2.0 && abs(eta) <= 2.5 ) * (pt > 10.0 && pt <= 30.0) * (0.75) +
(abs(eta) >= 2.0 && abs(eta) <= 2.5 ) * (pt > 30.0 && pt <= 50.0) * (0.85) +
(abs(eta) >= 2.0 && abs(eta) <= 2.5 ) * (pt > 50.0 && pt <= 70.0) * (0.85) +
(abs(eta) >= 2.0 && abs(eta) <= 2.5 ) * (pt > 70.0 ) * (0.85) +
(abs(eta) > 2.5) * (0.00)
```

Listing B.2: Phase I original electron energy resolution

```
(abs(eta) <= 2.5) * (energy > 0.1 && energy <= 2.5e1) * (energy*0.015) +
(abs(eta) <= 2.5) * (energy > 2.5e1) * sqrt(energy^2*0.005^2 + energy*0.027^2
    + 0.15^2) +
(abs(eta) > 2.5 && abs(eta) <= 3.0) * sqrt(energy^2*0.005^2 + energy*0.027^2 +
     0.15^2) +
(abs(eta) > 3.0 && abs(eta) <= 5.0) * sqrt(energy^2*0.08^2 + energy*1.97^2)
```

Listing B.3: Phase I original muon efficiency

```
(pt <= 2.0) * (0.00) +
(abs(eta) <= 2.40) * (pt > 2.0 && pt <= 3.0) * (0.51) +
(abs(eta) <= 2.40) * (pt > 3.0 && pt <= 4.0) * (0.85) +
(abs(eta) <= 2.40) * (pt > 4.0 && pt <= 11.0) * (0.93) + \
(abs(eta) <= 2.40) * (pt > 11. && pt <= 50.) * (0.96) + \
(abs(eta) <= 2.40) * (pt > 50. && pt <= 70.) * (0.98) + \
(abs(eta) <= 2.40) * (pt > 70.0 ) * (1.00) + \
(abs(eta) > 2.40) * (0.00)}
```

Listing B.4: Phase I original muon momentum resolution

```
(abs(eta) <= 1.5) * (pt > 0.1 && pt <= 1.0) * (0.015) +
(abs(eta) <= 1.5) * (pt > 1.0 && pt <= 1.0e1) * (0.012) +
(abs(eta) <= 1.5) * (pt > 1.0e1 && pt <= 2.0e2) * (0.015) +
(abs(eta) <= 1.5) * (pt > 2.0e2) * (0.03) +
(abs(eta) > 1.5 && abs(eta) <= 2.5) * (pt > 0.1 && pt <= 1.0) * (0.015) +
(abs(eta) > 1.5 && abs(eta) <= 2.5) * (pt > 1.0 && pt <= 1.0e1) * (0.015) +
(abs(eta) > 1.5 && abs(eta) <= 2.5) * (pt > 1.0e1 && pt <= 2.0e2) * (0.025) +
(abs(eta) > 1.5 && abs(eta) <= 2.5) * (pt > 2.0e2) * (0.03)
```

B.2. Phase I adapted

The electron efficiency and resolution parameterizations are the same as for Phase I original.

Listing B.5: Phase I adapted muon efficiency

```
(pt <= 2.0)  * (0.00) + \
(abs(eta) <= 2.40) * (pt >  2.0 && pt <= 3.0)  * (0.51*0.959) +
(abs(eta) <= 2.40) * (pt >  3.0 && pt <= 4.0)  * (0.85*0.959) +
(abs(eta) <= 2.40) * (pt >  4.0 && pt <= 11.0) * (0.93*0.959) +
(abs(eta) <= 2.40) * (pt >  11. && pt <= 50.)  * (0.96*0.959) +
(abs(eta) <= 2.40) * (pt >  50. && pt <= 70.)  * (0.98*0.959) +
(abs(eta) <= 2.40) * (pt > 70.0 )  * (1.00*0.959) +
(abs(eta) > 2.40)  * (0.00)
```

Listing B.6: Phase I adapted muon inverse momentum resolution

```
(0.0297527+0.00014987*pt-6.30357e-8*pt*pt+2.65056e-11*pt*pt*pt)
```

B.3. Phase I aged

Listing B.7: Phase I aged electron efficiency

```
(pt <= 4.0) * (0.00) +
(abs(eta) <= 1.45 ) * (pt > 4.0 && pt <= 6.0) * (0.5*0.50) +
(abs(eta) <= 1.45 ) * (pt > 6.0 && pt <= 8.0) * (0.5*0.70) +
(abs(eta) <= 1.45 ) * (pt > 8.0 && pt <= 10.0) * (0.7*0.85) +
```

```
(abs(eta) <= 1.45 ) * (pt > 10.0 && pt <= 30.0) * (0.90*0.94) +
(abs(eta) <= 1.45 ) * (pt > 30.0 && pt <= 50.0) * (0.95*0.97) +
(abs(eta) <= 1.45 ) * (pt > 50.0 && pt <= 70.0) * (0.95*0.98) +
(abs(eta) <= 1.45 ) * (pt > 70.0 ) * (1.0) +
(abs(eta) > 1.45 && abs(eta) <= 1.55) * (pt > 4.0 && pt <= 10.0) * (0.5*0.35)
   +
(abs(eta) > 1.45 && abs(eta) <= 1.55) * (pt > 10.0 && pt <= 30.0) * (0.5*0.40)
    +
(abs(eta) > 1.45 && abs(eta) <= 1.55) * (pt > 30.0 && pt <= 70.0) * (0.8*0.45)
    +
(abs(eta) > 1.45 && abs(eta) <= 1.55) * (pt > 70.0 ) * (0.8*0.45) +
(abs(eta) >= 1.55 && abs(eta) <= 2.0 ) * (pt > 4.0 && pt <= 10.0) * (0.7*0.75)
    +
(abs(eta) >= 1.55 && abs(eta) <= 2.0 ) * (pt > 10.0 && pt <= 30.0) *
   (0.80*0.85) +
(abs(eta) >= 1.55 && abs(eta) <= 2.0 ) * (pt > 30.0 && pt <= 50.0) *
   (0.85*0.95) +
(abs(eta) >= 1.55 && abs(eta) <= 2.0 ) * (pt > 50.0 && pt <= 70.0) *
   (0.85*0.95) +
(abs(eta) >= 1.55 && abs(eta) <= 2.0 ) * (pt > 70.0 ) * (0.85*1.0) +
(abs(eta) >= 2.0 && abs(eta) <= 2.5 ) * (pt > 4.0 && pt <= 10.0) * (0.7*0.65)
   +
(abs(eta) >= 2.0 && abs(eta) <= 2.5 ) * (pt > 10.0 && pt <= 30.0) * (0.7*0.75)
    +
(abs(eta) >= 2.0 && abs(eta) <= 2.5 ) * (pt > 30.0 && pt <= 50.0) * (0.8*0.85)
    +
(abs(eta) >= 2.0 && abs(eta) <= 2.5 ) * (pt > 50.0 && pt <= 70.0) * (0.8*0.85)
    +
(abs(eta) >= 2.0 && abs(eta) <= 2.5 ) * (pt > 70.0 ) * (0.8*0.85) +
(abs(eta) > 2.5) * (0.00)
```

Listing B.8: Phase I aged electron energy resolution

```
(abs(eta) <= 2.5) * (energy > 0.1 && energy <= 2.5e1) * (energy*0.015) +
(abs(eta) <= 2.5) * (energy > 2.5e1) * sqrt(energy^2*0.005^2 + energy*0.027^2
   + 0.15^2) +
(abs(eta) > 2.5 && abs(eta) <= 3.0) * sqrt(energy^2*0.005^2 + energy*0.027^2 +
    0.15^2) +
(abs(eta) > 3.0 && abs(eta) <= 5.0) * sqrt(energy^2*0.08^2 + energy*1.97^2)
```

Listing B.9: Phase I aged muon efficiency

```
(pt <= 10.0) * (0.00) +
(abs(eta)<=0.1)*(pt>10)*(0.89865) +
(abs(eta)>0.1 && abs(eta)<=0.2)*(pt>10)*(0.894596) +
(abs(eta)>0.2 && abs(eta)<=0.3)*(pt>10)*(0.764087) +
(abs(eta)>0.3 && abs(eta)<=0.4)*(pt>10)*(0.881295) +
(abs(eta)>0.4 && abs(eta)<=0.5)*(pt>10)*(0.913192) +
(abs(eta)>0.5 && abs(eta)<=0.6)*(pt>10)*(0.897579) +
(abs(eta)>0.6 && abs(eta)<=0.7)*(pt>10)*(0.894978) +
(abs(eta)>0.7 && abs(eta)<=0.8)*(pt>10)*(0.878466) +
(abs(eta)>0.8 && abs(eta)<=0.9)*(pt>10)*(0.831849) +
(abs(eta)>0.9 && abs(eta)<=1.0)*(pt>10)*(0.806424) +
(abs(eta)>1.0 && abs(eta)<=1.1)*(pt>10)*(0.756892) +
(abs(eta)>1.1 && abs(eta)<=1.2)*(pt>10)*(0.728583) +
(abs(eta)>1.2 && abs(eta)<=1.3)*(pt>10)*(0.773855) +
```

```
(abs(eta)>1.3 && abs(eta)<=1.4)*(pt>10)*(0.776296) +
(abs(eta)>1.4 && abs(eta)<=1.5)*(pt>10)*(0.769977) +
(abs(eta)>1.5 && abs(eta)<=1.6)*(pt>10)*(0.838174) +
(abs(eta)>1.6 && abs(eta)<=1.7)*(pt>10)*(0.854358) +
(abs(eta)>1.7 && abs(eta)<=1.8)*(pt>10)*(0.8565) +
(abs(eta)>1.8 && abs(eta)<=1.9)*(pt>10)*(0.857182) +
(abs(eta)>1.9 && abs(eta)<=2.0)*(pt>10)*(0.85591) +
(abs(eta)>2.0 && abs(eta)<=2.1)*(pt>10)*(0.844826) +
(abs(eta)>2.1 && abs(eta)<=2.2)*(pt>10)*(0.81742) +
(abs(eta)>2.2 && abs(eta)<=2.3)*(pt>10)*(0.825831) +
(abs(eta)>2.3 && abs(eta)<=2.4)*(pt>10)*(0.774208) +
(abs(eta) > 2.40) * (0.00)
```

Listing B.10: Phase I aged muon inverse momentum resolution

```
(0.0297527+0.00014987*pt-6.30357e-8*pt*pt+2.65056e-11*pt*pt*pt)
```

B.4. Phase II

Listing B.11: Phase II electron efficiency

```
(pt <= 4.0) * (0.00) +
(abs(eta) <= 1.45 ) * (pt > 4.0 && pt <= 6.0) * (0.50) +
(abs(eta) <= 1.45 ) * (pt > 6.0 && pt <= 8.0) * (0.70) +
(abs(eta) <= 1.45 ) * (pt > 8.0 && pt <= 10.0) * (0.85) +
(abs(eta) <= 1.45 ) * (pt > 10.0 && pt <= 30.0) * (0.94) +
(abs(eta) <= 1.45 ) * (pt > 30.0 && pt <= 50.0) * (0.97) +
(abs(eta) <= 1.45 ) * (pt > 50.0 && pt <= 70.0) * (0.98) +
(abs(eta) <= 1.45 ) * (pt > 70.0 ) * (1.0) +
(abs(eta) > 1.45 && abs(eta) <= 1.55) * (pt > 4.0 && pt <= 10.0) * (0.35) +
(abs(eta) > 1.45 && abs(eta) <= 1.55) * (pt > 10.0 && pt <= 30.0) * (0.40) +
(abs(eta) > 1.45 && abs(eta) <= 1.55) * (pt > 30.0 && pt <= 70.0) * (0.45) +
(abs(eta) > 1.45 && abs(eta) <= 1.55) * (pt > 70.0 ) * (0.55) +
(abs(eta) >= 1.55 && abs(eta) <= 2.0 ) * (pt > 4.0 && pt <= 10.0) * (0.75) +
(abs(eta) >= 1.55 && abs(eta) <= 2.0 ) * (pt > 10.0 && pt <= 30.0) * (0.85) +
(abs(eta) >= 1.55 && abs(eta) <= 2.0 ) * (pt > 30.0 && pt <= 50.0) * (0.95) +
(abs(eta) >= 1.55 && abs(eta) <= 2.0 ) * (pt > 50.0 && pt <= 70.0) * (0.95) +
(abs(eta) >= 1.55 && abs(eta) <= 2.0 ) * (pt > 70.0 ) * (1.0) +
(abs(eta) >= 2.0 && abs(eta) <= 4.0 ) * (pt > 4.0 && pt <= 10.0) * (0.65) +
(abs(eta) >= 2.0 && abs(eta) <= 4.0 ) * (pt > 10.0 && pt <= 30.0) * (0.75) +
(abs(eta) >= 2.0 && abs(eta) <= 4.0 ) * (pt > 30.0 && pt <= 50.0) * (0.90) +
(abs(eta) >= 2.0 && abs(eta) <= 4.0 ) * (pt > 50.0 && pt <= 70.0) * (0.90) +
(abs(eta) >= 2.0 && abs(eta) <= 4.0 ) * (pt > 70.0 ) * (0.90) +
(abs(eta) > 4.0) * (0.00)
```

Listing B.12: Phase II electron energy resolution

```
(abs(eta) <= 1.5) * (energy > 0.1 && energy <= 2.5e1) * (energy*0.015) +
(abs(eta) <= 1.5) * (energy > 2.5e1) * sqrt(energy^2*0.005^2 + energy*0.027^2
    + 0.15^2) +
(abs(eta) > 1.5 && abs(eta) <= 4.0) * sqrt(energy^2*0.008^2 + energy*0.092^2 +
     0.088^2)
```

Listing B.13: Phase II muon efficiency

```
(pt <= 2.0) * (0.00) +
(abs(eta) <= 4.00) * (pt > 2.0 && pt <= 3.0) * (0.51) +
(abs(eta) <= 4.00) * (pt > 3.0 && pt <= 4.0) * (0.85) +
(abs(eta) <= 4.00) * (pt > 4.0 && pt <= 11.0) * (0.93) +
(abs(eta) <= 4.00) * (pt > 11. && pt <= 50.) * (0.96) +
(abs(eta) <= 4.00) * (pt > 50. && pt <= 70.) * (0.98) +
(abs(eta) <= 4.00) * (pt > 70.0 ) * (1.00) +
(abs(eta) > 4.00) * (0.00)
```

Listing B.14: Phase II inverse muon momentum resolution

```
(abs(eta) <= 1.5) * (pt > 0.1 && pt <= 1.0) * (0.015) +
(abs(eta) <= 1.5) * (pt > 1.0 && pt <= 1.0e1) * (0.013) +
(abs(eta) <= 1.5) * (pt > 1.0e1 && pt <= 2.0e2) * (0.02) +
(abs(eta) <= 1.5) * (pt > 2.0e2) * (0.05) +
(abs(eta) > 1.5 && abs(eta) <= 2.5) * (pt > 0.1 && pt <= 1.0) * (0.015) +
(abs(eta) > 1.5 && abs(eta) <= 2.5) * (pt > 1.0 && pt <= 1.0e1) * (0.015) +
(abs(eta) > 1.5 && abs(eta) <= 2.5) * (pt > 1.0e1 && pt <= 2.0e2) * (0.04) +
(abs(eta) > 1.5 && abs(eta) <= 2.5) * (pt > 2.0e2) * (0.05) +
(abs(eta) > 2.5 && abs(eta) <= 3.0) * (pt > 0.1 && pt <= 1.0) * (0.017) +
(abs(eta) > 2.5 && abs(eta) <= 3.0) * (pt > 1.0 && pt <= 10.0) * (0.03) +
(abs(eta) > 2.5 && abs(eta) <= 3.0) * (pt > 10.0 && pt <= 100.0) * (0.05) +
(abs(eta) > 2.5 && abs(eta) <= 3.0) * (pt > 100.0) * (0.30) +
(abs(eta) > 3.0 && abs(eta) <= 3.5) * (pt > 0.1 && pt <= 1.0) * (0.02) +
(abs(eta) > 3.0 && abs(eta) <= 3.5) * (pt > 1.0 && pt <= 10.0) * (0.04) +
(abs(eta) > 3.0 && abs(eta) <= 3.5) * (pt > 10.0 && pt <= 100.0) * (0.07) +
(abs(eta) > 3.0 && abs(eta) <= 3.5) * (pt > 100.0) * (0.30) +
(abs(eta) > 3.5 && abs(eta) <= 4.0) * (pt > 0.1 && pt <= 1.0) * (0.025) +
(abs(eta) > 3.5 && abs(eta) <= 4.0) * (pt > 1.0 && pt <= 10.0) * (0.05) +
(abs(eta) > 3.5 && abs(eta) <= 4.0) * (pt > 10.0 && pt <= 100.0) * (0.20) +
(abs(eta) > 3.5 && abs(eta) <= 4.0) * (pt > 100.0) * (0.80)
```

C. Additional 14 TeV distinction potential plots

This appendix includes the distinction potential plots for the individual electron and muon channels, as described in section 8.3.

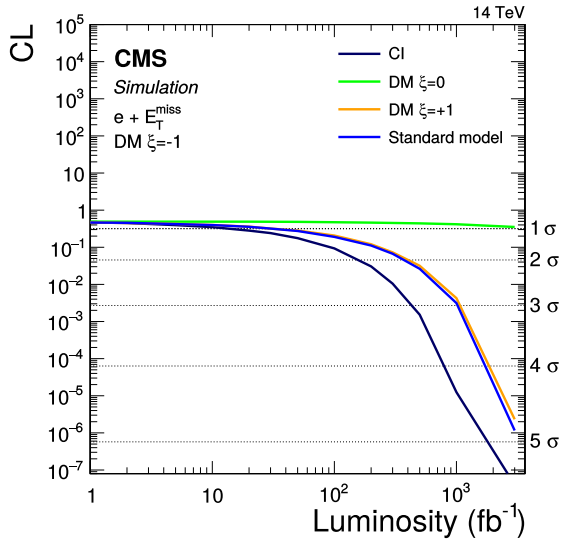

(a) DM, $\xi = -1$

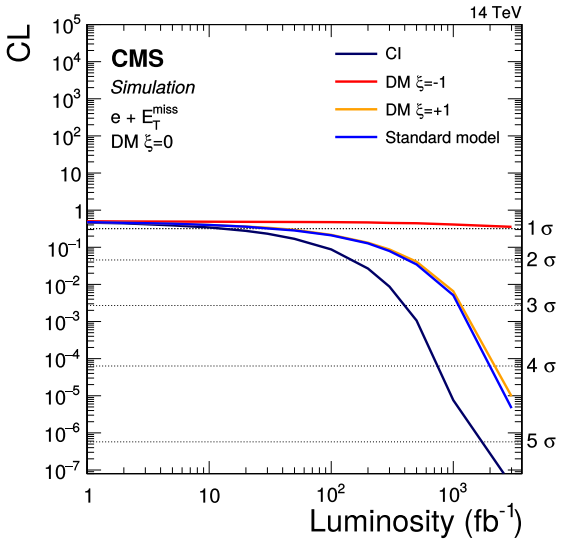

(b) DM, $\xi = 0$

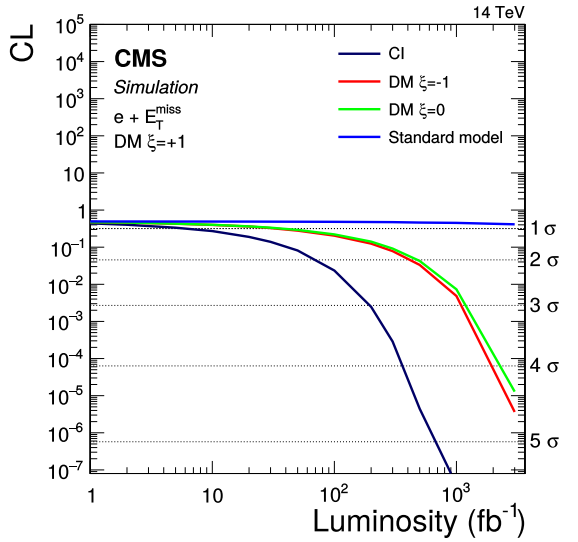

(c) DM, $\xi = +1$

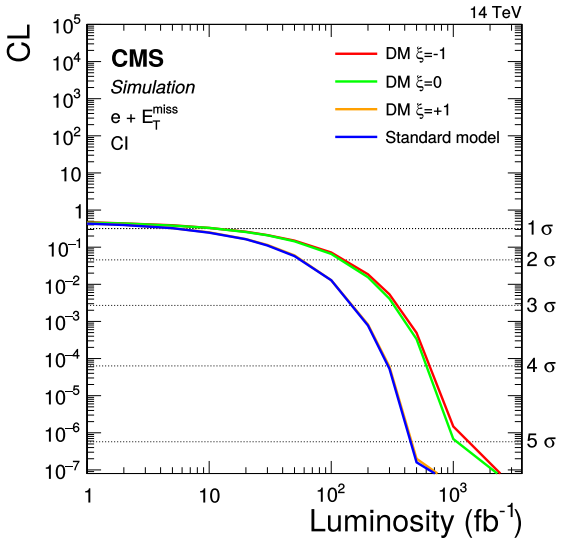

(d) HNC-CI

Figure C.1.: Distinction potential of the dark matter and contact interaction scenarios to each other for the electron channel. The different lines indicate different null hypotheses, to which the hypothesis named in the plot label is compared.

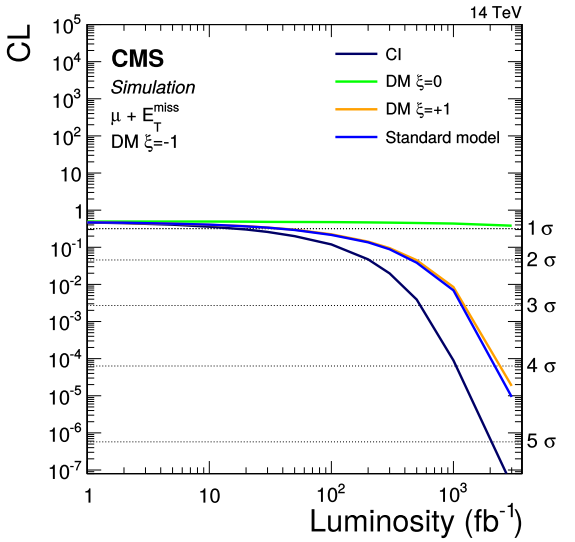

(a) DM, $\xi = -1$

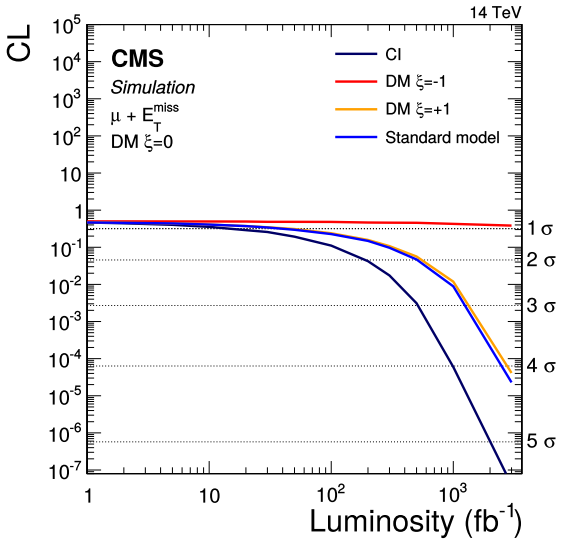

(b) DM, $\xi = 0$

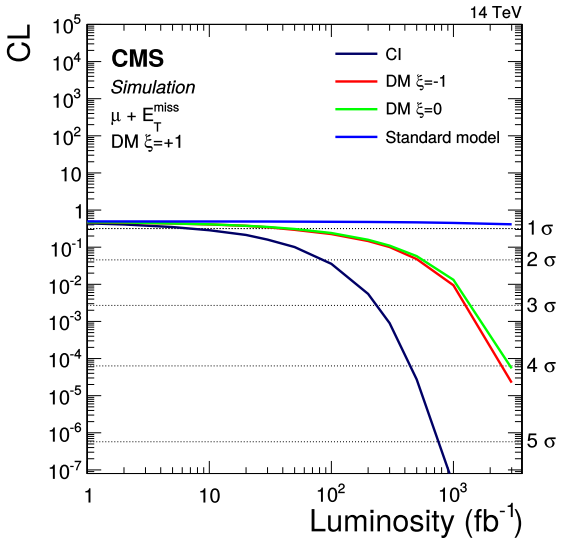

(c) DM, $\xi = +1$

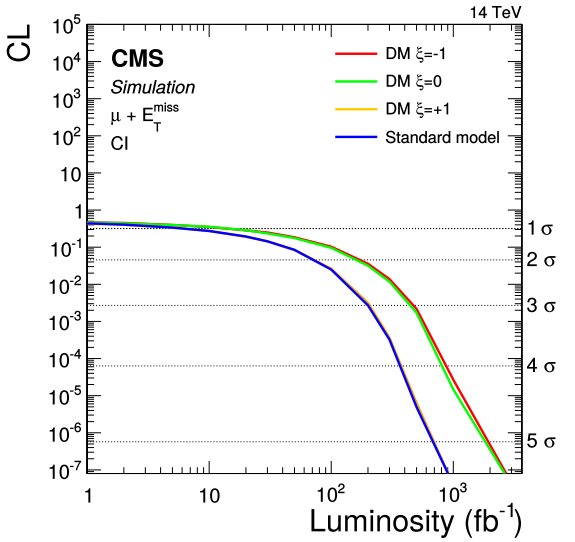

(d) HNC-CI

Figure C.2.: Distinction potential of the dark matter and contact interaction scenarios to each other for the muon channel. The different lines indicate different null hypotheses, to which the hypothesis named in the plot label is compared.

Bibliography

[1] CMS Collaboration, "Search for physics beyond the standard model in final states with a lepton and missing transverse energy in proton-proton collisions at sqrt(s) = 8 TeV", *Phys.Rev.* **D91** (2015), no. 9, 092005, arXiv:1408.2745. doi:10.1103/PhysRevD.91.092005.

[2] CMS Collaboration, "Search for new physics in final states with a lepton and missing transverse energy in pp collisions at the LHC", *Phys.Rev.* **D87** (2013), no. 7, 072005, arXiv:1302.2812. doi:10.1103/PhysRevD.87.072005.

[3] P. Millet, "Search for new physics in pp collision events with one electron and missing transverse energy using CMS data", Master's thesis, RWTH Aachen, 2013. http://web.physik.rwth-aachen.de/~hebbeker/theses/millet_master.pdf.

[4] S. Erdweg, "Search for Dark Matter and W′ in the final state with one muon and missing transverse energy with CMS", Master's thesis, RWTH Aachen, 2013. http://web.physik.rwth-aachen.de/~hebbeker/theses/erdweg_master.pdf.

[5] CMS Collaboration, "Projected Performance of an Upgraded CMS Detector at the LHC and HL-LHC: Contribution to the Snowmass Process", arXiv:1307.7135.

[6] CMS Collaboration, J. Butler, D. Contardo, M. Klute et al., "Technical Proposal for the Phase-II Upgrade of the CMS Detector", Technical Report CERN-LHCC-2015-010. LHCC-P-008, CERN, Geneva, Jun, 2015. http://cds.cern.ch/record/2020886.

[7] D. Griffiths, "Introduction to Elementary Particles". Wiley, 2008.

[8] T. Hebbeker, "Skriptum zur Vorlesung Elementarteilchenphysik I". RWTH SS 2007.

[9] Particle Data Group, "Review of Particle Physics", *Chin. Phys.* **C38** (2014) 090001. doi:10.1088/1674-1137/38/9/090001.

[10] ATLAS Collaboration, "Observation of a new particle in the search for the Standard Model Higgs boson with the ATLAS detector at the LHC", *Phys. Lett.* **B716** (2013) 1–29, arXiv:1207.7214. doi:10.1016/j.physletb.2012.08.020.

[11] CMS Collaboration, "Observation of a new boson at a mass of 125 GeV with the CMS experiment at the LHC", *Phys. Lett.* **B716** (2012) 30–61, arXiv:1207.7235. doi:10.1016/j.physletb.2012.08.021.

[12] G. Altarelli, "The Standard model and beyond", *Nucl.Phys.Proc.Suppl.* **75** (1999) 37, arXiv:hep-ph/9809532. doi:10.1016/S0920-5632(99)00213-3.

[13] G. Altarelli, B. Mele, and M. Ruiz-Altaba, "Searching for New Heavy Vector Bosons in $p\bar{p}$ Colliders", *Z.Phys.* **C45** (1989) 109. doi:10.1007/BF01552335; 10.1007/BF01556677.

[14] D. Berdine, N. Kauer, and D. Rainwater, "Breakdown of the Narrow Width Approximation for New Physics", *Phys. Rev. Lett.* **99** (2007) 111601, arXiv:hep-ph/0703058. doi:10.1103/PhysRevLett.99.111601.

[15] S. Thomas and C. Kilic, "Madgraph implementation of the SSMS/SSMO W′ boson models". Personal communication, 2011, July.

[16] E. Accomando, D. Becciolini, S. De Curtis et al., "Interference effects in heavy W'-boson searches at the LHC", *Phys. Rev.* **D85** (2012) 115017, arXiv:1110.0713. doi:10.1103/PhysRevD.85.115017.

[17] E. Boos, V. Bunichev, L. Dudko et al., "Interference between W' and W in single-top quark production processes", *Phys. Lett.* **B655** (2007) 245–250, arXiv:hep-ph/0610080. doi:10.1016/j.physletb.2007.03.064.

[18] J. C. Pati and A. Salam, "Lepton number as the fourth "color"", *Phys. Rev. D* **10** (Jul, 1974) 275–289. doi:10.1103/PhysRevD.10.275.

[19] TWIST Collaboration, "Precise measurement of parity violation in polarized muon decay", *Phys. Rev.* **D84** (2011) 032005, arXiv:1104.3632. doi:10.1103/PhysRevD.84.032005.

[20] G. Senjanovic, "Spontaneous Breakdown of Parity in a Class of Gauge Theories", *Nucl.Phys.* **B153** (1979) 334–364. doi:10.1016/0550-3213(79)90604-7.

[21] TWIST Collaboration, "Precise measurement of parity violation in polarized muon decay", *Phys. Rev.* **D84** (2011) 032005, arXiv:1104.3632. doi:10.1103/PhysRevD.84.032005.

[22] G. Senjanovic, "Left-Right Symmetric Gauge Theories", *eConf* **C8007241** (1980) 39.

[23] R. N. Mohapatra and G. Senjanovic, "Neutrino Mass and Spontaneous Parity Violation", *Phys.Rev.Lett.* **44** (1980) 912. doi:10.1103/PhysRevLett.44.912.

[24] Y. Zhang, H. An, X. Ji et al., "General CP Violation in Minimal Left-Right Symmetric Model and Constraints on the Right-Handed Scale", *Nucl.Phys.* **B802** (2008) 247–279, arXiv:0712.4218. doi:10.1016/j.nuclphysb.2008.05.019.

[25] P. Fileviez Perez, "Type III Seesaw and Left-Right Symmetry", *JHEP* **0903** (2009) 142, arXiv:0809.1202. doi:10.1088/1126-6708/2009/03/142.

[26] M. Nemevsek, F. Nesti, G. Senjanovic et al., "First Limits on Left-Right Symmetry Scale from LHC Data", *Phys.Rev.* **D83** (2011) 115014, arXiv:1103.1627. doi:10.1103/PhysRevD.83.115014.

[27] T. Appelquist, H.-C. Cheng, and B. A. Dobrescu, "Bounds on universal extra dimensions", *Phys. Rev. D* **64** (2001) 035002, arXiv:hep-ph/0012100. doi:10.1103/PhysRevD.64.035002.

[28] K. Kong, S. C. Park, and T. G. Rizzo, "Collider Phenomenology with Split-UED", *JHEP* **04** (2010) 081, arXiv:1002.0602. doi:10.1007/JHEP04(2010)081.

[29] N. Arkani-Hamed, S. Dimopoulos, and G. R. Dvali, "The Hierarchy problem and new dimensions at a millimeter", *Phys. Lett.* **B429** (1998) 263–272, arXiv:hep-ph/9803315.

doi:10.1016/S0370-2693(98)00466-3.

[30] N. Arkani-Hamed, S. Dimopoulos, and G. R. Dvali, "Phenomenology, astrophysics and cosmology of theories with submillimeter dimensions and TeV scale quantum gravity", *Phys. Rev.* **D59** (1999) 086004, arXiv:hep-ph/9807344. doi:10.1103/PhysRevD.59.086004.

[31] PAMELA Collaboration, "An anomalous positron abundance in cosmic rays with energies 1.5-100 GeV", *Nature* **458** (2009) 607–609, arXiv:0810.4995. doi:10.1038/nature07942.

[32] AMS Collaboration, "First Result from the Alpha Magnetic Spectrometer on the International Space Station: Precision Measurement of the Positron Fraction in Primary Cosmic Rays of 0.5–350 GeV", *Phys.Rev.Lett.* **110** (2013) 141102. doi:10.1103/PhysRevLett.110.141102.

[33] T. Flacke, K. Kong, and S. C. Park, "A Review on Non-Minimal Universal Extra Dimensions", *Mod.Phys.Lett.* **A30** (2015), no. 05, 1530003, arXiv:1408.4024. doi:10.1142/S0217732315300037.

[34] S. C. Park and J. Shu, "Split Universal Extra Dimensions and Dark Matter", *Phys.Rev.* **D79** (2009) 091702, arXiv:0901.0720. doi:10.1103/PhysRevD.79.091702.

[35] D. Kim, Y. Oh, and S. C. Park, "W' in new physics models at the LHC", arXiv:1109.1870.

[36] Y. Oh, "Reinterpretation of the SSM W′ limits to limits on KK bosons in the sUED model.". Personal communication, 2012.

[37] E. Fermi, "Versuch einer Theorie der β-Strahlen. I", *Zeitschrift für Physik* **88** (1934), no. 3-4, 161–177. doi:10.1007/BF01351864.

[38] E. Eichten, K. D. Lane, and M. E. Peskin, "New Tests for Quark and Lepton Substructure", *Phys. Rev. Lett.* **50** (1983) 811–814. doi:10.1103/PhysRevLett.50.811.

[39] K. D. Lane, F. E. Paige, T. Skwarnicki et al., "Simulations of supercollider physics", *Phys. Rept.* **278** (1997) 291–371, arXiv:hep-ph/9412280. doi:10.1016/S0370-1573(96)00018-X.

[40] E. Eichten, I. Hinchliffe, K. Lane et al., "Supercollider physics", *Rev. Mod. Phys.* **56** (Oct, 1984) 579–707. doi:10.1103/RevModPhys.56.579.

[41] F. Schneider, "Search for New Physics in Final States with One Muon and Missing Transverse Energy with CMS Data", Master's thesis, RWTH Aachen, 2012. http://web.physik.rwth-aachen.de/~hebbeker/theses/schneider_master.pdf.

[42] GEM Collaboration, "GEM Technical Design Report",. doi:10.2172/10124115.

[43] G. Busoni, A. De Simone, E. Morgante et al., "On the Validity of the Effective Field Theory for Dark Matter Searches at the LHC", *Phys.Lett.* **B728** (2014) 412–421, arXiv:1307.2253. doi:10.1016/j.physletb.2013.11.069.

[44] Y. Bai and T. M. Tait, "Searches with Mono-Leptons", *Phys.Lett.* **B723** (2013) 384–387, arXiv:1208.4361. doi:10.1016/j.physletb.2013.05.057.

[45] G. Busoni, A. De Simone, J. Gramling et al., "On the Validity of the Effective Field Theory for Dark Matter Searches at the LHC, Part II: Complete Analysis for the *s*-channel", *JCAP* **1406** (2014) 060, arXiv:1402.1275. doi:10.1088/1475-7516/2014/06/060.

[46] I. M. Shoemaker and L. Vecchi, "Unitarity and Monojet Bounds on Models for DAMA, CoGeNT, and CRESST-II", *Phys.Rev.* **D86** (2012) 015023, arXiv:1112.5457. doi:10.1103/PhysRevD.86.015023.

[47] N. F. Bell, Y. Cai, J. B. Dent et al., "Dark matter at the LHC: EFTs and gauge invariance", arXiv:1503.07874.

[48] R. D. Cousins, "Why isn't every physicist a Bayesian?", *American Journal of Physics* **63** (1995), no. 5, 398–410. doi:http://dx.doi.org/10.1119/1.17901.

[49] A. L. Read, "Modified frequentist analysis of search results (the CL_s method)",. http://cds.cern.ch/record/451614.

[50] A. L. Read, "Presentation of search results: The CL(s) technique", *J. Phys.* **G28** (2002) 2693–2704. [,11(2002)]. doi:10.1088/0954-3899/28/10/313.

[51] T. Junk, "Confidence level computation for combining searches with small statistics", *Nucl. Instrum. Meth.* **A434** (1999) 435–443, arXiv:hep-ex/9902006. doi:10.1016/S0168-9002(99)00498-2.

[52] J. Neyman and E. S. Pearson, "On the Problem of the Most Efficient Tests of Statistical Hypotheses", *Phil. Trans. R. Soc. A* **231** (1933), no. 694-706, 289–337. doi:10.1098/rsta.1933.0009.

[53] G. Cowan, K. Cranmer, E. Gross et al., "Asymptotic formulae for likelihood-based tests of new physics", *Eur.Phys.J.* **C71** (2011) 1554, arXiv:1007.1727. doi:10.1140/epjc/s10052-011-1554-0.

[54] A. Wald, "Tests of Statistical Hypotheses Concerning Several Parameters When the Number of Observations is Large", *Trans. Amer. Math. Soc.* **54** (November, 1943) 426–482. doi:10.2307/1990256.

[55] R. E. Kass and L. Wasserman, "The Selection of Prior Distributions by Formal Rules", *JASA* **91** (1996), no. 435, 1343–1370. doi:10.1080/01621459.1996.10477003.

[56] (ed.) L. Evans and (ed.) P. Bryant, "LHC Machine", *JINST* **3** (2008) S08001. doi:10.1088/1748-0221/3/08/S08001.

[57] J. Blewett, "200-GeV Intersecting Storage Accelerators", *eConf* **C710920** (1971) 501.

[58] R. Veness, D. Ramos, P. Lepeule et al., "Installation and commissioning of vacuum systems for the LHC particle detectors", Number CERN-ATS-2009-005, p. 4 p. Jul, 2009.

[59] CMS Collaboration, "The CMS experiment at the CERN LHC", *JINST* **3** (2008), no. S08004,. doi:10.1088/1748-0221/3/08/S08004.

[60] CMS Collaboration, K. Klein, "The CMS silicon strip tracker: Overview and status", in *Proceedings, 2005 Europhysics Conference on High Energy Physics (EPS-HEP 2005)*, volume HEP2005, p. 378. 2006. arXiv:physics/0610259.

[61] CMS Collaboration, "CMS Tracking Performance Results from early LHC Operation", *Eur.Phys.J.* **C70** (2010) 1165–1192, arXiv:1007.1988. CMS-TRK-10-001. doi:10.1140/epjc/s10052-010-1491-3.

[62] CMS Collaboration, "Energy resolution of the barrel of the CMS electromagnetic calorimeter", *JINST* **2** (2007) P04004. doi:10.1088/1748-0221/2/04/P04004.

[63] P. Lecomte, D. Luckey, F. Nessi-Tedaldi et al., "High-energy proton induced damage study of scintillation light output from PbWO-4 calorimeter crystals", *Nucl. Instrum. Meth.* **A564** (2006) 164–168. doi:10.1016/j.nima.2006.04.043.

[64] CMS HCAL Collaboration, "Studies of the response of the prototype CMS hadron calorimeter, including magnetic field effects, to pion, electron, and muon beams", *Nucl. Instrum. Meth.* **A457** (2001) 75–100, arXiv:hep-ex/0007045. doi:10.1016/S0168-9002(00)00711-7.

[65] CMS Collaboration, "Performance study of the CMS barrel resistive plate chambers with cosmic rays", *JINST* **5** (2010), no. 03, T03017, arXiv:0911.4045. doi:10.1088/1748-0221/5/03/T03017.

[66] CMS Collaboration, "Performance of CMS muon reconstruction in pp collision events at $\sqrt{s} = 7$ TeV", *JINST* **7** (2012) P10002, arXiv:1206.4071. doi:10.1088/1748-0221/7/10/P10002.

[67] CMS Collaboration, "Technical proposal for the upgrade of the CMS detector through 2020", Technical Report CERN-LHCC-2011-006, LHCC-P-004, CERN, Geneva, Jun, 2011. https://cds.cern.ch/record/1355706.

[68] A. Canepa, "Selected Highlights from the LHC and HL-LHC Physics Program",. ATL-PHYS-SLIDE-2015-011, https://cds.cern.ch/record/1984417.

[69] A. Dominguez, D. Abbaneo, K. Arndt et al., "CMS Technical Design Report for the Pixel Detector Upgrade", Technical Report CERN-LHCC-2012-016, CMS-TDR-11, CERN, Geneva, Sep, 2012. http://cds.cern.ch/record/1481838.

[70] CMS Collaboration, "Radiation background with the CMS RPCs at the LHC", *JINST* **10** (2015), no. 05, C05031, arXiv:1406.2859. doi:10.1088/1748-0221/10/05/C05031.

[71] A. Tricomi, "Upgrade of the CMS tracker", *JINST* **9** (2014) C03041. doi:10.1088/1748-0221/9/03/C03041.

[72] CMS Collaboration, R. Paramatti, "Design options for the upgrade of the CMS electromagnetic calorimeter", Technical Report CMS-CR-2014-305, CERN, Geneva, Oct, 2014. https://cds.cern.ch/record/1957099.

[73] K. Hoepfner, "CMS upgrade and future plans", *EPJ Web of Conferences 95* **95** (2015) 03016. doi:10.1051/epjconf/20159503016.

[74] CMS Collaboration, D. A. Petyt, "Perspectives of the CMS phase-II upgrade for HL-LHC", Technical Report CMS-CR-2014-289, CERN, Geneva, Oct, 2014. https://cds.cern.ch/record/1955161.

[75] D. Abbaneo, M. Abbrescia, P. Aspell et al., "A GEM Detector System for an Upgrade of the High-eta Muon Endcap Stations GE1/1 + ME1/1 in CMS", arXiv:1211.1494.

[76] CMS Collaboration, "Electron reconstruction and identification at sqrt(s) = 7 TeV", Technical Report CMS-PAS-EGM-10-004, CERN, 2010. https://cds.cern.ch/record/1299116.

[77] CMS Collaboration, "CMS Luminosity Based on Pixel Cluster Counting - Summer 2013 Update", Technical Report CMS-PAS-LUM-13-001, CERN, Geneva, 2013. https://cds.cern.ch/record/1598864.

[78] S. van der Meer, "Calibration of the effective beam height in the ISR", Technical Report CERN-ISR-PO-68-31. ISR-PO-68-31, CERN, Geneva, 1968. https://cds.cern.ch/record/296752.

[79] S. White, R. Alemany-Fernandez, H. Burkhardt et al., "Luminosity Optimization and Calibration in the LHC", in *Particle accelerator. Proceedings, 23rd Conference, PAC'09, Vancouver, Canada, May 4-8, 2009*, p. WE6PFP015. 2010.

[80] S. Baffioni, C. Charlot, F. Ferri et al., "Electron reconstruction in CMS", *Eur. Phys. J.* **C49** (2007) 1099–1116. doi:10.1140/epjc/s10052-006-0175-5.

[81] W. Adam, S.Baffioni, F. Beaudette et al., "Electron Reconstruction in CMS". internal CMS note CMS-AN-2009/164. http://cms.cern.ch/iCMS/jsp/openfile.jsp?tp=draft&files=AN2009_164_v4.pdf, 2009.

[82] CMS Collaboration, "Energy Calibration and Resolution of the CMS Electromagnetic Calorimeter in pp Collisions at $\sqrt{s} = 7$ TeV", *JINST* **8** (2013) P09009, arXiv:1306.2016. doi:10.1088/1748-0221/8/09/P09009.

[83] J. Hauptman, "Particle Physics Experiments at High Energy Colliders". Physics textbook. Wiley, 2011.

[84] CMS Collaboration, "Particle-Flow Event Reconstruction in CMS and Performance for Jets, Taus, and MET", Technical Report CMS-PAS-PFT-09-001, CERN, Apr, 2009. http://cds.cern.ch/record/1194487.

[85] CMS Collaboration, "Particle-flow commissioning with muons and electrons from J/Psi and W events at 7 TeV", Technical Report CMS-PAS-PFT-10-003, CERN, 2010. http://cds.cern.ch/record/1279347.

[86] CMS Collaboration, "Missing transverse energy performance of the CMS detector", *JINST* **6** (2011) P09001, arXiv:1106.5048. doi:10.1088/1748-0221/6/09/P09001.

[87] CMS Collaboration, "Determination of Jet Energy Calibration and Transverse Momentum Resolution in CMS", *JINST* **6** (2011) P11002, arXiv:1107.4277. doi:10.1088/1748-0221/6/11/P11002.

[88] CMS Collaboration, "MET performance in 8 TeV data", Technical Report CMS-PAS-JME-12-002, CERN, 2013. http://cds.cern.ch/record/1543527.

[89] H. Liu, L. Gouskos, I. Melzer-Pellmann et al., "Fake missing transverse momentum in the 2012 dataset". internal CMS note CMS-AN-2012/268 http://cms.cern.ch/iCMS/jsp/openfile.jsp?tp=draft&files=AN2012_268_v2.pdf, 2012.

[90] CMS Collaboration, "MET Optional Filters", 2015-07-30. https://twiki.cern.ch/twiki/bin/view/CMS/MissingETOptionalFilters?rev=66.

[91] CMS Collaboration, "HEEP Electron ID and isolation". Unpublished, Jun, 2015. https://twiki.cern.ch/twiki/bin/viewauth/CMS/HEEPElectronID?rev=68.

[92] S. Chang, S. Erdweg, K. Hoepfner et al., "Search for new physics in the single lepton + MET final states with the full 2012 dataset at sqrt(s)=8 TeV", *CMS Analysis Note* **CMS AN-12-423** (2013). http://cms.cern.ch/iCMS/jsp/openfile.jsp?tp=draft&files=AN2012_423_v10.pdf.

[93] CMS Collaboration, "Performance of muon identification in pp collisions at s**0.5 = 7 TeV", Technical Report CMS-PAS-MUO-10-002, CERN, 2010. http://cds.cern.ch/record/1279140.

[94] CMS Collaboration, "Baseline muon selections for Run-I", 2015-07-12. https://twiki.cern.ch/twiki/bin/view/CMSPublic/SWGuideMuonId?rev=60.

[95] T. Sjöstrand, S. Mrenna, and P. Z. Skands, "PYTHIA 6.4 Physics and Manual", *JHEP* **05** (2006) 026, arXiv:hep-ph/0603175. doi:10.1088/1126-6708/2006/05/026.

[96] P. Nason, "A new method for combining NLO QCD with shower Monte Carlo algorithms", *JHEP* **11** (2004) 040, arXiv:hep-ph/0409146. doi:10.1088/1126-6708/2004/11/040.

[97] S. Frixione, P. Nason, and C. Oleari, "Matching NLO QCD computations with Parton Shower simulations: the POWHEG method", *JHEP* **11** (2007) 070, arXiv:0709.2092. doi:10.1088/1126-6708/2007/11/070.

[98] S. Alioli, P. Nason, C. Oleari et al., "A general framework for implementing NLO calculations in shower Monte Carlo programs: the POWHEG BOX", *JHEP* **06** (2010) 043, arXiv:1002.2581. doi:10.1007/JHEP06(2010)043.

[99] S. Frixione and B. R. Webber, "Matching NLO QCD computations and parton shower simulations", *JHEP* **06** (2002) 029, arXiv:hep-ph/0204244. doi:10.1088/1126-6708/2002/06/029.

[100] J. Alwall et al., "MadGraph/MadEvent v4: the new web generation", *JHEP* **09** (2007) 028. doi:10.1088/1126-6708/2007/09/028.

[101] GEANT4 Collaboration, "GEANT4: A simulation toolkit", *Nucl. Instrum. Meth.* **A506** (2003) 250–303. doi:10.1016/S0168-9002(03)01368-8.

[102] J. Allison et al., "Geant4 developments and applications", *IEEE Trans. Nucl. Sci.* **53** (2006) 270. doi:10.1109/TNS.2006.869826.

[103] CMS Collaboration, "Measuring Electron Efficiencies at CMS with Early Data", Technical Report CMS-PAS-EGM-07-001, CERN, Dec, 2008. https://cds.cern.ch/record/1194482.

[104] S. Alioli, P. Nason, C. Oleari et al., "NLO single-top production matched with shower in POWHEG: s- and t-channel contributions", *JHEP* **09** (2009) 111, arXiv:0907.4076. [Erratum: JHEP02,011(2010)]. doi:10.1007/JHEP02(2010)011, 10.1088/1126-6708/2009/09/111.

[105] G. Balossini, G. Montagna, C. Carloni Calame et al., "Combination of electroweak and QCD corrections to single W production at the Fermilab Tevatron and the CERN LHC", *Journal of High Energy Physics* **2010** (2010) 1–49. doi:10.1007/JHEP01(2010)013.

[106] C. M. Carloni Calame, G. Montagna, O. Nicrosini et al., "Precision electroweak calculation of the charged current Drell-Yan process", *JHEP* **12** (2006) 016, arXiv:hep-ph/0609170. doi:10.1088/1126-6708/2006/12/016.

[107] H.-L. Lai, M. Guzzi, J. Huston et al., "New parton distributions for collider physics", *Phys. Rev. D* **82** (Oct, 2010) 074024. doi:10.1103/PhysRevD.82.074024.

[108] J. Pumplin, D. R. Stump, J. Huston et al., "New generation of parton distributions with uncertainties from global QCD analysis", *JHEP* **07** (2002) 012, arXiv:hep-ph/0201195. doi:10.1088/1126-6708/2002/07/012.

[109] S. Dittmaier and M. Krämer, "Electroweak radiative corrections to W-boson production at hadron colliders", *Phys. Rev. D* **65** (Mar, 2002) 073007, arXiv:hep-ph/0109062. doi:10.1103/PhysRevD.65.073007.

[110] D. Kim, Y. Oh, Y. Yang et al., "PDF Uncertainties and K-factor for the W' search at 8 TeV collisions", *CMS Analysis Note: AN-12-172* (2012). http://cms.cern.ch/iCMS/jsp/openfile.jsp?tp=draft&files=AN2012_172_v5.pdf.

[111] R. Gavin, Y. Li, F. Petriello, S. Quackenbush, "FEWZ 2.0: A code for hadronic Z production at next-to-next-to-leading order", arXiv:1011.3540.

[112] R. Gavin, Y. Li, F. Petriello et al., "W physics at the LHC with FEWZ 2.1", arXiv:1201.5896.

[113] CMS Collaboration, "ECAL Detector Performance, 2011 Data", *CMS Performance Note: DP-12-007* (2012).

[114] B. Clerbaux et al., "Search for High Mass Resonances Decaying to Electron Pairs at 8 TeV with the Full 2012 dataset", *CMS Note* **2012/415** (2012).

[115] CMS Collaboration, "Measurement of Momentum Scale and Resolution of the CMS Detector using Low-mass Resonances and Cosmic Ray Muons", Technical Report CMS-PAS-TRK-10-004, CERN, 2010. Geneva, 2010.

[116] CMS Collaboration, "Utilities for Accessing Pileup Information for Data", 2015. [Online; accessed 12-July-2015].

[117] M. Botje et al., "The PDF4LHC Working Group Interim Recommendations", arXiv:1101.0538.

[118] A. Vicini, "Practical implementation of the PDF4LHC recipe",. http://www.hep.ucl.ac.uk/pdf4lhc/PDF4LHC_practical_guide.pdf.

[119] D. Bourilkov, R. C. Group, and M. R. Whalley, "LHAPDF: PDF use from the Tevatron to the LHC", in *TeV4LHC Workshop - 4th meeting Batavia, Illinois, October 20-22, 2005*. 2006. arXiv:hep-ph/0605240.

[120] A. D. Martin, W. J. Stirling, R. S. Thorne et al., "Parton distributions for the LHC", *Eur. Phys. J. C* **63** (2009) 189, arXiv:0901.0002. doi:10.1140/epjc/s10052-009-1072-5.

[121] NNPDF Collaboration, "Impact of heavy quark masses on parton distributions and LHC Phenomenology", *Nucl. Phys. B* **849** (2011) 296, arXiv:1101.1300. doi:10.1016/j.nuclphysb.2011.03.021.

[122] F. Garwood, "Fiducial Limits for the Poisson Distribution", *Biometrika* **28** (1936), no. 3/4, pp. 437–442.

[123] ATLAS Collaboration, "Search for high-mass diboson resonances with boson-tagged jets in proton-proton collisions at $\sqrt{s}$ = 8 TeV with the ATLAS detector", arXiv:1506.00962.

[124] CMS Collaboration, "Search for massive resonances decaying into pairs of boosted bosons in semi-leptonic final states at $\sqrt{s} = 8$ TeV", *JHEP* **08** (2014) 174, arXiv:1405.3447. doi:10.1007/JHEP08(2014)174.

[125] CMS Collaboration, "Search for W prime to tbbar in the all-hadronic final state", Technical Report CMS-PAS-B2G-12-009, CERN, Geneva, 2014.

[126] CMS Collaboration, "Search for dark matter, extra dimensions, and unparticles in monojet events in proton–proton collisions at $\sqrt{s} = 8$ TeV", *Eur. Phys. J.* **C75** (2015), no. 5, 235, arXiv:1408.3583. doi:10.1140/epjc/s10052-015-3451-4.

[127] CMS Collaboration, "CMS Physics Results". Unpublished, Jul, 2015. http://cms-results.web.cern.ch/cms-results/public-results/publications/.

[128] ATLAS and CMS Collaboration, "Expected pileup values at the HL-LHC", Technical Report CERN-CMS-NOTE-2013-003, CERN, Geneva, Jul, 2013.

[129] R. Rahmat, R. Kroeger, and A. Giammanco, "The Fast Simulation of The CMS Experiment", *Journal of Physics: Conference Series* **396** (2012), no. 6, 062016.

[130] J. de Favereau, C. Delaere, P. Demin et al., "DELPHES 3: a modular framework for fast simulation of a generic collider experiment", *JHEP* **2014** (2014), no. 2, arXiv:1307.6346. doi:10.1007/JHEP02(2014)057.

[131] A. Avetisyan, J. M. Campbell, T. Cohen et al., "Methods and Results for Standard Model Event Generation at $\sqrt{s}$ = 14 TeV, 33 TeV and 100 TeV Proton Colliders (A Snowmass Whitepaper)", arXiv:1308.1636.

[132] CMS Collaboration, "CMS technical design report, volume II: Physics performance", *J. Phys.* **G34** (2007) 995–1579. doi:10.1088/0954-3899/34/6/S01.

[133] C. Hof, "Detection of New Heavy Charged Gauge Bosons with the Future CMS Detector", Diploma thesis, RWTH Aachen, 2005. http://web.physik.rwth-aachen.de/~hebbeker/theses/hof_diploma.pdf.

[134] D0 Collaboration, "Search for W' bosons decaying to an electron and a neutrino with the D0 detector", *Phys. Rev. Lett.* **100** (2008) 031804, arXiv:0710.2966. doi:10.1103/PhysRevLett.100.031804.

[135] CDF Collaboration, "Search for a New Heavy Gauge Boson W' with Electron + missing ET Event Signature in $p\bar{p}$ collisions at $\sqrt{s} = 1.96$ TeV", *Phys. Rev.* **D83** (2011) 031102, arXiv:1012.5145. doi:10.1103/PhysRevD.83.031102.

[136] CMS Collaboration, "Search for a heavy gauge boson W' in the final state with an electron and large missing transverse energy in pp collisions at $\sqrt{s} = 7$ TeV", *Phys. Lett.* **B698** (2011) 21–39, arXiv:1012.5945. doi:10.1016/j.physletb.2011.02.048.

[137] CMS Collaboration, "Search for a W' boson decaying to a muon and a neutrino in pp collisions at $\sqrt{s} = 7$ TeV", *Phys. Lett.* **B701** (2011) 160–179, arXiv:1103.0030. doi:10.1016/j.physletb.2011.05.048.

[138] ATLAS Collaboration, "Search for a heavy gauge boson decaying to a charged lepton and a neutrino in 1 fb-1 of pp collisions at sqrt(s) = 7 TeV using the ATLAS detector", *Phys. Lett.* **B705** (2011) 28–46, arXiv:1108.1316. doi:10.1016/j.physletb.2011.09.093.

[139] ATLAS Collaboration, "ATLAS search for a heavy gauge boson decaying to a charged lepton and a neutrino in pp collisions at $\sqrt{s} = 7$ TeV", *Eur. Phys. J.* **C72** (2012) 2241, arXiv:1209.4446. doi:10.1140/epjc/s10052-012-2241-5.

[140] CMS Collaboration, "Search for leptonic decays of W' bosons in pp collisions at $\sqrt{s} = 7$ TeV", *JHEP* **08** (2012) 023, arXiv:1204.4764. doi:10.1007/JHEP08(2012)023.

[141] ATLAS Collaboration, "Search for new particles in events with one lepton and missing transverse momentum in pp collisions at $\sqrt{s}$ = 8 TeV with the ATLAS detector", *JHEP* **09** (2014) 037, arXiv:1407.7494. doi:10.1007/JHEP09(2014)037.

[142] CMS Collaboration, "ECFA CMS Phase I and II Studies". Unpublished, Nov, 2015. https://twiki.cern.ch/twiki/bin/view/CMS/HiggsWG/Phase2UpgradeStudies?rev=63.

Acknowledgements

I would like to express my sincere gratitude to my advisor, Prof. Thomas Hebbeker, for his support and guidance throughout the research and for providing an environment that made this work possible. I am especially thankful for the opportunity for my research stay at CERN. I thank Prof. Christopher Wiebusch for agreeing on being the second referee of this thesis.

I want to thank Dr. Kerstin Hoepfner for her advise, commitment, and encouragement. Her leadership of the W′ team made the analysis so successful. My appreciation goes to all current and former members of this team, namely Sören Erdweg, Simon Knutzen, Viktor Kutzner, Klaas Padeken, Philipp Millet, Fabian Schneider, and Jan Schulte. We have worked as a team on this analysis and I have benefited a lot from this.

I also thank all the other members of the institute. I am very grateful for your support during my time in the institute. The extraordinary spirit among us coworkers made the research and work in the institute a pleasure every day. I'd like to mention especially those I have been directly working with: Andreas Albert, Michael Brodski, Deborah Duchardt, Matthias Endres, Thomas Esch, Andreas Güth, Markus Merschmeyer, Arnd Meyer, Paul Papacz, Holger Pieta, Tobias Pook, Markus Radziej, Stefan Schmitz, Daniel Theyssier, and Sebastian Thüer.

I also want to thank the administrative staff and the people from our IT department. You have provided an excellent service that I could profit from.

The experiment, this work is based on, is the labor of thousands people of the CMS collaboration. Thank you for providing the possibility to work with such an amazing machine and for being a supportive community.

I thank my parents, Brigitte Olschewski and Dr. Gerhard Olschewski, my brothers, Dr. Jörg Olschewski and Tim Olschewski, as well as Ina Simon for their unconditional support.